

Polymer-Clay Nanocomposites

The importance of particle
dimensions



© 2001 John Wiley & Sons, Inc. All rights reserved.

Stellingen

1. De hoge stijfheid en lage permeabiliteit van polymeer-klei nanocomposieten moeten worden toegeschreven aan de hoge aspectverhouding van de kleiplaatjes en niet aan hun extreem kleine afmetingen.
Dit proefschrift: Hoofdstukken 9 en 10.
2. Velen zien de Halpin-Tsai vergelijkingen als empirisch. Ze kunnen echter worden gerelateerd aan 'mean-field' en zelfconsistente modellen waardoor ze een brede toepasbaarheid hebben. Hierdoor zijn ze niet alleen geschikt voor de mechanische eigenschappen, maar ook voor de berekening van de diëlektrische- en transporteigenschappen van composieten.
Dit proefschrift: Appendix C.
3. De donkere lijnen in een TEM opname van een polymeer-klei nanocomposiet ontstaan niet door absorptie van elektronen, maar door interferentie van elektronengolven die verstrooid worden door de kleiplaatjes. Ze mogen daarom niet worden geïnterpreteerd als de doorsnedes van kleiplaatjes.
Dit proefschrift: Appendix D.
4. Het permeabiliteitsmodel van Fredrickson en Bicerano is niet correct, omdat voor lage concentraties aan vulstof, de permeabiliteit geen unieke functie is van het product van volumefractie en aspectverhouding.
G. H. Fredrickson en J. Bicerano, J. Chem. Phys. 110(4), 1999, p 2181-2188.
Dit proefschrift: Hoofdstuk 10.
5. De mate van exfoliatie van kleiplaatjes in een polymeer-klei nanocomposiet kan worden bepaald uit de stijfheid of uit de thermische uitzetting van het composiet, door modelleren. Een dergelijke bepaling is betrouwbaarder en eenvoudiger uit te voeren dan een TEM of röntgenanalyse.
Dit proefschrift: Hoofdstuk 3
6. In een unidirectioneel composiet versterken vezels beter dan plaatjes, omdat bij eenzelfde volumefractie en aspectverhouding de afstand tussen vezels kleiner is dan de afstand tussen plaatjes.
7. Elk composietmodel dat is gebaseerd op een twee-dimensionele voorstelling van een composiet, impliceert dat de vulstof oneindig lang is in de derde dimensie. De meeste onderzoekers onderkennen dit niet, wat leidt tot foute voorspellingen van bijvoorbeeld de mechanische en barrière eigenschappen van composieten.
J.E. Ashton, J.C. Halpin, P.H. Petit, Primer on composite materials: Analysis, Techn. Publ. Co., 1969
T. Matsuoka, Toyota Chuo Kenyusho R&D Rebyu 29(1), 1994, p 49-57.
D.M. Eitzman, R.R. Melkote and E.L. Cussler, AIChE Journal 42(1), 1996, p 2-9.
8. Als kleiplaatjes 10 tot 100 keer zo groot waren dan ze in werkelijkheid zijn, dan zouden nanocomposieten met veel klei nog altijd transparant zijn maar stijver en makkelijker verwerkbaar.
9. De meeste artikelen over 'shear thinning' gaan eigenlijk over 'shear rate thinning'.
10. Infraroodspectroscopie is uitermate geschikt voor een snelle en nauwkeurige bepaling van de oriëntatie, de kristallijne structuur en de moleculaire spanningen in polymeren.

Stellingen

11. Govindaraj e.a. introduceren een nieuwe functie om relaxatieverschijnselen te analyseren, door de tijdsconstante τ te modificeren tot $\tau^* = \tau^2/\omega^{1-\omega}$. Daar $0 < \omega < 1$, heeft τ^* niet langer de dimensie van tijd, waardoor de noodzakelijke dimensieloze schaling met de tijd t en de hoekfrequentie ω verloren gaat. Bovendien wordt de respons in het tijdsdomein complex, omdat τ^* complex is. De nieuwe relaxatiefunctie mist daardoor elke betekenis.
G. Govindaraj en R. Murugaraj, Mat. Sci. Eng. B77,2000, p 60-66
12. De energie die met een windturbine kan worden opgewekt, wordt primair bepaald door de lengte van de rotorbladen en niet door hun aantal.
13. De eenvoudige wereldwijde communicatie via het internet, zal leiden tot een toename van het vliegverkeer, net zo als de introductie van de computer leidde tot een toename van de papierconsumptie.
14. Als de dalende interesse voor techniek in het westen aanhoudt zal, in navolging van de industrie, ook het zwaartepunt van de exacte wetenschap naar Azië verhuizen.
15. Bestaande associaties in het brein van een volwassene helpen hem in het aanleren verwerken van nieuwe vaardigheden, maar hinderen hem in de perfecte beheersing ervan. Een kind met minder associaties in haar/zijn brein leert aanvankelijk langzamer, maar beheerst de nieuwe vaardigheden uiteindelijk tot een hogere graad van perfectie.
16. Terrorismebestrijding mag niet blijven steken in symptoombestrijding.
17. Ook vee moet het recht krijgen om ziek te worden.

Martin van Es

12 november 2001

Propositions

1. The high stiffness and low permeability of polymer-clay nanocomposites should be attributed to the high aspect ratio of the clay platelets and not to their extremely small size.
This thesis: Chapters 9 and 10.
2. Many regard the Halpin-Tsai equations as being empirical. They can however be related to mean-field and self-consistent models and therefore have a broad applicability. Therefore they are not restricted to the mechanical properties, but also allow calculation of the dielectric and transport properties of composites.
This thesis: Appendix C.
3. The dark lines in a TEM image of a polymer-clay nanocomposite are not the result of absorption of electrons, but rather of interference of electron waves that are diffracted by the clay platelets. They should therefore not be interpreted as the cross sections of clay platelets.
This thesis: Appendix D.
4. The permeability model of Fredrickson and Bicerano is incorrect, since at low filler concentrations, the permeability is not a unique function of the product of volume fraction and aspect ratio.
G. H. Fredrickson and J. Bicerano, J. Chem. Phys. 110(4), 1999, p 2181-2188
This thesis: Chapter 10.
5. The extent of exfoliation of clay platelets in a polymer-clay nanocomposite can be quantified from the stiffness or from the thermal expansion coefficient of the composite by composite modelling. Such an assessment is sounder and simpler to perform, than a TEM or X-ray analysis.
This thesis: Chapter 3
6. In a unidirectional composite fibres reinforce better than platelets do, since at the same volume fraction and aspect ratio, the interfibre distance is lower than the interplatelet distance.
7. Any composite model based on a two-dimensional representation of a composite, implies that the filler is infinitely long in the third dimension. Most researchers fail to recognise this, which leads to wrong predictions of e.g. the mechanical and transport properties of composites.
J.E. Ashton, J.C. Halpin, P.H. Petit, Primer on composite materials: Analysis, Techn. Publ. Co., 1969
T. Matsuoka, Toyota Chuo Kenyusho R&D Rebyu 29(1), 1994, p 49-57.
D.M. Eitzman, R.R. Melkote and E.L. Cussler, AIChE Journal 42(1), 1996, p 2-9.
8. If clay platelets were 10 to 100 times larger than they actually are, nanocomposites with a lot of clay would still keep their transparency, but would be stiffer and easier processable.
9. Most articles about 'shear thinning' actually deal with 'shear rate thinning'.
10. Infrared spectroscopy is suited eminently for a quick and accurate determination of the orientation, the crystalline structure and the molecular stresses in polymers.

Propositions

11. Govindaraj et al. propose a new function to analyse relaxation processes, by modifying the time constant τ to $\tau^* = \tau / t^{1-g}$, with $t = \sqrt{-1}$. Since $0 < g < 1$, τ^* no longer has the dimension of time, so that the necessary dimensionless scaling with time t and angular frequency ω is lost. Furthermore, the response in the time-domain becomes complex, because τ^* is complex. The new relaxation function therefore does not make any sense.
G. Govindaraj and R. Muruguraj, Mat. Sci. Eng. B77, 2000, p 60-66
12. The energy generated by a wind turbine is determined primarily by the length of the rotor blades, and not by their number.
13. The worldwide easy communication by the Internet, will lead to an increase in air traffic, just like the introduction of the computer led to an increase in paper consumption.
14. If the low interest for technology in the West continues, the centre point of science will follow that of the industry and shift towards Asia.
15. Existing associations in the brain of an adult will speed up the learning of new skills, but will hinder him in a perfect mastering of these skills. A child with fewer associations in its brain learns slower, but eventually masters the new skills to a higher level of perfection.
16. Fighting terrorism should not be limited to fighting symptoms.
17. Cattle too should get the right to become ill.

Martin van Es

12 November 2001

TR 3769

3769

766508

31010 91

Polymer-Clay Nanocomposites

The importance of particle dimensions

Proefschrift

ter verkrijging van de graad van doctor
aan de Technische Universiteit Delft,
op gezag van de Rector Magnificus prof. Ir. K.F. Wakker,
voorzitter van het College voor Promoties,
in het openbaar te verdedigen
op maandag 12 november 2001 om 13.30 uur
door



Martin Antonius van Es

Ingenieur Fysische Techniek
Geboren te Amsterdam

Dit proefschrift is goedgekeurd door de promotor:

Prof. dr. ir. J. van Turnhout

Samenstelling promotiecommissie:

Rector magnificus

Prof. dr. ir. J. van Turnhout

Prof. dr. ir. F. H. J. Maurer

Prof. dr. ir. R. Marissen

Prof. dr. ir. E. van der Giessen

Prof. dr. G. Groeninckx

Prof. dr. ir. J.J. Elmendorp

Dr. A. Gusev

Voorzitter

Technische Universiteit Delft, promotor

Universiteit Lund

Technische Universiteit Delft / DSM

Rijksuniversiteit Groningen

Katholieke Universiteit Leuven

Technische Universiteit Delft

Eidgenössische Technische Hochschule Zürich

Voor mijn vader

Summary	xi
1 General introduction	1
1.1 The quest for better polymer properties	1
1.2 Polymer-clay nanocomposites	2
1.3 Platelet reinforced composites	3
1.4 Why do nanocomposites have good properties?	4
1.5 Composite modelling	5
1.6 Objectives of research described in this thesis	5
1.7 Scope of thesis	5
1.8 References	7
2 Making polymer-clay nanocomposites	9
2.1 What is a nanocomposite?	9
2.2 What is clay?	10
2.3 Separating the clay layers	11
2.4 References	11
3 Theory	13
Abstract	13
3.1 General theory for the elastic properties of anisotropic materials	13
3.2 Composite models for the elastic properties of platelet filled materials	17
3.2.1 Stiffness of a material filled with unidirectional inclusions	17
3.2.2 Stiffness of a material with non-aligned inclusions	27
3.2.3 Approximation for composites with randomly oriented fibres or platelets	33
3.2.4 Correcting Halpin-Tsai equations for platelet reinforcement	36
3.2.5 Composite models to describe visco-elastic behaviour	39
3.3 Thermal expansion of two-phase composites	39
3.4 References	43
4 Validation of composite models	45
Abstract	45
4.1 Introduction	46
4.2 Validation of composite models by comparison with experimental results	46
4.3 Validation of Mori-Tanaka model by comparison with finite element model	50
4.3.1 Finite element computer program Palmyra	50
4.3.2 Platelets in a matrix: analytical versus finite element calculations	51
4.4 Conclusions	53
4.5 References	54

5	Preparation of materials	55
	Abstract	55
5.1	Preparation of PA6/clay nanocomposites	55
5.1.1	Materials	55
5.1.2	Extruding the master batch	56
5.1.3	Diluting the master batch	57
5.2	Preparation of HDPE-clay nanocomposites	57
5.2.1	Materials	57
5.2.2	Preparation of HDPE nanocomposites on a mini-extruder	57
5.2.3	Preparation of HDPE nanocomposites on a kneader	58
5.3	References	58
6	Clay morphology and polymer mobility	59
	Abstract	59
6.1	TEM analysis of nanocomposites	60
6.1.1	Sample preparation	60
6.1.2	Quantitative data from TEM analysis	60
6.1.3	TEM images of PA6-nanocomposites	61
6.1.4	TEM images of HDPE nanocomposites	72
6.2	Polymer mobility of nanocomposites measured by solid state NMR	73
6.2.1	Short introduction into ^1H -NMR T_2 relaxation spectroscopy	74
6.2.2	Experimental	75
6.2.3	NMR results	77
6.2.4	Evaluation of NMR results	81
6.3	Conclusions	81
6.4	References	82
7	Melting and crystallisation of nanocomposites	83
	Abstract	83
7.1	Introduction	84
7.2	PA and PA6/6T6I nanocomposites	84
7.2.1	Materials and experimental techniques	85
7.2.2	DSC results	85
7.2.3	FTIR-results	87
7.2.4	Explanation for the decrease in melting temperature upon addition of clay	93
7.2.5	Explanation for the existence of a high temperature melting transition	93
7.2.6	Crystallisation behaviour	94
7.2.7	Evaluation of the melting and crystallisation behaviour	94
7.3	PE nanocomposites	95
7.3.1	Materials and experimental techniques	95
7.3.2	DSC results	95
7.4	Conclusions	98
7.5	References	99

8 Dielectric properties of nanocomposites	101
Abstract	101
8.1 Introduction	102
8.2 Theory	102
8.2.1 The dielectric constant	102
8.2.2 Relaxation mechanisms	103
8.3 Experiments	105
8.3.1 Sample preparation	105
8.3.2 Dielectric measurements	105
8.4 Results and discussion	106
8.4.1 Relaxation mechanisms	106
8.4.2 Activation energy fine structure	112
8.5 Conclusions	113
8.6 References	114
9 Mechanical properties of nanocomposites	115
Abstract	115
9.1 Viscoelastic properties of compression moulded PA6 nanocomposites	116
9.1.1 Preparation of samples and experimental technique	116
9.1.2 DMA results	116
9.2 Mechanical properties of injection moulded PA6-nanocomposites	123
9.2.1 Flexural and tensile modulus of injection moulded PA6 nanocomposites.	124
9.2.2 Yield stress and toughness of PA6-nanocomposites	125
9.3 Thermal expansion of PA6-nanocomposites	126
9.3.1 Procedure to determine the thermal expansion coefficient	126
9.3.2 Modelling the thermal expansion of PA6-nanocomposites.	127
9.4 Visco-elastic properties of compression moulded PE-clay nanocomposites	129
9.4.1 Materials	129
9.4.2 DMA measurements	129
9.4.3 DMA results	129
9.5 Discussion	133
9.6 Conclusions	134
9.7 References	134
10 Permeability of nanocomposites	135
Abstract	135
10.1 Introduction	136
10.2 Elementary diffusion theory	137
10.2.1 Fick's first and second law of diffusion	137
10.3 Modelling of diffusion in a material filled with impenetrable platelets	139
10.3.1 Relationship between permeability and diffusivity	139

10.3.2	Similarities between diffusion models for platelet filled composites	140
10.3.3	Analytical models for transport properties of platelet filled composites	141
10.3.4	Random walk simulation of transport through platelet filled composites	151
10.3.5	Effect of polydispersity of platelet diameters	152
10.4	Effect of misalignment of platelets on diffusivity	153
10.5	Diffusion of water in PA6 nanocomposites	155
10.5.1	Absorption measurement and determination of diffusivity	155
10.6	Evaluation and conclusions	157
10.6.1	Evaluation	157
10.7	Conclusions	160
10.8	References	160
11	Rheology of nanocomposites	163
	Abstract	163
11.1	Introduction	164
11.1.1	Conventional particulate filled polymers	164
11.1.2	Nanocomposites	166
11.1.3	Scope	166
11.2	HDPE with nano- and micrometer particles of low aspect ratio	167
11.2.1	Preparation	167
11.2.2	Morphology	170
11.2.3	Rheology	171
11.2.4	Conclusions on HDPE with low aspect ratio particles	173
11.3	HDPE-nanocomposites with clay platelets of high and low aspect ratio	174
11.3.1	Materials	174
11.3.2	The effect of clay aspect ratio on the rheology of HDPE nanocomposites	174
11.3.3	Conclusions on HDPE nanocomposites	176
11.4	PA6 with nano- and micrometer particles of high and low aspect ratio	176
11.4.1	Small strain shear rheology	177
11.4.2	Large strain shear rheology	178
11.4.3	Comparing small strain and large strain shear viscosities	178
11.4.4	Extensional rheology	181
11.4.5	Discussion	181
11.5	Conclusions	183
11.6	References	184
Appendix A:	Eshelby's equivalent inclusion method	185
A.1	The elastic field in an inclusion with an eigenstrain	185
A.2	The elastic field in an inhomogeneity	186
A.3	Eshelby's Tensor	187
A.3.1	Spheroid with axes a_1, a_2, a_3 ; $a_1=a_2$, $\alpha=a_3/a_1$ in an isotropic matrix	187
A.3.2	Spheroid with axes a_1, a_2, a_3 ; $a_1=a_2$, $\rho=a_1/a_3$ in an anisotropic matrix	188
A.3.3	Expressing the Eshelby tensor as a 6x6 matrix	189

A.4	Matlab subroutines to calculate Eshelby's tensor	189
A.4.1	Isotropic matrix	189
A.4.2	Anisotropic matrix	190
A.5	References	192
Appendix B:	Numerical calculation of composite stiffness	193
B.1	Transforming tensors into matrices	193
B.2	Rotating a matrix	196
B.3	MATLAB computer programs	198
B.3.1	The Mori-Tanaka function	199
B.3.2	The functions 'material' and 'orthomat'	201
B.3.3	Functions to calculate the Eshelby tensor	201
B.3.4	Function to average a matrix	202
B.3.5	Rotation of the matrices	204
B.3.6	Integration of the matrices	205
B.4	References	206
Appendix C:	Universal use of composite models	207
C.1	Models for mechanical, dielectrical and transport properties	207
C.2	Conclusions	208
C.3	References	208
Appendix D:	Errors in data analysis of nanocomposite TEM images	209
D.1	Determining the volume fraction from TEM images	209
D.2	Why are clay platelets depicted as single lines in a TEM image?	211
D.3	Conclusions	212
Appendix E:	Time and frequency response of composites	213
E.1.	Linear systems and Fourier or Laplace transformation	213
E.2.	The correspondence principle	214
E.3.	Practical calculation of the time response of composites.	214
E.4	References	215
List of abbreviations		217
List of symbols		219
Samenvatting		I
Curriculum Vitae		V
Dankwoord		VI
Index		VII

What is a polymer-clay nanocomposite?

A polymer-clay nanocomposite is a polymer that contains nanometer sized clay particles. Such a nanocomposite can have favourable properties, like high stiffness and barrier resistance. The best properties are obtained if the clay is fully exfoliated into single clay layers with a thickness of about one nanometer and a diameter of 20-500 nanometers.

During exfoliation, the clay particles do not only become much smaller but simultaneously their shape changes from cubical blocks to flat platelets. The shape of a clay platelets is usually expressed in its aspect ratio. This is the ratio between the diameter and the thickness of a platelet.

As a result of their small dimensions, the clay platelets have a large specific surface area of about 700 m²/g. Their small size also results in small inter platelet distances in a polymer-clay nanocomposite. At a loading of 1 weight percent of clay these distances are about 250 nanometers while they are merely 10 nanometers at a loading of 20 weight percent.

Why do nanocomposites have good properties?

In the scientific literature the favourable properties of polymer-clay nanocomposites are often assigned to the extreme small dimensions of the clay platelets. It is argued that in a nanocomposite most of the polymer molecules are in direct contact with clay platelets. This changes the behaviour of the polymer molecules in such a way that the resultant nanocomposite material obtains favourable properties. According to this argument the aspect ratio of the clay platelets is of minor importance.

Doubt about this hypothesis gave rise to start the research described in this thesis. This doubt was instigated by the knowledge that the properties of conventional (micro)composites, with fibres or platelets of a few micrometers or larger, mainly originate from the high aspect ratio of the fibres or platelets and not from their absolute size. Furthermore, it is known that an adsorbed polymer layer on the surface of a filler usually has a thickness of 1 to 5 nanometers. Thus, in conventional nanocomposites with distances between clay platelets in the order of 100 nanometers it could be assumed that this adsorbed phase would be of minor importance.

In this thesis we will discuss which properties of polymer-clay nanocomposites originate from the small dimensions (high specific surface area) of the clay platelets and which from their high aspect ratio.

The effect of particle shape and particle size can be distinguished by comparing the properties of nanocomposites with those of microcomposites or with the results of micromechanical composite calculations. Mica platelets strongly resemble clay platelets in their shape and crystal structure. However, their absolute size is about 1000 times larger. Hence, the reason for the use of mica based microcomposites as reference throughout this thesis.

Since the aspect ratios of the reference mica platelets always deviate somewhat from that of the clay platelets, a direct comparison of properties is difficult. A scientifically correct comparison of the properties of nanocomposites and microcomposites can be performed, by using mathematical composite models. With composite models the properties of composites can be calculated.

Objectives of the research described in this thesis

- Determine which properties of polymer-clay nanocomposites originate from the small dimensions of the clay platelets and which from their high aspect ratio.
- Develop and validate composite models for the calculation of the elastic and barrier properties of platelet-reinforced composites.
- Determine how clay platelets influence the properties of polymer-clay nanocomposites, like stiffness, thermal expansion, crystallisation, gas diffusion, rheology and dielectric relaxation.
- Gain insight in the differences between nanocomposites and microcomposites by direct comparison of their properties and by using composite models.

Development and validation of a mechanical composite model for platelet reinforcement

For the calculation of the stiffness and thermal expansion of platelet-reinforced polymers the Mori-Tanaka model was chosen. In principle this analytical micromechanical model is only suited for composites with perfectly oriented platelets. By using an orientation distribution function also a random orientation can be accounted for.

Since the practical use of the Mori-Tanaka model and of the orientation distribution function is rather cumbersome, some simplified theories are introduced. These tools enable us to perform composite calculations quickly and accurately.

To test the validity of the Mori-Tanaka model the results of this model are compared with experimental results of microcomposites. The Mori-Tanaka results are also compared to the results of finite element calculations. Both the experimental data and finite element results indicate that the Mori-Tanaka model gives reliable predictions of stiffness and thermal expansion of platelet filled composites.

Morphology of nanocomposites and mobility of the polymer phase

Two series of nanocomposites were made by extruding either polyamide-6 or polyethylene together with clay. The clay was pretreated so as to aid dispersion in the polymers. In the test series with polyamide-6 the amount of clay platelets was varied and in the series with polyethylene their aspect ratio was varied.

The shape and dispersion of clay platelets in the polymers was made visible by transmission electron microscopy (TEM). Scrutiny of the dark lines in TEM pictures of polymer-clay nanocomposites reveal that they are not a direct image of the clay platelets, but instead are the result of the interference of electron waves. Care has to be taken with the interpretation of TEM pictures from polymer-clay nanocomposites.

The mobility of the polymer phase in nanocomposites is studied with proton solid-state nuclear magnetic resonance experiments (NMR). *A part of the polymer phase in polyamide-6-clay nanocomposites appears to be as mobile as a low molecular liquid.* By increasing the weight percentage of clay the amount of polymer with high mobility rises. At 20 weight percent of clay about 10 percent of the polyamide-6 phase is as mobile as a liquid.

Thermal behaviour of nanocomposites

The crystallisation and melting behaviour of polyamide-6 and polyethylene nanocomposites was analysed with differential scanning calorimetry (DSC) and with infrared spectroscopy (IR). DSC was used to determine the melting temperatures and IR to define the types of crystals.

The polyamide-6 nanocomposites appear to have three distinct melting points near 212 °C, 225°C and 240°C. Usually polyamide-6 contains solely α -crystalline material that melts near 225 °C. *By addition of clay two new phases emerge with melting points below and above that of the α -crystalline phase.* The melting point of the low-melting phase lies at 212°C and that of the high-melting phase at 240 °C.

The low melting phase is already mentioned in the literature and is assigned to γ -crystalline material. The high melting phase has not been mentioned before. Infrared spectroscopy reveals that this phase also consists of γ -crystalline material.

The high melting point probably emerges because part of the γ -crystalline phase is confined between the clay platelets and consequently experiences a restricted mobility. Therefore, a higher temperature is required to melt this part of the γ -crystalline phase ($T_m = \Delta H/\Delta S$, ΔS decreases so T_m increases).

Dielectric behaviour of nanocomposites

The mobility and relaxation mechanisms of the polymer phase in polyamide-6-clay nanocomposites were determined with dielectric relaxation spectroscopy (DRS). For this purpose measurements were performed at frequencies between 0.11 and 960 kHz and temperatures between -130 and 200 °C.

The most important difference with unfilled polyamide-6 is that nanocomposites show a second 'glass' transition at about 40 °C below the usual glass transition. The strength of this transition increases as the amount of clay increases. Dynamic mechanical analysis (DMA) confirms the existence of this transition.

By studying the activation energy it can be concluded that confinement is a relative notion and is determined by the temperature and frequency of the measurement. At low temperatures and high frequencies the polymer does not show any confinement, because movement then occurs at a length scale that is smaller than the distance between clay platelets. Confinement only shows up at high temperatures and low frequencies, when molecular motions require a length scale larger than the distance between clay platelets.

Stiffness and thermal expansion of nanocomposites

The stiffness of polyamide-6-clay nanocomposites and polyethylene-clay nanocomposites was determined by dynamic mechanical analysis (DMA) and by tensile testing. Both types of nanocomposites become stiffer with further addition of clay.

At low clay content (<5 weight percent), the stiffness of nanocomposites derived experimentally, corresponds to the stiffness of polymer-mica microcomposites and is correctly predicted by composite models. *The measurements and calculations show that the high stiffness of nanocomposites mainly originates from the high aspect ratio of the clay platelets and not from their small size (high specific surface area).*

The stiffness of nanocomposites with more than 10 weight percent of clay is lower than that of corresponding polymer-mica microcomposites. At these loadings, composite models overestimate the stiffness of polymer-clay nanocomposites. The low effectiveness of clay at high loadings is attributed to the smaller distance between clay platelets at these loadings, as is observed by transmission electron microscopy. For instance, above 10 weight percent the distance between the clay platelets is smaller than 20 nm. As a result, the effective aspect ratio of the clay platelets decreases, while at the same time a highly mobile polymer phase appears in the confined space between clay platelets. Confinement also leads to lower crystallinity and crystal perfection of the crystalline polymer phase. All these effects can only result in a lower stiffness of the polymer-clay nanocomposite.

Contrary to statements in the scientific literature, the small dimensions of the clay platelets result in a lower stiffness of the nanocomposite.

Theoretical considerations show that the thermal expansion coefficient and stiffness of a composite are closely related. The stiffer the composite, the lower the thermal expansion will be, while the composite will expand most in the direction of lowest stiffness. It is found that the theory accurately predicts the relationship between the thermal expansion and stiffness of polyamide-6-clay nanocomposites.

Barrier properties of nanocomposites

Clay platelets in nanocomposites are known to retard the diffusion of gases or liquids. In order to determine which mechanisms are responsible for the retardation of diffusion, the water uptake of a series of polyamide-6-clay nanocomposites has been monitored. The diffusion coefficient of water in the PA6-nanocomposites was determined by assuming simple Fickian diffusion.

The permeability of polymer-clay nanocomposites was compared with the predictions of composite models. To this end several analytical models, found in the literature, were analysed that relate permeability to the morphology of multi-phase materials. Since none of the models could predict the permeability of platelet filled composites at high volume fractions, a new model was developed. This model is a combination of Brydges model, which is suitable for ribbons at high volume fractions and Hatta's model suitable for platelets at low volume fractions. The results of this new theory agree with the results of finite element calculations.

By the modification of Nielsen's transport equation, an expression is generated to estimate the effect of misalignment of platelets on diffusivity. This expression reveals that random alignment of clay platelets can seriously decrease the barrier resistance (diffusivity) of nanocomposites.

The good agreement between experiment and Hatta's model suggests that mainly the aspect ratio and the amount of clay platelets determine the barrier resistance of nanocomposites. *Changes in polymer properties, due to the high specific surface area of the clay platelets, do not significantly change the barrier resistance of PA6-clay nanocomposites.*

Rheology of nanocomposites

The effects of the size and aspect ratio of clay platelets on the rheological behaviour of nanocomposites were investigated. For this purpose, polyamide-6 and polyethylene were filled with spheres and platelets with dimensions between 10^{-9} and 10^{-4} m. The rheology of these materials is determined under shear deformation and tensile deformation.

The visco-elastic behaviour of polymer nanocomposites in the molten state proves to be very different from that in the solid state. *Contrary to the behaviour in the solid phase it is found that in the molten state, the effect of particle size on visco-elasticity is strong, whereas the effect of clay aspect ratio is small.*

Unlike microcomposites, nanocomposites have a high melt strength and high melt viscosity, which do not collapse at large shear deformation. Two mechanisms are suggested to explain these effects: tethering of polymer chains on the clay platelets and the existence of an electrical double layer on the clay platelets.

General introduction

1.1 The quest for better polymer properties

In polymer research, there is a continuous search towards cheap, readily processable materials that are stiffer, stronger, tougher and lighter. In the early days of polymer research, the main route to achieve improved properties was by polymerisation of new monomers. Later, co-polymerisation of different monomers or blending of polymers further improved these properties. Although a wide variety of properties can be achieved this way, the ultimate properties of pure, non-oriented polymers are limited. High strength and stiffness can only be achieved by orientation of polymer chains, as is done in aramide, carbon and polyethylene fibres. These fibres have mechanical properties that are about 100 times better than their non-oriented counterparts. If properly oriented, polymer fibres are stronger than steel at a much lower weight.

The properties of non-oriented polymers are often improved by adding stiff particles or stiff and strong fibres. They are then referred to as compounds or composites. Compounds and composites are analogous to concrete, which is reinforced by gravel or steel bars.

By incorporating long, high strength fibres into a thermosetting polymer matrix, high-performing composites can be made with a strength and stiffness comparable to those of metals. The low weight and high strength of polymer composites makes them ideal for use in space- or aircraft, and in sports utilities like skis, tennis rackets and golf-clubs. So in general high performance composites are used in applications that combine optimum strength with low weight and where price is of minor importance. The use of high performance composites is still limited, because of their high price and labour-intensive production.

Easy processable composites can be made by incorporating short fibres into a thermoplastic matrix like a polyamide or polyester. Strength and stiffness of these relatively cheap and easily processable 'thermoplastic composites' are inferior to those of high performance composites because, during processing, fibres seriously break down and fibre orientation is difficult to control.

Thermoplastic composites are being used extensively in automotive and E&E (electronic & electrical) applications like door handles, air intake manifolds, connectors and power tools. All these applications require high strength, high processing throughput and freedom of design at a moderate price.

Polymers are also being filled with cheap, low performing inorganic materials like chalk, clay or talc. These so called 'polymer compounds' generally show a moderate increase in stiffness compared to that of the neat polymer, while keeping the low price and ease of processing. Polymer compounds are being used even more extensively than thermoplastic composites because of their very low price and attractive properties. Applications of polymer compounds are found in many products like car bumpers, garden furniture and PVC pipes.

Polymer-clay nanocomposites are a relatively new class of reinforced polymers with particles that are about 1000 times smaller than in conventional composites and compounds.

Polymer-clay nanocomposites possess a unique combination of properties. They have relatively high strength and stiffness, combine high barrier resistance and good flame retardancy and can be processed easily. Nanocomposites also offer the possibility to obtain composite properties without drastically affecting optical transparency. At present, a few commercial applications exist like films for food packaging, high barrier bottles, body panels of cars and engine covers.

1.2 Polymer-clay nanocomposites

Nanocomposites can be defined as materials filled with particles that are smaller than 100 nm in at least one dimension. They can be obtained by dispersing small particles in a material or by creation of filler particles during processing. In general, nano-sized particles can reinforce a material, nucleate crystallisation or increase viscosity. Nano-sized particles are also known to increase the resistance against transport of liquids or gases and the resistance against fire. In electrical applications nanoparticles can make a material (semi) conductive or add special magnetic properties to a material [1].

Nanocomposites are not restricted to polymers. This can be illustrated by the versatile list of materials that is found by using the word 'nanocomposite' as the keyword in a literature search. Some of the hits are listed below:

- Nano-sized ceramic particles in metals
- Materials with a designed molecular architecture
- Materials with nano-sized crystals
- Carbon nano-tubes in polymers
- Nano-structured semiconductors
- Well dispersed clay platelets in polymers

The list of materials carrying the name 'nanocomposites' is rather extensive. Hence, it is necessary to specify to which kind of nanocomposite one is referring. In this thesis, only polymer-clay nanocomposites are considered. Throughout this thesis, often simply 'nanocomposites' is used to refer to 'polymer-clay nanocomposites'. Polymer-clay nanocomposites have a polymer matrix filled with fully separated layers of clay.

Layered silicates, like smectic clays, talc and mica have since long been used as inexpensive fillers for polymers. In conventional filled polymers these fillers are only partly broken up during mixing, resulting in a phase with dimensions ranging from 0.5 μm to 100 μm . The properties of these polymer compounds are marginally better than those of unfilled polymers. In polymer-clay nanocomposites the silicate is dispersed much more finely, resulting in a polymer filled with silicate platelets with dimensions in the order of $1 \times 100 \times 100$ nanometer and a surface area of about 700 square meters per gram. The silicate platelets in polymer-clay nanocomposites are not only much smaller than in polymer compounds, also their aspect ratio (width/thickness) is much larger.

In 1987, Okada et al. [2] reported about making a PA6-clay nanocomposite. They first made the clay compatible with the PA6 by modifying it with an organic ammonium salt. Subsequently caprolactam was polymerised in the presence of the modified clay. Since this first publication, research groups all over the world, have synthesised many other nanocomposites. Giannelis [3] and Lagaly [4] wrote extensive overview articles on the preparation and properties of nanocomposites. A general overview on polymer-clay nanocomposites is also given in a recent book edited by Pinnavaia and Beall [5].

In Table 1.1, some examples of polymer-clay nanocomposites are listed. The table also mentions the procedures used to make the nanocomposites; the polymerisation route, the melt-compounding route or the solution blend route. In the polymerisation route,

nanocomposites are made by polymerising monomers in the presence of organically modified clay. Nanocomposites can also be made by melt compounding or solution mediated routes. In the melt-compounding route, organically modified clay is mixed with a polymer in an extruder. The solution-blending route consists of dissolving a polymer and organically modified clay in a mutual solvent and subsequently removing the solvent.

Type of polymer in polymer-clay nanocomposite	Route to make nanocomposite	References
Polyamide-6	Polymerisation	2, 6
Epoxy	Polymerisation	7, 8
Poly (methyl methacrylate)	Polymerisation	9, 10
Poly (ϵ -caprolactone)	Polymerisation	11
Polyurethane	Polymerisation	12
Polyimide	Polymerisation	13, 14
Polyamide 12	Polymerisation	15
Polyester	Polymerisation	16, 17
Polyamide-6	Melt compounding	18, 19
Polypropylene	Melt compounding	20, 21
Polyethylene	Melt compounding	22
Polyamide-66	Melt compounding	23
Polypropylene	Solution blending	24
Polyethylene	Solution blending	25
Poly (vinyl-pyrrolidone)	Solution blending	26
Poly (vinyl alcohol)	Solution blending	27
Poly (ethylene oxide)	Solution blending	28

Table 1.1 Selection of polymer nanocomposites made since the first publication on PA6-clay nanocomposites in 1987.

Nanocomposites show an improvement of properties at much lower filler contents than in conventional polymer compounds. At a filler content of 3-4 weight%, a PA6-clay nanocomposite shows mechanical stiffness, dimension stability and barrier properties normally found in a conventional 20 weight% PA6-clay compound [28,29]. Nanocomposites also offer extra benefits like low density, good melt flow, better surface properties, improved dimension stability, flame-retardant properties and recyclability.

1.3 Platelet reinforced composites

Between 1965 and 1985 a lot of research was undertaken on composites reinforced with platelets [30-36]. The general idea was that platelets with high aspect ratio could reinforce in two directions while fibres can only reinforce in one direction. Therefore, reinforcement by platelets would give better isotropic properties than fibres. The barrier properties of platelet reinforced composites also got attention in those days. Most research was performed on mica-reinforced plastics. In addition, glass platelets, aluminium diboride, steel discs, aluminium platelets and silicon carbide platelets received some attention. In general, platelet-reinforced composites were found to increase stiffness, dimensional stability and barrier properties.

The early enthusiasm was damped because impact strengths of platelet-reinforced composites were low. Also serious decrease of aspect ratio and incomplete wetting of the platelets occurred during extrusion and injection moulding, which led to poor properties.

However, impressive properties were obtained, by avoiding the decrease of aspect ratio, using elaborate compression moulding techniques [30, 31]. By filling a styrene-acrylonitrile copolymer with 50 vol% of mica, using compression moulding, a flexural modulus of 53.1 GPa and a flexural strength of 207 MPa was obtained. These excellent properties illustrate the potential of platelet reinforcement.

1.4 Why do nanocomposites have good properties?

Since the discovery of nanocomposites numerous publications on nanocomposites have appeared. Most authors only show the results of synthesis and characterisation of nanocomposites. It is remarkable that only a few authors try to explain the properties of nanocomposites.

Giannelis [3] points at the large aspect ratio and orientation of the filler particles and stresses the importance of the interface. Kojima [28] suggests that the properties may depend on ion-bonding strength and orientation of the polymer and the clay. He proposes an empirical mixing law that relates stiffness to the fraction of constrained polymer material. Hui et al. [37] also stresses the importance of the interface. He uses composite modelling to calculate the stiffness of nanocomposites. Yano et al. [13] uses a quantitative model to explain the effect of aspect ratio on the diffusional properties of nanocomposites. Kuchta et al. [38] suggests that thermal stability, tensile modulus and barrier properties are intimately related to the crystal structure and to the permanent attachment of polymer chains to the surface of the clay platelets. Shelley [39] concludes that the high stiffness, strength and barrier properties of nanocomposites are a consequence of the presence of a constrained fraction of polymer with high stiffness.

The research described in this thesis was started because I doubted that the properties of nanocomposites mainly depend on the presence of a constrained polymer phase. This doubt was instigated by the knowledge that the properties of conventional (micro)composites, with fibres or platelets of a few micrometers or larger in size, mainly originate from the high aspect ratio of the fibres or platelets.

Furthermore it is known that the thickness of an absorbed polymer layer on polymer-filler interface usually has a thickness of 1 to 5 nanometers [35]. In conventional nanocomposites, with distances between clay platelets in the order of 100 nanometers or more, the amount of absorbed polymer will therefore be small, only a few percent. It was therefore anticipated that the absorbed (confined) phase would have a minor influence on the properties of nanocomposites, like stiffness and barrier resistance.

Generally, the properties of nanocomposites can be affected by two morphological parameters: the size and the aspect ratio of the clay layers. The size is important because small particles have a higher specific surface area and thus create more polymer interphase than large particles. The aspect ratio is of importance because clay layers with large aspect ratios are more effective in reinforcing a polymer than layers with small aspect ratio.

Much can be learned by comparing the properties of nanocomposites with those of conventional platelet reinforced composites. The surface area of platelets in conventional composites is about 1000 times smaller than in nanocomposites. Therefore, the amount of interphase in conventional platelet reinforced composites can be neglected. This offers a possibility to study which properties of nanocomposites are caused by the small size of the platelets and which are not.

In this thesis we will discuss which properties of polymer-clay nanocomposites originate from the small dimensions (high specific surface area) of the clay platelets and which from their aspect ratio.

1.5 Composite modelling

It is well known that the mechanical properties of fibre filled composites can be calculated mathematically by composite modelling. In particular, the stiffness of fibre filled composites can be predicted accurately. For this calculation, knowledge is required about the orientation and the aspect ratio of the fibres. In addition, the properties of the fibres and polymer matrix must be known.

Not much is known about the micromechanical modelling of platelet-reinforced composites. Only a few models that account for platelet reinforcement can be found in the literature [36-37, 40-44]. Most models for platelet reinforcement are not validated by comparison with experimental results. Therefore the reliability of these models is questionable. So, before performing composite modelling on nanocomposites, a reliable composite model must be found for platelet reinforcement. This model should also include the effect of platelet orientation and prove its reliability by comparison with experiments.

1.6 Objectives of research described in this thesis

- Determine which properties of polymer-clay nanocomposites originate from the small dimensions of the clay platelets and which from their high aspect ratio.
- Develop and validate composite models for the calculation of the elastic and barrier properties of platelet-reinforced composites.
- Determine how clay platelets influence the properties of polymer-clay nanocomposites, like stiffness, thermal expansion, crystallisation, gas diffusion, rheology and dielectric relaxation.
- Gain insight into the differences between nanocomposites and microcomposites by direct comparison of their properties and by using composite models.

1.7 Scope of thesis

This thesis essentially consists of three parts. In the first part some theoretical composite models are introduced. The second part discusses the morphology and molecular mobility of nanocomposites while in the last part the knowledge of all preceding chapters about composite modelling, morphology and molecular mobility is applied to explain the mechanical, diffusional and rheological properties of nanocomposites.

Chapter 2 explains how polymer-clay nanocomposites are made. We describe what nanocomposites are and which problems are encountered in making nanocomposites. To understand the formation of nanocomposites, some indispensable knowledge about the chemical and crystalline structure of layered silicates is given. Several strategies to separate clay layers are explained.

The necessary mathematical tools to calculate the elastic properties of platelet-reinforced composites are developed in Chapter 3. A general introduction in continuum mechanics is presented. Continuum mechanics is used to derive a theoretical model that uses spheroidal particles to calculate the elastic properties of unidirectional composites. By adapting the aspect ratio of the spheroids, the model can be made suitable for fibre, sphere and platelet filled composites. It is shown that, by a proper choice of parameters, the empirical Halpin-Tsai model coincides with the more elaborate tensor based theoretical model. An orientation distribution function is introduced to account for the effect of platelet orientation.

The procedure of orientation averaging is greatly simplified by introduction of a simple model that calculates the effect of random orientation on stiffness. An exact tensor model is introduced to determine the expansion coefficient of a two-phase composite.

In Chapter 4 the models introduced in Chapter 3 are validated. Two methods are used for validation of the theoretical models. In the first method, the experimental stiffness of conventional platelet filled composites is compared to the stiffness predicted by composite modelling. The second method relies on finite element calculations to check the validity of the analytical models introduced in Chapter 3.

In Chapter 5 the preparation PA6 and PE nanocomposites is described that are used throughout this thesis. A detailed description is given of the types of polymers and clays used and of the compounding details used to make the nanocomposites.

The central theme of Chapter 6 is the morphology of the clay platelets and the mobility of the polymer phase in the nanocomposites. The morphology of nanocomposites is studied by Transmission Electron Microscopy (TEM). TEM images visualise the separation of clay platelets, their length and their orientation. A critical evaluation is given on how to extract quantitative information from TEM images of nanocomposites. An extended evaluation on this subject is given in Appendix D. The mobility of the polymer phase in polyamide-6 nanocomposites was studied with solid state NMR spectroscopy.

Another morphological feature of nanocomposites is the crystallinity of the polymer phase. In Chapter 7 the effect of nano-dispersed clay platelets on the crystalline structure of the polymer matrix is discussed. DSC and FTIR-techniques are used to determine the effect of polymer confinement on melting and crystallisation. A theory is given that qualitatively explains the remarkable experimental results.

The mobility of polymer chains that are confined between clay platelets is studied by dielectric relaxation spectroscopy in Chapter 8. A short introduction on the effect of frequency and temperature on dielectric transitions is given. Calculation of the activation energy fine structure enables a detailed study of the cooperative motion of polymer chains near the glass-transition. The effect of confinement on the extent of cooperative motion is studied. A qualitative explanation is given to explain the observed results.

In Chapter 9 the elastic properties of some polymer-clay nanocomposites are discussed and compared with theoretical calculations. The effects of clay loading and clay-orientation on the elastic properties are studied by DMA measurements and tensile tests. Parameters like the aspect ratio of the clay platelets and polymer crystallinity are used to quantitatively explain the observed stiffness and expansion coefficient of nanocomposites.

Clay platelets form a barrier against transport of gases or liquids through nanocomposites. In Chapter 10 the effect of clay morphology on the barrier resistance of nanocomposites is studied by comparing diffusion measurements with theoretical results. First, it is explained how diffusion measurements are performed and evaluated. Next, several theoretical models that predict diffusion are introduced and discussed. A new model to predict diffusion through a composite filled with platelets is introduced. The validity of this model is checked by comparing its results with the results of finite element modelling. A theory is introduced to evaluate the effects of polydispersity and misalignment on diffusion. The diffusion of water in PA6 nanocomposites is determined and compared to theoretical predictions. Results found in literature about water transmission through polyimide nanocomposites are also discussed.

Chapter 11 deals with the melt rheology of nanocomposites. This is done by measuring the rheology of polyethylene and polyamide-6 that are filled with spheres and platelets of varying sizes and aspect ratios. Rheological properties of nano-composites with nanometer sized spheres and platelets are compared to micro-composites with micrometer-sized particles. Aspect ratios varied between 1 and 200 and particle sizes between 1 nm and 10 μm .

The special features of nanocomposite rheology become evident by comparing the rheological properties of nanocomposites with those of microcomposites.

1.8 References

- [1] D.Y. Godovski, *Electron behaviour and magnetic properties of polymer nanocomposites*, Adv. Pol. Sci. **119**, 1995, p 79-122
- [2] A. Okada et al, *Synthesis and characterisation of a nylon-6 clay hybrid*, Polym. Prepr. **28**, 1987, p 447-448
- [3] E.P. Giannelis, *Polymer layered nanocomposites*, Adv. Mater. **8**, 1996 p 29-35
- [4] G. Lagaly, *Introduction: from clay mineral-polymer interaction to clay mineral-polymer nanocomposites*, Appl. Clay Sci. **15**, 1999, p 1-9
- [5] T.J. Pinnavaia and G.W. Beall eds, *Polymer-Clay Nanocomposites*, Wiley, Chichester, 2000
- [6] Y. Kojima et al, *One-pot synthesis of nylon 6-clay hybrid*, J. Pol. Sci. A Pol. Chem. **31**, 1993 p 1755-1758
- [7] P.B. Messerschmidt, E.P. Giannelis, *Synthesis and characterisation of layered silicate-epoxy nanocomposites*, Chem. Mater. **6**, 1994, p 1719
- [8] M.S.Wang and T.J. Pinnavaia, *Clay-polymer nanocomposites formed from acidic derivatives of montmorillonite and an epoxy resin*, Chem. Mater. **6**, 1994, p 468-474
- [9] Dong Choo Lee and Lee Wook Jang, *Preparation and characterisation of PMMA-clay hybrid composite by emulsion polymerization*, J. Appl. Pol. Sci. **61**, 1996, p 1117-1122
- [10] L. Biasci et al, *Functionalisation of montmorillonite by methyl methacrylate polymers containing side chain ammonium cations*, Polymer **35(15)**, 1994, p 3296-3304
- [11] P. Messerschmidt and E. Giannelis, *Polymer layered silicate nanocomposites: in situ intercalative polymerization of caprolactone in layered silicates*, Chem. Mater. **5**, 1993, p 1064-1066
- [12] C. Zilg, R. Thomas, R. Mülhaupt and J. Finter, *Polyurethane nanocomposites containing laminated anisotropic organophilic layered silicates*, Adv. Mater. **11(1)**, 1999, p 49-52
- [13] K. Yano, A. Usuki, A. Okada, *Synthesis and properties of polyimide-clay hybrid films*, J. Pol. Sci. A: Pol. Chem. **35(11)**, 1997, p 2289-2294
- [14] T. Lan, P.D. Kaviratna, T.J. Pinnavaia, *On the nature of polyimide-clay hybrid composites*, Chem. Mater. **6**, 1994, p 573-575
- [15] P. Reichert, J. Kressler, R.Thomann, R.Mülhaupt and G.Stöppelmann, *Nanocomposites based on synthetic layered silicate and polyamide-12*, Acta Polymer. **49**, 1998, p 116-123
- [16] X. Kornmann, L.A. Berglund, J.Sterte, *Nanocomposites based on montmorillonite and unsaturated polyester*, Pol. Eng. Sci. **38(8)**, 1998, p 1351-1358
- [17] J.C. Matayabas, S.R. Turner, *High I.V. polyester compositions containing platelet particles*, Patent WO 98/29499 Eastman Chemicals
- [18] R. Korbee, *Process for the preparation of polyamide nanocomposite composition*, Patent Appl. WO 99/29767 DSM
- [19] L. Liu, Z. Qi, X. Zhu, *Studies on nylon 6/clay nanocomposites by melt intercalation process*, J. Appl. Pol. Sci. **71**, 199, p 1133-1138
- [20] M. Kato, A. Usuki, A. Okada, *Synthesis of polypropylene oligomer clay intercalation compounds*, J. Appl. Pol. Sci. **66**, 1997, p 1781-1785
- [21] A. Usuki, M. Kato, A. Okada, *Synthesis of polypropylene-clay hybrid*, J. Appl. Pol. Sci. **67**, 1997, p 137-139
- [22] F.D. Kuchta, P. J. Lemstra, A. Keller, L. F. Batenburg, H.R. Fischer, *Materials with improved properties from polymer-ceramic nanocomposites*, MRS proceedings April Meeting 1999, San Francisco, USA.

- [23] L.A. Goettler, D.W. Recktenwald, *Nylon nanocomposites: Performance attributes and potential applications*, Proceedings of Additives '98, Orlando, Florida, USA, Feb. 17, 1998
- [24] Y. Kurokawa, H. Yasuda, A. Oya, *Preparation of a nanocomposite of polypropylene and smectite*, J. Mat. Sci. Letters **15**, 1996, p 1481-1483
- [25] H.G. Jeon, H.T. Jung, S.W. Lee, S.D. Hudson, *Morphology of polymer/silicate nanocomposites; High density polyethylene and a nitrile copolymer*, Polymer Bulletin **41**, 1998, p 107-113
- [26] G.W. Beall, A. Sorokin, S. Tsipursky, A. Goldman, *Intercalates and exfoliates formed with oligomers and polymers and composite materials containing same*, Patent EP0747451A2
- [27] N. Ogata, S. Kawakage, T. Ogiwara, *Poly(vinyl alcohol)-clay and poly(ethylene oxide)-clay blends prepared using water as solvent*, J. Appl. Pol. Sci. **66**, 1997, p 573-581
- [28] Y. Kojima et al, *Mechanical properties of nylon 6-clay hybrid*, J. Mat. Res. **8**(5), 1993, p 1185-1189
- [29] Y. Kojima et al, *Sorption of water in nylon 6-clay hybrid*, J. Appl. Pol. Sci. **49**, 1993, p 1259-1264
- [30] F.W. Maine and P.D. Shepherd, *Mica reinforced plastics: a review*, Composites, Sept. 1974, p 193-200
- [31] J. Lusi, R.T. Woodhams and M. Xanthos, *The effect of platelet aspect ratio on the flexural properties of mica reinforced plastics*, Pol. Eng. Sci. **13**(2), 1973, p 139-145
- [32] B. Glavinchevski and M. Piggot, *Steel disc reinforced polycarbonate*, J. Mat. Sci. **8**, 1973, p 1373-1382
- [33] H.S. Katz and J.V. Milewski, *Handbook of Fillers and Reinforcements for Plastics*, van Nostrand Reinhold, New York, 1978, section VIII, p 331-370.
- [34] J.E. Ashton, J.C. Halpin, P.H. Petit, *Primer on Composite Materials: Analysis*, Technomic Publishing Co., 1969, Chapter 5
- [35] F.H.J. Maurer, R. Kosfeld and T. Uhlenbroich, *Interfacial interaction in kaolin-filled polyethylene composites*, Colloid. Polym. Sci. **263**(8), 1985, p 624-630
- [36] Tai Te Wu, *The effect of inclusion shape on the elastic moduli of two-phase material*, Int. J. Solids Structures **2**, 1966, p 1-8.
- [37] C.Y. Hui and D. Shia, *Simple formula for the effective moduli of unidirectional aligned composites*, Pol. Eng. Sci. **38**(5), 1998, p 774-782.
- [38] F.D. Kuchta, P. J. Lemstra, A. Keller, L. F. Batenburg, H.R. Fischer, *Polymer crystallisation studied in confined dimensions using nanocomposites from polymers and layered minerals*, MRS Proceedings April Meeting 1999 San Francisco, USA
- [39] J. S. Shelley, *Mechanical Reinforcement and Environmental Effects on a Nylon6/Clay Nanocomposite*, PhD Thesis University of Utah, May 2000, See also J.S. Shelley, P.T. Mather and K.L. DeVries, Polymer **42**, 2001, p 5849-5858
- [40] T.S. Chow, *Elastic moduli of filled polymers: The effect of particle shape*, J. Appl. Phys. **48**(10), 1977, p 4072-4075.
- [41] G.E Padaver, and N. Beecher, *On the strength and stiffness of planar reinforced plastic resins*, Pol. Eng. Sci. **10**(3), 1970, p 185-192
- [42] V.R. Riley, *Interaction Effects in Fiber Composites*, Polymer Conf. Series, Univ. of Utah, June 1970
- [43] G.P. Tandon and G.J. Weng, *The effect of aspect ratio of inclusions on the elastic properties of unidirectionally aligned composites*, Pol. Comp. **5**(4), 1984, p 327-333.
- [44] T. Mori and K. Tanaka, *Average stress in matrix and average elastic energy of materials with misfitting inclusions*, Acta Metall. **21**, 1973, p 571-574.

Making polymer-clay nanocomposites

2.1 What is a nanocomposite?

To make polymer-clay nanocomposites, all the clay particles must be fully separated into individual layers of clay. This so-called 'exfoliation' process is depicted in Fig. 2.1.

Exfoliating clay in a polymer is not simple. To understand the extent of this problem, think of clay particles as a thick book. Each page in the book represents an individual silicate layer with a thickness of 1 nanometer. The pages of the book are glued together. The problem to make polymer-clay nanocomposites is comparable to individually disperse all the pages of the book in a pool of viscous liquid.

To solve this problem first the glue between the pages must be dissolved and subsequently the book must be put in the pool and stirred vigorously to separate the pages. Polymer-clay nanocomposites are made like wise. First the bonds between individual clay layers are broken (intercalation) and subsequently all clay layers are dispersed in a polymer (exfoliation).

In 1987 researchers at Toyota succeeded in exfoliating the stacked layers of a montmorillonite clay into a PA6 matrix [1]. It was found that the well-dispersed layers had a high aspect ratio and strongly reinforced the nylon. To understand how to weaken the bond between clay layers and how to completely disperse individual clay platelets in a polymer, some knowledge of the crystalline structure of layered silicates is essential.

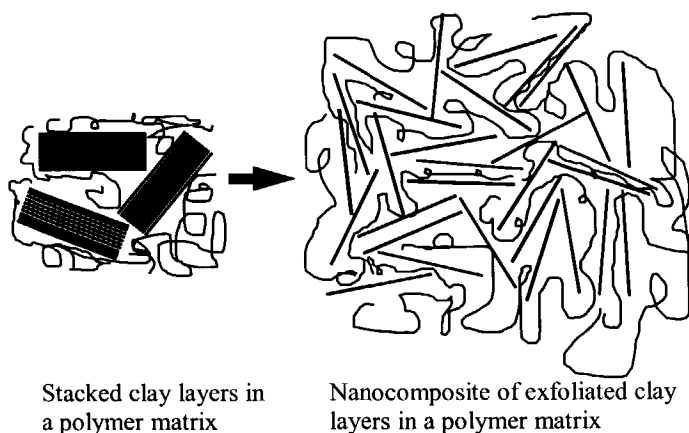


Figure 2.1 Exfoliation of primary clay layers in a polymer matrix

2.2 What is clay?

Layered silicates as talc, mica, and smectic clays are built up of regularly stacked layers, each having a thickness d_0 of about 1 nanometer and a length of about 50-1000 nanometers. All these layered silicates have the same crystalline structure. Each layer is built up of three sheets, two sheets on the outside of the layer and one sheet in the middle of the layer. Therefore this group of materials is referred to as 2:1 layered silicates. The sheets on the outside are made of interconnected SiO_4 tetrahedrals, while the inner sheet has an octahedral configuration and contains metal cations like Al^{3+} or Mg^{2+} and hydroxyl groups. Fig. 2.2 shows a schematic drawing of a 2:1 layered silicate.

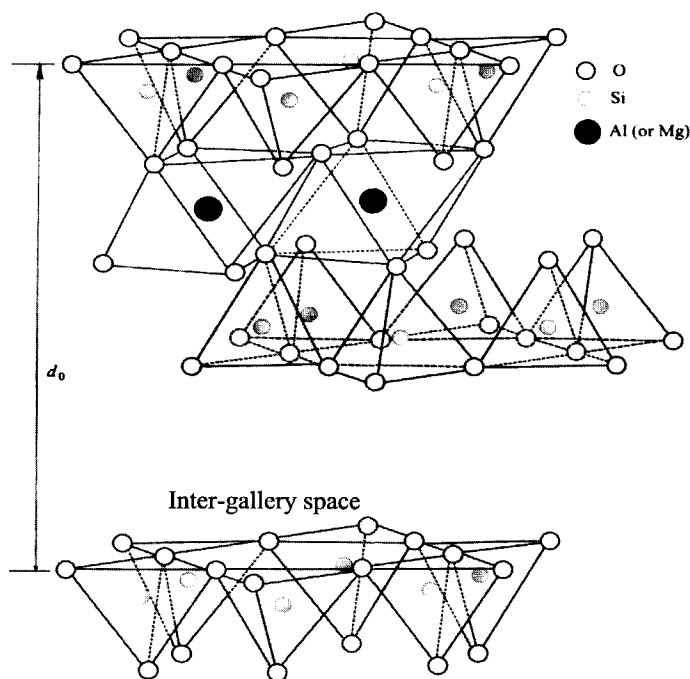


Figure 2.2 Crystalline structure of a 2:1 layered silicate

In talc all sites in the inner sheet are occupied by Mg^{2+} [2] and all sites in the outer sheets by $\text{Si}^{(4+)}$. By substitution of Mg^{2+} in a talcum crystal by Al^{3+} , Fe^{2+} , or Fe^{3+} , a mica or a smectic clay crystal is obtained. Hence the different types of 2:1 layered silicates only differ in the amount and kind of metal cations incorporated in the crystal. In talc, with all sites in the inner sheet occupied by Mg^{2+} , the crystal is electrostatically neutral. Owing to the absence of ionic attraction in a talcum crystal, the talcum layers are relatively easy to separate by mechanical action. Therefore, talcum is one of the softest silicates known.

In smectic clays and mica not all octahedral sites are occupied by cations. This results in negatively charged silicate layers. Between the silicate layers of mica and smectic clays, cations as Na^+ , Ca^{2+} or K^+ act as counter charges in the inter-gallery space and provide a strong ionic bond between adjacent layers. More information about clays can be found in [2].

2.3 Separating the clay layers

Already in 1974, Maine [3] thought about single clay layers as a potential reinforcing material for polymers. He rejected the idea because he thought that clay clusters could not be broken into separate layers. Indeed dispersing forces in an extruder usually are not high enough to break the ionic bonds between clay-layers. Therefore, it is impossible to make polymer-clay nanocomposites by simple mechanical action.

Fortunately some of the 2:1 clays, like hectorite, montmorillonite and saponite can be swollen in water. Their ionic charge is just high enough to let water enter the inter-gallery space and swell the clay. During this swelling procedure the distance between the clay platelets is increased and the strength of the ionic bond is decreased. Talc cannot be swollen in water because it has no inter-gallery-cations. This renders the talc crystal hydrophobic, making it impossible for water to enter the inter-gallery space. Mica has a too high concentration of interlayer cations. This makes the bond strength between the clay layers too large for water to enter the inter-gallery space.

The simplest way to make nanocomposites is to swell the clay in water in the presence of a polymer. Based on this principle Korbee [4] managed to make PA6-clay nanocomposites by addition of water to a PA6-clay compound while being extruded.

In most cases the clay must first be made compatible with the polymer to make a nanocomposite. To do this, first the clay is swollen in water. Next organic molecules are inserted between the clay layers, by exchanging the original inter-layer cations by organic cations or by addition of organic molecules with chemical groups that form complexes with the cations [5]. This process is called intercalation and leads to swollen clays with a relatively small (1-40 Å) distance between the layers. The amount of cations that can be exchanged is expressed in the cation exchange capacity. The cation exchange capacity of a typical sodium montmorillonite is in the order of 80 to 140 milli-equivalents per 100 grams of clay.

After removing the water, the clay layers stay separated to some extent because of the presence of the organic molecules. This lowers the ionic interaction between the clay platelets and provides an environment that is compatible with polymers. By insertion of polymers (or monomers) into the swollen inter-layer space, completely exfoliated layers can be obtained and a nanocomposite is made. For a general overview of the synthesis, characterisation and properties of polymer-clay nanocomposites one is referred to the book of Pinnavaia and Beal [6].

2.4 References

- [1] A. Okada et al, *Synthesis and characterisation of a PA6-clay hybrid*, Polym. Prepr. **28**, 1987, p 447-448
- [2] G.W. Brindley and G. Brown, *Crystal Structures of Clay Minerals and their X-ray Identification*, Mineralogical Society, 1980
- [3] F.W. Maine and P.D. Shepherd, *Mica reinforced plastics: a review*, Composites September 1974, p 193-200
- [4] R. Korbee, *Process for the preparation of polyamide nanocomposite composition*, Patent Appl. WO 99/29767 DSM
- [5] References in table 1.1 of this thesis.
- [6] T.J. Pinnavaia and G.W. Beall eds., *Polymer-Clay Nanocomposites*, Wiley, Chichester, 2000.

Abstract

In this chapter the necessary tools will be presented to calculate the mechanical stiffness and thermal expansion of platelet filled composites. First a general introduction is given into continuum mechanics, introducing all the terms used for modelling the elastic properties of a nanocomposite. Next some models for unidirectional platelet reinforced composites are introduced. In nanocomposites, perfect alignment is seldom found. It will be shown that this can be accounted for by introducing an orientation distribution function. Since in most cases the mathematics behind composite models and randomisation of the orientation are complicated, simple to use approximations are given to calculate the stiffness of composites with uni-axial as well as randomly oriented inclusions.

3.1 General theory for the elastic properties of anisotropic materials

In order to explain the terminology used throughout this thesis, a short introduction is given in continuum mechanics. A more extensive explanation is given by Ward [1] and Hearmon [2].

As is shown in Fig. 3.1, three stresses P_x , P_y and P_z can be distinguished that are acting on an infinitesimal small cube. Each stress can be resolved into 3 components:

$$\begin{aligned} P_x &= \sigma_{xx} + \sigma_{xy} + \sigma_{xz} \\ P_y &= \sigma_{yx} + \sigma_{yy} + \sigma_{yz} \\ P_z &= \sigma_{zx} + \sigma_{zy} + \sigma_{zz} \end{aligned}$$

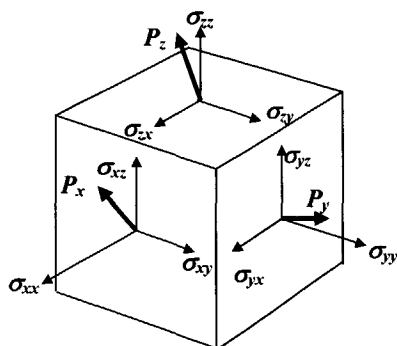


Figure 3.1 Stresses acting on an infinitesimal cube

Part of this chapter is published in:

M. van Es, F. Xiqiao, J. van Turnhout and E. van der Giessen, *Comparing Polymer-Clay Nanocomposites with Conventional Composites using Composite Modelling in Specialty Polymer Additives*, ed. by S.Al-Malaika, A. Golovoy, C.A. Wilkie, Blackwell Science, Oxford, 2001, Ch 21, p 391-413

Here the first subscript refers to the plane on which the stress acts and the second subscript to the direction of the stress. A plane is defined by the direction of the normal to that plane. For example σ_{xy} acts on the plane perpendicular to the x direction while the force on this plane is directed in the y-direction. In an elastic body, stresses and strains are related by Hooke's law:

$$\begin{aligned}\sigma_{xx} &= C_{xxxx}\epsilon_{xx} + C_{xxyy}\epsilon_{yy} + C_{xxzz}\epsilon_{zz} + C_{xxyz}\epsilon_{yz} + C_{xxzy}\epsilon_{zy} + C_{xxzx}\epsilon_{xz} + C_{xxzx}\epsilon_{zx} + C_{xxxy}\epsilon_{xy} + C_{xxyx}\epsilon_{yx} \\ \sigma_{yy} &= C_{yyxx}\epsilon_{xx} + C_{yyyy}\epsilon_{yy} + C_{yyzz}\epsilon_{zz} + C_{yyyz}\epsilon_{yz} + C_{yyzy}\epsilon_{zy} + C_{yyxz}\epsilon_{xz} + C_{yyzx}\epsilon_{zx} + C_{yyxy}\epsilon_{xy} + C_{yyyx}\epsilon_{yx} \\ &\vdots \\ \sigma_{yx} &= C_{yxxx}\epsilon_{xx} + C_{yxyy}\epsilon_{yy} + C_{yxzz}\epsilon_{zz} + C_{yxyz}\epsilon_{yz} + C_{yxzy}\epsilon_{zy} + C_{yxcz}\epsilon_{xz} + C_{yxzx}\epsilon_{zx} + C_{yxcy}\epsilon_{xy} + C_{yycx}\epsilon_{yx}\end{aligned}$$

Or in tensor notation:

$$\sigma_{ij} = C_{ijkl} \epsilon_{kl} \quad (3.1)$$

where σ_{ij} and ϵ_{kl} are the stress and strain components and C_{ijkl} the elastic stiffnesses. In the summation convention used in tensor notation, a product like $C_{ijkl} \epsilon_{kl}$ represents the sum of all possible combinations of repeated indices. The indices can take the values 1, 2 and 3 representing the x, y, and z directions respectively. In the notation used above 81 elastic stiffness-components C_{ijkl} can be distinguished.

The inverse relation is given by:

$$\epsilon_{xx} = S_{xxxx}\sigma_{xx} + S_{xxyy}\sigma_{yy} + S_{xxzz}\sigma_{zz} + \dots \text{etc.}$$

or in tensor notation:

$$\epsilon_{ij} = S_{ijkl} \sigma_{kl} \quad (3.2)$$

where S_{ijkl} are the elastic compliance's. The relationship between C_{ijkl} and S_{ijkl} can be written as:

$$S_{ijpq} C_{pqkl} = (\delta_{ik} \delta_{jl} + \delta_{il} \delta_{jk})/2 \quad (\delta_{ik} = 1 \text{ if } i=k; \delta_{ik} = 0 \text{ if } i \neq k) \quad (3.3)$$

The total torque on the body in Fig. 1 must be zero to prevent the body from spinning, therefore: $\sigma_{xy} = \sigma_{yx}$; $\sigma_{xz} = \sigma_{zx}$ and $\sigma_{yz} = \sigma_{zy}$, leaving 6 independent stresses acting on the cube. This reduces the 81 compliances and stiffnesses to 36. By using the strain energy function, it can be shown that both S_{ijkl} and C_{ijkl} must be symmetric:

$$C_{ijkl} = C_{klij} \text{ and } S_{ijkl} = S_{klij} \quad (3.4)$$

leaving 21 independent constants for a general elastic solid.

Since only 6 independent stresses and strains exist, often an abbreviated nomenclature is used with only 6 stress and strain components. In this nomenclature the subscripts ij are replaced by a single subscript:

$$xx \text{ or } 11 = 1, yy \text{ or } 22 = 2, zz \text{ or } 33 = 3, yz \text{ or } 23 = 4, xz \text{ or } 13 = 5 \text{ and } xy \text{ or } 12 = 6 \quad (3.5)$$

A large advantage of this condensed *engineering notation* is that all elastic relationships between stress and strain can now be represented as a 6x6 matrix instead as a tensor with 81 components. Using condensed subscripts the generalised Hooke's law can be written as:

$$\sigma_p = C_{pq} e_q \quad (3.6)$$

or equivalently:

$$e_p = S_{pq} \sigma_q \quad (3.7)$$

Instead of tensor strain components ϵ_{ij} , now engineering strains e_p are used. Using tensor notation, strain is defined as:

$$\epsilon_{ij} = \frac{1}{2} \left(\frac{\partial u_i}{\partial x_j} + \frac{\partial u_j}{\partial x_i} \right) \quad (3.8)$$

where u_i is the displacement in the i -direction. When using engineering components of strain, shear strain is defined as the angle γ of deformation shown in Fig. 3.2. Due to this definition, engineering components of shear strain are *twice* as large as the components of shear strain used in tensor notation. The following relation exists between tensor strain and engineering strain:

$$\epsilon_{ij} = e_{ij} \text{ if } i = j \text{ and } \epsilon_{ij} = \frac{1}{2} e_{ij} \text{ if } i \neq j \quad (3.9)$$

where e_{ij} is the engineering strain.

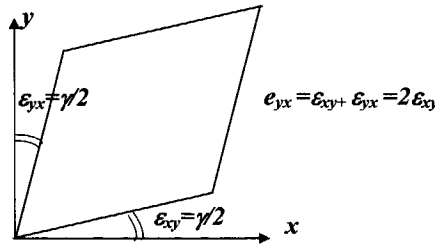


Figure 3.2 Definition of shear deformation using engineering components of strain

In the literature often a mixed notation for engineering strain is used, i.e. e_4 is written as e_{yz} etc. In doing calculations, one should be therefore careful to check if tensor or engineering strains are used.

In a general anisotropic material, 21 independent elastic constants can be distinguished. If the anisotropic material contains planes or axis of symmetry, the amount of independent elastic constants is much reduced. If the x , y and z directions are parallel to the symmetry directions, the material has an orthorhombic symmetry (3 orthogonal planes of symmetry) and the engineering stiffness relation can be written as:

$$\begin{pmatrix} \sigma_1 \\ \sigma_2 \\ \sigma_3 \\ \sigma_4 \\ \sigma_5 \\ \sigma_6 \end{pmatrix} = \begin{pmatrix} C_{11} & C_{12} & C_{13} & 0 & 0 & 0 \\ C_{12} & C_{22} & C_{23} & 0 & 0 & 0 \\ C_{13} & C_{23} & C_{33} & 0 & 0 & 0 \\ 0 & 0 & 0 & C_{44} & 0 & 0 \\ 0 & 0 & 0 & 0 & C_{55} & 0 \\ 0 & 0 & 0 & 0 & 0 & C_{66} \end{pmatrix} \begin{pmatrix} e_1 \\ e_2 \\ e_3 \\ e_4 \\ e_5 \\ e_6 \end{pmatrix} \quad (3.10)$$

And the engineering compliance relation as:

$$\begin{pmatrix} e_1 \\ e_2 \\ e_3 \\ e_4 \\ e_5 \\ e_6 \end{pmatrix} = \begin{pmatrix} S_{11} & S_{12} & S_{13} & 0 & 0 & 0 \\ S_{12} & S_{22} & S_{23} & 0 & 0 & 0 \\ S_{13} & S_{23} & S_{33} & 0 & 0 & 0 \\ 0 & 0 & 0 & S_{44} & 0 & 0 \\ 0 & 0 & 0 & 0 & S_{55} & 0 \\ 0 & 0 & 0 & 0 & 0 & S_{66} \end{pmatrix} \begin{pmatrix} \sigma_1 \\ \sigma_2 \\ \sigma_3 \\ \sigma_4 \\ \sigma_5 \\ \sigma_6 \end{pmatrix} \quad (3.11)$$

It can be shown that for an orthorhombic material the compliance engineering constants S_{ij} can be written as:

$$\begin{aligned} S_{11} &= 1/E_{11} & S_{12} &= -\nu_{12}/E_{11} & S_{13} &= -\nu_{13}/E_{11} \\ S_{21} &= -\nu_{21}/E_{22} = S_{12} & S_{22} &= 1/E_{22} & S_{23} &= -\nu_{23}/E_{22} \\ S_{31} &= -\nu_{31}/E_{33} = S_{13} & S_{32} &= -\nu_{32}/E_{33} = S_{23} & S_{33} &= 1/E_{33} \\ S_{44} &= 1/G_{23} & S_{55} &= 1/G_{13} & S_{66} &= 1/G_{12} \end{aligned} \quad (3.12)$$

$$\nu_{ij} = \nu_{ji}(E_{ij}/E_{ii})$$

An orthorhombic material thus has nine independent elastic constants i.e.: E_{11} , E_{22} , E_{33} , G_{23} , G_{13} , G_{12} , ν_{23} , ν_{13} , ν_{12} . Where E_{11} , E_{22} and E_{33} are the Young's moduli in the x, y and z directions, G_{23} , G_{13} and G_{12} are the shear moduli in the yz, xz and xy planes and ν_{23} , ν_{13} and ν_{12} are the Poisson's ratios. The Poisson's ratio is a measure of the strain in the direction perpendicular to the applied strain. If a strain is applied in the m-direction the strain in the n-direction becomes: $e_n = -\nu_{mn}e_m$; $n, m = 1, 2, 3$.

The relationships between C_{ij} and E , G and ν are more complicated. They can easily be calculated though, by using $S_{ij} = C_{ij}^{-1}$.

If the material possesses transverse symmetry around the z-axis, as is shown in Fig. 3.3 then the properties in the x and y directions are equal. This is a special type of symmetry with $E_{11} = E_{22}$; $G_{13} = G_{23}$; $\nu_{13} = \nu_{23}$ and $G_{12} = E_{11}/2(1 + \nu_{12}) = 2(S_{11} - S_{12})$. This reduces the amount of independent constants to five i.e.: E_{11} , E_{33} , G_{13} , ν_{13} and ν_{12} .

In an isotropic material the properties in all directions are equal so: $E_{11} = E_{22} = E_{33} = E$; $\nu_{12} = \nu_{13} = \nu_{23} = \nu$ and $G_{12} = G_{23} = G_{13} = G = E/(2 + 2\nu)$. Now the amount of independent elastic constants is reduced to two: E and ν .

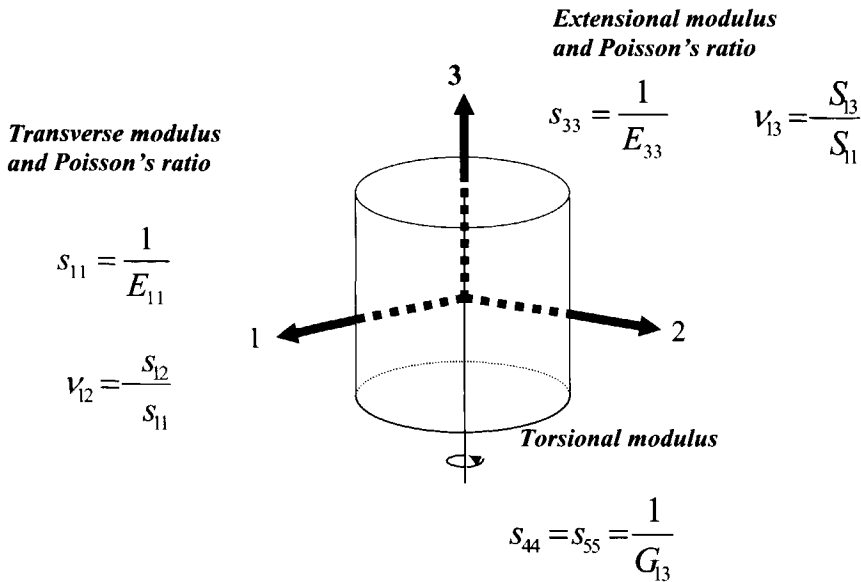


Figure 3.2 The elastic constants of a material with transverse symmetry

3.2 Composite models for the elastic properties of platelet filled materials

In a composite often three phases can be distinguished; a matrix, a filler and a matrix-filler interface. The mechanical and morphological properties of these phases determine the mechanical properties of the composite. According to present-day composite theory the elastic properties of a polymer composite are determined by the shape, volume fraction and mechanical properties of polymer, filler and polymer-filler interface. Particle size doesn't enter the equations for calculation of the elastic properties [3].

Most composite models assume isotropic properties of the constituent phases. If the mechanical and morphological properties of the constituents are known, properties like stiffness and thermal expansion can be predicted.

An excellent review about composite models is given by Hull [4]. More recently Aboudi [5] reviewed the theoretical background of frequently used composite models. Beside mechanical properties and thermal expansion, composite models can also be used to estimate mass diffusion, thermal conductivity, electrical conductivity, magnetic permeability and optical properties of polymers [6-8].

For fibres and spheres, approximate equations have been derived which have proven to accurately predict stiffness and thermal expansion [4,5,9,10]. Also for platelets a number of equations is available [9, 11-19]. Probably because of its simplicity, Padaver and Beecher's theory [12] is the most used theory for platelet reinforcement.

3.2.1 Stiffness of a material filled with unidirectional inclusions

In this section, three models will be introduced to calculate the stiffness a composite: the Halpin-Tsai model, the Mori-Tanaka model and the Takanayagi model. The Halpin-Tsai

model is an empirical model that is often used to calculate the stiffness of fibre-reinforced materials. The Mori-Tanaka model is a theoretical, micromechanical model that enables calculation of the stiffness of fibre, sphere and plate reinforced composites.

By using the results of the Mori-Tanaka model, the Halpin-Tsai model will be adapted for calculation of the stiffness of platelet-reinforced composites.

The Takanayagi model is a theoretical model that greatly oversimplifies the true stress fields in a composite. Here it is extended to 3 dimensions and mainly used to gain understanding about the factors that determine the reinforcement of a composite.

3.2.1.1 Halpin-Tsai model for unidirectional fibre reinforced composites

In Fig. 3.4 a material with unidirectional short fibres is depicted. This material possesses fibre symmetry around the 3-axis. As explained before, the amount of independent elastic constants then is five. Most models in the literature either only give a limited number of elastic constants, or are mathematically rather complicated to use. The most used and very simple set of equations to calculate the elastic constants of a unidirectional short fibre composite is given by Halpin and Tsai. The advantage of the Halpin-Tsai's theory over other short-fibre theories is that it is the only simple theory that gives predictions of all elastic constants over a broad range of volume fractions, making it possible to do 3 dimensional (3D) calculations.

All the five elastic constants of a unidirectional short fibre composite can be estimated by using Halpin-Tsai's equations [9]:

$$\frac{M_c}{M_m} = \frac{(1 + \zeta \eta c_r)}{(1 - \eta c_r)} \quad 3.13)$$

where

$$\eta = \frac{(\frac{M_r}{M_m} - 1)}{(\frac{M_r}{M_m} + \zeta)} \quad 3.14)$$

in which M_c is the composite Young's or shear modulus E_{11} , E_{33} , G_{12} or G_{13} . M_r is the corresponding filler modulus E_r or G_r and M_m the corresponding matrix modulus E_m or G_m .

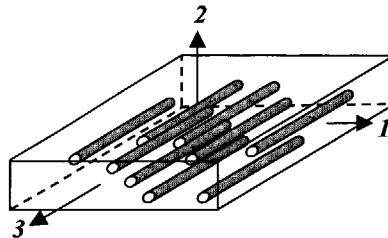


figure 3.4 Schematic drawing of a unidirectional short-fibre filled composite

c_r is the volume fraction of filler. ζ is a factor that depends on the shape of the filler particle and on the type of modulus to be calculated. The shape factor ζ can be fitted to experimental results. Ashton et al. [9] fitted the shape factor to theoretical equations for

ribbon reinforcement and found that the equations can also be used to predict fibre reinforcement. They advised the following shape factors to be used for fibre reinforcement.

To calculate:	E_{33}	use	$\zeta = 2 l/d$ (l = length of fibre, d is thickness).3.15)
	E_{11} , or E_{22}	use	$\zeta = 2$
	G_{12}	use	$\zeta = 1/(3-4\nu_m)$
	G_{13} or G_{32}	use	$\zeta = 1$

Note that ζ depends on which modulus is calculated. The Poisson ratios can be calculated with the equations below:

$$\begin{aligned} \nu_{31} = \nu_{32} &\approx c_r \nu_r + (1-c_r) \nu_m & 3.16) \\ \nu_{12} = \nu_{21} &= (E_{11}/2G_{12}) - 1 \\ \nu_{13} = \nu_{23} &= \nu_{31} E_{11}/E_{33} \end{aligned}$$

3.2.1.2 Mori-Tanaka method for unidirectional composites

As mentioned before many theories have been proposed to calculate the elastic properties of composites. In the simplest approach, particle-particle interactions are neglected. This is valid for diluted systems. By increasing the volume fraction or aspect ratio of the inclusions the distance between the inclusions is decreased. This leads to overlapping stress fields of neighbouring inclusions and accordingly leads to stronger particle-particle interactions. Since the primary clay platelets in nanocomposites have very high aspect ratios, the composite model used must account for particle-particle interactions.

A very useful model to calculate the reinforcement of isotropic particles in an isotropic matrix is given by Tandon and Weng [17]. On a purely theoretical basis, Tandon et al. derived closed form analytical equations to calculate the stiffness of a material filled with aligned spheroidal particles. The theory is a combination of Eshelby's equivalent inclusion method [18] and of Mori-Tanaka's average stress theory [20]. By using either prolate or oblate spheroids, Tandon's theory can predict the reinforcing effect of fibres, spheres and platelets.

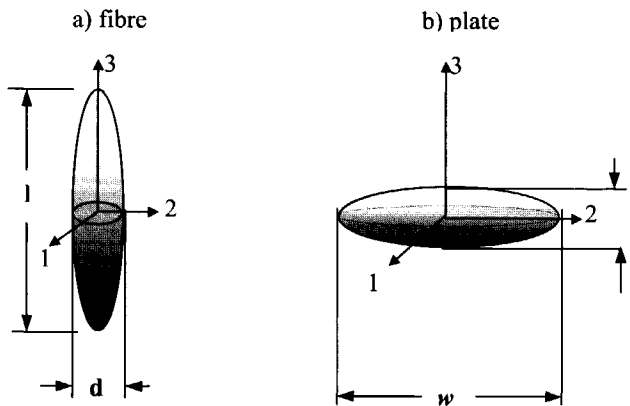


Figure 3.5 Spheroids representing a fibre or a plate

Figs. 3.5a and 3.5b show spheroids shaped like a fibre and like a plate respectively. The theory presumes that there is no direct contact between filler particles. It is a large

improvement compared to an earlier theory for ellipsoid reinforcement derived by Chow [6] that is limited to dilute systems. Much theoretical background on this subject was reviewed and completed by Mura [21]. He also suggested a more general scheme that will be presented below. It was introduced by Norris [22] and completed by Chen [23] and is based upon the same assumptions as used by Tandon and Weng but without the restriction of isotropic phases.

Consider a representative volume element (RVE) as shown in Fig. 3.6 in which a homogeneous elastic matrix is filled with unidirectionally oriented spheroid shaped inclusions. The 3-axis coincides with the axis of symmetry of the spheroids. Fig. 3.5 shows that the spheroids are shaped as either a fibre or a platelet. In both cases the RVE possesses transverse symmetry around the 3-axis and thus has five independent elastic constants. The volume average stresses and strains in the matrix and the inclusions are related by Hooke's law:

$$\bar{\sigma}_m = C_m \bar{\epsilon}_m \quad (3.17)$$

and

$$\bar{\sigma}_r = C_r \bar{\epsilon}_r \quad (3.18)$$

where the index m denotes the matrix and r denotes the reinforcing phase. σ_m , ϵ_m and σ_r , ϵ_r are the stress and strain in the matrix and in the reinforcing phase respectively. C_m represents the stiffness tensor of the matrix and C_r that of the reinforcing phase. The elastic stiffness tensor C_c of the composite is defined by:

$$\bar{\sigma}_c = C_c \bar{\epsilon}_c \quad (3.19)$$

where $\bar{\sigma}_c$ and $\bar{\epsilon}_c$ are the average stress and average strain in the composite.

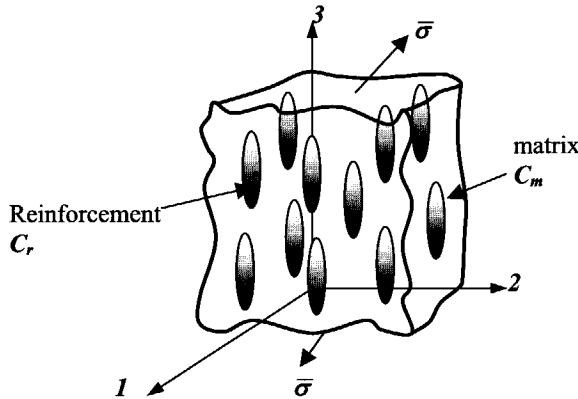


Figure 3.6 Composite reinforced with unidirectionally aligned spheroids

The average stress and average strain in the composite are equal to the volume average of the stresses and strains in the phases of the composite. For a two-phase composite this becomes:

$$\bar{\sigma}_c = c_m \bar{\sigma}_m + c_r \bar{\sigma}_r \quad \text{and} \quad \bar{\epsilon}_c = c_m \bar{\epsilon}_m + c_r \bar{\epsilon}_r \quad (3.20)$$

where $c_m = 1 - c_r$ and c_r are the volume fractions of matrix and reinforcing phase respectively. The Mori-Tanaka approach assumes that the average strain in the interacting inclusions $\bar{\epsilon}_r$, can be approximated by that of a single inclusion embedded in an infinite matrix subjected to the uniform average matrix strain $\bar{\epsilon}_m$.

It is a *mean field approach*, which assumes that the effect of all local stress concentrations on the deformation of the composite can be replaced by a single average stress. This assumption is reasonable as long as particles do not touch each other. According to Eshelby's theory [18, 21] the average strain in an inclusion $\bar{\epsilon}_r$ is related to the uniform strain $\bar{\epsilon}_m$ in the matrix by:

$$\bar{\epsilon}_r = A \bar{\epsilon}_m \quad (3.21)$$

The tensor A is called the '*strain concentration tensor*' and can be written as [5, 24]:

$$A = [P_m C_m^{-1} (C_r - C_m) + I]^{-1} \quad (3.22)$$

where P_m is the well-known Eshelby's tensor and I is the identity tensor. P_m only depends on the elastic properties of the matrix and the shape of the inclusion. The components of the Eshelby's tensor for aligned spheroids are given in Appendix A. Appendix A also explains Eshelby's approach and shows how Eqn. 3.22 can be derived. For other inclusion shapes, explicit expressions of the components of P_m in terms of the moduli C_m and the inclusion shape are given by Mura [21]. If all the inclusions have the same shape and orientation the strain concentration tensor A is equal for each inclusion and does not need to be averaged over all directions. By combining 3.17), 3.18) and 3.21) the stress inside the inclusions can be written as:

$$\bar{\sigma}_r = C_r A \bar{\epsilon}_m = C_r A (C_m)^{-1} \bar{\sigma}_m \equiv B \bar{\sigma}_m \quad (3.23)$$

where $B = C_r A (C_m)^{-1}$ is referred to as the '*stress concentration tensor*'. Combination of 3.17), 3.19), 3.20), 3.21) and 3.23) gives:

$$\bar{\sigma} = c_m \bar{\sigma}_m + c_r B \bar{\sigma}_m = (c_m I + c_r B) C_m \bar{\epsilon}_m = C_c \bar{\epsilon}_c = C_c (c_m I + c_r A) \bar{\epsilon}_m \quad (3.24)$$

where I is the unit tensor. From 3.24) it follows:

$$C_c = (c_m C_m + c_r B C_m) (c_m I + c_r A)^{-1} = (c_m C_m + c_r C_r A) (c_m I + c_r A)^{-1} \quad (3.25)$$

And

$$S_c = C_c^{-1} = (c_m S_m + c_r S_r B) (c_m I + c_r B)^{-1} \quad (3.26)$$

where S_c is the compliance tensor of the composite and $S_m = (C_m)^{-1}$ and $S_r = (C_r)^{-1}$ are the compliance tensors of the matrix and inclusions respectively.

Eqns. 3.25) and 3.26) relate the elastic properties of the composite to those of the matrix and the inclusions. They are generally valid for composites containing aligned anisotropic inclusions in an anisotropic matrix.

Tandon and Weng [17] used the same assumptions as above but they use a different calculation scheme to calculate the stiffness tensor of a composite with aligned isotropic spheroids. Instead of simply using the stress concentration tensor as done in this thesis, they go back to Eshelby's approach and use the 'eigenstrain' and 'eigenstress' concepts to arrive at explicit equations for the five independent components of the composite's stiffness tensor. Since they use Mori-Tanaka's average stress theory together with Eshelby's result like is done in this thesis, their results is equal to ours.

It was numerically confirmed that, for isotropic spheroids in an isotropic matrix, Eqns. 3.25) and 3.26) indeed give the same results as the closed form equations given by Tandon and Weng. However Eqns. 3.25) and 3.26) are more generally applicable, because with these equations it is not only possible to calculate the reinforcement of isotropic particles in an isotropic matrix but also that of *anisotropic particles* in an *anisotropic matrix*. Furthermore, the equations are not restricted to spheroid shaped particles.

According to Mura [21] when an anisotropic inclusion is contained in an isotropic matrix, the Eshelby's tensor \mathbf{P} doesn't differ from that of an isotropic inclusion. This means that the Eshelby's tensor \mathbf{P} can be used for both isotropic and anisotropic spheroids. In the first part of Appendix A closed form expression are given for Eshelby's tensor \mathbf{P} of an isotropic matrix. If the matrix is anisotropic, \mathbf{P} has a more complicated form. Mura [21] gave integral expressions for the different components of \mathbf{P} of an anisotropic matrix. These are given in the second part of Appendix A.

The stiffness of a unidirectional PA6-clay nanocomposite is calculated at different weight fractions of clay. For the PA6 matrix, elastic properties in dry condition and at room temperature are used ($E_m = 3.0$ GPa; $\nu_m = 0.35$). Since the stiffness of a clay platelet in a nanocomposite cannot be measured, it is assumed that the stiffness equals that of a perfect mica crystal ($E_r = 172$ GPa; $\nu_r = 0.2$ [25]). This is justified because the crystal structures of mica and montmorillonite are very similar, as was explained in Chapter 2.

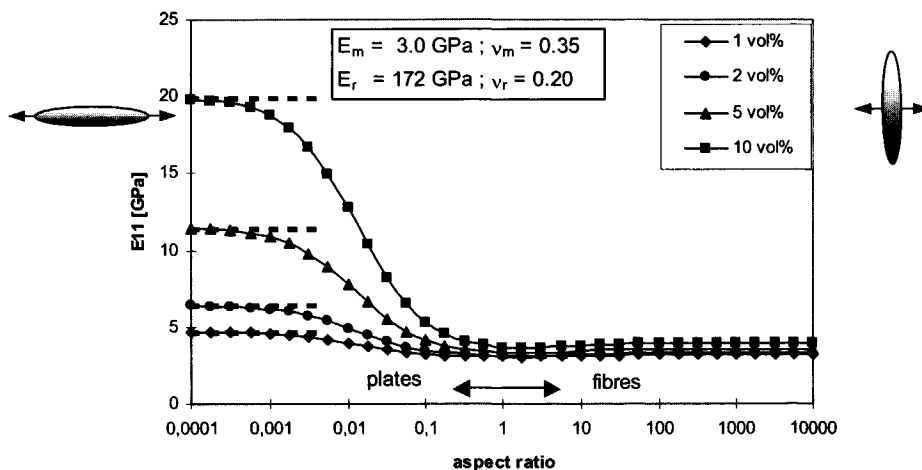


Figure 3.7 Young's modulus E_{11} of a composite with uniaxially oriented spheroids. Mori-Tanaka's estimates are represented by solid lines. The optimum possible reinforcement, calculated by the rule of mixtures, is given by the dotted lines.

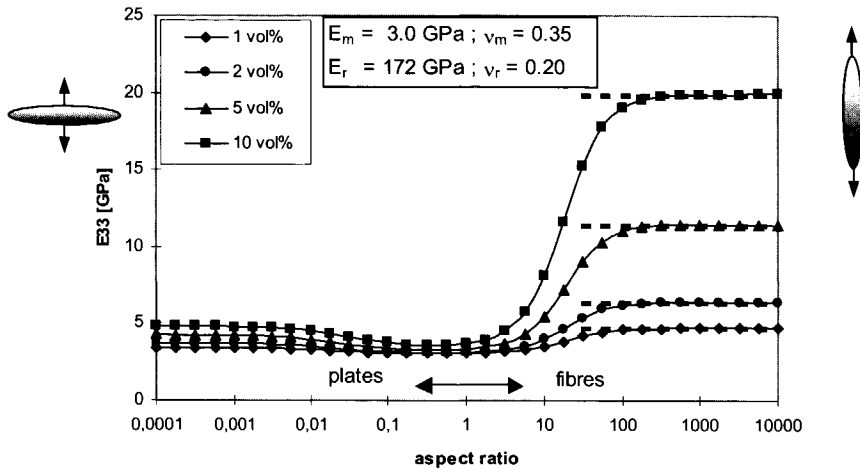


Figure 3.8 Young's modulus E_{33} of a composite with uniaxially oriented spheroids. Mori-Tanaka's estimates are represented by solid lines. The optimum possible reinforcement, calculated by the rule of mixtures, is given by the dotted lines.

Figs. 3.7 and 3.8 show the modulus in the 11 and 33 direction of a composite with isotropic uniaxially oriented spheroids, calculated using Eqn. 3.25. As expected, the reinforcement is mainly found in the 'long' direction of the spheroid. With platelets (aspect ratio < 1) these are the 1 and 2 directions, while with fibres it is the 3 direction. By comparing the reinforcement of extremely thin platelets (aspect ratio ≤ 0.0001) with that of extremely long fibres (aspect ratio $\geq 1/1000$) it can be seen that both inclusion shapes have the same ultimate reinforcement that coincides with the rule of mixtures. The rule of mixtures is given by the dotted lines.

While fibres with an aspect ratio of 100 already approach optimum reinforcement, platelets need an aspect ratio of 1/1000. This implies that in the unidirectional case, fibres are more effective than platelets. Owing to the two dimensional reinforcement of platelets it is often said that platelets are more effective than fibres. As shown here this is not true for unidirectional composites. Platelets are indeed more effective than fibres in the case of randomly oriented composites, as will be shown later in Fig. 3.17.

3.2.1.3 Takanayagi's model extended to 3 dimensions

In the Takanayagi theory [1] it is assumed that the stiffness of a composite can be represented by a unit cell that contains a single inclusion. Using Takanayagi's theory two models are possible, the series/mixed-parallel and the parallel/mixed-series models, which are schematically depicted in Fig. 3.9. If there is efficient stress transfer normal to the direction of stress, the series/mixed-parallel model should be used. In case of weak stress transfer, the parallel/mixed-series model is more adequate. Nanocomposites have inclusions with high aspect ratios that adhere well to the polymer matrix. Therefore, the series/mixed-parallel model is most suited for nanocomposites.

Traditionally the Takanayagi model is used as a 2-dimensional model, which implies that all the phases in figure 3.9 are thought to extend infinitely in the direction perpendicular to the plane of the page. In a 2-dimensional presentation, it is therefore impossible to discriminate between fibre or platelet reinforcement. By neglecting the third dimension it is

implicitly assumed that the filler has the shape of an infinite long ribbon. Accordingly, the 2-dimensional theory will not give correct answers for fibres or platelets.

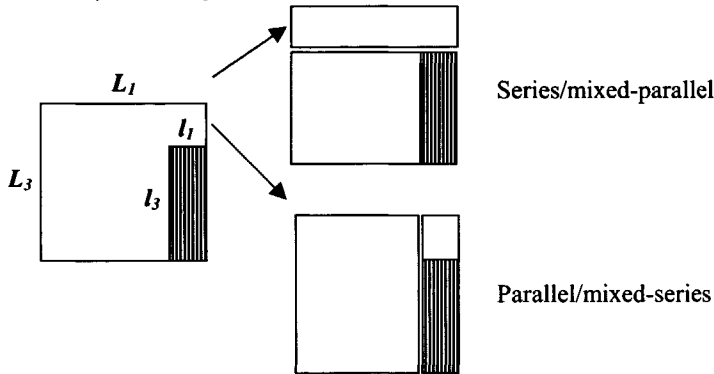


Figure 3.9 Two possible combinations of the two components in the Takayanagi model. The stress is applied in the vertical direction.

We have therefore extended the Takayanagi model to 3-dimensions. In doing so it becomes possible to distinguish between fibre and platelet reinforcement. Fig. 3.10 shows an inclusion with dimensions $l_3 \times l_1 \times l_1$ in a unit cell with dimensions $L_3 \times L_1 \times L_1$. If $l_3 > l_1$, the inclusion has the shape of a fibre, while if $l_3 < l_1$ the inclusion has the shape of a platelet. If $l_3 = l_1$ the inclusion is cubical shaped. The parallel direction of a fibre shaped inclusion is the 3-direction, while for a platelet shaped inclusion it is the 1-(or 2)-direction. The Young's moduli of the unit cell can be calculated with the series/mixed parallel model:

$$\frac{1}{E_{33}} = \frac{1}{E_{a33}} \frac{l_3}{L_3} + \frac{1}{E_m} \left(1 - \frac{l_3}{L_3}\right); \quad E_{a33} = E_r \frac{l_1^2}{L_1^2} + E_m \left(1 - \frac{l_1^2}{L_1^2}\right) \quad 3.27$$

$$\frac{1}{E_{11}} = \frac{1}{E_{a11}} \frac{l_1}{L_1} + \frac{1}{E_m} \left(1 - \frac{l_1}{L_1}\right); \quad E_{a11} = E_r \frac{l_3 l_1}{L_3 L_1} + E_m \left(1 - \frac{l_3 l_1}{L_3 L_1}\right) \quad 3.28$$

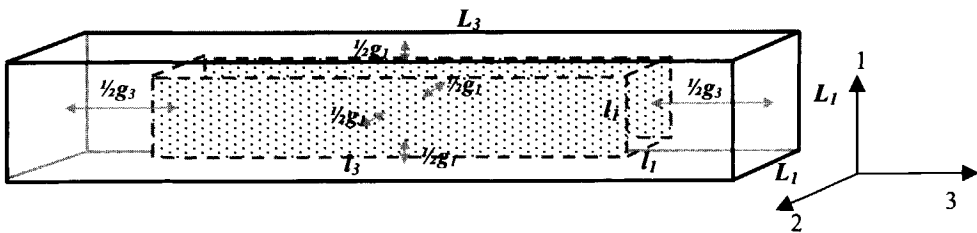


Figure 3.10 3-D Takayanagi unit cell containing an inclusion that has a varying distance from the borders of the unit cell. By assuming $g_1 = g_2 = g_3 = g$ the Takayanagi unit cell can be scaled with respect to the inclusion, giving a unique solution for any volume fraction between 0 and 1.

Here E_{33} and E_{11} are the Young's moduli of the composite in the 3-direction and in the 1-direction respectively. E_m is the Young's modulus of the matrix and E_r is the Young's modulus of the inclusion. Eqns. 3.27) and 3.28) indicate that the composite stiffness depends on the dimensions of the inclusion (l_1, l_3) and of the unit cell (L_1, L_3).

If the inclusion in Fig. 3.10 has a high aspect ratio and the unit cell is cubical shaped, the inclusion might become longer than the unit cell. To prevent the inclusion from sticking out of the unit cell, the long side of the inclusion $l_{//}$ must always be smaller than the long side of the unit cell $L_{//}$. This can be achieved by *scaling* the shape of the unit cell to the shape of the inclusions as will be shown below.

In a true composite, inclusions will tend to maintain at a certain distance from adjacent inclusions. This suggests that the distances between the sides of adjacent inclusions will be about equal to the distances between the ends of adjacent inclusions. This gives a clue on how to scale the unit cell.

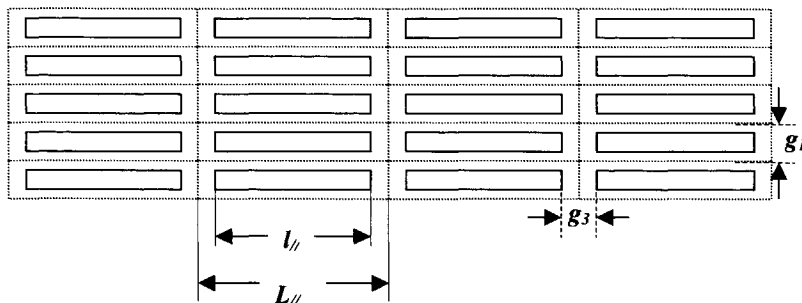


Figure 3.11 A composite build up of a number of Takayanagi unit cells

Figure 3.11 shows a composite that is build up from Takayanagi unit cells. The figure shows that the distances between the ends of the inclusions are equal to g_z and the distances between the sides of the inclusions are equal to g_l . According to the argument given above the scaling should be performed in such a manner that $g_l = g_z = g$. This enables us to calculate the stiffness of the composite for any volume fraction.

The volume fraction of the inclusion in Fig. 3.10 equals $c_r = l_3 l_1^2 / L_3 L_1^2$, and the aspect ratio $\alpha = l_3 / l_1$. One of the dimensions can be chosen arbitrarily, say $l_1 = 1$. Note that $\alpha = l_3$ if $l_1 = 1$. For fibre-like inclusions $\alpha > 1$, while for platelet-like inclusions $\alpha < 1$. The volume fraction of the inclusion can now be written as:

$$c_r = \frac{l_3 l_1^2}{(l_3 + g_z)(l_1 + g_l)^2} = \frac{\alpha}{(\alpha + g_z)(1 + g_l)^2} = \frac{\alpha}{\alpha + 2\alpha g_l + \alpha g_l^2 + g_z + 2g_z g_l + g_z g_l^2}$$

By assuming that $g_l = g_z = g$ it is easy to derive that g is the maximum real root of the third order polynomial:

$$\begin{aligned} g^3 + (\alpha + 2)g^2 + (2\alpha + 1)g + \alpha(1 - 1/c_r) &= 0 \\ l_1 &= 1 \quad ; \quad l_3 = \alpha \quad ; \quad L_1 = 1 + g \quad ; \quad L_3 = \alpha + g \end{aligned} \quad 3.29)$$

Now all dimensions can be expressed in α and c_r , which makes it possible to calculate the stiffness of the composite by using Eqns. 3.27 and 3.28 for all volume fractions up to 1.

If the inclusions are ordered as in Fig. 3.11, a maximum parallel stiffness will be found if $l_{//} = L_{//}$, because then the inclusions become continuous. Setting $l_{//} > L_{//}$ is meaningless since

than the inclusion sticks through the walls of the unit cell. As $L_{//}/l_{//}$ increases, the distance between the ends increases and stress transfer between inclusions becomes less effective. This leads to a decreasing stiffness as is illustrated in Fig. 3.12. In Fig. 3.12 the effect of the shape of the unit cell on the Young's modulus is depicted. The inclusion is assumed to have an aspect ratio of either 100 (fibre) or 1/100 (platelet). Young's moduli ($E_{//}$, E_{\perp}) are plotted as a function of the normalised length of the unit cell $L_{//}/l_{//}$. The shape is varied while keeping the volume of the unit cell constant. This is done by increasing the parallel dimension of the unit cell, while simultaneously decreasing the perpendicular dimension accordingly. In case of a fibre $L_{//}/l_{//} = L_3/l_3$, while in case of a platelet $L_{//}/l_{//} = L_1/l_1$.

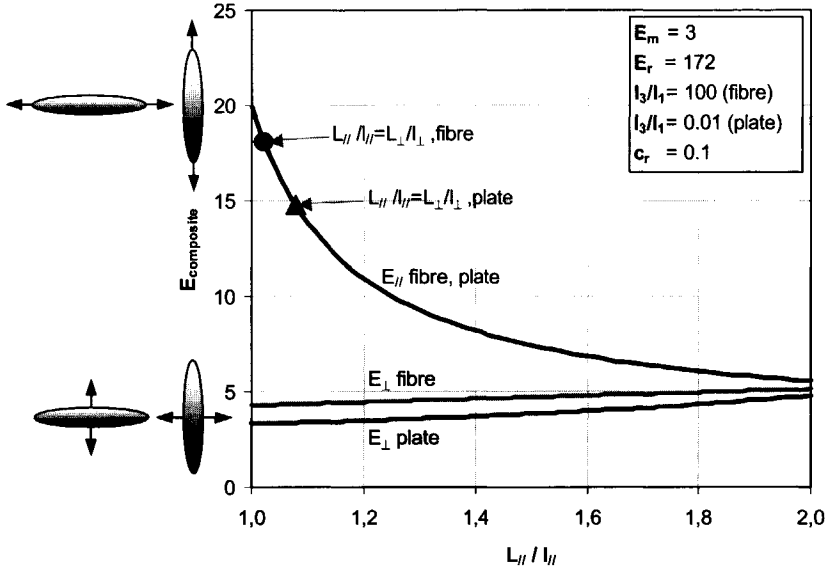


Figure 3.12 Effect of the shape of the 3D-Takanayagi unit cell on the parallel and perpendicular Young's moduli of a composite. The calculated composite stiffness depends of the choice of $L_{//}/l_{//}$. Note that the parallel stiffness of the composite decreases as the length of the unit cell increases with respect to the length of the inclusion.

In order to obtain a unique solution for the composite stiffness at the chosen volume fraction, also the results of a scaled unit cell are also indicated, viz. by symbols. Using a scaled unit cell it is found that fibres approach each other much more closely than platelets. As a result the parallel stiffness of fibre-reinforced composites is higher than that of platelet reinforced composites.

The stiffness of the composite in case $g_1 = g_3 = g$ is also marked by symbols in Fig. 3.12. In case the inclusion is a fibre it is found that g is much smaller than if the inclusion is a platelet. This implies that in a composite fibres approach each other much more closely than platelets. As a result the parallel stiffness of fibre-reinforced composites is higher than that of comparable platelet reinforced composites. This result agrees well with the predictions of the Mori-Tanaka theory of the last section as is shown in Fig. 3.13.

In Fig. 3.13 the results of the 3-dimensional Takanayagi model with a scaled unit cell are compared to the results of the Mori-Tanaka's theory. In case the aspect ratio is close to

unity, the Takanayagi model overestimates the stiffness of the composite because the series/mixed-parallel model is not adequate in that case. At high aspect ratios, the 3D-Takanayagi model with a scaled unit cell ($g_1=g_3=g$) gives Young's moduli that are similar to those predicted by the Mori-Tanaka model. Both models predict that at a given aspect ratio, fibres give a higher parallel stiffness than platelets.

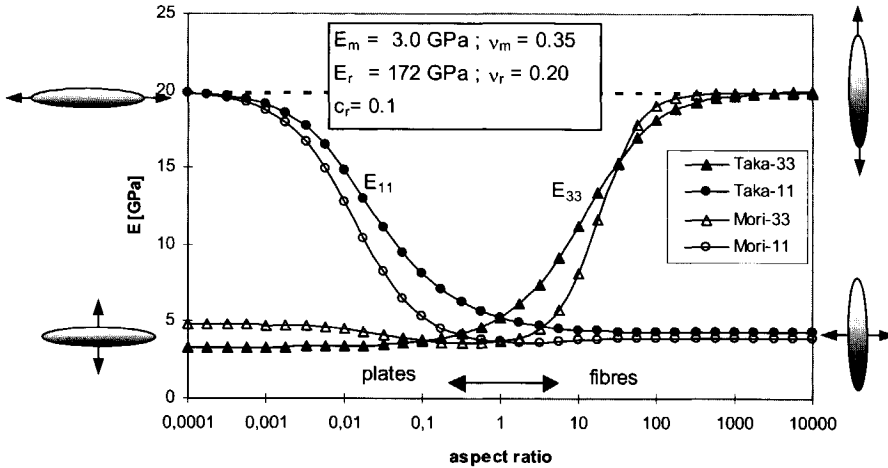


Figure 3.13 Young's modulus of a unidirectional composite filled platelets or fibres. (Fibres: aspect ratio >1 ; Plates aspect ratio <1). Takanayagi's composite theory is compared with Mori-Tanaka's theory. For Takanayagi's theory the shape of the unit cell is chosen such that the distance from the inclusion to the surface of the unit cell is constant.

It can be concluded that the conventional two-dimensional Takanayagi model implicitly assumes ribbon reinforcement. Only by extending the model to 3 dimensions it becomes possible to distinguish between fibres and platelets.

The result of the conventional non-scaled Takanayagi model (either in 2 or 3 dimensions) strongly depends on the shape of the unit cell or equivalently on the arrangement of the inclusions. However, by scaling the unit cell, the Takanayagi model gives a unique relationship between aspect ratio and parallel Young's modulus, which resembles that of the Mori-Tanaka theory.

The predictions of the Takanayagi model are not thought to be as accurate as those of the Mori-Tanaka model. However, the simplicity of the model has the benefit of being very understandable. From the results it can be deduced why fibres in unidirectional composites need a lower aspect ratio than platelets to give the same reinforcement. The reason is that at a given aspect ratio and filler content, the edges of adjacent platelets are much further apart than the edges of fibres. This lowers the effectiveness to transfer stress to adjacent inclusions, which results in a lower Young's modulus.

3.2.2 Stiffness of a material with non-aligned inclusions

In this section the elastic properties of a composite are calculated with filler particles that are not fully aligned. To this end often the orientation average of either the compliance tensor \mathbf{S} or the stiffness tensor \mathbf{C} is calculated. In doing so, implicitly the assumption is made that the

composite experiences either a plane stress (Reuss or series assumption) or a plane strain (Voigt or parallel assumption). The Voigt or Reuss approximations usually give very different results. The Reuss approximation normally overestimates the contribution of the softer phase to the composite modulus while the Voigt approximation overestimates the contribution of the harder phase. The Voigt and Reuss approximations can be considered as upper and lower bounds on the elastic constants of composite materials. Since these bounds can lie an order of magnitude apart, they often are not of much practical use.

Arridge [26, p 142-154] gives a detailed procedure on how to actually perform the averaging procedure. He also gives closed form expressions for the average compliance tensor $\langle S \rangle$ and stiffness tensor $\langle C \rangle$.

To prevent the problems of working with two bounds, the Mori-Tanaka scheme mentioned earlier will be introduced. It will be shown that, by using the Mori-Tanaka approach for non-aligned inclusions, it is possible to find a self-consistent expression for $\langle C \rangle$ and $\langle S \rangle$ such that $\langle C \rangle = \langle S \rangle^{-1}$. Arridge [26, p 154-157] also uses a similar self-consistent approach to calculate the elastic constants of a composite with non-aligned inclusions. The expressions found by Arridge are more complicated than the ones derived below.

3.2.2.1 Coordinate transformations

As is shown in Fig. 3.14 an inclusion is chosen with a global co-ordinate system $\underline{e} = (o - x_1, x_2, x_3)$ and a local coordinate system $\underline{e}' = (o - x'_1, x'_2, x'_3)$. In general, three angles are required to describe the relative orientation of two orthogonal coordinate systems. To transform global coordinates into local coordinates a coordinate transformation must be performed.

This transformation consists of three successive rotations that are depicted in Fig. 3.14. To determine these three angles, first rotate the global coordinate system \underline{e} by an angle ϕ around the x_3 -axis such that the new ζ_1 axis is perpendicular to the x_2 - x_3 plane:

$$\underline{\zeta} = [R_3(\phi)]\underline{e} \quad 3.30)$$

where $R_3(\phi)$ denotes the rotation matrix belonging to rotation of an angle ϕ around the 3-axis. Now perform a second rotation by an angle θ around the ζ_1 -axis such that the new ξ_3 axis is parallel to the x'_3 axis:

$$\underline{\xi} = [R_1(\theta)]\underline{\zeta} \quad 3.31)$$

here $R_1(\theta)$ denotes the rotation matrix belonging to rotation of an angle θ around the 1-axis. Finally rotate around the ξ_3 -axis, which now coincides with the 3'-axis, by an angle ψ to obtain the co-ordinate system \underline{e}' :

$$\underline{e}' = [R_3(\psi)]\underline{\xi} \quad 3.32)$$

Now three successive rotation have been performed:

$$\underline{e}' = [R_3(\psi)][R_1(\theta)][R_3(\phi)]\underline{e} = \begin{bmatrix} \omega_{11} & \omega_{12} & \omega_{13} \\ \omega_{21} & \omega_{22} & \omega_{23} \\ \omega_{31} & \omega_{32} & \omega_{33} \end{bmatrix} \underline{e} = [\Omega]\underline{e} \quad 3.33)$$

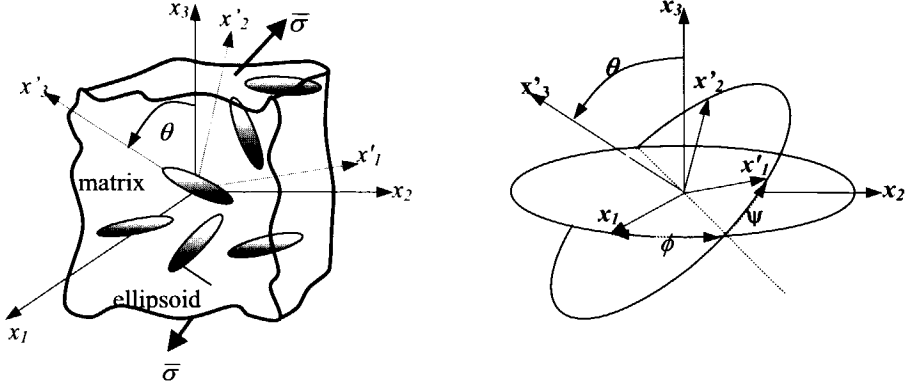


Figure 3.14 The relationship between local and global coordinates in a composite with randomly oriented ellipsoids

A rotation around the 1-axis is represented by:

$$R_1(\gamma) = \begin{bmatrix} 1 & 0 & 0 \\ 0 & \cos \gamma & \sin \gamma \\ 0 & -\sin \gamma & \cos \gamma \end{bmatrix} \quad 3.34)$$

and a rotation around the 3-axis by:

$$R_3(\gamma) = \begin{bmatrix} \cos \gamma & \sin \gamma & 0 \\ -\sin \gamma & \cos \gamma & 0 \\ 0 & 0 & 1 \end{bmatrix} \quad 3.35)$$

The matrix multiplication in Eqn. 3.33) yields the complete transformation matrix:

$$\begin{bmatrix} e'_1 \\ e'_2 \\ e'_3 \end{bmatrix} = \begin{bmatrix} \cos \psi \cos \phi - \cos \theta \sin \phi \sin \psi & \cos \psi \sin \phi + \cos \theta \cos \phi \sin \psi & \sin \psi \sin \theta \\ -\sin \psi \cos \phi - \cos \theta \sin \phi \cos \psi & -\sin \psi \sin \phi + \cos \theta \cos \phi \cos \psi & \cos \psi \sin \theta \\ \sin \theta \sin \phi & -\sin \theta \cos \phi & \cos \theta \end{bmatrix} \begin{bmatrix} e_1 \\ e_2 \\ e_3 \end{bmatrix} \quad 3.36)$$

To change from local to global coordinates the coordinate transformation matrix must be inverted. It can be shown that this can be done by interchanging the rows and columns of $[\Omega]$:

$$\underline{e} = \Omega^{-1} \underline{e}' = \Omega^T \underline{e}' \quad 3.37)$$

This specific set of rotations, assigns three angles to the relative orientation of two orthogonal systems. Of course, it is possible to perform another set of rotations for the coordinate transformation, which will yield different expressions for Ω . The transformation matrix in 1.36 is the one that is generally used in physics.

As shown above a vector \underline{v} needs only a single multiplication with Ω to perform the coordinate transformation. Therefore, a vector is said to be a tensor of rank 1. In condensed tensor notation, using the Einstein summation convention of summation at repeated indices, this looks like:

$$v_i = \omega_{ii'} v_{i'} \quad (3.38)$$

or in expanded notation:

$$v_i = \sum_{i'=1}^3 \omega_{ii'} v_{i'} \quad (3.39)$$

Stress and strain are tensors of rank 2 and are related as:

$$\varepsilon_{ij} = \omega_{ii'} \omega_{jj'} \varepsilon_{i'j'}, \text{ and } \sigma_{ij} = \omega_{ii'} \omega_{jj'} \sigma_{i'j'} = \sum_{i'=1}^3 \sum_{j'=1}^3 \omega_{ii'} \omega_{jj'} \sigma_{i'j'} \quad (3.40)$$

The compliance tensor S and the stiffness tensor C are tensors of rank 4, so:

$$C_{ijkl} = \omega_{ii'} \omega_{jj'} \omega_{kk'} \omega_{ll'} C_{i'j'k'l'} = \sum_{i'=1}^3 \sum_{j'=1}^3 \sum_{k'=1}^3 \sum_{l'=1}^3 \omega_{ii'} \omega_{jj'} \omega_{kk'} \omega_{ll'} C_{i'j'k'l'} \quad (3.41)$$

If the orientation function $\Phi(\theta, \phi, \psi)$ of the inclusions is known it is possible to estimate the overall elastic moduli by correct averaging. The probability of finding an inclusion within the solid angle $(\theta+d\theta, \phi+d\phi, \psi+d\psi)$ is given by $\Phi(\theta, \phi, \psi) \sin \theta d\theta d\phi d\psi$. The orientation function $\Phi(\theta, \phi, \psi)$ has to satisfy the normalisation condition:

$$\int_0^{2\pi} \int_0^{2\pi} \int_0^\pi \Phi(\theta, \phi, \psi) \sin \theta d\theta d\phi d\psi = 1 \quad (3.42)$$

For random orientation this condition is satisfied if $\Phi(\theta, \phi, \psi) = 1/8\pi^2$. The orientation average of a quantity $Q(\theta, \phi, \psi)$ with an orientation function $\Phi(\theta, \phi, \psi)$ is given by:

$$\langle Q \rangle = \int_0^{2\pi} \int_0^{2\pi} \int_0^\pi Q(\theta, \phi, \psi) \Phi(\theta, \phi, \psi) \sin \theta d\theta d\phi d\psi \quad (3.43)$$

As mentioned before simple averaging of $C(\theta, \phi, \psi)$ or $S(\theta, \phi, \psi)$ is not correct since this will only give bounds on the elastic moduli with $\langle C \rangle \neq \langle S \rangle^{-1}$. Therefore a *self-consistent* approach will be used to make sure that $\langle C \rangle = \langle S \rangle^{-1}$. Again, it is assumed that all the inclusions in the two-phase composite have the same spheroidal shape. Since the x'_3 axis is parallel to the axis of rotational symmetry of the spheroid, rotation around this axis doesn't change the orientation of the spheroid. Therefore, ψ can be chosen at will. Choosing $\psi = 0$ in 3.36) gives:

$$\begin{bmatrix} e'_1 \\ e'_2 \\ e'_3 \end{bmatrix} = \begin{bmatrix} \cos \phi & \sin \phi & 0 \\ \cos \theta \sin \phi & \cos \theta \cos \phi & \sin \theta \\ \sin \theta \sin \phi & -\sin \theta \cos \phi & \cos \theta \end{bmatrix} \begin{bmatrix} e_1 \\ e_2 \\ e_3 \end{bmatrix} \quad (3.44)$$

and:

$$\begin{bmatrix} e_1 \\ e_2 \\ e_3 \end{bmatrix} = \begin{bmatrix} \cos \phi & \cos \theta \sin \phi & \sin \theta \sin \phi \\ \sin \phi & \cos \theta \cos \phi & -\sin \theta \cos \phi \\ 0 & \sin \theta & \cos \theta \end{bmatrix} \begin{bmatrix} e'_1 \\ e'_2 \\ e'_3 \end{bmatrix} \quad (3.45)$$

In this case the simpler orientation function $\Phi(\theta, \phi)$ can be used with normalisation condition:

$$\int_0^{2\pi} \int_0^\pi \Phi(\theta, \phi) \sin \theta d\theta d\phi = 1 \quad (3.46)$$

For random orientation $\Phi(\theta, \phi) = 1/4\pi$. The orientation average of a quantity $Q(\theta, \phi)$ that only depends on θ and ϕ can be calculated as:

$$\langle Q \rangle = \int_0^{2\pi} \int_0^\pi Q(\theta, \phi) \Phi(\theta, \phi) \sin \theta d\theta d\phi \quad (3.47)$$

If fibre symmetry is assumed, the orientation function Φ only depends on θ . Arridge [26] used an expansion in terms of Legendre polynomials for $\Phi(\theta)$:

$$\Phi(\theta) = \sum_{n=0}^{\infty} a_n P_n \quad (3.48)$$

In which P_n is a function of $\cos \theta$ only: $P_n = P_n(\cos \theta)$. P_n are orthogonal functions. The factors a_n depend on P_n as:

$$a_n = \frac{2n+1}{2} \int_0^\pi \Phi(\theta) P_n(\cos \theta) \sin \theta d\theta = \frac{2n+1}{2} \langle P_n(\cos \theta) \rangle \quad (3.49)$$

It can be shown that for mechanical properties, no terms higher than a_4 are required. In case of fibre symmetry, only the even Legendre polynomials are needed. Therefore, we only require:

$$a_0 = \frac{1}{2}, a_2 = \frac{5}{2} \langle P_2 \rangle \text{ and } a_4 = \frac{9}{2} \langle P_4 \rangle. \quad (3.50)$$

P_2 and P_4 are given by:

$$\begin{aligned} P_2 &= \frac{3}{2} \cos^2 \theta - \frac{1}{2}; \\ P_4 &= \frac{35}{8} \cos^4 \theta - \frac{15}{4} \cos^2 \theta + \frac{3}{8} \end{aligned} \quad (3.51)$$

Using these equations, it is easy to show that for:

Random orientation:	$a_0 = 1/2, a_2 = 0, a_4 = 0.$	
Full alignment ($\theta = 0$)	$a_0 = 1/2, a_2 = 5/2, a_4 = 9/2.$	
$\theta = 30^\circ$	$a_0 = 1/2, a_2 = 25/16, a_4 = 27/256$	3.52)
$\theta = 60^\circ$	$a_0 = 1/2, a_2 = -5/16, a_4 = -333/256.$	
Random orientation in plane ($\theta = 90^\circ$)	$a_0 = 1/2, a_2 = -5/4, a_4 = 27/16.$	

The moments a_n of the distribution function can also be determined from Eqn. 3.49). If the moments a_n of the orientation distribution function are known $\Phi(\theta)$ can be constructed with Eqns. 3.48) and 3.51).

If the inclusions are normally distributed around an average value of $\sin \bar{\theta}$, with a standard deviation of $\pm \sin \delta$ then $\Phi(\sin \theta)$ can be written as:

$$\Phi(\sin \theta) = \frac{1}{\sin \delta \sqrt{2\pi}} e^{-\frac{1}{2} \left(\frac{\sin \theta - \sin \bar{\theta}}{\sin \delta} \right)^2} \quad 3.53)$$

Here $\sin \theta$ is used rather than θ to assure that Φ is a periodic function with a period equal to 2π . The orientation average can then be calculated with Eqn. 3.47). Which should be modified however, because Eqn. 3.53.) is not normalised to 1. The same applies to $\langle P_n(\cos \theta) \rangle$.

In Appendix B it will be explained how the orientation average is calculated in practise. Instead of using the tensor equation 3.47), matrix equations will be used.

Using infrared dichroism, $\langle P_2 \rangle$ can be determined. Raman spectroscopy, N.M.R., and birefringence can find both $\langle P_2 \rangle$ and $\langle P_4 \rangle$. By using X-ray even higher order terms like $\langle P_6 \rangle$ etc. can be determined.

3.2.2.2 Mori-Tanaka scheme for non-aligned composites

Now consider a RVE with many differently oriented inclusions and their orientations characterised by $\Phi(\theta, \phi)$. According to the Mori-Tanaka scheme it is assumed that all particles experience the same average matrix stress σ_m and average matrix strain ϵ_m . Contrary to the aligned case, the inclusions now are all differently oriented. Therefore all inclusions respond differently to the average matrix stress σ_m and average matrix strain ϵ_m . The orientation of a spheroid can be characterised by two angles θ and ϕ as was indicated in Fig. 3.14.

According to Eqns. 3.21) and 3.23), strain and stress inside the inclusion can be written as:

$$\epsilon_r(\theta, \phi) = A(\theta, \phi) \epsilon_m \quad 3.54)$$

$$\sigma_r(\theta, \phi) = B(\theta, \phi) \sigma_m = C_r A(\theta, \phi) C_m^{-1} \sigma_m \quad 3.55)$$

The average strain and stress in the inclusions can now be written as:

$$\langle \epsilon_r \rangle = \left[\int_{\phi=0}^{2\pi} \int_{\theta=0}^{\pi} Q(\theta, \phi) A(\theta, \phi) \sin \theta d\theta d\phi \right] \epsilon_m \equiv \langle A(\theta, \phi) \rangle \epsilon_m \quad 3.56)$$

$$\langle \sigma_r \rangle = \left[\int_{\phi=0}^{2\pi} \int_{\theta=0}^{\pi} Q(\theta, \phi) B(\theta, \phi) \sin \theta d\theta d\phi \right] \varepsilon_m \equiv \langle B(\theta, \phi) \rangle \sigma_m \quad 3.57)$$

where the angle brackets denote the orientation average. A and B are 4th-ordered tensors, like the stiffness and compliance tensors C_c and S_c . So their angular dependence becomes:

$$A_{ijkl}(\theta, \phi) = \omega_{ii'} \omega_{jj'} \omega_{kk'} \omega_{ll'} A_{i'j'k'l'}, \quad B_{ijkl}(\theta, \phi) = \omega_{ii'} \omega_{jj'} \omega_{kk'} \omega_{ll'} B_{i'j'k'l'} \quad 3.58)$$

Similarly to Eqns. 3.25) and 3.26), the effective moduli of the composite can now be written as:

$$C_c = (c_m C_m + c_r \langle B \rangle C_m)(c_m I + c_r \langle A \rangle)^{-1} = (c_m C_m + c_r \langle C_r A \rangle)(c_m I + c_r \langle A \rangle)^{-1} \quad 3.59)$$

and

$$S_c = C_c^{-1} = (c_m S_m + c_r \langle S_r B \rangle)(c_m I + c_r \langle B \rangle)^{-1} \quad 3.60)$$

So, in order to calculate the effective moduli C or S the volume averages $\langle A \rangle$ and $\langle B \rangle$ need to be known. The strain concentration tensor A and the stress concentration tensor B are known in local coordinates. Their orientational dependence can be calculated using Eqn. 3.58). Their average can then be calculated by performing the double integration in Eqns. 3.56) and 3.57). As long as tensor quantities are used exclusively, all equations hold without any restrictions. *In practise though it is convenient to express stresses and strains in engineering units and use the condensed matrix notation.* How this is done in praxis is explained in Appendix B.

Although the Mori-Tanaka averaging scheme uses the mean field approach, it does not mean that it is flawless. As Lielens points out [27], the Mori-Tanaka scheme can lead to non-physical behaviour because it can give results that lie outside the Voigt or Reuss averages. Therefore Lielens suggests using Voigt (or additive) averaging instead of Mori-Tanaka averaging. Lielens also gives a critical contemplation on the validity of averaging unidirectional results to obtain the elastic properties of a randomly oriented composite. As was already mentioned before, Arridge also gives *self-consistent* expressions for the orientation average of composites. It is not clear yet if the averaging scheme suggested by Arridge has the same disadvantages as the Mori-Tanaka scheme. This will become clear after implementation of Arridge's theory in computer code, which is left for future work.

3.2.3 Approximation for composites with randomly oriented fibres or platelets

The methods to determine the orientation-averaged stiffness of a composite are rather cumbersome to use in praxis. Therefore in this section extremely simple estimates will be introduced to estimate the Young's modulus of 3D-randomly oriented composites.

Laminate theory [4,28] gives an extremely simple approximation to calculate the stiffness of a sheet with fibres that are randomly oriented in the plane of the sheet (2D-random). It will be shown that a pseudo 3D-random stiffness can be obtained by repeatedly using the 2D randomising procedure. Laminate theory shows that the in-plane Young's

modulus of a sheet with fibres that are randomly oriented in the plane of the sheet can be approximated by:

$$E_{\text{random } 2D} = 0.375 E_{//} + 0.625 E_{\perp} \quad (3.61)$$

The index 2D in Eqn. 3.61 is added to specify the two dimensional random orientation of the fibres. This equation is obtained by appropriate summation of the Young's moduli of unidirectional composite plates that are stacked into a laminate as shown in Fig. 3.15. $E_{//}$ is the highest (parallel) modulus and E_{\perp} the lowest (perpendicular) modulus of the unidirectional plates. Both $E_{//}$ and E_{\perp} can be calculated by using the theory of the preceding sections.

To simulate a 2D-randomly oriented laminate, the orientations of the plates in the stack are evenly distributed between 0° and 90° as indicated in Fig. 3.15. As a result of this stacking procedure a material is obtained with a pseudo random in-plane stiffness equal to $E_{11}' = E_{22}' = E_{\text{random } 2D}$, which can be calculated with Eqn. 3.61). By the rotating procedure the stiffness in the direction perpendicular to the 1-2 plane, E_{33}' , is not changed and remains equal to E_{\perp} . After the rotation the highest modulus is found in the 1 and in the 2-directions and the lowest modulus in the 3-direction.

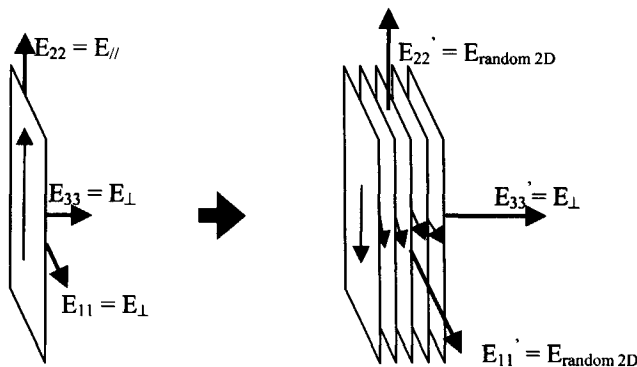


Figure 3.15 Stacking of unidirectional plates into a pseudo 2D random plate

By stacking so much plates that the thickness of the stack is equal to the width of the plates a cube is obtained as is depicted in Fig. 3.16:

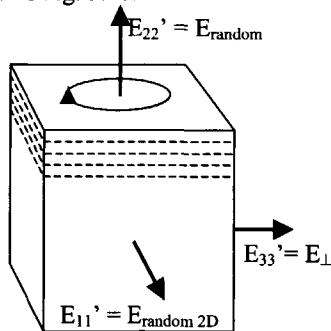


Figure 3.16 Cube of stacked plates after the first randomising step around the 3-axis and start of a second randomising step around the 2 axis.

To obtain the 3D-stiffness, the structure is repeatedly randomised around another axis. The second randomisation step is obtained by randomising around the 2-axis as is indicated in Fig. 3.16. Slices are cut out of the cube and the same randomisation procedure is repeated as before, but now around the 2-axis. Each slice has a high and a low stiffness. For a correct calculation it is essential that $E_{//}$ in Eqn. 3.61) is always taken to be the highest Young's modulus of the sheet. The procedure is repeated several times around another axis. After several steps, a pseudo 3D-random stiffness is obtained. To illustrate the calculation, a few steps of the procedure are given:

1st step, rotate around 3-axis: $E_{high} = E_{//}$, $E_{low} = E_{\perp}$

$$E_{33}' = E_{\perp}$$

$$E_{11}' = E_{22}' = 0.375 E_{//} + 0.625 E_{\perp}$$

2nd step, rotate around 2-axis: $E_{high} = E_{11}'$, $E_{low} = E_{33}'$

$$E_{22}'' = E_{22}' = 0.375 E_{//} + 0.625 E_{\perp}$$

$$E_{11}'' = E_{33}'' = 0.375 E_{11}' + 0.625 E_{33}' = 0.141 E_{//} + 0.859 E_{\perp}$$

3-rd step, rotate around 1-axis: $E_{high} = E_{22}''$, $E_{low} = E_{33}''$

$$E_{11}''' = E_{11}'' = 0.141 E_{//} + 0.859 E_{\perp}$$

$$E_{22}''' = E_{33}''' = 0.375 E_{22}'' + 0.625 E_{33}'' = 0.174 E_{//} + 0.826 E_{\perp}$$

4-th step, rotate around 3-axis: $E_{high} = E_{22}'''$, $E_{low} = E_{11}'''$

$$E_{33}'''' = E_{33}''' = 0.174 E_{//} + 0.826 E_{\perp}$$

$$E_{11}'''' = E_{22}'''' = 0.375 E_{22}''' + 0.625 E_{11}''' = 0.194 E_{//} + 0.806 E_{\perp}$$

5-th step, rotate around 2-axis: $E_{high} = E_{11}''''$, $E_{low} = E_{33}''''$

$$E_{22}''''' = E_{22}'''' = 0.194 E_{//} + 0.806 E_{\perp}$$

$$E_{11}''''' = E_{33}''''' = 0.375 E_{11}'''' + 0.625 E_{33}'''' = 0.186 E_{//} + 0.814 E_{\perp}$$

etc.

It can be seen that after 5 steps the stiffnesses in all 3 directions are almost equal. After a few more randomisation steps around different axis the stiffnesses converge to the simple but quite accurate approximation:

$$E_{random\ 3D\ fibre} \cong 0.184 E_{//} + 0.816 E_{\perp} \quad 3.62)$$

To calculate the stiffness of a composite with 3D-random oriented platelets the same procedure is applied. A sheet filled with in-plane oriented platelets is already randomly isotropic in the plane of the sheet. The sheet now has two stiff directions instead of one. Therefore we start with: $E_{11} = E_{//}$, $E_{22} = E_{//}$ and $E_{33} = E_{\perp}$

1st step, rotate around 2-axis: $E_{high} = E_{//}$, $E_{low} = E_{\perp}$

$$E_{22}' = E_{//}$$

$$E_{11}' = E_{33}' = 0.375 E_{//} + 0.625 E_{\perp}$$

2-nd step: rotate around 1-axis, $E_{high} = E_{22}'$, $E_{low} = E_{33}'$

$$E_{11}'' = E_{11}' = 0.375 E_{//} + 0.625 E_{\perp}$$

$$E_{22}'' = E_{33}'' = 0.375 E_{22}' + 0.625 E_{33}' = 0.609 E_{//} + 0.391 E_{\perp}$$

3-rd step: rotate around 3-axis, $E_{high} = E_{22}'', E_{low} = E_{11}''$

$$E_{33}''' = E_{33}'' = 0.609 E_{//} + 0.391 E_{\perp}$$

$$E_{11}''' = E_{22}''' = 0.375 E_{22}'' + 0.625 E_{11}'' = 0.463 E_{//} + 0.537 E_{\perp}$$

etc.

As before, this quickly converges simply to :

$$E_{random\ 3D\ platelet} \cong 0.49 E_{//} + 0.51 E_{\perp} \quad (3.63)$$

In Fig. 3.17 this simple averaging procedure is compared to the more elaborate averaging procedure introduced in the preceding section 3.2.2. As can be seen, the extremely simple Eqns. 3.62) and 3.63) give results that almost coincide with the results that are obtained by the elaborate calculations needed to obtain $\langle A \rangle$ and $\langle B \rangle$ by the Mori-Tanaka averaging scheme. In this example the difference between the simple averaging scheme and the elaborate Mori-Tanaka averaging scheme is always smaller than 7%.

Fig. 3.17 also demonstrates that slender platelets are more effective than slender fibres in reinforcing a composite with randomly oriented particles.

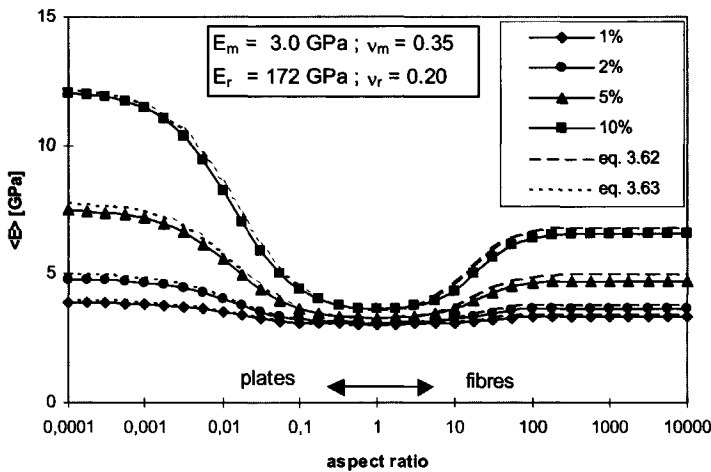


Figure 3.17 Young's modulus of a composite with 3D-randomly oriented spheroids. The solid lines are calculated by using the simple approximations 3.62 and 3.63 of this section while the dotted lines are calculated by using the elaborate Mori-Tanaka averaging scheme.

3.2.4 Correcting Halpin-Tsai equations for platelet reinforcement

As Ashton et al. [9] showed, the Halpin-Tsai equations can be used to estimate the modulus of materials that are reinforced with fibres. For a crude estimate Ashton used a shape factor $\zeta = 2w/t$ to calculate the Young's modulus of a composite with in-plane oriented platelets. Xanthos [29] rejected the Halpin-Tsai theory because he found that the stiffness of epoxy-mica composites predicted by the theory was much higher than the measured stiffness.

In this section it will be shown theoretically that the overestimation is a consequence of using $\zeta = 2w/t$ for platelet reinforcement. It is better to use a different shape factor. By

comparing Halpin-Tsai's equations with Mori-Tanaka's theory, the correct ζ -factor for platelet reinforcement will be found.

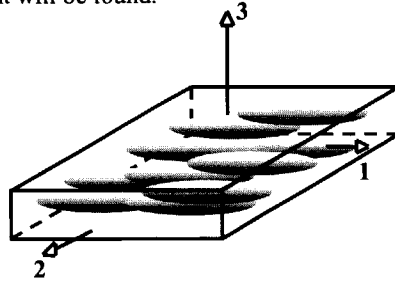


Figure 3.18 Schematic drawing of a sheet filled with in plane oriented platelets.

If a material is reinforced with unidirectionally aligned platelets as in Fig. 3.18 the material possesses transverse symmetry around the 3-axis. To calculate the Young's and shear moduli of this material the Halpin-Tsai equation 3.13) should be used with the following shape factors:

To calculate:	E_{33}	use	$\zeta = 2$	
	E_{11} , or E_{22}	use	$\zeta = 2/3 \, w/t$	3.64)
	G_{12}	use	$\zeta = 3/4 \, w/t$	
	G_{13} or G_{23}	use	$\zeta = t/w$	

The Poisson's ratios can be calculated by the following equations:

$$\begin{aligned}
 \nu_{13} &= \nu_{23} \approx c_r \nu_r + c_m \nu_m \\
 \nu_{12} &= \nu_{21} = (E_{11}/2G_{12}) - 1 \\
 \nu_{31} &= \nu_{32} = \nu_{13} E_{33}/E_{11}
 \end{aligned}
 \tag{3.65}$$

where c_r = volume fraction of the reinforcement and c_m = volume fraction of the matrix.

In Fig. 3.19 the longitudinal Young's modulus of a polymer filled with 2 vol% unidirectionally aligned platelets (oblate spheroids) is compared to that of 2 vol% fibres (prolate spheroids). The lines represent Halpin-Tsai's estimates and the symbols represent results of Mori-Tanaka's calculations. A filler modulus of 172 GPa is used as is typical for mica [25] and a polymer Young's modulus of 3 GPa as is typical for an amorphous polymer at a temperature below the glass transition.

Fig. 3.19 shows that at a given aspect ratio, fibre reinforcement gives higher unidirectional stiffness than platelet reinforcement. At high aspect ratio both reinforcements approach the limit given by the rule of mixtures. For fibres, this limit is reached at an aspect ratio of about 100, while for platelet this limit is reached at an aspect ratio of about 1000. As can be seen, Halpin-Tsai's equation can be fitted to coincide with Mori-Tanaka's equation by using an appropriate definition for the shape factor ζ . By using $\zeta = 2/3 \, w/t$ a very good fit for the stiff direction of a unidirectional platelet reinforced composite is found. To calculate G_{12} or G_{13} for unidirectional platelet reinforcement, a very good fit is found by using $\zeta = 3/4 \, w/t$ and $\zeta = t/w$ respectively. See Appendix C for more details. Note that the fit is satisfactory independent of the values of the volume fractions or elastic constants of the phases.

It was found that by using these shape factors the differences between both theories are smaller than 5% as long as $w/t > 5$ and $E_r/E_m > 10$. A reasonable fit for E_{33} ($=E_{\perp}$) can be

found by using $\zeta = 2$. The fit for E_L is not as good though as for $E_{//}$, G_{23} or G_{12} . In Appendix C it is shown that theoretically the shape factor for G_{12} should lie between $0.73 w/t$ and $0.85 w/t$ which coincides with $3/4 w/t$ that was determined by fitting.

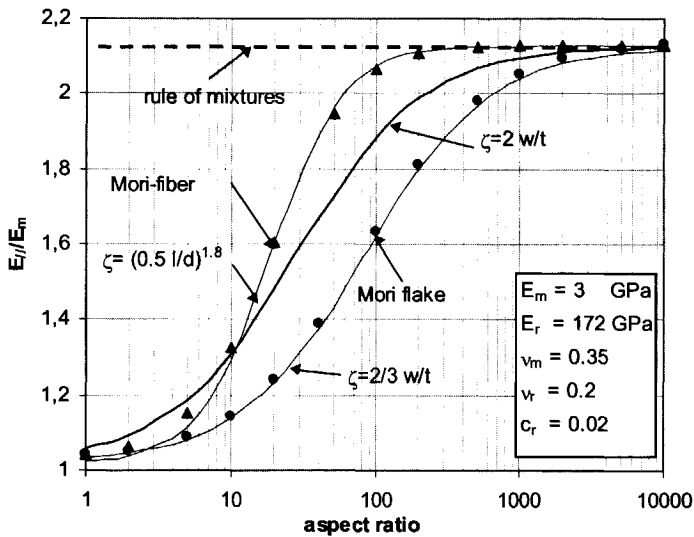


Figure 3.19 Calculated Young's-modulus of a unidirectional composite reinforced with platelets. Comparison between Halpin-Tsai's and Mori-Tanaka's theory. By using $\zeta = 2/3 w/t$ for platelets or a shape factor $\zeta = (0.5 l/d)^{1.8}$ for fibres, Halpin-Tsai's theory and Mori-Tanaka's theory agree very well. The shape factor $\zeta = 2 w/t$ used so far, gives results in-between those of Mori-Tanaka's results for fibres and platelets.

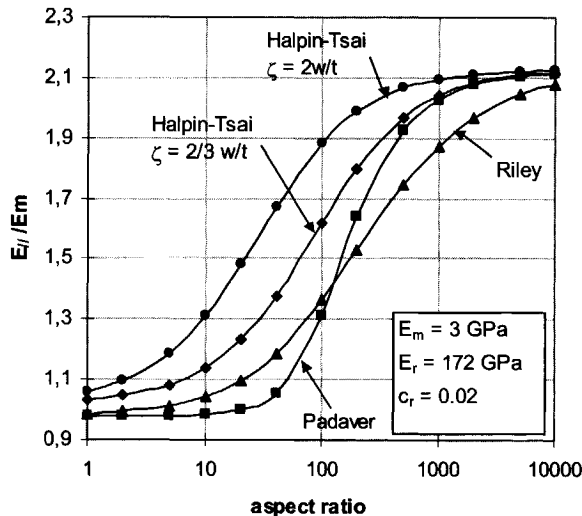


Figure 3.20 Comparison between the modified Halpin-Tsai equation and other composite models for platelet reinforcement.

At low aspect ratio the predicted Young's-modulus for platelets in Fig. 3.19 is lower than for fibres. In the limiting case of $w/t \rightarrow \infty$ both predictions for fibres and platelets are equal and coincide with the rule of mixtures. For fibres, this limiting value is reached at a lower aspect ratio than for platelets. In most literature a shape factor $\zeta = 2 w/t$ is used as was suggested by Ashton et al. [9]. From Fig. 3.19 it can be seen that this overestimates the stiffness of platelet reinforcement.

In Fig. 3.20 the modified Halpin-Tsai equation is compared to other theories for platelet reinforcement derived by Padaver [12] and Riley [13]. As can be seen, the corrected Halpin-Tsai's theory with $\zeta = 2/3 w/t$ gives results which come close to the results of both Padaver's and Riley's theories. Using $\zeta = 2 w/t$ clearly leads to an overestimation of $E_{//}$.

3.2.5 Composite models to describe visco-elastic behaviour

All above equations were derived, presuming that the constituents are purely elastic. According to the correspondence principle [30, 31, 32] these equations can also be written in a complex manner by replacing every elastic constant by its complex counterpart (E becomes $E' + iE''$, α becomes $\alpha' + i\alpha''$ etc). In this way the equations can also be used to calculate the loss modulus E'' of a composite and thus describe the visco-elastic behaviour of composites. In Appendix E it is further explained how the time response of a composite can be calculated.

3.3 Thermal expansion of two-phase composites

If the temperature of a two-phase composite is increased, both phases will try to expand. The phase with the higher expansion coefficient will want to expand more than the phase with the lower expansion coefficient. As a result, the phase with the higher expansion coefficient experiences a compressional stress, while the phase with the lower expansion coefficient experiences an extensional stress.

For the very simple two-phase composite, with matrix m and reinforcement r depicted in Fig. 3.21, the total expansion of the composite can be calculated rather easily.

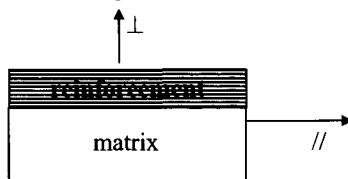


Figure 3.21 Simple two-phase composite.

In the perpendicular direction, both phases can expand freely so the expansion coefficient becomes:

$$\alpha_{\perp} = c_r \alpha^{(r)} + c_m \alpha^{(m)} \quad (3.66)$$

The expansion in the parallel direction can be obtained as follows. Assume that the total thermal expansion of the composite in the parallel direction can be written as:

$$\epsilon_{//} = \alpha_{//} \Delta T \quad (3.67)$$

where ΔT is the change in temperature. This generates stresses in the parallel direction equal to:

$$\begin{aligned}\sigma_{//}^{(r)} &= E^{(r)} (\alpha_{//} \Delta T - \alpha^{(r)} \Delta T) \\ \sigma_{//}^{(m)} &= E^{(m)} (\alpha_{//} \Delta T - \alpha^{(m)} \Delta T)\end{aligned}\quad 3.68)$$

The total stress on the composite remains zero:

$$\sigma_{//} = c_r \sigma_{//}^{(r)} + c_m \sigma_{//}^{(m)} = 0 \quad 3.69)$$

By substituting 3.68) in 3.69) one gets:

$$c_r E^{(r)} (\alpha_{//} \Delta T - \alpha^{(r)} \Delta T) + c_m E^{(m)} (\alpha_{//} \Delta T - \alpha^{(m)} \Delta T) = 0 \quad 3.70)$$

and $\alpha_{//}$ becomes:

$$\alpha_{//} = \frac{c_r E^{(r)} \alpha^{(r)} + c_m E^{(m)} \alpha^{(m)}}{c_r E^{(r)} + c_m E^{(m)}} = \frac{c_r E^{(r)} \alpha^{(r)} + c_m E^{(m)} \alpha^{(m)}}{E_{//}} \quad 3.71)$$

Using $c_m = 1 - c_r$ and $E_{//} = c_r E^{(r)} + c_m E^{(m)}$, Eqn. 3.71) can also be written as:

$$\alpha_{//} = (\alpha^{(r)} - \alpha^{(m)}) \left(\frac{1}{E^{(r)}} - \frac{1}{E^{(m)}} \right)^{-1} \left(\frac{1}{E_{//}} - \frac{1}{E^{(m)}} \right) + \alpha^{(m)} \quad 3.72)$$

So for the simple two-phase composite in Fig. 3.21 the parallel expansion coefficient is a function of the parallel stiffness of the composite, of the thermal expansion coefficient of the phases and of their stiffnesses. The volume fraction of the reinforcement does not enter this equation because it is incorporated in the composite stiffness $E_{//}$.

For a general two-phase composite the thermal expansion can be written as [5,8]:

$$\alpha_{ij} = (\alpha_{kl}^{(r)} - \alpha_{kl}^{(m)}) (S_{klmn}^{(r)} - S_{klmn}^{(m)})^{-1} (S_{mnij} - S_{mnij}^{(m)}) + \alpha_{ij}^{(m)} \quad 3.73)$$

where α is the thermal expansion tensor and S is the compliance tensor. Eqns. 3.72) and 3.73) have the same appearance. The difference between the two equations is that Eqn. 3.72) only contains scalar quantities and is valid only for the composite in Fig. 3.21, while Eqn. 3.73) contains tensor quantities and is generally valid.

For a macroscopically isotropic composite 3.73) can be rewritten as:

$$\alpha = \alpha_m + \frac{\alpha_m - \alpha_r}{1/K_m - 1/K_r} \left[\frac{1}{K} - \frac{1}{K_m} \right] \quad 3.74)$$

For transverse isotropic two-phase composites with their axes of symmetry coinciding with the 3-axis, Eqn. 3.73) becomes:

$$\alpha_{33} = \alpha_m + \frac{\alpha_m - \alpha_r}{1/K_m - 1/K_r} \left[\frac{3(1 - 2\nu_{31})}{E_{33}} - \frac{1}{K_m} \right] \quad 3.75)$$

and

$$\alpha_{11} = \alpha_m + \frac{\alpha_m - \alpha_r}{1/K_m - 1/K_r} \left[\frac{3}{2k_{12}} - \frac{3\nu_{31}(1 - 2\nu_{31})}{E_{33}} - \frac{1}{K_m} \right] \quad 3.76$$

where ν is the Poisson's ratio, K is the bulk modulus and k_{12} is the plane strain bulk modulus defined as:

$$\frac{1}{k_{12}} = 4 \left(\frac{1}{E_{11}} - \frac{\nu_{31}^2}{E_{33}} \right) - \frac{1}{G_{12}} \quad 3.77$$

Eqn. 3.73) was used to calculate the coefficient of linear thermal expansion (CLTE) of a composite filled with 2 vol% of platelets. Both matrix and filler were assumed to have isotropic properties. As in the previous examples the matrix and filler have elastic properties equal to dry polyamide-6 and mica respectively. To use Eqn. 3.73) first the compliance S of the composite needs to be calculated. This is done with the Mori-Tanaka theory that was explained in Sections 3.2.1 and 3.2.2. The Halpin-Tsai approximation of section 3.2.4. proved to be not accurate enough for this calculation. This is mainly due to the low accuracy in the determination of E_{\perp} . Figs. 3.22 a) and b) show the calculated CLTE of a composite with aligned spheroids, while Fig. 3.22 c) shows that of a 3D-randomly oriented composite.

Before discussing the figures an attempt is made to intuitively understand the thermal expansion of an aligned composite. For the sake of clarity it is assumed that the matrix is incompressible ($K_m = \infty$) and the filler is stiff and does not expand upon increasing the temperature. Also perfect adhesion between matrix and filler is assumed. If the composite is heated, the matrix will try to expand, while the filler will try to resist the expansion. The resistance of the filler against expansion will be largest in the direction of highest composite stiffness. Therefore, the CLTE will be lowest in the direction of highest stiffness. Since the matrix is incompressible, the total volumetric expansion of the matrix is not changed by the presence of the filler. Consequently the thermal expansion of the composite will be decreased in the stiffest direction while it will be increased in the softest direction.

An aligned composite with platelets has two stiff directions, while a composite with aligned fibres has only one stiff direction. Since the total volumetric expansion is constant, the expansion in the soft direction will be larger with aligned platelets than with aligned fibres. In a 3D randomly oriented composite with an incompressible matrix, the thermal expansion will not change upon increasing the aspect ratio of the filler. In a true composite, the matrix is not incompressible and consequently the expansion coefficient is lowered even in case of randomly oriented fillers.

As expected, Figs. 3.22a) and b) show that the CLTE of an aligned composite is lowest in the direction of highest stiffness. In addition, the CLTE in the softest direction is larger than the CLTE of the matrix. The perpendicular expansion of the composites filled with platelets (α_{33} Fig. 3.22b) is larger than that of the composite filled with fibres (α_{11} Fig. 3.22a). This is in agreement with the intuitive discussion given earlier. The stiffnesses of these composites is plotted in Figs. 3.7 and 3.8.

In case of 3D-random in Fig. 3.22 c) the expansion is decreased upon addition of slender particles (either very high or very low aspect ratio). This is a consequence of the compressibility of the matrix ($\nu_m = 0.35$). The CLTE is not as low though as in the stiff directions of the aligned composite.

From the discussion above it is obvious that the CLTE is very sensitive for the bulk modulus or Poisson's ratio of the matrix. Lowering the bulk modulus or the Poisson's ratio of the matrix would therefore be an effective way of lowering the CLTE of a composite.

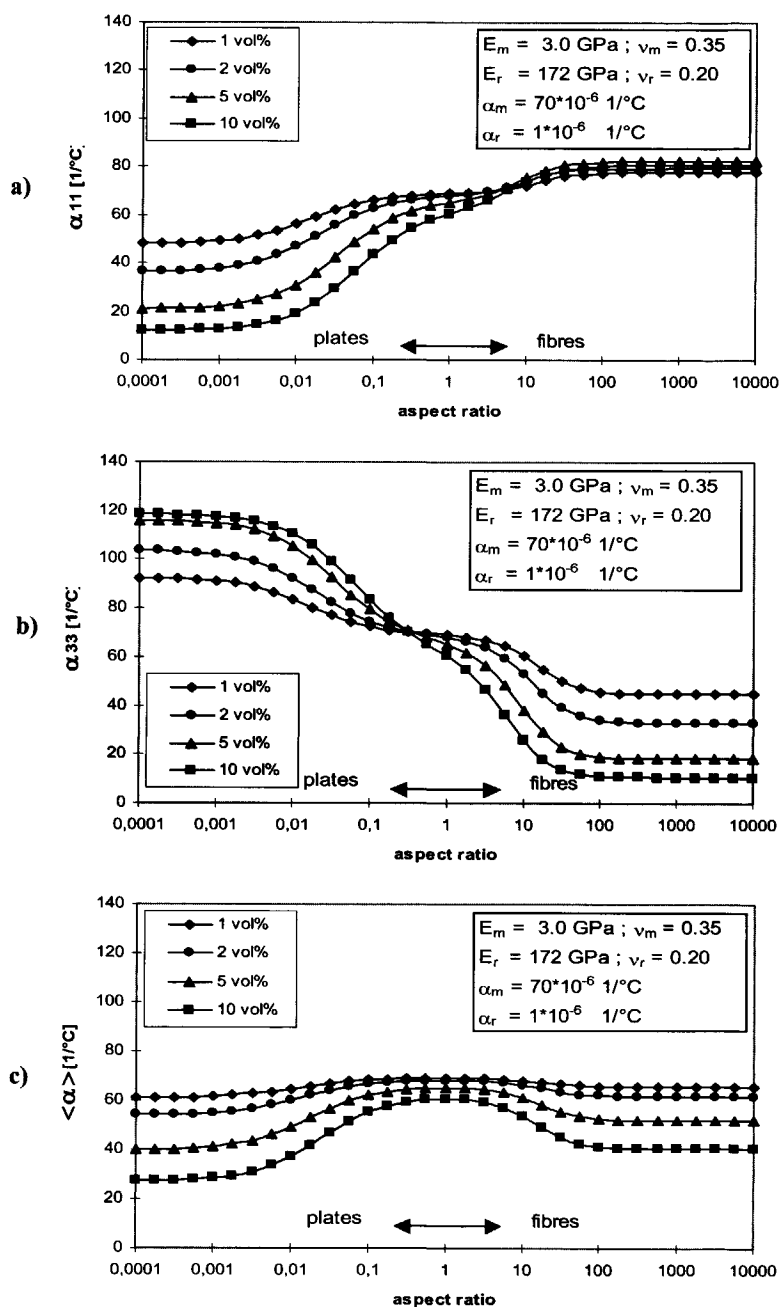


Figure 3.22 Theoretical predictions of the thermal expansion coefficient of a composite filled with spheroids.

- a)** Thermal expansion coefficient in the 11-direction of a unidirectional oriented composite.
- b)** Thermal expansion coefficient in the 33-direction of a unidirectional oriented composite.
- c)** Thermal expansion coefficient of a 3D randomly oriented composite.

3.4 References

- [1] I.M. Ward, *Mechanical Properties of Solid Polymers 2nd ed.*, Wiley, 1985.
- [2] R.F.S. Hearmon, *An Introduction to Applied Anisotropic Elasticity*, Oxford, 1961.
- [3] T.S. Chow, *Mesoscopic Physics of Complex Materials*, Springer, Berlin, 2000, Ch. 7.
- [4] D. Hull, *An Introduction to Composite Materials*, Cambridge, Cambridge University Press, 1981.
- [5] J. Aboudi, *Mechanics of Composite Materials*, Elseviers, Amsterdam, 1991.
- [6] D. Yu. Godovski, *Electron behavior and magnetic properties of polymer nanocomposites*, Adv. Pol. Sci. **119**, 1995, p 79-122.
- [7] P.A.M. Steeman and F.H.J. Maurer, *An interlayer model for the complex dielectric constant of composites: an extension to ellipsoidally shaped particles*, Colloid Pol. Sci. **270**, 1992, p 1069-1079.
- [8] R.M. Christensen, *Mechanics of Composite Materials*, Wiley, New York, 1979.
- [9] J.E. Ashton, J.C. Halpin, P.H. Petit, *Primer on composite materials: Analysis*, Technomic Publishing Co., 1969, Chapter 5.
- [10] F.H.J. Maurer, *Zur Beschreibung des Elastischen und Viscoelastischen Verhaltens Teilchengefüllter Verbundwerkstoffe mit einer Zwischenschicht*, PhD Thesis, University of Duisburg, 1983.
- [11] T.S. Chow, *Elastic moduli of filled polymers: The effect of particle shape*, J. Appl. Phys. **48(10)**, 1977, p 4072-4075.
- [12] G.E. Padaver, and N. Beecher, *On the strength and stiffness of planar reinforced plastic resins*, Pol. Eng. Sci. **10(3)**, 1970, p 185-192.
- [13] V.R. Riley, *Interaction effects in fiber composites*, Polymer Conf. Series, Univ. of Utah, June 1970.
- [14] K. Iisaka and K. Shibayama, *Effect of orientation of two dimensional filler on dynamic mechanical properties of cured epoxy resin*, J. Appl. Pol. Science **20**, 1976, p 813-823
- [15] K. Iisaka, *Dynamic visco-elastic properties of composite materials*, Compos. Polym. **1(3)**, 1988, p 199-220.
- [16] C.Y. Hui and D. Shia, *Simple formula for the effective moduli of unidirectional aligned composites*, Pol. Eng. Sci. **38(5)**, 1998, p 774-782.
- [17] G.P. Tandon and G.J. Weng, *The effect of aspect ratio of inclusions on the elastic properties of unidirectionally aligned composites*, Polymer Composites **5(4)**, 1984, p 327-333.
- [18] J.D. Eshelby, *The determination of the elastic field of an ellipsoidal inclusion and related problems*, Proc. R. Soc. **A241**, 1957, p 376-396.
- [19] Tai Te Wu, *The effect of inclusion shape on the elastic moduli of two-phase material*, Int. J. Solids Structures **2**, 1966, p 1-8.
- [20] T. Mori and K. Tanaka, *Average stress in matrix and average elastic energy of materials with misfitting inclusions*, Acta Metall. **21**, 1973, p 571-574.
- [21] T. Mura, *Mechanics of Elastic and Inelastic Solids*, Nijhoff, The Hague, 1982.
- [22] A.N. Norris, *An examination of the Mori-Tanaka effective medium approximation for multiphase composites*, J. Appl. Mech. **56**, 1989, p 83-88.
- [23] T. Chen, G.J. Dvorak, Y. Benveniste, *Mori-Tanaka estimates of the overall moduli of certain composite materials*, J. Appl. Mech. **59**, 1992, p 539-546.
- [24] Appendix A of this thesis.
- [25] H.R. Shell and K.H. Ivey, *Fluorine Micas*, Bulletin **647**, Bureau of Mines, U.S. Department of the interior, 1969.
- [26] R.G.C. Arridge, *An Introduction to Polymer Mechanics*, Taylor&Francis, London, 1985.

- [27] Gregory Lielens, *Micro-Macro Modelling of Structured Materials*, PhD Thesis University of Louvain la Neuve, Belgium, 1999. See also G. Lielens, P. Pirotte, A. Couniot, F. Dupret and R. Keunings, *Prediction of thermo-mechanical properties for compression moulded composites*, *Composites A* **29A**, 1998, p 63-70.
- [28] S.W. Tsai, J.C. Halpin, N.J. Pagano, *Composite Materials Workshop*, Technomic Publishing Co., Stamford, Conn. USA, 1968.
- [29] M. Xanthos, *High Aspect Ratio Mica Reinforced Thermosets*, PhD Thesis University of Toronto, Canada 1974.
- [30] R.M. Christensen, *Theory of Viscoelasticity*, Academic Press, New York 1971, p 41.
- [31] J.M. Whitney and R.L. McCullough, *Micromechanical Materials Modeling*, Technomic Publishing Co., Lancaster, USA, 1990.
- [32] R.F. Eduljee and R.L. McCullough, *Elastic Properties of Composites*, in *Structure and Properties of Composites*, ed. by T.W. Chou, V.C.H. Weinheim 1993, Ch 9, p 381-474.

Validation of composite models

Abstract

In polymer-clay nanocomposites the exfoliated clay particles have the shape of platelets. As will be shown in later chapters the stiffness of nanocomposites levels off at high volume fractions. This levelling off is not predicted by composite modelling or observed experimentally in comparable mica filled composites. To find out the reason for this deviation a composite model is required that gives reliable estimates of Young's modulus and thermal expansion of platelet reinforced composites. Any difference between model prediction and experimental results of nanocomposites can then be assigned to the special behaviour of nanocomposites. This way it can be distinguished to which degree the increase in stiffness of nanocomposites should be attributed to a change in properties of the polymer matrix or to the high aspect ratio of the clay platelets.

To this end the analytical the micromechanical composite models that were introduced in Chapter 3 are validated by comparing them with experiments on microcomposites and with finite element modelling. In most cases the modified Halpin-Tsai model is used as an analytical model. Since this model was modified such that it accurately fits with the Mori-Tanaka model, validation of this model automatically implies validation of the Mori-Tanaka model. The comparison is performed at a wide range of volume fractions and aspect ratios of the platelets.

The differences between Mori-Tanaka predictions of Young's moduli and the experimentally determined Young's moduli of polymers filled with platelets are small. Young's moduli of platelet-reinforced composites are predicted with a typical error of 10% and a maximum error of 25 %.

Mori-Tanaka's estimates also compare well with finite element calculations. Mori-Tanaka predictions of thermal expansion almost coincide over the whole range of volume fractions and aspect ratios considered. At low aspect ratios or low volume fractions, Mori-Tanaka's estimates of the Young's modulus agree very well with the estimates of finite element modelling. In this range the typical difference between both models is smaller than 5 %. The Mori-Tanaka model tends to underestimate the Young's modulus somewhat, if both volume fraction and aspect ratio are large.

4.1 Introduction

In Chapter 3 a theoretical model was introduced to calculate the elastic properties of platelet filled composites. The model is based on Eshelby's equivalent inclusion method and on Mori-Tanaka's average stress theory. The parameters in the composite model are the matrix stiffness tensor C_m , the filler stiffness tensor C_r , the volume fraction c_r , the filler aspect ratio α and the orientation distribution function $\Phi(\theta, \phi, \psi)$. The model assumes perfect adhesion between matrix and dispersed phase and assumes that the material is homogeneous. This implies that the dispersed phase is well distributed through the polymer and that the dimensions of the tested sample is always much larger than the largest dimension of the filler particles. Implicitly, the model also assumes that the stiffness of the polymer is not changed by the presence of the clay.

In this chapter, the model will be tested by comparing its results with experimental results and with results from finite element modelling. For rigorous testing of the model, one would like to vary all theoretical parameters experimentally and check whether the composite model predicts the correct results. Although particle size is no parameter in the composite model, it would be preferable to also test the effect of particle size on composite stiffness.

All experimental results needed to test the model are obtained from the literature. Most work has been done on mica-reinforced composites. This is a fortunate coincidence, since clay platelets in nanocomposites have the same molecular and crystal structure as mica platelets have. Most articles on mica reinforcement fail to give information on particle aspect ratio and orientation. Only those publications that do supply morphological information are used.

Instead of using Mori-Tanaka's theory to predict the stiffness of the mica filled composites the modified Halpin-Tsai equations were used in some cases. As was shown in Chapter 3, the modified Halpin-Tsai equation gives results that coincide with Mori-Tanaka's model. Using the Halpin-Tsai equations has the obvious advantage of being simple. Very often, authors who publish experimental results do not specify the Poisson's ratios of the phases. The theory of Halpin and Tsai does not require the input of Poisson's ratios to calculate the stiffness of a composite.

Although comparison with experimental results gives information on the usefulness of the composite model, it does not prove its theoretical correctness. The theoretical correctness of the Mori-Tanaka theory is proven by comparing the results of (analytical) composite modelling with the results of 3D-finite element modelling. To this end, a recently developed finite element software package, Palmyra [1] is used. Not only the stiffness is calculated with the finite element model but also the expansion coefficient. This also enables us to test the equations for the expansion coefficient given in Chapter 3.

4.2 Validation of composite models by comparison with experimental results

Lusis et al. [2] and Xanthos [3] reported on the effect of aspect ratio on the flexural properties of reinforced plastics. By grinding two naturally occurring micas, phlogopite and muscovite, mica platelets were made with aspect ratios ranging from 10 to 267. The thickness of the platelets was in the order of 2 μm . The muscovite micas were dispersed in water containing a styrene/acrylic acid copolymer latex. After removal of the water, a composite with unidirectional well-dispersed mica particles was obtained. The phlogopite mica was dispersed in a polyester resin (Reichert PolyLite 31-000). Both polystyrene-copolymer and polyester resins had a flexural modulus of 3.5 GPa. The tensile modulus of the mica platelets used by Lusis is obtained from an epoxy-mica laminate with 60 vol% of perfectly oriented continuous

mica sheets. This laminate had a Young's modulus of 90 GPa. Using the rule of mixtures results in an effective Young's modulus for mica of 150 GPa. This is a little lower than the 172 GPa reported for a perfect mica crystal [4].

Fig. 4.1 shows the flexural modulus of the unidirectional mica composites as a function of mica volume fraction at different aspect ratios. The solid lines represent the (modified) Halpin-Tsai predictions and the symbols represent the experimental values. As can be seen from Fig. 4.1, the stiffness of all samples is predicted rather well by the Halpin-Tsai equation with a shape factor $\zeta = 2/3 w/t$ as proposed in Chapter 3 of this thesis.

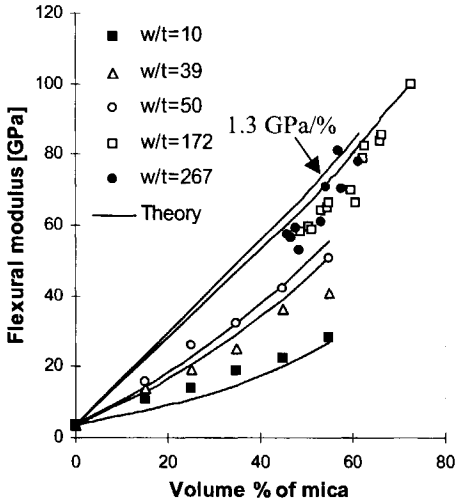


Figure 4.1 Flexural modulus of composites filled with unidirectional mica sheets of different aspect ratios as a function of mica volume fraction. From Lusi et al. [2]. Symbols represent experimental values and solid lines represent theoretical predictions. For theoretical prediction the Halpin-Tsai equations are used with a new shape factor $\zeta = 2/3 w/t$, a matrix Young's modulus of 3.5 GPa and a filler Young's modulus of 150 GPa.

Open symbols: muscovite mica in PS-copolymer.

Closed symbols: phlogopite mica in polyester.

Lines: modified Halpin-Tsai estimates.

If, instead of $\zeta = 2/3 w/t$ a shape factor $\zeta = 2 w/t$ is used, as was suggested by Ashton et al. [5], the deviation between the predicted and measured modulus is much larger. In fact, Lusi rejected the Halpin-Tsai equations because using $\zeta = 2 w/t$ resulted in a large discrepancy between theory and experiment.

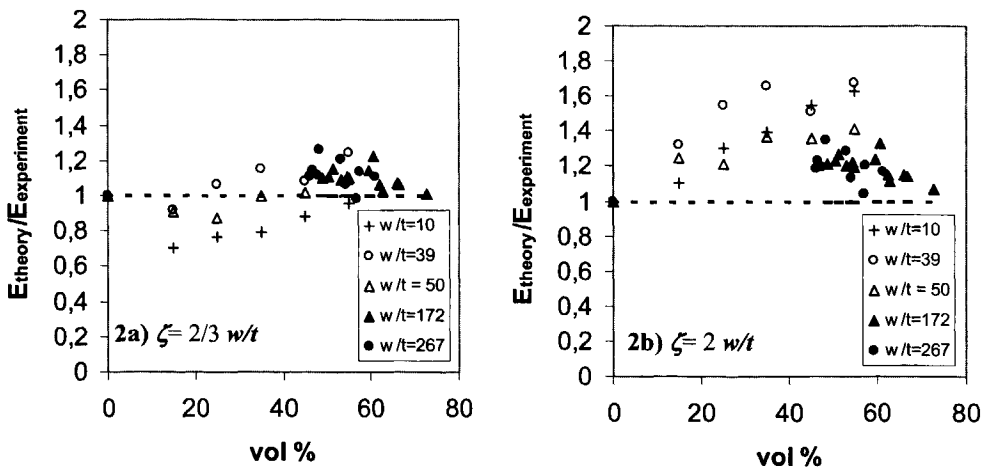


Figure 4.2 Ratio of theoretical and experimental Young's modulus of mica-composites.

a) Using shape factor $\zeta = 2/3 w/t$ as suggested in Chapter 3 of this thesis.

b) Using shape factor $\zeta = 2 w/t$ as suggested by Ashton et al. [5].

This is illustrated in Figs. 4.2a and 4.2b. Using $\zeta = 2/3 \text{ w/t}$, the maximum difference between theory and experiment is about 30%, while it is 75% by using $\zeta = 2 \text{ w/t}$. This illustrates that the suggested theory gives a much better prediction of stiffness than the theories used up to date. In several articles the Halpin-Tsai equation is found to predict much higher Young's moduli of platelet reinforced plastics than was actually measured [2,5]. It is thought that this is due to using the wrong shape factor.

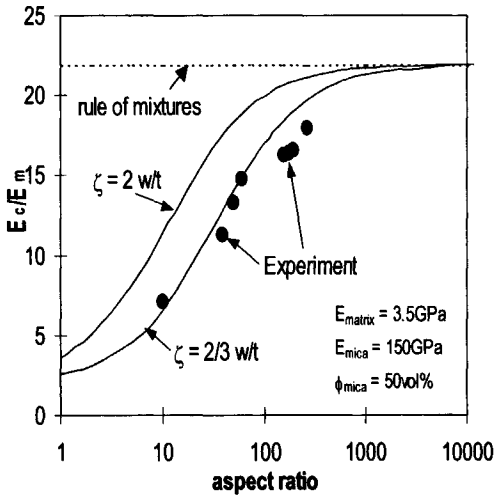


Figure 4.3 Young's modulus of PS-copolymer composites filled with 50 vol% of unidirectional mica flakes as a function of flake aspect ratio. Symbols represent experimental values and solid lines represent theoretical predictions. The dotted line denotes the maximum attainable modulus for continuous mica sheets. For theoretical prediction, the Halpin-Tsai equations were used with a matrix Young's modulus of 3.5 GPa, a filler Young's modulus of 150 GPa and shape factors of $\zeta = 2/3 \text{ w/t}$ and $\zeta = 2 \text{ w/t}$ respectively.

Fig. 4.3 shows the stiffness as a function of aspect ratio of mica composites with 50% of mica. Halpin-Tsai predictions for $\zeta = 2/3 \text{ w/t}$ and $\zeta = 2 \text{ w/t}$ are also shown. The graph clearly illustrates the good prediction of the Young's modulus by using a shape factor of $\zeta = 2/3 \text{ w/t}$.

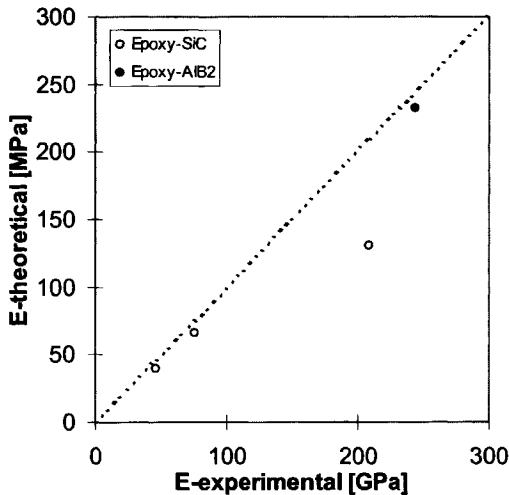


Figure 4.4 Comparison of theoretical and experimental Young's modulus of unidirectional epoxy-SiC and epoxy-AlB₂ composites. Data are taken from Padaver and Beecher [6].

The work of Lusiš et al. [2] is the only example found in the literature, where the aspect ratio was determined from direct microscopic examination of the composite. To ensure reliable results, the aspect ratios were calculated as the number average of about 100 platelets. The aspect ratio distribution was narrow because the mica platelets were fractionated.

Therefore, the number averaged aspect ratio does not differ very much from the weight-averaged aspect ratio. For not fractionated samples, Lusi used the weight average aspect ratio because the weight-average aspect ratio correlated better with the observed flexural properties.

Padaver and Beecher [6] presented data of unidirectionally oriented epoxy-SiC and epoxy-AlB₂ composites filled at high volume fractions of 0,4-0,65 respectively and aspect ratios between 40 and 500. In Fig. 4.4 these data are compared with Halpin-Tsai calculations again using $\zeta = 2/3 w/t$. As can be seen the Halpin-Tsai prediction is very good except for one measurement.

Iisaka [7,8] reported on the effect of the orientation of muscovite mica flakes on the stiffness of an epoxy-mica composite. It is regrettable that he did not pay much attention on accurate determination of the aspect ratio. The aspect ratio was determined from the flake diameter and flake thickness before the mica was added to the polymer. So any breakdown of flake diameter during production of the composites was not accounted for. In his first article [7] Iisaka mentions a flake diameter of 470 μm and a flake thickness of 1 μm and thus uses an aspect ratio of 470 for his calculations. In a later article [8], that reports about the same composites, he mentions a flake diameter of 41 μm and a flake thickness of 1 μm . The correct aspect ratio of the mica flakes is thus unclear.

Fig. 4.5 shows the storage modulus in the glassy state of the epoxy-mica composites with uniaxially and random oriented flakes. The figure also includes the theoretical estimates calculated by using the modified Halpin-Tsai equation. The stiffness of the unidirectionally oriented composite is calculated using $\zeta = 2/3 w/t$. The stiffness of the randomly oriented composite is calculated with the simplified equation for random orientation of flakes: $E_{\text{random 3D platelet}} \approx 0.49E_{\parallel} + 0.51E_{\perp}$. (Chapter 3). E_{\parallel} and E_{\perp} are calculated with the Halpin-Tsai equation by using $\zeta = 2/3 w/t$ and $\zeta = 2$ respectively.

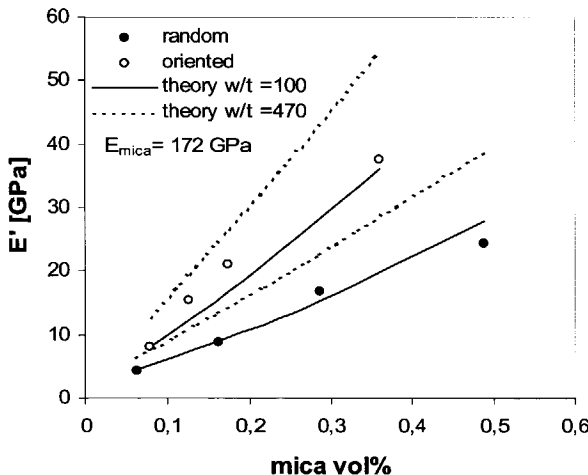


Figure 4.5 the 1 Hz storage modulus of mica-epoxy composites with unidirectional and randomly oriented mica flakes. Data are taken from Iisaka [7,8]

Fig. 4.5 shows that the stiffness of both unidirectional and randomly oriented composites is fitted well by using an aspect ratio of 100. Using an aspect ratio of 470 leads to over-estimation of the Young's moduli, while an aspect ratio of 41 (not shown) leads to under estimation. Due to inaccurate determination of the aspect ratio, the effect of aspect ratio on the stiffness is unclear from these experiments. The effect of orientation on stiffness is correctly predicted by the simplified equation for random orientation of platelets.

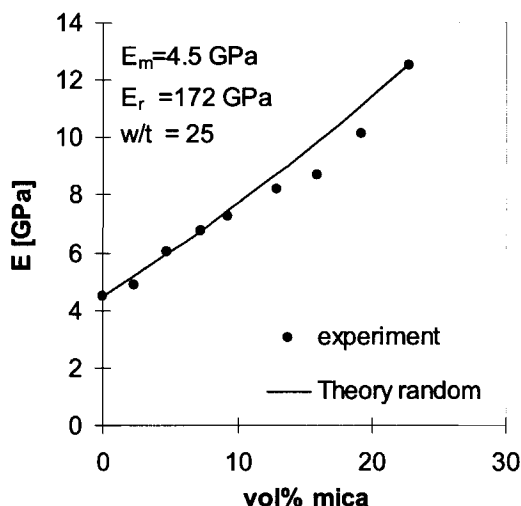


Figure 4.6 Comparison between measured and calculated Young's modulus of mica filled polyester [9]. Random orientation of the mica platelets is assumed. The effect of random orientation is estimated by: $E_{\text{random 3D platelet}} \cong 0.49E_{\parallel} + 0.51E_{\perp}$. E_{\parallel} and E_{\perp} are calculated with the Halpin-Tsai equation using a shape factor of $\zeta=2/3$ w/t and $\zeta=2$ respectively.

In another publication, Roy and Phani [9] made mica-filled polyester composites by adding dry ground mica powder, with an aspect ratio of 25, to an isophthalic polyesters resin. No special care was taken to orient the flakes. Therefore, it is assumed that the flakes are randomly oriented. As can be seen in Fig. 4.6, again a very good agreement between measurement and calculation is found.

4.3 Validation of Mori-Tanaka model by comparison with finite element model

In order to test the validity of the Mori-Tanaka model, the results of the model are compared with the results of a finite element computer program called Palmyra.

4.3.1 Finite element computer program Palmyra

Palmyra is a computer program used to design composite materials and to calculate their physical properties. The programme essentially fills a periodic continued base cell with a number of inclusions. The orientation of the inclusions, their shape and their properties can be specified. Palmyra builds a three-dimensional mesh of hundreds of thousands of non-overlapping tetrahedron elements that fully cover the volume of the periodic cell. The sizes of the mesh tetrahedrons vary with the local morphology in order to get a higher resolution at the interfaces and where inclusion objects are very close.

An energy minimisation approach is used to calculate physical properties like Young's modulus and thermal expansion. Newer versions of the program are also able to calculate other properties like thermal conductivity, dielectric properties, electric conductivity, refraction index and transport properties (permeability and diffusivity). The Palmyra model can handle different inclusion shapes. For calculation of nanocomposite reinforcement flat platelets were used instead of oblate spheroids that are used in the Mori-Tanaka model. Gusev et al. [1] wrote an article about the use of Palmyra to visualise the fibre packing of fibre filled composites and calculate their elastic properties.

4.3.2 Platelets in a matrix: analytical versus finite element calculations

In a joint programme between DSM and the ETH-Zürich, some Finite element (FE) calculations were performed on PP filled with oriented talcum particles. Palmyra is a flexible and accurate FE programme but requires a lot of computing time (typically 15 minutes to 12 hours on an up to date year 2001 SUN computer, depending on the complexity of the calculation). The amount of computer time required by Palmyra depends on the amount of nodes in a base cell. If a base cell only contains a few particles, the amount of nodes is limited and the calculations are relatively fast. Unfortunately, calculations on small base cells are not representative for the composite under study.

In order to obtain representative results, two strategies can be employed. One is to make the base cell large enough to be representative for the whole composite. Another is to make several non-representative base cells with only a few particles and average their results. The latter strategy is faster than the former and is therefore employed in the calculations that are presented in this section. An example of a single periodic base cell is given in Fig. 4.7. Every base cell contains 20 aligned platelets that are positioned in space by a Monte Carlo simulation. The results of 7 Monte Carlo snapshots are averaged to obtain the final result.

FE modelling of platelets with a very high aspect ratio has some limitations. One of them is caused by the small radius of curvature at the ends of inclusions with high aspect ratio that can result in high stress concentrations. High mesh densities are required to calculate these stress-concentrations accurately. This increases the amount of computing time. To prevent extremely long computing time the aspect ratio of the particles is limited to 50.

The following matrix and inclusion properties were used in the calculations that are listed in Table 4.1 and plotted in Figs. 4.8 and 4.9:

Matrix:	Polypropylene;	$E_m=1$ GPa;	$\nu_m=0.35$;	$\alpha_m=100 \cdot 10^{-6} \text{ } 1/^{\circ}\text{C}$
Inclusions:	Talc;	$E_r=100$ GPa;	$\nu_r=0.25$;	$\alpha_r=5 \cdot 10^{-6} \text{ } 1/^{\circ}\text{C}$

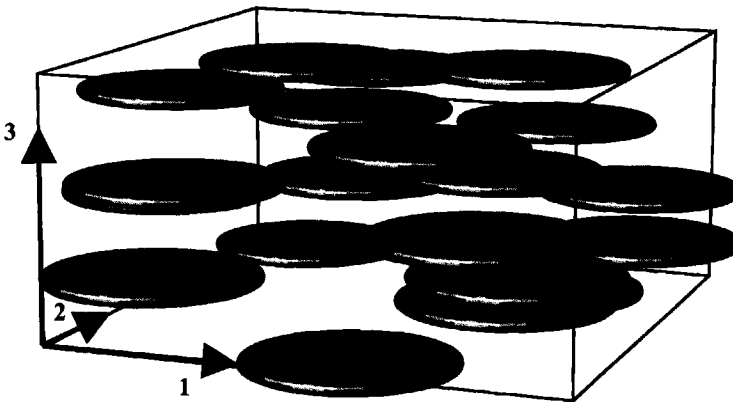


Figure 4.7 Example of a small periodic base cell with 20 aligned flat plates as was used in the finite element model. The position of the plates in space is determined by shaking the box in a Monte Carlo simulation. The results of 7 Monte Carlo snapshots were averaged to obtain the final results.

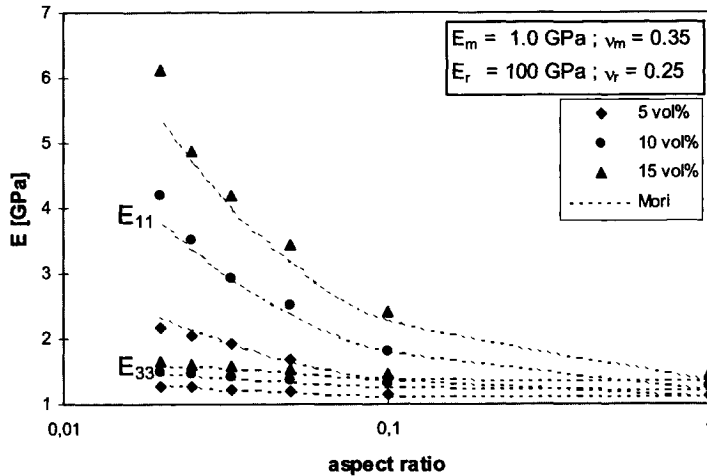


Figure 4.8 Young's moduli E_{11} and E_{33} of PP with talc, calculated with Mori-Tanaka theory and with Palmyra finite element software. Dotted lines represent Mori-Tanaka calculations. Symbols represent Palmyra calculations.

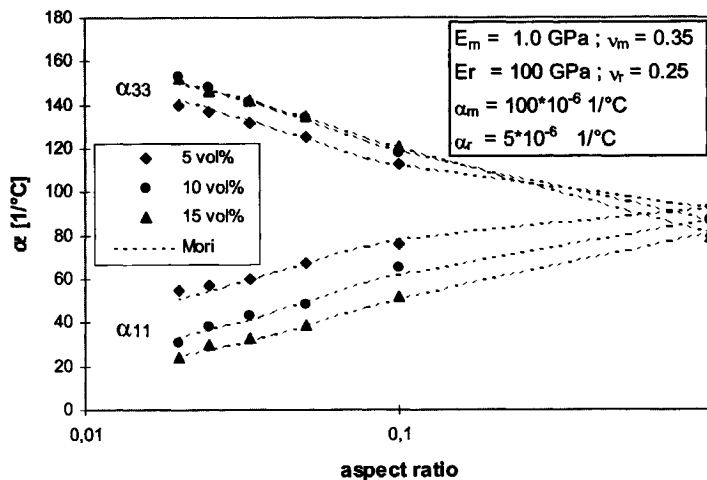


Figure 4.9 Thermal expansion coefficients α_{11} and α_{33} of PP with talc, calculated with Mori-Tanaka theory and with Palmyra finite element software. Dotted lines represent Mori-Tanaka calculations. Symbols represent Palmyra calculations.

At low volume fractions and aspect ratios Mori-Tanaka estimates of Young's modulus agree rather well with Palmyra results. Differences are within a few percent. Only at higher volume fraction and higher aspect ratios the Mori-Tanaka calculations of the parallel stiffness are systematically lower than Palmyra's. Despite this systematic difference the agreement is very good. Deviations are always less than 20%. The trends are always in agreement. In the perpendicular direction the stiffness is not much increased. This is predicted by Palmyra and by Mori-Tanaka's calculations.

The Mori-Tanaka estimates for Young's moduli and thermal expansions almost coincide with the Palmyra estimates. The use of oblate spheroids in the Mori-Tanaka model gives good estimates for the reinforcement of flat platelets as are used in the Palmyra model.

Mori-Tanaka's estimates of the expansion coefficients of the composites agree very well with Palmyra's predictions. This is not surprising since the Young's moduli agree very well too.

vol%	w/t	Mori-Tanaka		Palmyra		Mori-Tanaka		Palmyra	
		E ₁₁	E ₃₃	E ₁₁	E ₃₃	α_{11}	α_{33}	α_{11}	α_{33}
		GPa	GPa	GPa	GPa	1/°C x10 ⁶	1/°C x10 ⁶	1/°C x10 ⁶	1/°C x10 ⁶
5	1	1,11	1,11	1,12	1,13	93	93	93	93
5	1/10	1,39	1,13	1,41	1,15	76	113	78	113
5	1/20	1,67	1,19	1,68	1,20	67	125	67	125
5	1/30	1,92	1,23	1,92	1,23	60	132	60	133
5	1/40	2,15	1,26	2,05	1,26	57	137	55	139
5	1/50	2,34	1,29	2,16	1,28	55	140	51	143
10	1	1,23	1,23	1,27	1,28	87	86	87	87
10	1/10	1,82	1,26	1,81	1,31	65	118	62	119
10	1/20	2,40	1,34	2,51	1,37	48	134	50	134
10	1/30	2,92	1,40	2,92	1,41	43	141	42	142
10	1/40	3,37	1,44	3,52	1,46	38	148	37	147
10	1/50	3,78	1,47	4,19	1,50	31	153	34	151
15	1	1,36	1,36	1,45	1,47	81	79	81	81
15	1/10	2,29	1,39	2,41	1,47	52	121	51	121
15	1/20	3,20	1,49	3,44	1,53	39	135	39	135
15	1/30	4,00	1,55	4,19	1,59	33	142	32	143
15	1/40	4,71	1,59	4,88	1,62	30	146	28	147
15	1/50	5,33	1,62	6,12	1,67	24	152	25	150

Table 4.1 Mori-Tanaka and Palmyra calculations of PP with talc.

4.4 Conclusions

The analytical Mori-Tanaka model gives estimates for the Young's modulus and the thermal expansion that agree very well with experimental results and with results from numerical finite element modelling.

By comparing the experimental results of Lusis et al. with analytical calculations, it is proven that the suggested composite model for platelet reinforcement works well. The stiffness of unidirectional mica composites with aspect ratios between 10 and 267 were predicted with a typical error of 10% and a maximum error of 30 %. This is a very good result if it is considered that *no fitting parameters are used*. Also the stiffness of unidirectionally epoxy-SiC an epoxy-AlB₂ composites are predicted well. The effect of random orientation of platelets was correctly predicted for epoxy-mica and epoxy-polyester composites.

The analytical Mori-Tanaka model gives results that almost coincide with results from finite element modelling. Only at high volume fractions or high aspect ratios the Mori-Tanaka model under estimates the true stiffness. This small underestimation is probably caused by the neglect of stress concentrations in the Mori-Tanaka model.

4.5 References

- [1] A. A. Gusev, *Numerical identification of the potential of whisker- and platelet-filled polymers*, *Macromolecules*, **34**(9), 2001, p 3081-3093.
- [2] J. Lusi, R.T. Woodhams and M. Xanthos, *The effect of aspect ratio on the flexural properties of mica reinforced plastics*, *Pol. Eng. Sci.* **13**(2), 1973, p 139-145
- [3] M. Xanthos, *High Aspect Ratio Reinforced Thermosets*, PhD. Thesis, University of Toronto, 1974.
- [4] H.R. Shell and K.H. Ivey, *Fluorine Micas*, Bulletin **647**, Bureau of Mines, U.S. Department of the interior, 1969.
- [5] J.E. Ashton, J.C. Halpin, P.H. Petit, *Primer on Composite Materials: Analysis*, Technomic Publishing Co., 1969, Chapter 5.
- [6] G.E. Padaver, and N. Beecher, *On the strength and stiffness of planar reinforced plastic resins*, *Pol. Eng. Sci.* **10**(3), 1970, p 185-192.
- [7] K. Iisaka and K. Shibayama, *Effect of orientation on two-dimensional filler on dynamic mechanical properties of cured epoxy resin*, *J. Appl. Pol. Sci.* **20**, 1976, p 813-823.
- [8] K. Iisaka, *Dynamic viscoelastic properties of composite material*, *Compos. Polym.* **1**(3), 1988, p 199-220.
- [9] P.K. Roy and K.K. Phani, *Elastic properties of mica filled polyester resin composites*, *Trans. Indian Ceram. Soc.* **46**(2), 1987, p 50-52.

Preparation of materials

Abstract

In this chapter the preparation is described of PA6/clay and HDPE/clay nanocomposites used throughout this thesis. All samples were made either by melt-extrusion or by melt-kneading of the clay together with the polymer. First a master batch was made which was subsequently diluted to the desired concentration. To refer to a sample throughout this thesis, always the amount of silicate in the sample is mentioned, not the total amount of organic modified clay added.

5.1 Preparation of PA6/clay nanocomposites

5.1.1 Materials

In order to study the effect of polymer crystallinity on the properties of nanocomposites, two series of nanocomposites were made, one with a PA6 matrix of normal crystallinity and one with a less crystalline matrix. Both nanocomposites are based on PA6 as the polymer matrix material. In the first series, pure PA6 is used; representing the high crystalline matrix. In the second series 25% 6T/6I, a terephthalic acid / isophthalic acid copolymer (Grivory® G21), was added to PA6 to represent a matrix with a low crystallinity. 6T/6I copolymers are known to decrease the crystallinity of PA6 [1]. Since in both cases the matrices mainly contain PA6 it is assumed that the chemical differences in polymer-clay interactions between both polymer matrices are small.

The PA6 used is an Akulon® K123 supplied by DSM with a number average molecular weight $M_n = 13000$ g/mol, a weight average molecular weight $M_w = 24000$ g/mol, and a relative viscosity in formic acid of 2.3.

Grivory® G21 is an amorphous aromatic nylon supplied by EMS-Chemie (Switzerland) and is a copolymer of terephthalic acid, isophthalic acid and 1,6-hexanediamine. It is completely miscible with PA6, has a melt index of about 75 ml/10min (275°C/5kg) and a glass transition temperature of 125 °C [1].

The organo-clay used (Cloisite® 20A) is produced by Southern Clay Products (USA). Cloisite® 20A is based on a water swellable sodium-montmorillonite with an exchange capacity of 95 meq. The sodium in the inter-gallery layers is completely exchanged with dimethyl-di-hydrogenated-tallow-amonium ions (2M2HT quad). Tallow is a natural occurring alkyl compound with a length of 14 to 18 CH₂ groups. By incinerating the clay at 450°C for 16 h it was determined that Cloisite® 20A contains 61.9w% of inorganic silicate and 38.1w% organic material. Based on the exchange capacity of 95 meq (= 95 millimol /100g silicate)

and the molar mass of the 2M2HT quad ($\approx \text{C}_{34}\text{H}_{72}\text{N} \approx 494 \text{ g/mole}$) all the charge on the clay would be just compensated for with 32 wt% of 2M2HT quads. So the organically treated clay (organo-clay) contains more organic treatment than is necessary to cover the whole surface. The addition of extra surfactant is done to obtain better and faster exfoliation in polymers.

Material	PA6-0.2%	PA6-1%	PA6-2.5%	PA6-5%	PA6-7.5%	PA6-10%	PA6-15%	PA6-20%
	%	%	%	%	%	%	%	%
Master batch	1,00	5,00	12,50	25,00	37,50	50,00	75,00	100,00
Silicate in MB	0,20	1,00	2,50	5,00	7,50	10,00	15,00	20,00
Quad in MB	0,13	0,67	1,68	3,35	5,03	6,70	10,05	13,40
PA6 in MB	0,67	3,33	8,33	16,65	24,98	33,30	49,95	66,60
PA6 added	99,00	95,00	87,50	75,00	62,50	50,00	25,00	0,00
Total	100,00	100,00	100,00	100,00	100,00	100,00	100,00	100,00

Table 5.1 Composition of PA6/Clay nanocomposites

Material	6TI-0.2%	6TI-1%	6TI-2.5%	6TI-5%	6TI-7.5%	6TI-10%	6TI-15%
	%	%	%	%	%	%	%
Master batch	1,00	5,00	12,50	25,00	37,50	50,00	75,00
Silicate in MB	0,20	1,00	2,50	5,00	7,50	10,00	15,00
Quad in MB	0,13	0,67	1,68	3,35	5,03	6,70	10,05
PA6 in MB	0,67	3,33	8,33	16,65	24,98	33,30	49,95
PA6 added	74,08	70,42	63,54	52,09	40,63	29,18	6,26
6T/6I added	24,92	24,58	23,96	22,91	21,87	20,83	18,74
Total	100,00	100,00	100,00	100,00	100,00	100,00	100,00

Table 5.2 Composition of PA6/6T6I/clay nanocomposites

5.1.2 Extruding the master batch

Before making the final PA6-nanocomposite first a master batch was made. P6-clay nanocomposite master batch containing 20 weight% of silicate was made by feeding a dry blended mixture of cryogenically milled PA6 and 32.3 weight% Cloisite® 20A to the hopper of a W&P ZSK 30 42D co-rotating twin screw extruder. The extruder was operated at 400 rpm.

The materials were made as described by Korbee [2]. Due to good exfoliation, the master batch had a very high melt viscosity. To prevent the extruder from shutting down on torque overload, the output rate was limited to 3 kg/hour.

5.1.3 Diluting the master batch

The master batch of the preceding section was diluted on the same extruder as was used to make the master batch. All samples were made using the same PA6/Cloisite 20A master batch. Samples with 0.2, 1, 2.5, 5, 7.5, 10, 15 and 20 wt% silicate were made. All samples are coded by their silicate content and not by their total content of organic modified clay. So, as can be seen in Table 5.1, sample PA6-20% contains 20% silicate, and 13.4% 2M2HT quaternair ammonium.

All samples in Table 5.2 have a PA6/6T6I ratio of 3/1. This was achieved by diluting the PA6/Cloisite® 20A master batch with a calculated mixture of PA6 and 6T/6I copolymer.

5.2 Preparation of HDPE-clay nanocomposites

HDPE nanocomposites with different types of clay are prepared in two runs. In the first run samples are made on a 5 cm³ DSM mini-extruder for rheology testing and in the second run samples were made on a Haake batch 60 cc kneader for DMA, DSC and TEM testing.

5.2.1 Materials

In both runs the same type of materials are used to prepare the nanocomposites:

Polymers:

- PEMZA, a melt grafted HDPE with 2 wt% of maleic anhydride (to exfoliate the clay).
- HDPE Stamylen® 8621 (DSM), a linear polyethylene with a density of 958 kg/m³, an melt flow rate at 190°C and 2,16 kg of 0.16 dg/min , at 5 kg of 0.89 dg/min and at 21.6 kg of 23 dg/min.

Clays:

- SAN, a synthetic smectite from CO-OP Chemical Co. (Japan) with an aspect ratio of about 20 and containing 38 wt% of 2M2HT organic modification.
- Cloisite® 20A, a montmorillonite from Southern Clay Products (USA) with an aspect ratio of about 100 and containing 39 wt% of 2M2HT organic modification.
- MAE, A synthetic mica from CO-OP Chemical Co. (Japan) with an aspect ratio of about 200 and containing 41 wt% of 2M2HT organic modification.

The selected clays are all modified with nearly 40 weight% of the same 2-methyl 2-hydrogenated tallow ammonium ions $[(CH_3)_2((CH_2)_{14-18})_2]$. This way, any difference found in the samples can be attributed to the type of silicate used and not to the type or the amount of organic treatment.

5.2.2 Preparation of HDPE nanocomposites on a mini-extruder

For testing of rheology, three types of HDPE-clay nanocomposites were made by melt extrusion at 200 °C and, 250 rpm during 5 min, using clay of different aspect ratios. The extruder used is a 5 cm³ DSM mini-extruder. This is a small batch twin-screw extruder suitable to make very small amounts of material. First concentrates were made by with 10 wt% of silicate by melt extrusion of organic modified clay in PE-g-ma. The concentrates were subsequently diluted in HDPE to a concentration of 2.5 wt% silicate. Table 5.3 lists the exact composition of the nanocomposites.

Material	PE 0%	PE 10% SAN	PE 10% 20A	PE 10% MAE	PE 2.5% SAN	PE 2.5% 20A	PE 2.5% MAE
	wt%	wt%	wt%	wt%	wt%	wt%	wt%
PE-g-MA	100	83.4	83.4	83.4	23.96	23.96	23.96
HDPE 8621					71.89	71.89	71.89
Synthetic smectite		16.6 (10)			4.15 (2.5)		
Montmorillonite			16.6 (10)			4.15 (2.5)	
Synthetic mica				16.6 (10)			4.15 (2.5)

Table 5.3 Composition of HDPE nanocomposites for rheology testing.
Numbers between brackets denote the weight percentage of silicate added.

5.2.3 Preparation of HDPE nanocomposites on a kneader

HDPE nanocomposites for DMA, DSC and TEM testing are made by melt compounding on a 60 cc Haake kneader during 10 minutes at 120 rpm and at a temperature of 180 °C.

Table 5.4 lists the compositions of the HDPE nanocomposites made. After preparation on the Haake kneader all samples are compression moulded at 180 °C on a Fontijne table press. The size of the mould was 150 x 80 x 0.5 mm. The following pressing program was used:

1. Heating for 5 minutes without any force exerted to melt the sample and fill the mould.
2. For 3 minutes a force of 10 kN is exerted on the material.
3. For 3 minutes a force of 50 kN is exerted on the material.
4. Cooling down to room temperature while a force of 180 kN is exerted on the material.

Material	PE 0%	PE 1% SAN	PE 5% SAN	PE 20% SAN	PE 1% Clois	PE 2.5% Clois	PE 5% Clois	PE 10% Clois	PE 15% Clois	PE 20% Clois	PE 1% MAE	PE 5% MAE	PE 20% MAE
	wt%	wt%	wt%	wt%	wt%	wt%	wt%	wt%	wt%	wt%	wt%	wt%	wt%
HDPE-g-MA	100	98.3	91.7	66.7	98.3	95.8	91.7	83.3	75	66.7	98.3	91.7	66.7
Synthetic smectite		1.7 (1)	8.3 (5)	33.3 (20)									
Montmorillonite					1.7 (1)	4.2 (2.5)	8.3 (5)	16.7 (10)	25 (15)	33.3 (20)			
Synthetic mica											1.7 (1)	8.3 (5)	33.3 (20)

Table 5.4 Composition of HDPE nanocomposites for DMA and DSC testing.
Numbers between brackets denote the amount of silicate added.

5.3 References

- [1] EMS Grivory G21 datasheet, *Produkt Einleitung Grivory G21*, Domat/EMS August 1992
- [2] R. Korbee, *Process for the preparation of polyamide nanocomposite composition*, Patent Appl. WO 99/29767 DSM

Clay morphology and polymer mobility

Abstract

TEM and ^1H -NMR experiments were performed on PA6 and PE-clay nanocomposites in order to learn how the clay and the polymer phases contribute to the properties of these nanocomposites. Clay morphology was investigated by TEM analysis and polymer mobility by ^1H -NMR. Clay morphology must be known in order to perform composite modelling, while knowledge of the molecular mobility is necessary for a correct interpretation of the properties of nanocomposites. Clay morphology is characterised by the extent of exfoliation of the clay platelets, their aspect ratio and their orientation. These data are crucial for correct composite modelling. ^1H -NMR gives data on the mobility of polymer chains that are confined in the narrow spaces between clay platelets. The exfoliation of clay in the nanocomposites proves to be excellent at loadings below 2.5 weight percent of clay. At higher loadings small tactoids of 2-3 platelets are observed that eventually organise into groups of about 50 platelets above 10 weight percent of clay. Above 5 weight percent of clay, ^1H -NMR-T2-relaxation shows the existence of a phase in PA6 nanocomposites with liquid-like mobility.

6.1 TEM analysis of nanocomposites

In nanocomposite research TEM is almost exclusively used to check for intercalation or exfoliation of clay platelets. In this thesis it also is attempted to extract parameters from TEM pictures like the aspect ratio, inter-particle distance and the state of orientation of the clay platelets.

6.1.1 Sample preparation

Samples for TEM analysis are prepared from compression moulded sheets that were used for DMA testing. This way it is ensured that the samples for mechanical measurement and for TEM have the same clay orientation and clay aspect ratio. The compression-moulded sheets were first embedded in an epoxy resin. Subsequently films with a thickness of about 70 nanometers were microtomed using liquid nitrogen for cooling. TEM pictures were taken on unstained samples with a Phillips CM200 TEM at an acceleration voltage of 120 kV.

6.1.2 Quantitative data from TEM analysis

To obtain morphological data from TEM pictures one must be very careful, because a lot of errors can be made. Preferably a TEM coupe should be much thinner than the dimensions of the smallest particle in the sample, to prevent overlapping of particles at different depths of the sample. For nanocomposites these demands cannot be met, because it is impossible to cut coupes of 1 nanometer or smaller. This makes it very difficult to determine the amount of clay or the distance between platelets.

Weight fraction of silicate	True volume fraction of silicate	Calculated particle distance \bar{D}_{calc} nm	Estimated volume fraction of silicate from TEM	Measured particle distance \bar{D}_{TEM} nm
0.002	0.0008	1250	-	1350
0.01	0.004	250	0.004	256
0.025	0.01	100	0.01	71
0.05	0.02	50	0.04	25
0.075	0.03	33	0.07	13
0.10	0.05	20	0.06	15
0.15	0.07	14	0.13	7
0.20	0.10	10	0.19	4

Table 6.1 Estimated volume fraction and particle distance obtained by using the 'fractional length' method.

As can be seen from the TEM pictures in Figs. 6.1-6.7, all nano platelets are depicted as lines. This seems to be convenient because in this way it is easy to distinguish the different clay particles and determine their length. It is not directly obvious though why clay platelets are depicted as lines. On the contrary, one might expect that the nano-platelets are shown as vague light grey areas.

In Appendix D it is explained why clay platelets are depicted as sharp lines. It also explains how a TEM image of a nanocomposites can show more lines than there are clay platelets present in sample. Using the 'fractional length method' as explained in Appendix D,

the volume fractions of clay and the average distance between platelets of the PA6-nanocomposites are calculated and listed in Table 6.1. It can be concluded from Table 6.1 that up to 2.5 wt% the estimated volume fraction from TEM images is equal to the true volume fraction. Above 2.5 wt% the volume fraction of platelets, calculated by the 'fractional length' method, is larger than the true volume fraction. This illustrates the earlier statement that the amount of lines seen on a TEM image can appear to be higher than the amount of platelets in the sample. The fact that the amount of particles counted per unit of surface in a TEM picture is larger than the true amount of particles per unit surface also illustrates the good exfoliation of the clay particles.

The complications mentioned above make it difficult to perform a quantitative analysis on TEM images of nanocomposites. Therefore TEM images are not suited to quantify the volume fraction or the distance between clay platelets. However, TEM is a valuable tool to estimate the length of the clay platelets and to check the extent of exfoliation and orientation of clay platelets in a nanocomposite.

6.1.3 TEM images of PA6-nanocomposites

Figs. 6.1 to 6.7 show TEM images of PA6-nanocomposites with 1, 2.5, 5, 10, 15 and 20 wt% of clay. The sample with 20 wt% of clay is also given at a high magnification in order to be able to study the morphology more closely. TEM images at lower and higher magnification were also taken but are not shown to limit the amount of photographs in this thesis. The in-plane orientation of the compression-moulded sheets is always given by the direction of an arrow in the images. The TEM images show the exfoliation, the length and orientation of the clay layers in PA6-nanocomposites. The length of the clay layers is about 100 nm. Since the thickness of a clay platelet is about 1 nm, the aspect ratio is 100.

At 1% clay, exfoliation is nearly complete. Only a few tactoids of 2 platelets are found. These tactoids might be difficult to distinguish on the images shown, but they are better visible at larger magnification. Platelets are mainly oriented along the plane of the sheet, but orientation is not perfect.

At 2.5 wt% the amount of tactoids is somewhat increased with respect to the sample with 1% clay. About half of the particles are completely exfoliated, while the rest is found in tactoids of 2-3 platelets. The orientation is better than at 1 wt%.

At 5 wt% of clay the majority of platelets are found in tactoids of two or three platelets. A minority of platelets is completely exfoliated. The tactoids themselves are very well dispersed in the sample. The orientation is nearly perfect.

At 10 wt% again roughly the same amount of particles is found in tactoids as at 5 wt%. The tactoids are well dispersed in the sample. The tactoids are randomly oriented.

At 15 and 20 wt% of clay, again most particles are found in tactoids of about 2 platelets. But now the tactoids orient themselves along adjacent tactoids and form highly oriented groups. These groups contain in the order of 50 clay platelets. The size of the groups typically is about 200 nm. The platelets inside a group are highly oriented. The groups themselves are randomly oriented. It seems that the overlap of platelets between these groups is low.

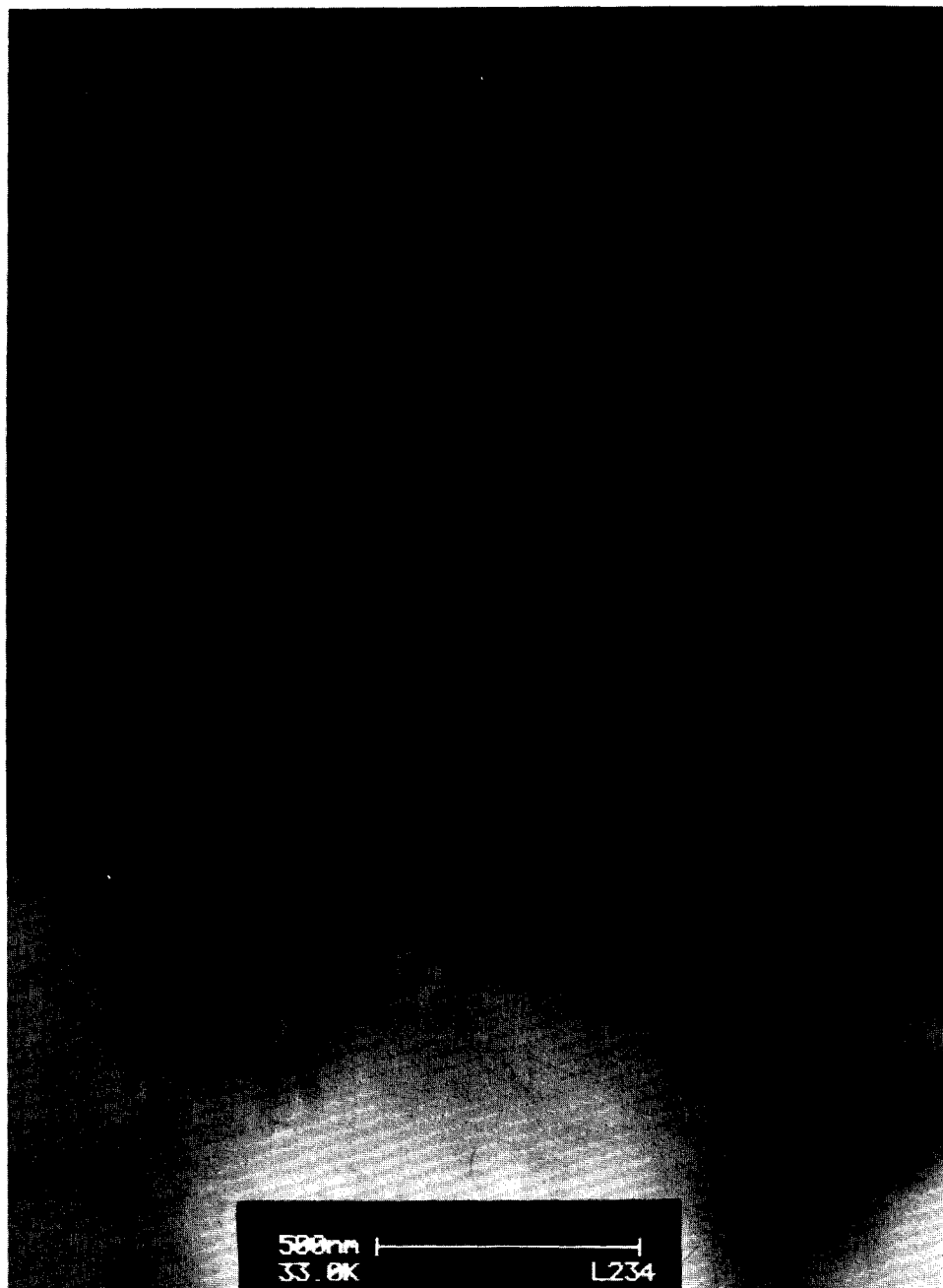


Figure 6.1 TEM image of a PA6-nanocomposite containing 1 wt% of montmorillonite clay. The arrow indicates the in-plane direction of the compression-moulded sheet.



Figure 6.2 TEM image of a PA6-nanocomposite containing 2.5 wt% of montmorillonite clay. The arrow indicates the in-plane direction of the compression-moulded sheet.



Figure 6.3 TEM image of a PA6-nanocomposite containing 5 wt% of montmorillonite clay. The arrow indicates the in-plane direction of the compression-moulded sheet.

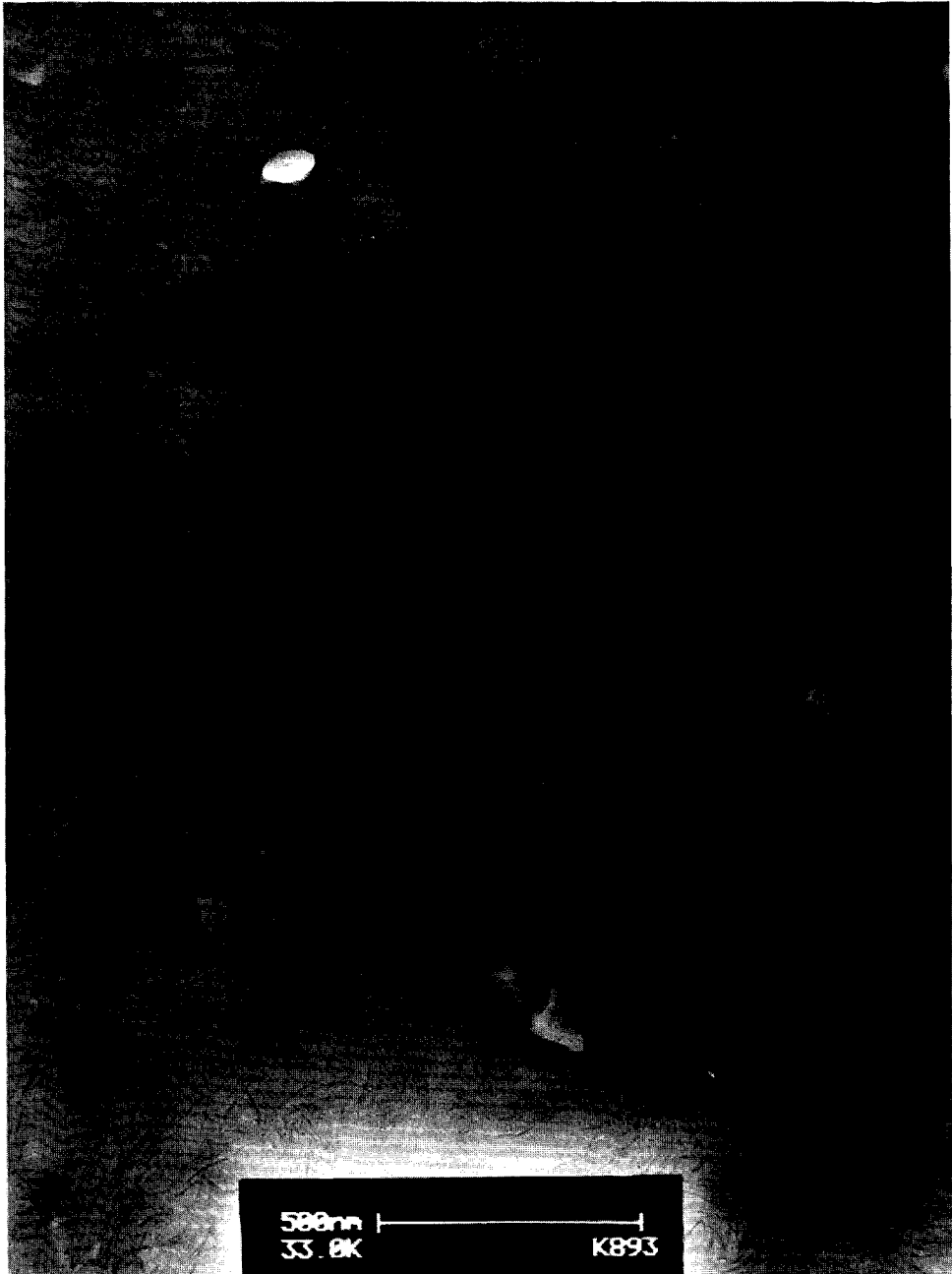


Figure 6.4 TEM image of a PA6-nanocomposite containing 10 wt% of montmorillonite clay. The arrow indicates the in-plane direction of the compression-moulded sheet.



Figure 6.5 TEM image of a PA6-nanocomposite containing 15 wt% of montmorillonite clay. The arrow indicates the in-plane direction of the compression-moulded sheet.



Figure 6.6 TEM image of a PA6-nanocomposite containing 20 wt% of montmorillonite clay. The arrow indicates the in-plane direction of the compression-moulded sheet.



Figure 6.7 TEM image of a PA6-nanocomposite containing 20 wt% of montmorillonite clay. The arrow indicates the in-plane direction of the compression-moulded sheet.



Figure 6.8 TEM image of HDPE nanocomposite containing 10 wt% of synthetic smectite clay.

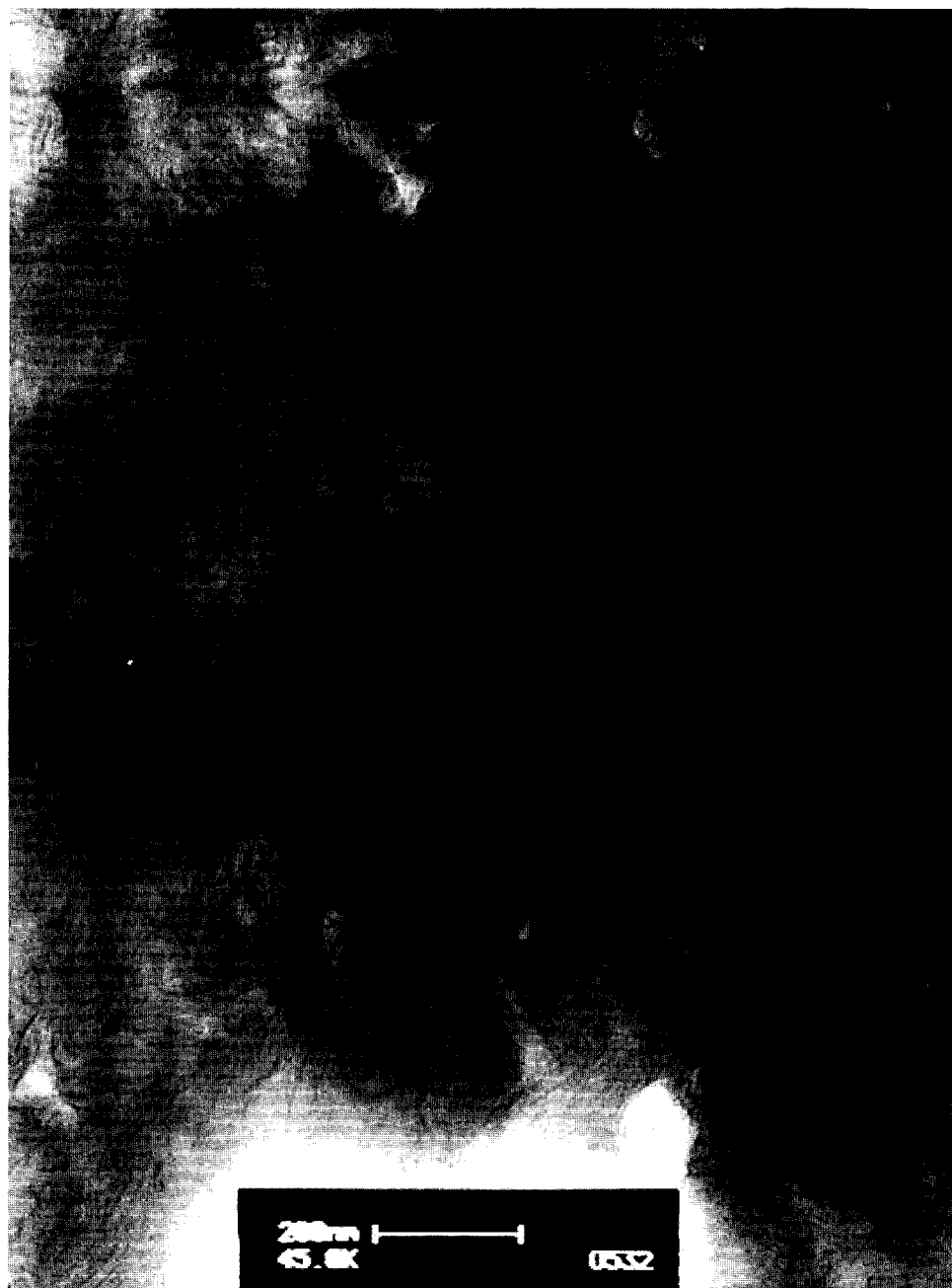


Figure 6.9 TEM image of HDPE nanocomposite containing 10 wt% of montmorillonite clay.

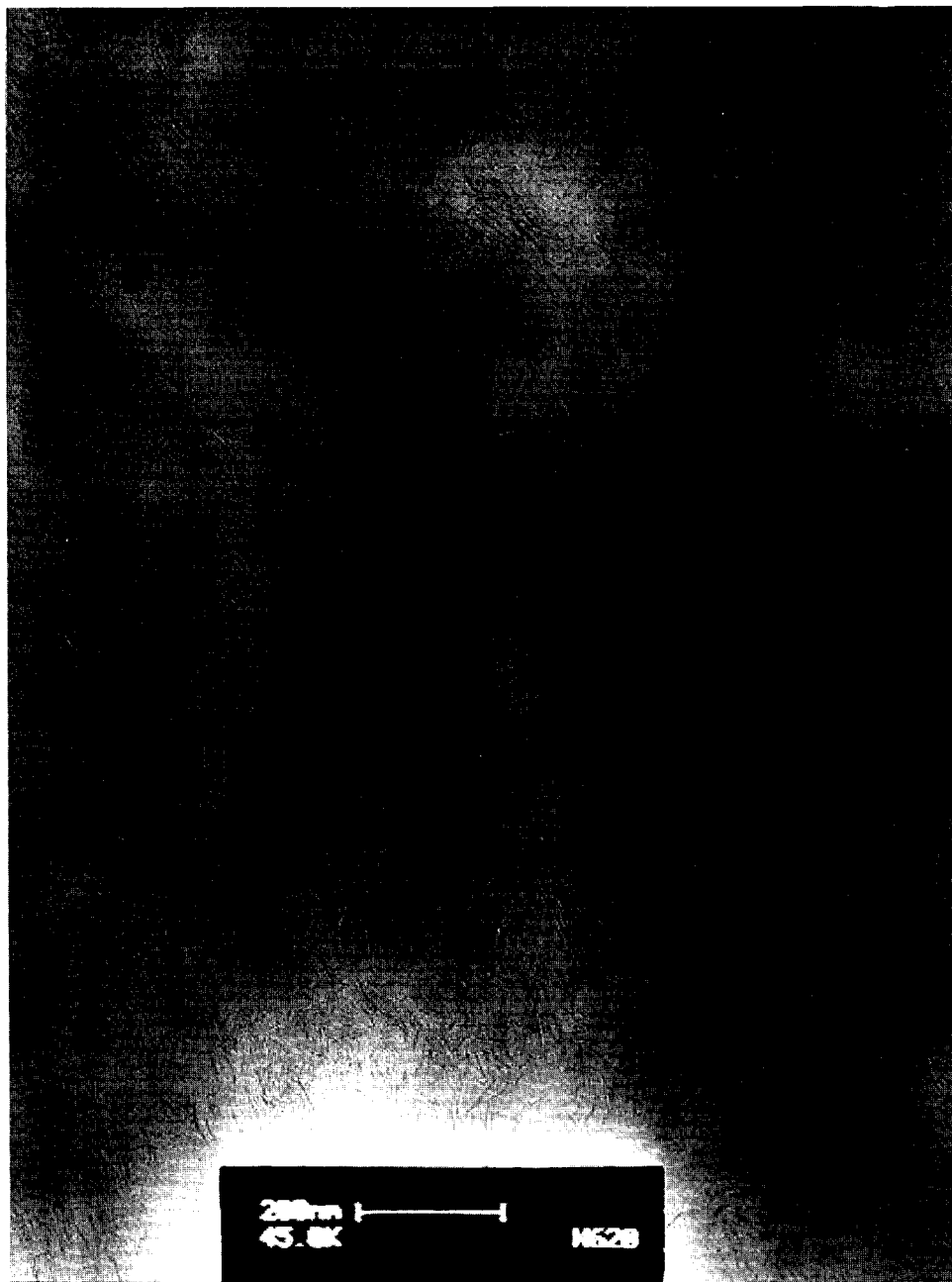


Figure 6.10 TEM image of HDPE nanocomposite containing 10 wt% of synthetic mica.

So at small volume fractions (1wt%) the clay platelets completely exfoliate and are found as single well-oriented platelets in the polymer. Upon increasing the concentration (2.5-5wt%), the clay tends to organise in well-oriented tactoids of 2-3 plates. At 10 wt% the tactoids are hindered so much by neighbouring tactoids that no macroscopic orientation is found. At 15 and 20 wt% of clay, the tactoids can no longer assume a free orientation and start to align into groups of about 50 platelets. Judging from the TEM pictures it seems that these groups of platelets move as a whole through the molten polymer. At these high concentrations, the clay platelets show a similar tendency to local ordering as liquid crystalline polymers do.

6.1.4 TEM images of HDPE nanocomposites

TEM images of HDPE with clays of different aspect ratio are shown in Figs. 6.8-6.11. From the images it can be concluded that all nanocomposites are well exfoliated. Details about tactoids are difficult to detect in these images because the resolution of the images is not high.

It can be concluded from Figs. 6.8-6.10 that the platelets in the nanocomposites are well exfoliated and randomly oriented. Most importantly, the aspect ratio from the synthetic smectite clay in Fig. 6.8 is clearly lower than that of the montmorillonite and the synthetic mica. The montmorillonite has clay platelets that have an aspect ratio in between that of the synthetic smectite and the synthetic mica.

Judging from the TEM images the average length of the synthetic smectite platelets is about 30 nm, the montmorillonite platelets are about 100 nm in length and the synthetic mica platelets about 150 nm. If it is assumed that all platelets are completely exfoliated, the aspect ratios of clays would be 30, 100 and 150 respectively. These estimates are rather inaccurate because the TEM pictures do not have a high enough resolution.

Figs. 6.11a-c show the dispersion of 5, 10 and 20 wt% montmorillonite clay in HDPE nanocomposites. From Fig. 6.11a it can be concluded that at 5 wt% the montmorillonite platelets are dispersed individually, while at 10 and 20 wt% the platelets tend to group together as was also observed in the PA6-nanocomposites.

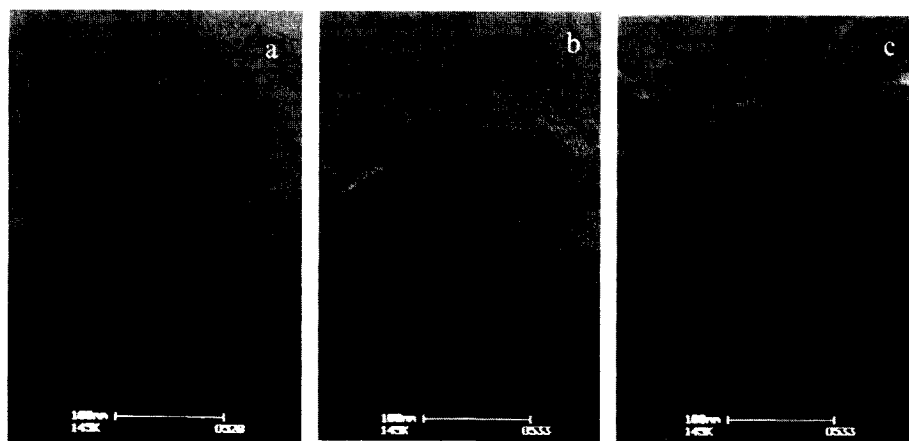


Figure 6.11 a-c HDPE-nanocomposite containing 5, 10 and 20 wt% montmorillonite

6.2 Polymer mobility of nanocomposites measured by solid state NMR

Completely exfoliated clay has a surface area of about 700 m²/g. This implies that if 99 wt% of polymer would evenly be spread out over 1 wt% of clay, the thickness of the polymer layer would only be 140 nm. In nanocomposite literature it is therefore often suggested that all polymer in a nanocomposite is part of the clay-polymer interface. The special properties of nanocomposites are therefore often assigned to the changed properties of this interphase. This interphase has a thickness of typically 1-5 nm [1,2]. Only a few research groups used solid state NMR to determine how polymer properties are affected by the presence of nano dispersed clay. Mathias et al. [3] used ¹⁵N solid-state NMR to observe the formation of γ -crystalline structure in PA6-nanocomposites.

Wong et al. [4] used proton NMR to determine the local dynamics as a function of temperature of poly-ethylene-oxide (PEO) that was confined in 0.8 nm narrow gaps between silicate layers. Line-shape measurements and spin-lattice relaxation measurements indicated the existence of both a highly mobile and a strongly inhibited phase. Below the melting point of PEO, a phase was found with a very high mobility, while above the melting point a phase remained with very low mobility. High mobility below the melting point was attributed to the absence of chain entanglements and the presence of excess free volume associated with the packing constraints of intercalated chains. Direct contact between the PEO and the silicate surface was thought to lead to the formation of a phase with low mobility that remains rigid at temperatures far above the melting point of bulk-PEO.

With solid-state proton NMR Manias et al. [5-6] found that the mobility of polystyrene (PS) molecules in the confined space between clay layers differs greatly from the mobility of unconfined polystyrene. PS in the centres of clay galleries proved to be more mobile than the bulk PS at comparable temperatures, while mobility of PS in direct contact with the clay's surface was inhibited. In another study [7] Manias used X-ray techniques to observe the swelling of clay during intercalation of PS. He observed that the diffusion coefficient of PS inside the clay galleries is larger than the self-diffusion coefficient of bulk PS. This again indicated that PS is more mobile inside the clay galleries than in the bulk.

All studies cited above were performed on polymer-clay nanocomposites with very high contents of clay (>50 wt%) and very small dimensions of confinement (typically 0.5-2 nm). The studies indicate that under these severe confinements two polymer phases are created; one phase with high mobility in the centre of the clay galleries and another phase with low mobility in contact with the surface of the clay. Although the mobility of severely confined (<2nm) polymer chains is strongly affected, it is by no means obvious that this also accounts for the mobility of less severely confined polymer chains (5-100nm) as are present in practical nanocomposites. Therefore it seems premature to assign the properties of practical nanocomposites to the changed mobility of the polymer phase.

No NMR studies were found in literature on nanocomposites with low amounts (0-20 wt%) of clay. Such a study could yield information on the amount of mobilised and immobilised polymer molecules in nano-composites with practical amounts of clay. In this thesis, the polymer mobility in PA6-clay nanocomposites with 1-20 wt% of clay is investigated with proton NMR relaxation. These nanocomposites contain less clay than the nanocomposites studied in the literature and consequently have a larger inter-layer distance (typically 5-100 nm).

6.2.1 Short introduction into ^1H -NMR T_2 relaxation spectroscopy

In order to better understand the NMR experiments that were conducted on the nanocomposites, some background knowledge about NMR spectroscopy seems appropriate. Here only a brief introduction is given. For a more detailed description we refer to the book on NMR spectroscopy by Sanders and Hunter [8].

A nucleus with an odd atom number has a magnetic moment. The magnetic moment of a nucleus is represented by its spin. A proton has a spin, $I = 1/2$, which in a magnetic field, align themselves either parallel (low energy orientation) or antiparallel (high energy orientation) to a magnetic field. Two energy levels are thus created by the so-called Zeeman splitting. The distance between these energy levels ΔE is proportional to the applied magnetic field.

$$\Delta E = h\gamma B_0 / 2\pi \quad (6.1)$$

where γ is the gyromagnetic ratio, h is Planck's constant and B_0 is the applied magnetic field. The amount of nuclei in the low energy level, labelled as the α -level, usually is higher than in the high energy level, which is labelled as the β -level. The ratio of populations in upper and lower levels is given by the Boltzmann equation:

$$N_\beta / N_\alpha = \exp(-\Delta E / kT) \quad (6.2)$$

where N_α is the population density of the low energy level and N_β is the population density of the high energy level. Transitions from the high energy level to the low energy level generate radiation of a frequency:

$$\omega = \gamma B_0 \quad (6.3)$$

In a NMR experiment a sample is placed in a static magnetic field. In this magnetic field a part of the nuclei occupy the high energy level according to equation 6.2. This gives the sample a net magnetisation in the direction of the static magnetic field. The static magnetic field is subsequently perturbed by a pulsed radio wave whose magnetic field is perpendicular to the static magnetic field. The frequency of the radio wave is matched to the resonance frequency of the nucleus of interest: $\omega_i = \omega_0 = \gamma B_0$. Due to the matching frequencies, the spinning nuclei will absorb energy and the population density of the high energy level is increased. After the pulse is stopped, the population of the high energy level will decay by relaxation mechanisms present in the sample until the static situation is restored. It is this decay that is measured. In a typical pulsed NMR experiment, the spin system is perturbed and the free induction decay is collected in the time after the pulse.

In practice the NMR apparatus consists of a super conductive coil that generates a strong magnetic field in the z-direction. Another coil is wound around the x direction (x-coil). A magnetic pulse in the x-direction is generated by sending a high frequency current through the x-coil for a fixed time. Then the current is stopped and the response is measured by either the same x-coil or another coil in the x-y plane.

Most often the sample is excited by sending a sequence of pulses in the x-direction and or y-direction. The duration of the pulse(s) is designed such that dispersion of the signal during the pulse is minimised. The magnetisation of a sample in an NMR experiment is depicted in Fig. 6.12. In equilibrium the magnetisation of the sample is parallel to the

direction of the strong static magnetic field B_0 . After perturbation by a pulse in the x-direction the magnetisation vector precesses around the z-direction with a frequency ω_0 . The precessing vector has a component in the xy plane. A receiver-coil in the xy plane produces a pulse every time the xy component of the magnetisation vector passes the coil. In absence of any relaxation mechanisms the system would maintain like this forever and a signal with constant amplitude would be generated.

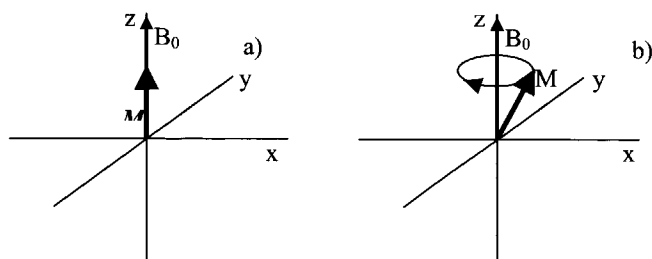


Figure 6.12 Bulk magnetisation of a sample in a NMR-experiment.
a) At equilibrium and b) after perturbation by a pulse in the x-y-plane

As a result of interaction between the spins and the surroundings or 'lattice' the magnetisation will eventually return to the equilibrium position, leading to a loss of the excess energy. This relaxation mechanism is referred to as T_1 or spin-lattice relaxation. The rate at which the system returns to equilibrium is expressed in the relaxation time constant T_1 . Due to T_1 -relaxation the signal in the xy-coil will decrease with time.

The signal generated by the coil in the xy-plane can also decrease by a second mechanism. The bulk magnetisation is the sum of all nuclear magnetisations. Immediately after an x-pulse, the xy component of the magnetisation ideally is directed exactly in the x-direction. As a result of additional processes the xy magnetisation will fan out or dephase, producing a net magnetisation in the xy-plane of zero. These additional mechanisms, which are referred to as T_2 or spin-spin relaxations, do not necessarily require any change in energy.

To obtain a NMR spectrum with high resolution, the duration of the pulse must be as short as possible. On the other hand the energy in the pulse must be as high as possible for a maximum response. Therefore often equipment is used that delivers a high-energy pulse in as short time as possible. By using a sequence of pulses with carefully designed duration it is possible to artificially increase the energy intensity of the radio pulse.

6.2.2 Experimental

PA6-clay nanocomposites were used with 0, 5, 7.5, 10, 15 and 20 wt% of montmorillonite clay as described in Chapter 5. Prior to NMR measurements, all PA6-nanocomposites were dried overnight at 125 °C under a nitrogen atmosphere. Proton T_2 relaxation experiments were performed between 25 and 160 °C, on a Bruker Minispec PC-120 spectrometer at a proton resonance frequency of 20 MHz. The temperature was controlled by a home-built temperature unit. Dry nitrogen was used for heating and cooling the samples. Temperature accuracy and stability was about 1°C.

To obtain accurate T_2 relaxation times, two different pulse sequences were employed. For determination of the low mobile fraction of the sample (with fast relaxation) a solid-echo

pulse sequence, SEPS, ($90^\circ_x - t - 90^\circ_y - t\text{-acq.}$) was used with $t = 0.009$ ms. Recording of data was started at time = 0 as the echo-decay reached its maximum. T_2 relaxation times shorter than 100 ms were recorded using this pulse sequence. For accurate measurement of long relaxation times it is necessary to account for inhomogeneity of the magnetic field B_0 in the sample that leads to dephasing and accordingly to shorter T_2 -relaxation times. Therefore a Hahn-echo pulse sequence, HEPS ($90^\circ_x - t' - 180^\circ_x - t'\text{-acq.}$) is used for measurement of long T_2 -relaxation times. By proper use of the HEPS it is possible to compensate for inhomogeneity of the magnetic field allowing accurate measurement of the long T_2 -relaxation time of the mobile phase.

The intensity of the magnetisation was recorded as a function of time. A schematic example of such a recording is depicted in Fig. 6.13.

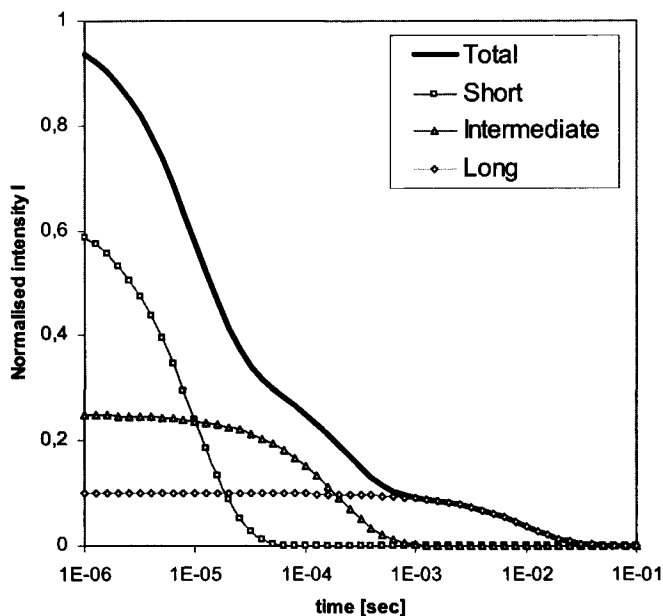


Figure 6.13 Schematic example of the relative intensity $I/I(0)$ of a magnetisation signal that contains three decaying exponentials.

The recorded intensity is interpreted as the sum of three decaying exponentials, with a short, intermediate and long T_2 -relaxation time. The functions W in front of each exponential are added to account for finite line width of the T_2 -relaxations. The line width can optionally be represented as a linear combination of Gaussian, Lorentz or Weibull functions.

$$I = W_S I_{Short} e^{\frac{-t}{T_2^S}} + W_I I_{Intermediate} e^{\frac{-t}{T_2^I}} + W_L I_{Long} e^{\frac{-t}{T_2^L}} \quad (6.4)$$

The normalised intensities of the T_2 -relaxations (T_2 -intensities) and T_2 -relaxation times of the samples were determined by fitting equation 6.4 through the normalised intensity. As a result of the normalisation procedure the T_2 -intensity of a phase is equal the fraction of hydrogen in that phase.

6.2.3 NMR results

To interpret the ^1H -NMR results shown below it must be realised that the intensity of the ^1H -magnetisation is proportional to the amount of hydrogen atoms while the T_2 -relaxation time is a measure of the mobility of the phase. The silicate-phase contains a neglectable amount of hydrogen and thus is invisible for ^1H -NMR. Therefore the normalised intensity directly reflects the fraction of hydrogen in the total organic phase. The organic phase on the clay (NC_{36}H_7) contains about 14.6 wt% of hydrogen, while the PA6 ($\text{NC}_6\text{H}_{11}\text{O}$)_n contains about 12.4 wt% of hydrogen. Thus, in a nanocomposite with 20 wt% of silicate, 13.3 wt% of organic modification and 66.7 wt% of PA6, about 19 % of all organic hydrogen atoms originate from the organic modification of the clay.

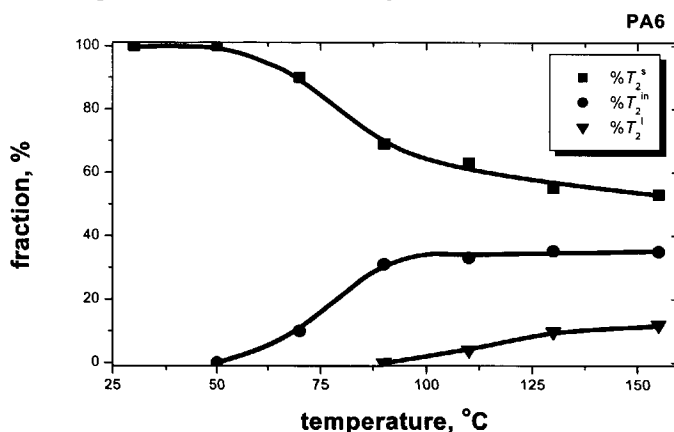


Figure 6.14 Fractions of rigid phase, amorphous phase and highly mobile phase in PA6 as a function of temperature:

Rigid phase (T_2^s), amorphous phase (T_2^{in}) and highly mobile phase (T_2^l)

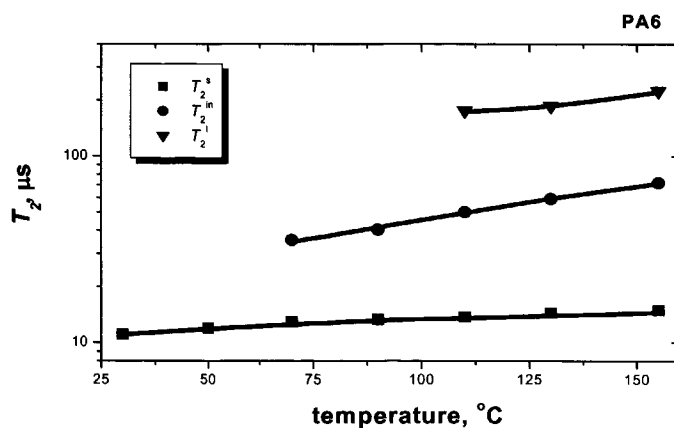


Figure 6.15 T_2 relaxation times of PA6 as a function of temperature.

T_2^s = short time \rightarrow rigid phase

T_2^{in} = intermediate time \rightarrow amorphous phase

T_2^l = long time \rightarrow highly mobile phase

Figs. 6.14 and 6.15 show the T_2 -intensities and the T_2 -relaxation times of unfilled PA6. Below the glass-transition (50 °C), pure PA6 only shows a single relaxation with a T_2 -relaxation time of 11-12 μ s, which is indicative for the rigid phase. The relaxation time of the rigid phase is relatively constant between 30°C and 160 °C and stays well below 20 μ s. Above 50 °C a second relaxation emerges with a T_2 -relaxation time between 30 and 75 μ s. This relaxation is indicative for the amorphous phase of the PA6, which softens near 50 °C. A third relaxation emerges above 100 °C. The intensity of this relaxation with a relaxation time near 200 μ s is relatively low. It is probably a product of the fitting procedure that allows three exponentials to be fitted. It is therefore questionable if this third relaxation really represents a distinct third phase. At 160 °C the total amount of rigid phase is about 53%. At 160 °C the only rigid organic phase is the crystalline PA6 phase. So the fraction of rigid phase could be interpreted as the crystallinity. Indeed a crystallinity of 53% is a very normal value for PA6.

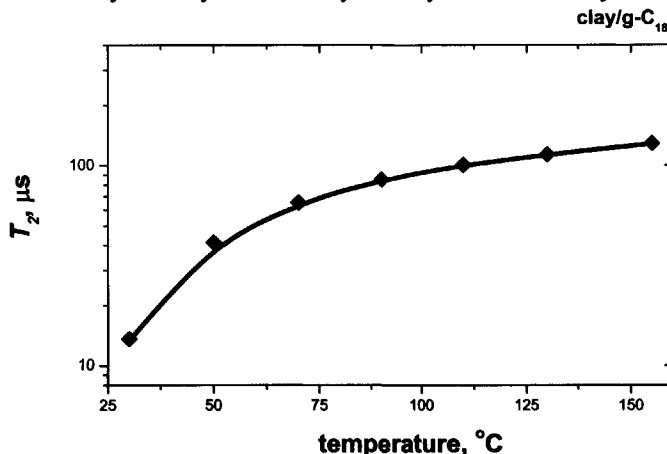


Figure 6.16 T_2 -relaxation time of organically modified montmorillonite clay

Fig. 6.16 shows the T_2 -relaxation time of the organically modified clay that was used in the PA6-clay nanocomposites (Cloisite 20A). It contains 62% silicate and 38% organics. Since silicate contains almost no hydrogen, all proton relaxation is assigned to the hydrogen in the organic modification on the clay. It is found that the organic modification only has a single T_2 -relaxation time that increases from about 12 μ s to 120 μ s as the temperature is raised from 30°C to 160°C. Judging from the T_2 -relaxation times it can be concluded that the organic phase on the clay is a little more mobile than the amorphous phase of pure PA6 while its temperature dependence is similar.

Figs. 6.17 and 6.18 show the fractions of the phases and the T_2 -relaxation times as a function of temperature of a PA6-clay nanocomposite with 20wt% of silicate and 13.3 wt% of organic modification. Measurements on pure PA6 are plotted as dotted lines for comparison. In contrast to pure PA6, the nanocomposite contains about 10% highly mobile phase. The amount of highly mobile phase does not change by increasing the temperature. The extremely long T_2 -relaxation time of about 7 ms indicates liquid like mobility of this phase. The evidence for the existence of a high mobile phase is very strong because at the end of the relaxation measurement (Fig. 6.13) it is the only phase left that still has a magnetisation.

Also the intermediate phase, which is thought to represent the amorphous PA6 phase, has a higher mobility than the amorphous phase of pure PA6. The amount of amorphous phase gradually increases as the temperature is raised. No distinct glass transition is present in the nanocomposite. At 160 °C about 53% of the hydrogen is present in the rigid phase that

contains the crystalline PA6 phase and possibly some polymer that is adsorbed to the surface of the clay. If the rigid phase would solely exist of crystalline PA6 then the crystallinity of the PA6 would be $53/(100-19) = 65.4\%$ (19% of all organic hydrogen atoms is present in the organic modification). A crystallinity of 65% seems to be rather much and is not substantiated by DSC measurements given in Chapter 7.

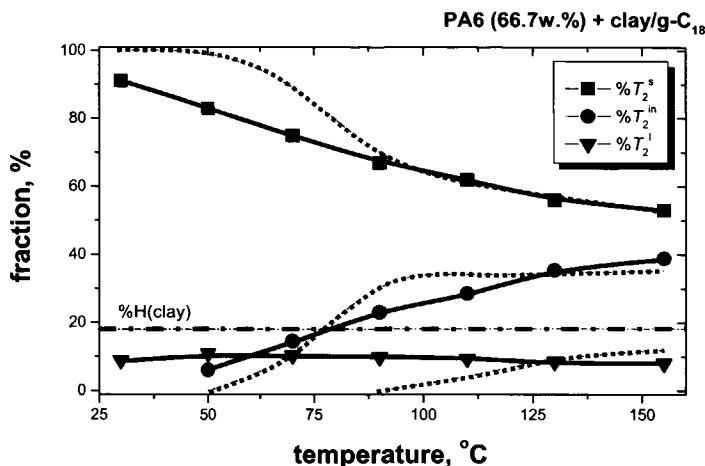


Figure 6.17 Fractions of rigid phase, amorphous phase and highly mobile phase in PA6-clay nanocomposite with 20 wt% of silicate and 13.4 wt% of organic modifications a function of temperature:

T_2^s = Rigid phase

T_2^{in} = Amorphous phase

T_2^l = Highly mobile phase

Solid line: PA6 nanocomposite

Dotted line: PA6

Dot-point: Modification on clay

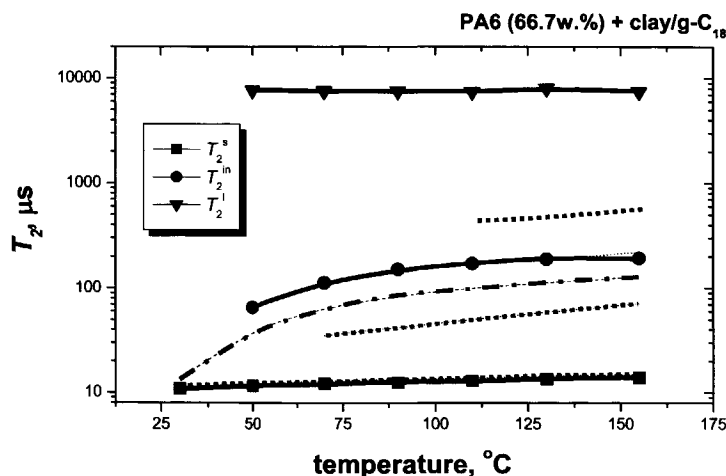


Figure 6.18 T₂ relaxation times as a function of temperature of a PA6-clay nanocomposite with 20 wt% of silicate and 13.3 wt% of organic modification.

T_2^s = short time -> rigid phase

T_2^{in} = intermediate time -> amorphous phase

T_2^l = long time -> highly mobile phase

Solid line: PA6 nanocomposite

Dotted line: PA6

Dot-point line: Modification on clay

Therefore it is likely that the rigid phase also contains some immobilized polymer present near the surface of the clay. Judging from the amount of crystalline phase in the unfilled polymer (53%) at least 12% (65%-53%) of the organic phase is immobilized.

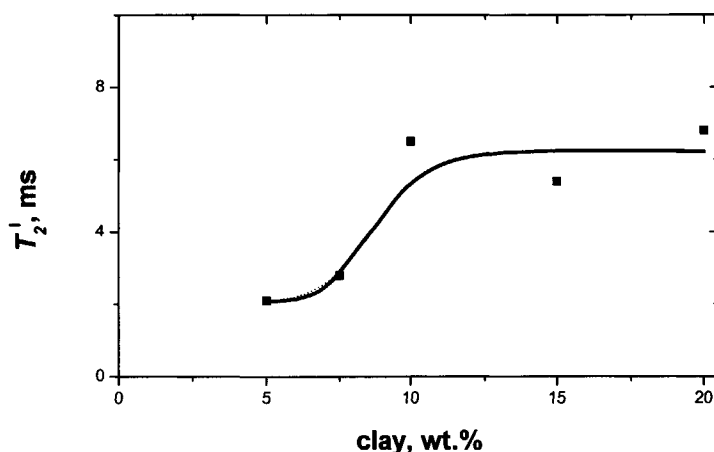


Figure 6.19 T_2 -relaxation time at 30 °C of the highly mobile phase as a function of the amount of silicate in PA6-clay nanocomposites.

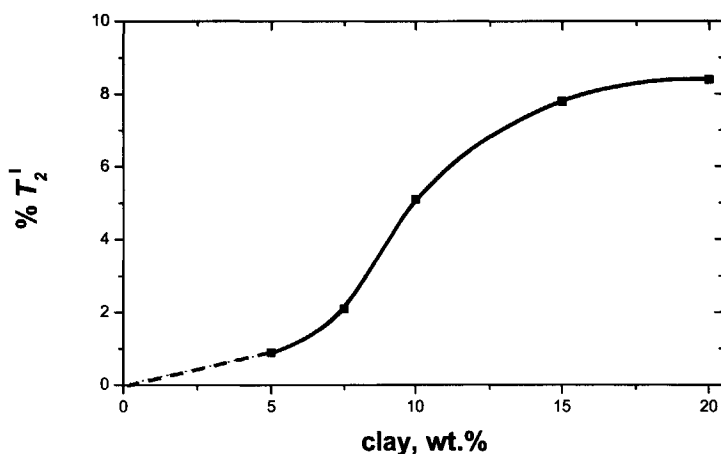


Figure 6.20 Fraction of highly mobile phase as a function of the amount of silicate in PA6-clay nanocomposites at 30 °C.

Figs. 6.19 and 6.20 show the T_2 -relaxation time and the amount of highly mobile phase at 30 °C as a function of silicate content. The T_2 -relaxation time of the highly mobile phase in Fig. 6.19 increases from 3 ms to 7 ms by raising the amount of silicate from 5 to 20 wt%. The mobility of this phase is always much higher than that of the amorphous PA6 phase which has a T_2 -relaxation time near 0.1 ms. Fig. 6.20 shows that at a loading of 5 wt% silicate the amount of highly mobile phase is only 1% while it gradually increases to about 8 % at 20 wt% of clay.

6.2.4 Evaluation of NMR results

The proton NMR measurements show that PA6-clay nanocomposites contain a highly mobile phase with liquid like mobility. Below 5 wt% of clay, the amount of mobile phase is below 1 wt% while it gradually increases up to nearly 8 wt% at 20 wt% of clay at 30 °C. The amount of mobile phase thus seems to be related to the amount of clay. Both the amount of organic modification and the amount of PA6 near a clay surface, increase proportionally with the amount of clay.

This poses the question if the highly mobile phase is situated in the organic modification or in the PA6 phase. Pure organic clay shows no highly mobile phase. This proves that the organic modification has no high mobility if it is severely confined between clay layers. The lack of a highly mobile phase in pure organic modified clay does not prove that the highly mobile phase is present in the PA6-phase. It could still be that the highly mobile phase is present in the organic modification.

To find an answer to this question magic angle spinning ^{13}C NMR was performed on the nanocomposite with 20 wt% of clay. By adjusting the waiting time after the magnetisation pulse it is possible to enhance either the slow relaxing phase (soft phase) or fast relaxing phase (rigid phase).

Enhancement of the soft phase increased the intensity of the peak that represents long CH_2 -sequences. Other peaks were not as much enhanced as this peak. If the soft phase would be PA6, all the peaks in the spectrum should be equally enhanced. Since this is not the case, this measurement indicates that the highly mobile phase is present in the organic modification.

The ^{13}C NMR measurement cannot be considered as an absolute prove that the highly mobile phase is present in the organic phase. The spectra were not conclusive enough to justify such a statement. More certainty could be obtained by making a nanocomposite with clay that contains no organic modification. If a highly mobile phase would then also be found it would prove that it is present in the PA6 phase. Up to now all attempts to do such an experiment failed because of difficulties in making a completely exfoliated nanocomposite of unmodified clay with a high concentration.

6.3 Conclusions

TEM on PA6/clay nanocomposites:

- The length of the clay layers is about 100 nm. Since the thickness of a clay platelet is about 1 nm, the aspect ratio is 100.
- At small volume fractions (1wt%) the clay platelets completely exfoliate and are found as single well-oriented platelets in the polymer.
- Upon increasing the concentration (2.5-5wt%), the clay tends to organise in well-oriented tactoids of 2-3 plates. The tactoids themselves are well dispersed.
- At 10 wt% tactoids consisting of 2-3 platelets are still well separated but they are hindered so much by neighbouring tactoids that no macroscopic or microscopic orientation is found.
- At 15 and 20 wt% of clay, the tactoids can no longer assume a free orientation and start to align into groups of about 50 tactoids. At these high concentrations, the clay platelets show a similar tendency to local ordering as liquid crystalline polymers do.

TEM on HDPE/clay nanocomposites

- TEM images show that all HDPE nanocomposites are well exfoliated and randomly oriented. Synthetic smectite, montmorillonite and synthetic mica have clay platelets with estimated aspect ratios of about 30 nm, 100 nm and 150 nm respectively. Due to low resolution of the TEM pictures these estimates are not accurate.
- At silicate contents above 10 wt%, clay platelets tend to group together as was also observed in PA6-nanocomposites.

NMR-spectroscopy

- In PA6-clay nanocomposites with 5wt% or more silicate layers, a phase is present with liquid like mobility. It is thought that the existence of this phase is a consequence of confinement of polymer chains between silicate layers.
- The high amount of rigid phase in PA6 nanocomposites also indicates the existence of a non-crystalline immobilised phase. The amount of non-crystalline immobilised phase is at least 12% in the PA6-clay nanocomposite with 20 wt% of clay.
- At practical concentrations, below 5wt% of silicate the amount of highly mobile phase is smaller than 1%. It is very unlikely that such a small amount of material is responsible for the high stiffness and low thermal expansion of nanocomposites. If the highly mobile phase has an influence at all, then it would lower the stiffness of a nanocomposite.

6.4 References

- [1] F.H.J. Maurer, R. Kosfeld and T. Uhlenbroich, *Interfacial interaction in kaolin-filled polyethylene composites*, Colloid. Polym. Sci. **263**(8), 1985, p 624-630
- [2] V.M. Litvinov, *Organosilicon Chemistry II. From Molecules to Materials*, Eds. N. Auner and J. Weis, WCH, Weinheim, 1996, p779-814
- [3] L.J. Mathias, R.D. Davis and W.L. Jarret, *Observation of α and γ crystal forms and amorphous regions of nylon6-clay nanocomposites using solid-state ^{15}N nuclear magnetic resonance*, Macromolecules **32**, 1999, p 7958-7960.
- [4] S. Wong, R. Vaia, E. Giannelis and D. Zax, *Dynamics in a poly(ethylene oxide) based nanocomposite polymer electrolyte probed by solid state NMR*, Solid State Ionics **86**, 1996, p 547-557.
- [5] D.B. Zax, D.K. Yang, R.A. Santhos, H. Hegemann, E.P. Giannelis, E. Manias, *Dynamical heterogeneity in nanoconfined poly(styrene) chains*, J. Chem. Physics **112**(6), 2000, p 2945-2951.
- [6] E. Manias, D.B. Zax and S.H. Anastasiadis, *Polymer/silicate intercalated nanocomposites: confinement induced segmental dynamics in 2 nm slits*, ACS Pol. Mat. Sci. Eng. **82**, 2000, p 259-260.
- [7] E. Manias, H. Chen, R.Krishnamoorti, J. Genzer, E.J. Kramer and E.P. Giannelis, *Intercalation kinetics of long polymers in 2 nm confinements*, Macromolecules **33**, 2000, p 7955-7966.
- [8] J.K.M. Sanders and B.K. Hunter, *Modern NMR Spectroscopy; A Guide for Chemists*, Oxford University Press, 1987.

Melting and crystallisation of nanocomposites

Abstract

The crystallisation and melting of polymer-montmorillonite nanocomposites was studied as a function of clay loading and clay aspect ratio. The polymer matrices used are Polyamide-6 (PA6), a blend of 75% PA6 and 25% aromatic polyamide (PA6/6T6I), and a HDPE grafted with maleic anhydride (HDPE). DSC measurements are used to measure the heat of melting and of crystallisation. An infrared technique, based on the derivative of the absorbance, is introduced to study the melting and crystallisation of the α and γ phases in PA6 nanocomposites.

DSC measurements show the emergence of a second melting transition in PA6-nanocomposites at 241 °C, well above the normal melting point of PA6. Infrared spectroscopy confirms the existence of the new melting transition. Both the normal and the new melting transition shift to lower temperatures upon addition of clay. A thermodynamical theory is introduced that qualitatively explains the observed results. The theory is based on confinement of polymer chains between clay platelets.

DSC measurements on HDPE-nanocomposites with clays of varying aspect ratio reveal that crystallisation is not sensitive to the aspect ratio of the clay. Upon addition of clay, HDPE nanocomposites show the same suppression of melting temperature as the polyamide nanocomposites. HDPE nanocomposites do not show a high temperature melting transition like the PA6 nanocomposites do.

7.1 Introduction

The mechanical properties of nanocomposites depend on the properties of the polymer and mineral phases in the nanocomposite. In conventional composites it is usually assumed that the properties of the polymer matrix are not essentially changed by the presence of the reinforcing phase. Therefore the properties of a conventional composite are thought to be a mixture of properties of the unfilled polymer and of the reinforcement. In nanocomposites the contact area between polymer and reinforcement is extremely large ($\approx 700 \text{ m}^2/\text{g}$). It can therefore be expected that properties of the polymer inside the nanocomposite are different from those of the unfilled polymer. In this chapter we will discuss how the crystalline structure of the polymer phase in polymer-clay nanocomposites is changed by the presence of exfoliated clay platelets.

PA6 is a semi-crystalline polymer with a relatively high melting temperature. The high melting temperature of PA6 is caused by the hydrogen bonds that provide strong attractive forces between adjacent chains. PA6 crystallises in the α -, β - or γ -structure, depending on environmental conditions. Under slow cooling PA6 crystallises in the α -structure and under fast cooling in the β -structure. The γ -structure is formed under extensional stress during fibre spinning or by addition of chemicals that change the nature of the hydrogen bonds [1]. In the early work of Toyota [2] it was discovered that the γ -structure is also present in PA6-clay nanocomposites. Recently Mathias et al. [3] suggested that the γ -structure in PA6 nanocomposites is a consequence of the bond between amine end groups and the clay surface. This inhibits the α -structure and forms the γ -structure by default.

In a polymer-clay nanocomposite, the distance between clay platelets is extremely small. At 20 wt% of clay the distance is about 10 nm while at 1 wt% it is about 200 nm. It can be expected that not only the crystalline structure but also crystallisation and melting kinetics are severely changed by the presence of the clay platelets. Not much is known about crystallisation and melting of nanocomposites. Kuchta et al. [4] found that lamellar thickening is suppressed in PA11-clay nanocomposites due to the external constraints of the clay layers in the host polymer. In another article, Kuchta et al. [5] reported that crystallisation was retarded in PE-clay nanocomposites, while no change in crystalline structure was observed due to the presence of clay platelets. Also Maurer et al. [6] noticed a reduction in crystallinity in highly filled PE-kaolin compounds with a high interfacial area. Nano dispersed clay was found to accelerate crystallisation in poly(ethylene terephthalate) [7], in PA6 [8] and in poly(ϵ -caprolactone) [9]. Kojima [10] et al. showed that the clay layers determine the orientation of PA6 chains in PA6-clay nanocomposites.

Although some literature exists on the crystalline structure of nanocomposites, no literature is found that focuses on the melting transition of nanocomposites. In this chapter the melting and crystallisation of PA6 nanocomposites is studied by DSC and FTIR. It will be shown that in PA6-clay nanocomposites a phase exists that melts above the normal melting temperature of PA6. Also the effect of clay aspect ratio on the crystallisation of HDPE-nanocomposites is studied.

7.2 PA and PA6/6T6I nanocomposites

In this section the melting and crystallisation behaviour of PA6 and PA6/6T6I nanocomposites, studied by DSC and by FTIR techniques, will be described.

7.2.1 Materials and experimental techniques

PA6-clay nanocomposites and PA6/6T6I-clay nanocomposites with 0-20 wt% of clay are prepared by melt intercalation on an extruder. The PA6/6T6I contained 75 wt% of PA6 and 25 wt% of 6T/6I (terephthalic/isophthalic copolymer). The 6T/6I was added to reduce the crystallinity of the matrix polymer. The clay used is a montmorillonite that is organically modified by 38 wt% 2-methyl-2-hydrogenated-tallow-ammonium. The preparation of the nanocomposites and their composition is extensively discussed in Chapter 5.

DSC measurements are performed with a Perkin Elmer DSC 7 at a heating/cooling rate of 10°C/min on granules as obtained after melt extrusion.

To perform FTIR measurements, the remainder of the compression moulded DMA films that are described in Chapter 9, were again compression moulded to very thin ($\approx 5\mu\text{m}$) films at a pressure of 18 tons between two 2 cm thick metal plates that were preheated to 300 °C. The samples were very thin in order to prevent over-absorption of the infrared spectrum at high concentrations of clay. After compression moulding the samples were naturally cooled down to room temperature in about 5 minutes.

The FTIR measurements were performed on a Perkin Elmer system 2000 FTIR spectrometer using a MCT detector for fast scanning. Each spectrum was obtained by averaging 20 scans. Spectra were measured as a function of temperature between 70 °C and 270 °C using a Beckman cell. Since the heating rate of this cell could not be adjusted at will, the heating element of the cell was used at full capacity. This resulted in a varying heating rate. Below 200 °C the heating rate was about 10 °C/min and above 200 °C about 4 °C/min. Below 200 °C measurements were performed every 10 °C, between 200 °C and 210 °C every 5 °C, between 210 °C and 240 °C every 3 °C, between 240 °C and 250 °C every 5 °C and above 250 °C every 10 °C.

7.2.2 DSC results

From the DSC heating curves in Figs. 7.1 and 7.2 it can be seen that both types of nanocomposites show a similar dependence of melting temperature on clay content. Without clay, the melting peak of PA6 lies at 222 °C and the melting peak of the 75/25 PA6/6T6I blend lies at 219.7 °C. These melting temperatures are typical for PA6 with a α -crystalline structure. At higher clay content, the melting temperature is shifted towards lower temperatures while at the same time a second peak emerges at temperatures well above the normal melting temperature of PA6. In the PA6 nanocomposites this high temperature-melting peak is more pronounced than in the PA6/6T6I nanocomposites.

All melting and crystallisation peak-temperatures and enthalpies are listed in Tables 7.1 and 7.2. To account for the presence of the amorphous 6T/6I polyamide and for the organically modified clay also the enthalpies per gram PA6 are listed. The enthalpies are determined by integration of the DSC curve. The integrated enthalpy is sensitive to the position of the baseline. Since the position of the baseline is uncertain, an error is introduced in the determination of the enthalpies. Especially at low enthalpies the relative error is large. Since the crystallisation peaks are much narrower (Figs. 7.7 and 7.8) than the melting peaks, positioning the base line can be done with more accuracy. This makes the error in crystallisation enthalpies smaller than the error in melt enthalpies. Therefore the crystallisation enthalpies are used as a measure for crystallinity.

Fig. 7.3 shows the peak temperatures of the low, $T_{\text{melt}}(1)$, and high, $T_{\text{melt}}(2)$, melt transitions as a function of clay content. $T_{\text{melt}}(1)$ of both PA6 and PA6/6T6I nanocomposites show a similar response to the presence of nano-dispersed clay. Both show a steep drop of

about 8°C at 1 wt% clay. Between 1 and 10 wt%, $T_{\text{melt}}(1)$ is independent of clay content and lies near 214°C, which is typical for γ -crystalline PA6. At concentrations above 10 wt% $T_{\text{melt}}(1)$ decreases to about 208 °C. A similar decrease in melting temperature was also observed by Kuchta et al. for PA11-clay nanocomposites [4].

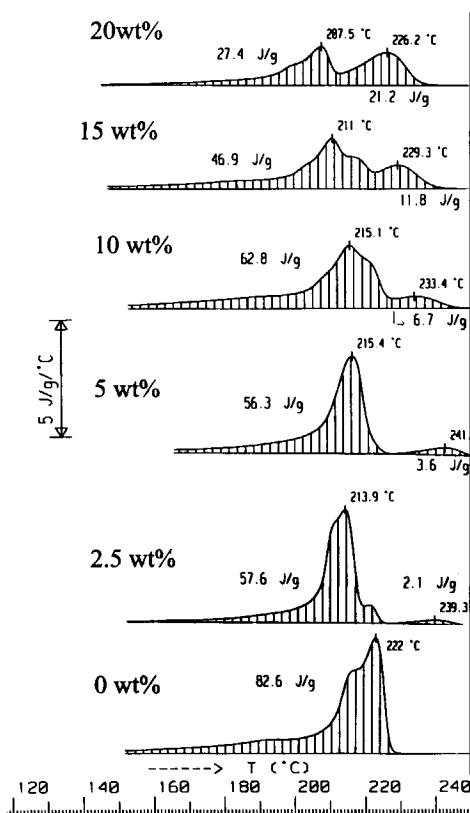


Figure 7.1 DSC heating curves of PA6 nanocomposites with 0, 2.5, 5, 10, 15 and 20wt% montmorillonite. Note the emergence of a second melting peak at high loadings.

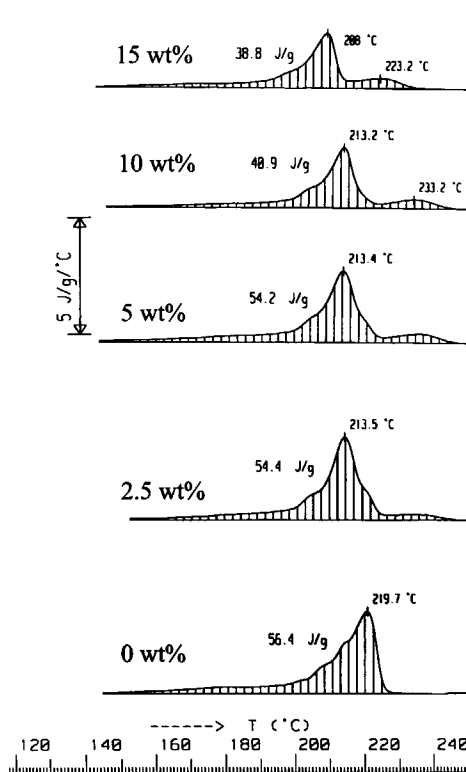


Figure 7.2 DSC heating curves of (75/25) PA6/6T6I nanocomposites with 0, 2.5, 5, 10 and 15wt% montmorillonite. Again a second melting peak emerges at high weight concentrations.

Initially $T_{\text{melt}}(2)$ is about 6°C higher for the PA6 nanocomposites than for the PA6/6T6I nanocomposites. Below 7.5 w% of clay $T_{\text{melt}}(2)$ lies near 241 °C for the PA6 and near 235°C for the PA6/6T6I nanocomposites. Between 7.5 w% and 15 w% both $T_{\text{melt}}(1)$ and $T_{\text{melt}}(2)$ drop about 12 °C.

From Fig. 7.5 it can be seen that the melt-enthalpy of the high temperature melting process, $\Delta H_{\text{melt}}(2)$, increases strongly upon addition of clay. The increase of $\Delta H_{\text{melt}}(2)$ in the PA6/6T6I nanocomposites levels off at about 7.5 wt% of clay, while in the PA6 nanocomposites $\Delta H_{\text{melt}}(2)$ increases exponentially up to 20 wt% of clay. The data in Table 7.1 reveal that at 20 wt% of clay almost half the amount of PA6 in the PA6 nanocomposite, melts at the high temperature transition.

Code	Org. Clay wt%	Sil. wt%	T _{melt1} °C	ΔH _{melt1} J/g	ΔH _{melt1} per g PA6 J/g	T _{melt2} °C	ΔH _{melt2} J/g	ΔH _{melt2} per g PA6 J/g	ΔH _{cryst} J/g	ΔH _{cryst} per g PA6 J/g	T _{cryst} °C
PA6-0	0	0	222.0	82.6	82.6	-	0	0	-82.8	-82.8	189.4
PA6-0.2	0.33	0.2	221.8	71.7	71.9	-	0	0	-71.1	-71.3	190.6
PA6-1.0	1.66	1.0	214.5	75.3	76.6	240	0.9	0.9	-68.4	-69.6	189.5
PA6-2.5	4.17	2.5	213.9	57.6	60.1	239.3	2.1	2.2	-65	-67.8	190.7
PA6-5.0	8.33	5.0	215.4	56.3	61.4	241.7	3.6	3.9	-63.7	-69.5	189.8
PA6-7.5	12.5	7.5	215.7	46.8	53.5	241.6	4.5	5.1	-60.9	-69.6	187.3
PA6-10	16.7	10	215.1	62.8	75.4	233.4	6.7	8.0	-59.2	-71.0	180.1
PA6-15	25.0	15	211.0	46.9	62.4	229.3	11.8	15.7	-52.8	-70.4	179.8
PA6-20	33.3	20	207.5	27.4	41.1	226.2	21.2	31.8	-43.8	-65.7	174.8

Table 7.1 DSC data of PA6-nanocomposites

Code	Org. clay wt%	Sil. wt%	T _{melt1} °C	ΔH _{melt1} J/g	ΔH _{melt1} per g PA6 J/g	T _{melt2} °C	ΔH _{melt2} J/g	ΔH _{melt2} per g PA6 J/g	ΔH _{cryst} J/g	ΔH _{cryst} per g PA6 J/g	T _{cryst} °C
Griv-0	0	0	219.7	56.4	75.2	-	0	0.0	-51.7	-68.9	174.6
Griv-0.2	0.33	0.2	220.0	58.9	78.8	-	0	0.0	-53.6	-71.7	178.4
Griv-1.0	1.66	1.0	213.1	56.7	76.9	-	1.0	1.4	-47.4	-64.3	178.3
Griv-2.5	4.17	2.5	213.5	52.3	72.8	235	2.1	2.9	-45.6	-63.5	178.2
Griv-5.0	8.33	5.0	213.4	50.2	73.0	236	4.0	5.8	-44.2	-64.3	177.3
Griv-7.5	12.5	7.5	212.7	40.7	62.0	234	4.7	7.2	-40.2	-61.2	175.1
Griv-10	16.7	10	213.2	36.2	57.9	233	4.7	7.5	-38.9	-62.3	172.5
Griv-15	25	15	208.0	33.8	60.1	223	5.0	8.9	-34.3	-60.9	166.1

Table 7.2 DSC data of PA/6T6I-nanocomposites

In Fig. 7.6 the heat of crystallisation shows a sharp drop at only 0.2 wt% of clay. PA6-clay nanocomposites crystallise in the γ -form. The heat of crystallisation of the γ -crystalline phase is 213 J/g and 243 J/g for the α - crystalline phase. So the steep drop in heat of crystallisation could be due to the lower heat of crystallisation of the γ -crystalline phase and is not necessarily due to a lower crystallinity.

7.2.3 FTIR-results

To distinguish between α - and γ -crystalline materials and to confirm the DSC results of the previous section, Fourier Transform Infrared spectroscopy (FTIR) was performed on the PA6 nanocomposites as a function of temperature.

Fig. 7.9 shows a series of spectra near 1420 cm^{-1} and 1310 cm^{-1} , at intervals of 10°C . The intensities of these bands are a measure of the amount of crystalline phase. To determine the amount of α -crystalline phase the band at 1420 cm^{-1} was used, while the amount of γ -crystalline phase was determined by the 1310 cm^{-1} band. Band assignments are given by Dechant [11].

The intensities of the 1420 cm^{-1} and 1310 cm^{-1} bands are determined by integration using Labspec 2.08 software. All intensities were weighted against the intensity of the 1370 cm^{-1} band, which was used as a thickness reference. Integration was performed between the following wavenumbers:

The α -band at 1310 cm^{-1} between 1294 cm^{-1} and 1329 cm^{-1} .

The γ -band at 1420 cm^{-1} between 1410 cm^{-1} and 1428 cm^{-1} .

The reference band at 1370 cm^{-1} between 1335 cm^{-1} and 1395 cm^{-1} .

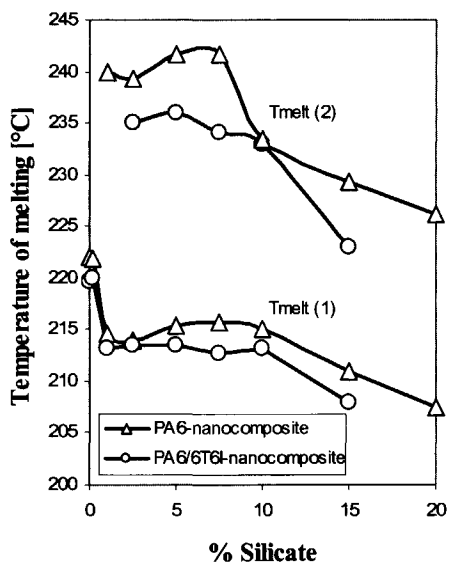


Figure 7.3 Melting peak temperatures as a function of clay concentration, of the low and high temperature melting transitions of PA6 and 75/25 PA6/6T6I nanocomposites

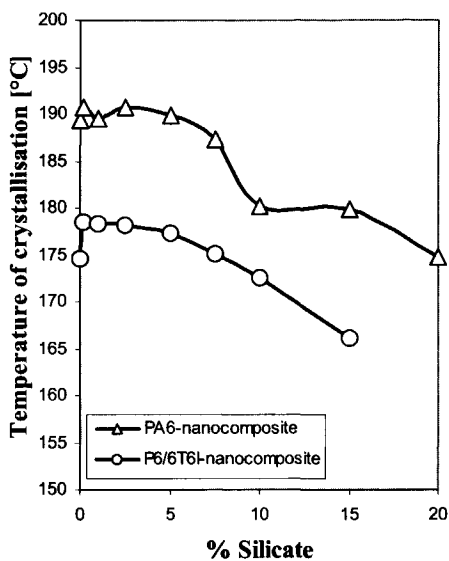


Figure 7.4 Crystallisation peak temperatures as a function of clay concentration, of PA6 and 75/25 6T/6I nanocomposites.

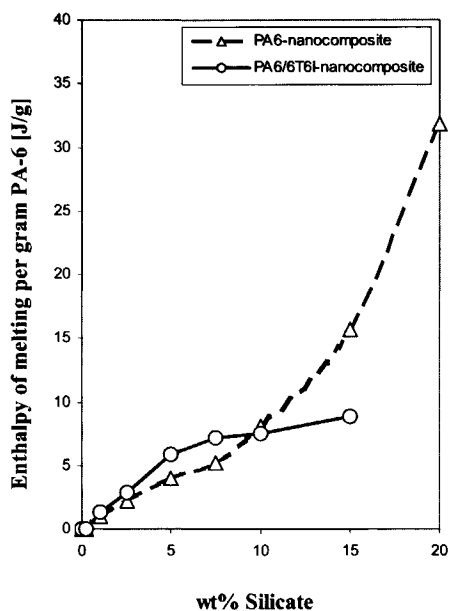


Figure 7.5 Enthalpy of melting of the high temperature melting transition, $\Delta H_{melt(2)}$, of PA6 and 75/25 PA6/6T6I nanocomposites as a function of clay concentration.

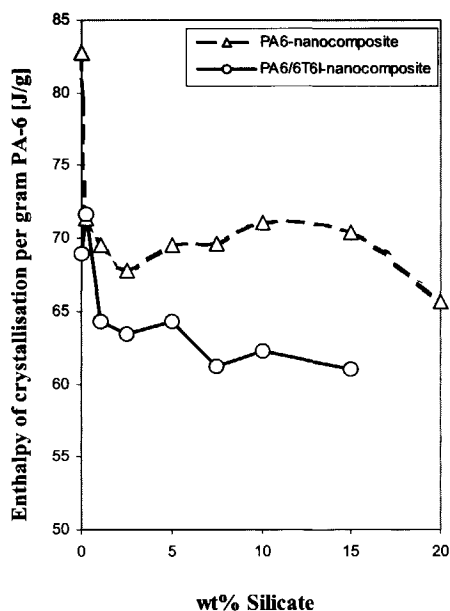


Figure 7.6 Enthalpy of crystallisation of PA6 and 75/25 PA6/6T6I nanocomposites as a function of clay concentration

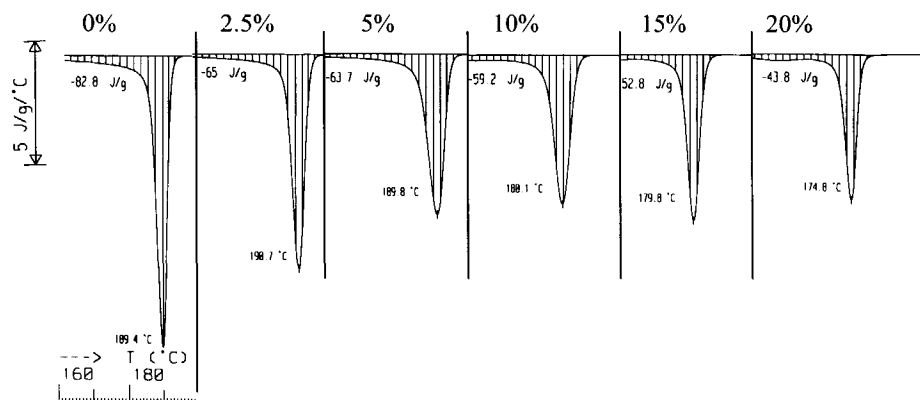


Figure 7.7 DSC crystallisation peaks of PA6 nanocomposites with 0, 2.5, 5, 10, 15 and 20wt% silicate

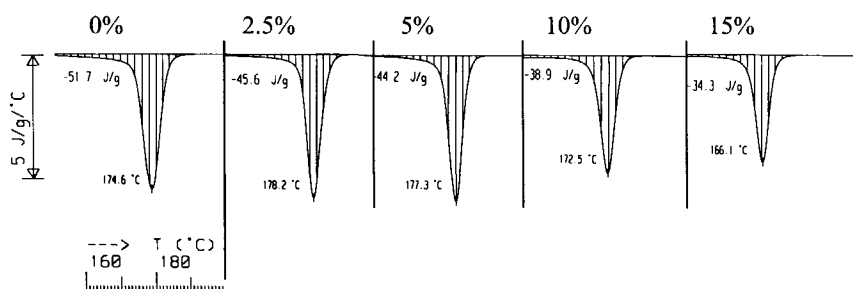


Figure 7.8 DSC crystallisation peaks of PA6/6T6I nanocomposites with 0, 2.5, 5, 10, 15 and 20wt% silicate

The intensity of a band is defined as the area between the baseline and the spectrum. The baseline is defined as a straight line through the integration limits. The α - and γ -band intensities are normalised by setting the band intensities at 270 °C to zero. In practise this was done by subtracting the band intensity at 270 °C from the band intensity at a given temperature.

To correct for differences in thickness between samples, the normalised intensities of the α -band and γ -band were divided by the intensity of the reference band. The so obtained normalised and thickness corrected intensity of the α - and γ - bands, I_{cryst} , is a measure of the amount of crystalline phase.

In Fig. 7.10 the intensities of both α - and γ -bands at 70 °C are plotted as a function of clay content. The amount of γ -crystalline phase increases by addition of clay. At 0% clay only α -bands are found, indicating a purely α -crystalline phase. Upon addition of clay the intensity of the γ -band increases while the α -band decreases.

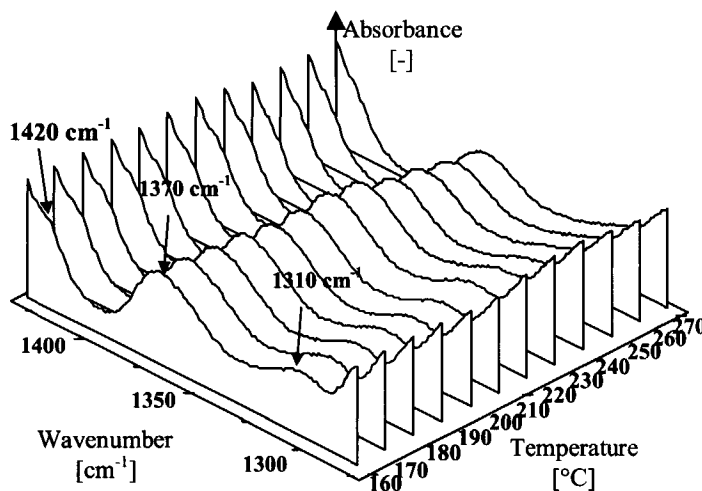


Figure 7.9 Infrared spectra of PA6 nanocomposite with 10 wt% of clay between 160 and 270 °C. The α -band at 1420 cm^{-1} and the γ -band at 1310 cm^{-1} are visible together with the thickness reference band at 1370 cm^{-1} .

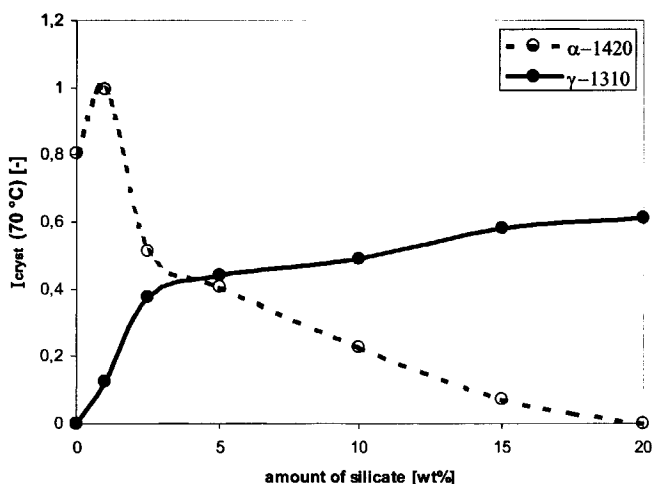


Figure 7.10 Effect of clay content on the intensity of the α - and γ -crystalline bands in PA6-clay nanocomposites.

At 1 wt% of clay the nanocomposite still is mainly α -crystalline while at 2.5 wt% both phases are present at nearly equal concentrations. Even at 10 wt% of clay the PA6 nanocomposite still contains a considerable amount of α -crystalline material. At 15 wt% and 20 wt% the amount of α -crystalline material is very low.

The intensity of the α and γ bands (I_{cryst}) of the nanocomposite with 15 wt% of clay is plotted in Fig. 7.11 as a function of temperature. The intensity of the γ -band is much higher

than the intensity of the α -band, indicating that this nanocomposite mainly contains γ -crystalline material. The intensity of the γ -band continuously drops between 70 and 200 °C. This can be explained in two ways, either the crystallinity strongly decreases in this region, which is unlikely, or the intensity of the infrared band decreases with temperature even at constant crystallinity. Above 200°C, the intensity suddenly shows a much steeper decrease. This is caused by melting of the crystalline phase. Above 260°C all crystalline material is melted.

The steep decrease above 200 °C prompted us to calculate the *derivative* of the intensity. The lower part of Fig. 7.11 shows the derivative $-dI_{\text{cryst}}/dT$. This is a measure for the amount of crystalline phase melted per °C. The amount of heat needed to melt the sample (ΔH) is proportional to the amount of crystalline phase in the sample and thus is also proportional to the intensity of a crystalline peak (I_{cryst}) in the IR-spectrum.

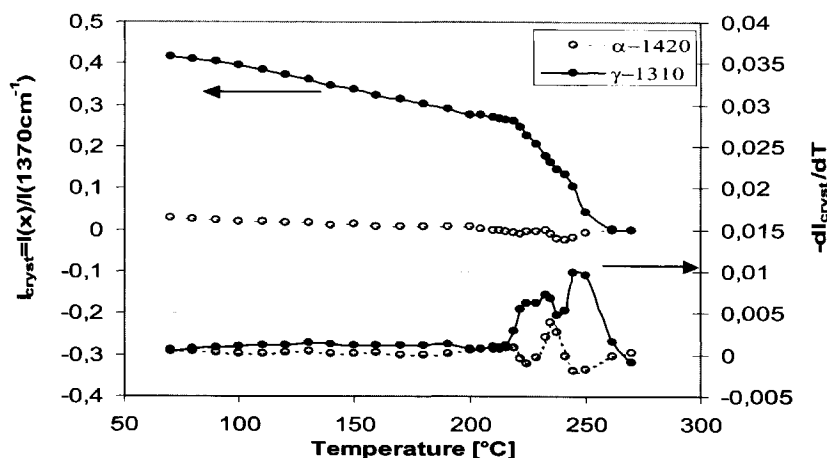


Figure 7.11 PA6-clay nanocomposite with 15 wt% of clay.

Left axis: Thickness corrected intensity I_{cryst} of the α - and γ -crystalline bands.

Right axis: The temperature derivative of the peak intensity $-dI_{\text{cryst}}/dT$.

Note that the disappearance of the γ -phase is accompanied by the emergence of the α -phase.

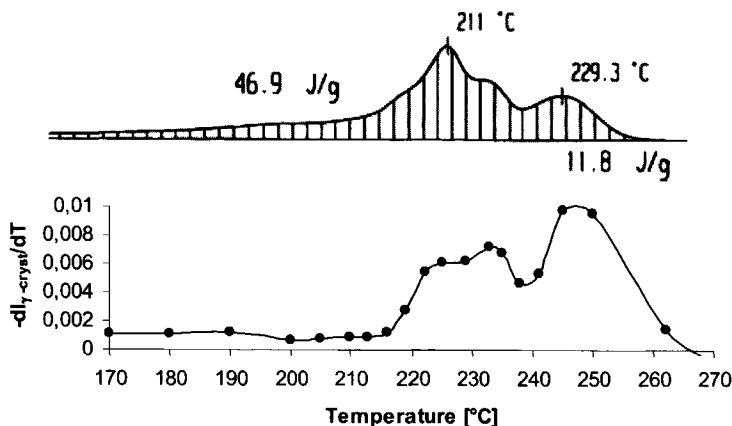


Figure 7.12 Melting of PA6 nanocomposite with 15 wt% of clay.

Upper part: dH/dT measured by DSC

Lower part: $-dI_{\gamma\text{-cryst}}/dT$ measured by FTIR

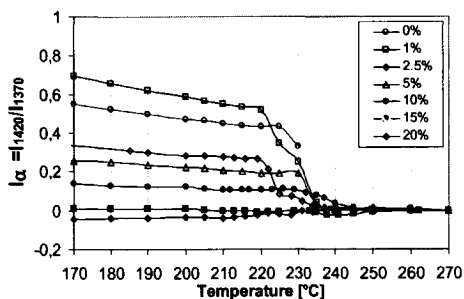


Figure 7.13 PA6 nanocomposites with 0-20wt % of clay. Intensity of the α -band (1420 cm^{-1}) as a function of temperature.

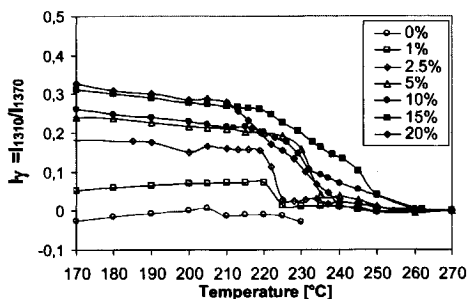


Figure 7.14 PA6 nanocomposites with 0-20wt % of clay. Intensity of the γ -band (1310 cm^{-1}) as a function of temperature.

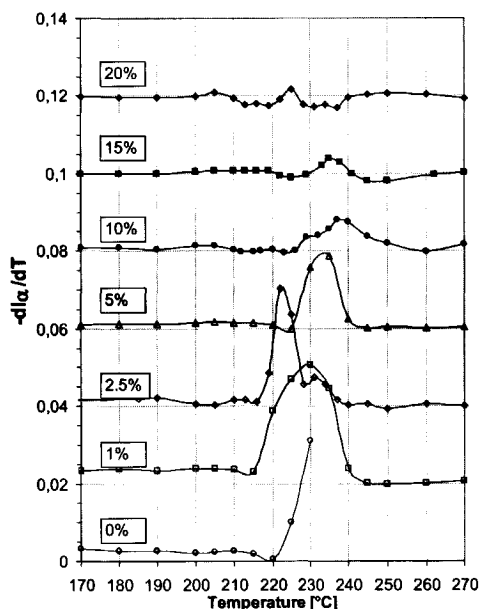


Figure 7.15 PA6 nanocomposites with 0-20 wt % of clay. First derivative to temperature of the α -band intensity as a function of temperature.

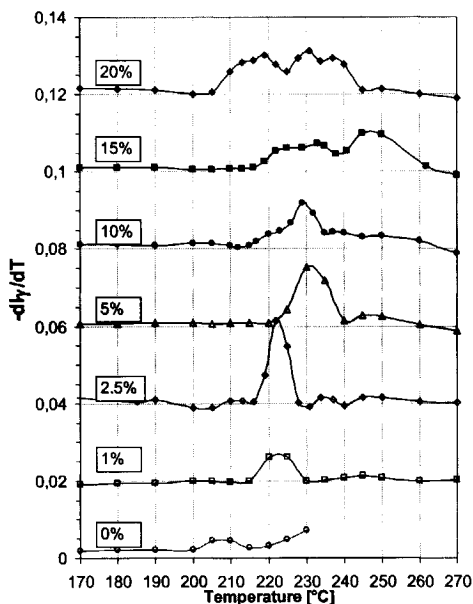


Figure 7.16 PA6 nanocomposites with 0-20 wt % of clay. First derivative to temperature of the γ -band intensity as a function of temperature.

In the DSC graphs of Figs. 7.1 and 7.2 the specific heat c_p is plotted on the y-axis. This is the amount of energy needed to increase the temperature of the sample by 1°C . In the melting zone nearly all energy is needed to melt the sample. So in the melting zone c_p is proportional to $-dI_{\text{cryst}}/dT$. The minus sign is needed, because during melting the amount of heat increases while the amount of crystalline phase decreases. The samples with 15 and with 20 wt% of clay are almost entirely γ -crystalline. So by plotting the derivative of the γ -band

intensity $-dI_{\gamma\text{-cryst}}/dT$, as a function of temperature, a curve should be obtained that resembles the DSC plot near the melting zone.

In Fig. 7.12 the DSC curve and $-dI_{\gamma\text{-cryst}}/dT$ are plotted as a function of temperature. The γ -band clearly shows the same transitions as the DSC-curve does. The peak temperatures near 230 °C and 245 °C are about 15 °C higher than found in the DSC measurement. Probably the relatively fast heating of the Beckmann cell causes the sample temperature to lag behind the measured temperature. The reason for this is that the temperature measurement of the Beckman cell is not optimised for fast heating. Normally it is operated at a constant temperature.

The α -phase in Fig. 7.11 shows a behaviour that is opposite from the γ -phase. In the melt transition, while the γ -phase is disappearing, some α -phase material is created. This indicates that some of the molten γ -crystalline material is immediately transformed into α -crystalline material. This γ to α transition was found in all the samples tested. This can be verified by comparing Figs. 7.15 and 7.16.

Band intensity of the PA6 nanocomposites I_{cryst} and the derivative $-dI_{\text{cryst}}/dT$ are plotted in Figs. 7.13 to 7.16. It is difficult to obtain detailed information about the melt transitions by only observing I_{cryst} in Figs. 7.13 and 7.14. A much better insight is obtained by observing $-dI_{\text{cryst}}/dT$ in Figs. 7.15 and 7.16. Like the DSC curve in Fig. 7.1, the γ -phase in the nanocomposite with 20 wt% of clay clearly shows two melting transitions. The graphs thus confirm the existence of a phase that melts above the normal melting point. Since the transition is only visible with the γ -band this phase has a γ -crystalline structure

7.2.4 Explanation for the decrease in melting temperature upon addition of clay

The decrease in melting temperature upon addition of clay can probably be attributed to a decrease in lamellar thickness of the polymer crystals. At increasing concentration the distance between clay platelets becomes so small that the growth of crystals is seriously hindered. As a result of this, crystals of smaller dimensions and lower perfection are formed with a correspondingly lower melting temperature. In lamellar crystals this leads to a decrease of the maximum size of crystal lamellae. Such a decrease in lamellar thickness has been experimentally verified for PA-11 nanocomposites by Kuchta et al. [4]. A strong dependence exists of the observed melting temperature T_m of a polymer crystal upon lamellar thickness, l [12]:

$$T_m = T_m^0 - \frac{2\gamma_e T_m^0}{l\Delta H_v} \quad (7.1)$$

where T_m^0 is the melting temperature at infinite crystal thickness, ΔH_v is the enthalpy of fusion per unit volume of the crystals and γ_e is the top and bottom surface energy of the lamellar crystals.

7.2.5 Explanation for the existence of a high temperature melting transition

An explanation for the existence of the high temperature melting transition might be found in the confinement of polyamide chains near the clay surface. According to thermodynamics the free energy per unit volume ΔG_v can be expressed as:

$$\Delta G_v = \Delta H_v - T\Delta S_v \quad (7.2)$$

where ΔH_v and ΔS_v are the enthalpies and entropies of fusion per unit volume respectively.

An idealised perfect crystal of infinite dimensions melts at $T = T_m^0$. At T_m^0 there is no change in free energy since melting and crystallisation are equally probable and so $\Delta G_v = 0$. From Eqn. 7.2 it then follows that for a perfect crystal:

$$T_m^0 = \frac{\Delta H_v}{\Delta S_v} \quad (7.3)$$

If the crystals are present in a confined environment, the amount of possible arrangements of the polymer chains is seriously limited. Consequently the entropy change ΔS_v upon melting is decreased, causing an increase in polymer melting temperature.

7.2.6 Crystallisation behaviour

Figs. 7.7 and 7.8 show the DSC cooling curves of some selected PA6 and PA6/6T6I nanocomposites. Unlike the melting peaks, the crystallisation peaks are very narrow and show no details. Fig. 7.4 shows that the crystallisation temperature drops considerably by addition of more than 5 wt% of clay. As a result of the presence of 25 wt% aromatic 6T6I polyamide in the PA6/6T6I nanocomposites their crystallisation temperature is about 10 °C lower than that of the PA6 nanocomposites. The PA6/6T6I nanocomposites show a 4 °C increase in crystallisation temperature at 0.2 wt% of clay. This suggests that clay in the PA6/6T6I nanocomposites acts as a nucleating agent.

In Fig. 7.6 the crystallisation enthalpy is plotted against the clay content. The enthalpy is corrected for the presence of non-crystallising material, by calculating the enthalpy per gram PA6. Both PA6 and PA6/6T6I nanocomposites show a sharp drop in crystallisation enthalpy at only 0.2 % clay. FTIR results show that between 0 and 1 % of clay the PA6 nanocomposites mainly contain α -crystalline material. So the drop in crystallisation enthalpy should point at a decrease in crystallinity of the sample. This contradicts the finding in Fig. 7.10 that shows an increase in the amount of α -phase at 1% of clay.

7.2.7 Evaluation of the melting and crystallisation behaviour

Apparently two melt transitions are present in the nanocomposites. One with a high and one with a low melting point. It is anticipated that the phase with the low melting point is present at some distance from the clay layers, while the phase with the high melting point is very close to the clay layers and is confined.

At low clay content, the distance between the clay layers is large enough to allow the PA6 crystals to obtain their undisturbed lamellar thickness. Consequently the melting temperature of the PA6 is not changed at low clay content. At increasing clay content, the amount of confined polymer is increased and a second melting peak emerges above the unconfined melting point.

At high clay content the clay layers approach each other so close that the crystalline lamellae can no longer obtain their undisturbed thickness. This leads to a decrease of lamellar

thickness and consequently to a lower melting point. Lamellae of PA-6 crystals typically have an undisturbed thickness in the order of 10 nm. At clay loadings below 5 wt% the distances between the clay platelets are larger than 50 nm (Table 6.1). At these loadings the PA6-lamellae are expected to grow relatively undisturbed. Above 10 wt%, as the distance between clay platelets becomes smaller than 20 nm, the PA6-lamellae start to feel the presence of the clay platelets. This implies that the melting temperature will stay constant up to about 10 wt% of clay, while above 10 wt%, the crystals become disturbed and the melting point will drop. These theoretical predictions correspond well with the experimental data plotted in Fig. 7.3.

The 6°C higher $T_{\text{melt}}(2)$ of the PA6 nanocomposites compared to the PA6/6T6I nanocomposites in Fig. 7.3 suggest a stronger interaction between the clay and the PA6 in the PA6 nanocomposites. Upon addition of clay, $\Delta H_{\text{melt}}(2)$ of the PA6/6T6I nanocomposites stops to increase at 7.5 wt% of clay while it continues to increase for the PA6 nanocomposites. This suggests that, above 7.5 wt% of clay, more polymer is confined in the PA6 nanocomposites than in the PA6/6T6I nanocomposites. So the PA6 in the PA6 nanocomposites interacts stronger and in larger quantities with the clay layers, than the PA6 in the PA6/6T6I nanocomposites.

7.3 PE nanocomposites

In this section the crystallinity and perfection of polymer crystals in HDPE-clay nanocomposites is studied by DSC experiments. The amount of clay and the aspect ratio of the clay are varied. The objective of the study is to obtain information on the crystalline morphology of the polymer matrix. These morphological data will be used in Chapter 9 to explain the mechanical stiffness of HDPE-clay nanocomposites.

7.3.1 Materials and experimental techniques

HDPE with 2 wt% of grafted maleic anhydride is used as the matrix polymer throughout this study. HDPE-nanocomposites with 0-20 wt% of clay are made on a Haake kneader. Three types of clays are used that differ only in the aspect ratio of the clay. The type and amount of organic modification of these clays are identical. The preparation of the nanocomposites is discussed in Chapter 5.

DSC experiments are performed on a Perkin Elmer DSC 7, between 30°C and 180°C at a heating rate of 10°C/min. Only the first heating curve is used. To assure equal thermal history for the DMA and the DSC samples, all DSC samples are taken from the same compression moulded samples as was used for DMA measurement.

7.3.2 DSC results

DSC curves of the PE-nanocomposites are plotted in Figs. 7.17 to 7.19. The melt enthalpy is determined by integration of the DSC curves between 80 and 140°C. Melt enthalpy and peak temperatures are listed in Table 7.3.

The DSC curves in Figs. 7.17-7.19 show that the melting behaviour is strongly influenced by the amount of clay added. The melting peaks shift to lower temperatures upon addition of clay. The effect of aspect ratio on the melting behaviour is small.

These findings can be better appreciated by plotting the crystallinity of the PE-phase as a function of clay content, as is done in Fig. 7.20. The crystallinity is determined by

correcting the total enthalpy for the true amount of PE in the sample and by using a melt enthalpy of 286.6 J/g for a 100% PE crystal [13].

At small loadings the clay seems to act as a nucleating agent and increases the crystallinity a few percent. At high clay contents the crystallinity is strongly suppressed. All types of clays seem to suppress the melting enthalpy by roughly the same amount. At 20 wt% of clay the synthetic mica suppresses the crystallinity a little less than the other clays.

The peak melting temperatures of the HDPE nanocomposites in Fig. 7.21 drop continuously as the amount of clay is increased. Again the differences between the clays are small. Synthetic smectite and Montmorillonite show exactly the same behaviour. At 20 wt% synthetic mica, the suppression of the melting point is a little smaller than for the other nanocomposites.

Sample	Mass [mg]	Onset [°C]	Peak [°C]	ΔH [J/g]	ΔH /g PE [J/g]	crystallinity
HDPE-g-MA	4.1	124.5	130.4	186.2	186.2	0.650
1% montmorillonite	5.4	124.2	129.9	184.6	187.7	0.655
2.5% montmorillonite	5.7	124.3	129.7	181.3	189.2	0.660
5% montmorillonite	5.5	122.9	129.4	172.1	187.7	0.655
10% montmorillonite	4.3	122.3	128.8	153.5	184.2	0.643
15% montmorillonite	5.2	119.3	127.7	132.8	177.0	0.618
20% montmorillonite	5.3	118.7	126.6	115.2	172.7	0.603
1% synthetic mica	4.4	124.3	129.5	186.4	189.6	0.661
5% synthetic mica	5.4	123.8	128.8	171.5	187.1	0.653
20% synthetic mica	5.7	119.2	127.9	119.1	178.6	0.623
1% synthetic smectite	5.1	125.0	129.9	186.1	189.2	0.660
5% synthetic smectite	5.3	123.6	129.3	173.0	188.7	0.658
20% synthetic smectite	5.7	117.9	126.9	113.4	170.1	0.593

Table 7.3 DSC data of HDPE-nanocomposites

Overall it can be concluded that nanoclay suppresses the melting point of PE. At small loadings, nanoclay acts as an ineffective nucleating agent and increases the crystallinity a little bit. At higher loadings nanoclay lowers the crystallinity. Upon addition of clay the crystallisation peak shifts to lower temperatures. The aspect ratio does not have much effect on the crystallinity or melting point of PE-clay nanocomposites.

The lower melting point is probably caused by the confinement of the lamellar thickness like in the PA6-nanocomposites. A second melting transition as was found in PA6-nanocomposites is not observed in HDPE nanocomposites.

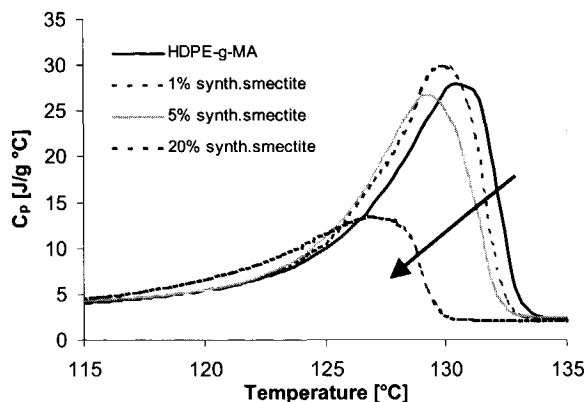


Figure 7.17 DSC heating curves of HDPE-nanocomposites with 0, 1, 5 and 20 wt% of synthetic smectite clay ($w/t \approx 30$)

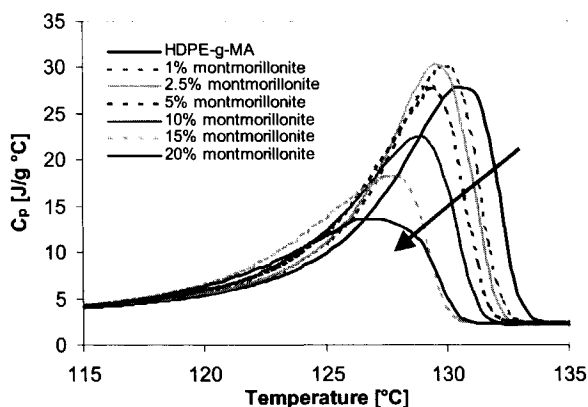


Figure 7.18 DSC heating curves of HDPE-nanocomposites with 0, 1, 2.5, 5, 10, 15 and 20 wt% of montmorillonite clay ($w/t \approx 100$)

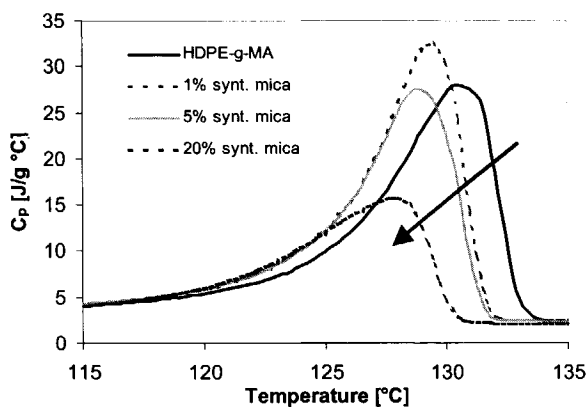


Figure 7.19 DSC heating curves of HDPE-nanocomposites with 0, 1, 5 and 20 wt% of synthetic mica clay ($w/t \approx 150$)

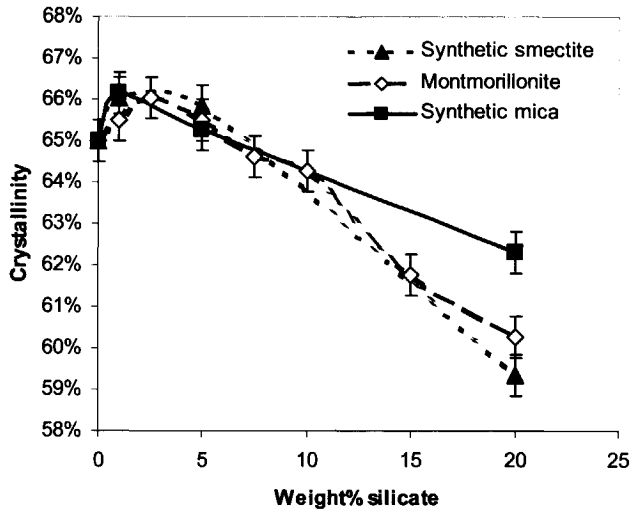


Figure 7.20 Crystallinity of the HDPE phase in the nanocomposites as a function of clay content.

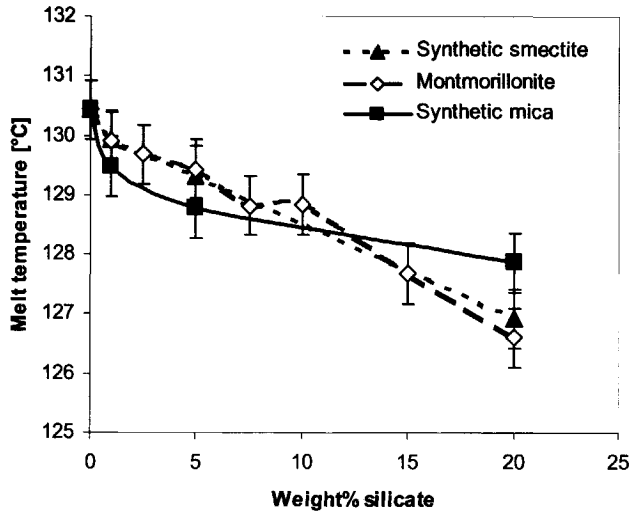


Figure 7.21 Peak temperature of the melting transition of HDPE nanocomposites as a function of clay content.

7.4 Conclusions

- Owing to a combination of DSC and temperature *derivative* FTIR measurements, the existence is proven of a second melting transition in PA6- nanocomposites above the

normal melting point of PA6. FTIR measurements confirm the existence of the high temperature melting transition and indicate that it consists of γ -crystalline material.

- Both the high and low temperature melting transitions shift to lower temperatures upon addition of clay.
- Both the existence of a second melting peak in PA6 nanocomposites, as the shift of the melting peaks to lower temperatures, is attributed to confinement of the polymer chains between the clay layers. A thermodynamical theory is given that qualitatively explains these findings.
- PA6-clay nanocomposites are not purely γ -crystalline. Depending on the amount of clay they may also contain a considerable amount of α -crystalline material. The amount of γ -phase increases upon addition of clay. Above 15 wt% of clay the PA6-nanocomposite is almost entirely γ -crystalline.
- Like PA6-nanocomposites, PE-nanocomposites show suppression of the melting temperature and crystallinity upon addition of clay.
- No significant effect is found of clay aspect ratio on the crystallinity or melting temperature of HDPE-clay nanocomposites.

7.5 References

- [1] G. Rotter, H. Ishida, *FTIR separation of nylon 6 chain conformations: Clarification of the mesomorphous and γ -crystalline phases*, J. Polym. Sci. B Polym. Phys. **30**, 1992, p 489-495.
- [2] Y. Kojima et al, *One-pot synthesis of nylon 6-clay hybrid*, J. Polym. Sci. A Polym. Chem. **31**, 1993, p 1755-1758
- [3] L. J. Mathias, R. D. Davis and W.L. Jarret, *Observation of α and γ -crystal forms and amorphous regions of nylon 6-clay nanocomposites using solid state ^{15}N nuclear magnetic resonance*, Macromolecules **33**, 1999, p 7958-7960
- [4] F.D. Kuchta, P. J. Lemstra, A. Keller, L. F. Batenburg, H.R. Fischer, *Polymer crystallisation studied in confined dimensions using nanocomposites from polymers and layered minerals*, Mat. Res. Soc. Symp. Proc. **628**, 2000, CC11.12.1-CC11.12.6.
- [5] F.D. Kuchta, P. J. Lemstra, A. Keller, L. F. Batenburg, H.R. Fischer, *Materials with improved properties from polymer-ceramic nanocomposites*, Mat. Res. Soc. Symp. Proc. **576**, 1999, p 363-368.
- [6] F.H.J. Maurer, R. Kosfeld and T. Uhlenbroich, *Interfacial interaction in kaolin-filled polyethylene composites*, Colloid. Polym. Sci. **263(8)**, 1985, p 624-630
- [7] Y. Ke, C. Long and Z. Qi, *Crystallization properties and crystal and nanoscale morphology of PET-Clay nanocomposites*, J. Appl. Polym. Sci. **71**, 1999, p 1139-1146.
- [8] L. Liu, Z. Qi, X. Zhu, *Studies on nylon 6/clay nanocomposites by melt intercalation process*, J. Appl. Polym. Sci. **71**, 1999, p 1133-1138.
- [9] G. Jimenez, N. Ogata, H. Kawai and T. Ogihara, *Structure and thermal/mechanical properties of poly(ϵ -caprolactone)-clay blend*, J. Appl. Polym. Sci. **64**, 1997, p 2211-2220.
- [10] Y. Kojima, A. Usuki, M. Kawasumi, A. Okada and T. Kurauchi, *Novel preferred orientation in injection moulded Nylon 6-clay hybrid*, J. Pol. Sci. B, Pol. Phys. **33**, 1995, 1039-1045.
- [11] J. Dechant, *Ultrarot Spektroskopische Untersuchungen an Polymeren*, Akademie Verlag, Berlin, DDR, 1972.
- [12] R. J. Young, *Introduction to Polymers*, Chapman and Hall, London, 1983, p 194.
- [13] G. Kämpf, *Characterization of Plastics by Physical Methods; Experimental Techniques and Practical Application*, Hanser, Munich, 1986, p 186.

Dielectric properties of nanocomposites

Abstract

Dielectric measurements were performed to study the relaxation mechanisms of PA6-nanocomposites with 0-20 wt% of clay. The measurements were made between -130 and 200 °C in a frequency range between 0.11 and 960 kHz. Four transitions can be distinguished in PA6 nanocomposites. Below 0°C, a weak secondary (β) transition is found in the nanocomposites as well as in the neat PA6. Upon addition of clay a new (α_2) glass transition emerges near 10 °C, well below the normal (α_1) glass transition. Above the glass transition, an electrode polarisation (EP) transition is found. The peak temperatures of these transitions are determined and plotted in an Arrhenius plot. Below 2.5 wt% of clay, the effect of clay on the position of the transitions is very small. The most striking effect is the emergence of the (α_2) glass transition. The strength of this transition increases strongly as the amount of clay is increased.

The effect of confinement of the polymer chains by the clay platelets is revealed by analysis of the activation energy fine structure. This analysis shows that confinement is a relative notion and depends on the frequency used to probe the sample. At high frequencies, the polymer does not experience any confinement because most motion occurs at a length-scale that is much smaller than the distance between the clay platelets. Confinement is only experienced at low frequencies as the length scale of cooperative motion exceeds the distance between the clay platelets.

8.1 Introduction

The central theme of this thesis is to use composite modelling to explain the properties of nanocomposites. Composite modelling usually assumes that the properties of the constituents are unchanged. In polymer-clay nanocomposites the surface of the clay is so large that it is likely that the properties of the polymer will change to some extent. In this chapter the changes in polymer properties will be studied by dielectric relaxation spectroscopy (DRS). DRS is a technique that is pre-eminently suitable to study relaxation mechanisms in polymer materials. It can be used to study how the relaxation mechanisms of the polymer matrix are changed by the presence of the clay.

The amount of literature on dielectric spectroscopy of nanocomposites is very limited. Only one research group around Anastasiadis [1-4] has published articles about this subject. In their articles, they investigated the segmental dynamics of polymer films that were confined in 1.5-2 nm wide galleries between clay platelets. A relaxation mode was found that is much faster than the bulk polymer α -relaxation and exhibits much weaker temperature dependence. This is attributed to the small interlayer spacing that restricts the co-operative volume of the α -transition. The existence of more mobile inter-phase regions as predicted by molecular dynamics and experimentally confirmed by solid state NMR, was also considered as a possible explanation. The data qualitatively support the cooperativity arguments without, however, being able to exclude the mobile inter-phase idea.

Where Anastasiadis used DRS on samples that contained mainly clay and only a little polymer, we have explored the use of DRS on practical nanocomposites that contain mainly polymer and only a little clay. It is clear that the confinement of polymer chains in practical nanocomposites is much smaller than in the nanocomposites studied by Anastasiadis. It is the objective of this study to find out how much the relaxation mechanisms of practical polymer-clay nanocomposites are changed by the presence of the clay.

8.2 Theory

8.2.1 The dielectric constant

If a material is submitted to an electric field, all charges in the material will experience a force that is directed parallel to the direction of this field. The charges respond by moving from their equilibrium positions and create an internal electric field that partly neutralises the applied electrical field. The ability of a material to neutralise an applied electrical field is expressed in its dielectric constant.

The dielectric constant is often determined by placing the material between two flat plates of a capacitor. The capacity C is a measure of the amount of charge Q that can be stored on the plates at a certain voltage U : $Q = CU$. If a material is placed between the plates of the capacitor, the induced electrical field inside the material will try to lower the applied electrical field. To keep the voltage over the capacitor intact, extra charge is transported to the plates of the capacitor. Therefore, by inserting a material, the capacity C of the capacitor is increased. The capacity of a capacitor is equal to:

$$C = \epsilon_0 \epsilon_r \frac{A}{d} \quad 8.1)$$

where $\epsilon_0 \epsilon_r$ is the permittivity of the material and ϵ_0 is the vacuum permittivity (8.85 pF/m). ϵ_r is the relative dielectric constant of the material. In vacuum ϵ_r equals unity, while in a

material ϵ_r , always is larger than unity. The word 'relative' and the index r are often omitted. In general, the dielectric constant is a complex quantity:

$$\epsilon^* = \epsilon' - i\epsilon'' \quad (8.2)$$

where ϵ' is the real part of the dielectric constant and is often simply referred to as the dielectric constant. ϵ' is a measure of the polarisability of the material. ϵ'' is the imaginary part, also known as the loss index and is a measure of the dielectric losses in the material.

8.2.2 Relaxation mechanisms

If a polymer is mechanically stressed, it can only relieve its stress by internal rearrangements of molecules. At very low temperatures, all molecules are frozen in and no rearrangements are possible. At this stage, the polymer will react purely elastic to any outside stress. As the temperature is increased, small parts of the polymer chains become mobile, enabling the polymer to relax a small part of the stress. If relaxation of stresses is possible, the material does no longer react purely elastic and becomes visco-elastic. Near the glass transition, the large parts of the polymer molecule become mobile and the stress on the polymer will relax more strongly. It is obvious that relaxation mechanisms are therefore of major importance for the mechanical behaviour of the polymer.

Dielectric relaxation spectroscopy is a technique that probes the intensity and frequency of the relaxation mechanisms as a function of temperature. This is usually done by performing frequency sweeps in a wide temperature range. The intensity and the frequency of the relaxations can give valuable information about the underlying molecular mechanisms. DRS is closely related to dynamic mechanical analysis (DMA). The major difference is that in DRS the forces on the molecules originate from an electrical field while in DMA they originate from a mechanical field. Therefore information on relaxation mechanisms that are found by dielectric spectroscopy can be used to explain the relaxations that are found by DMA. A big advantage of DRS over DMA is the very wide frequency range of about 9 decades that can be applied. The wide frequency range makes it possible to study relaxation mechanisms in more detail. In addition, the high accuracy of the technique and the relative simplicity of doing experiments are advantageous.

At very high frequencies or at very low temperatures only the clouds of electrons around the atoms of the material are mobile enough to follow the alternating electric field without delay. The electric field elongates the electron clouds and separates the centres of gravity of the negatively charged electron clouds and the positively charged atomic cores. This creates induced dipoles in the material. These dipoles create an electric field that is directed opposite to the applied field. This effectively increases the dielectric constant of the material and is the origin of the high frequency dielectric constant ϵ_∞ .

Polar groups in a material have an associated permanent dipole moment. At low frequencies, these dipoles are mobile enough to rotate in the direction of the applied electric field, and thus increase the dielectric constant. At high frequencies, the dipoles are unable to follow the alternating electric field. Although the forces on the dipoles are relatively high in this stage, the displacements of the dipoles are extremely small and the net energy absorption (energy = force \times displacement) can be neglected. At very low frequencies, the dipoles will rotate more in the direction of the applied field. Now the displacement of the dipoles is relatively large but the frictional forces between the dipole and its neighbouring atoms is low because of the low rotation velocity of the dipoles. Again, the net energy absorption is very

small. Energy is only absorbed at intermediate frequencies where the dipoles experience frictional forces that cannot be neglected and will be displaced over some distance. The energy absorption is at a maximum at the typical relaxation frequency ω_m or equivalently, at the typical relaxation time τ_m . A much-used empirical equation to describe the frequency dependence of a relaxation mechanism is the Havriliak-Negami equation:

$$\epsilon^*(\omega) = \epsilon_\infty + \frac{\Delta\epsilon}{(1 + (i\omega\tau_m)^\alpha)^\beta} \quad 8.3)$$

where ω is the radial frequency and $\Delta\epsilon$ is the relaxation strength. α and β are shape parameters, α mainly determines the width of the transition and β the asymmetry. The shape parameters α and β usually are constrained to $0 < \alpha, \beta < 1$, however β might exceed 1, provided $\alpha, \beta \leq 1$.

In general, the frictional forces will be higher at a low temperature than at a high temperature. Accordingly, the relaxation time will increase at lower temperatures. The temperature dependence of local relaxation mechanisms can be described by the well-known Arrhenius equation:

$$\tau(T) = \tau_\infty e^{E_A/kT} \quad 8.4)$$

where T is the temperature, k is Boltzmann's constant, $\tau(T)$ the relaxation time of the transition and τ_∞ the shortest possible relaxation time (at $T \rightarrow \infty$), which for local motions is in the order of 10^{-13} s. The Arrhenius equation also defines the thermal activation energy of dipole rotation E_A . In general, the Arrhenius equation gives an accurate description of the dynamics of relaxation mechanisms that originate from local motions of the polymer chain. A single, temperature independent, activation energy is usually enough to characterise such transitions. By plotting the logarithm of the relaxation frequency of the ϵ'' maximum as a function of $1/T$, a straight line is obtained. E_A can be determined from the slope of this line.

Near the glass transition (α -transition) large parts of the polymer chain become mobile and the movement of the polymer-chain is no longer restricted to a local scale. The mobility is now determined by the amount of free volume in the polymer. Consequently, the relaxation time can no longer be described by the Arrhenius equation. The relaxation time is instead given by the Vogel-Fulcher-Tammann (VFT) equation:

$$\tau(T) = \tau_\infty e^{E_v/k(T-T_v)} \quad 8.5)$$

where E_v is the VFT activation energy and T_v the VFT temperature. The VFT equation will yield a curved line in an Arrhenius plot.

In general, the relaxation time of a transition is determined by the surroundings of a polymer chain. In a nanocomposite, not all polymer chains have the same surrounding. This creates a distribution of relaxation times that will widen the transition, or even add a separate maximum to the ϵ'' - ω curve. Widening of the relaxation distribution makes the determination of a characteristic relaxation time more uncertain. Detailed information on the mobility of the polymer chain can be obtained by an activation energy fine-structure analysis by means of differential sampling that was introduced by van Turnhout et al. [5-7]. This analysis assigns an activation energy to every point in the temperature-frequency plane, instead of only to the maximum of the ϵ'' - ω curve:

$$E_A(\omega, T) = -kT^2 \frac{\partial \varepsilon' / \partial T}{\partial \varepsilon' / \partial \ln \omega} \quad (8.6)$$

$E_A(\omega, T)$ represents the apparent activation energy of the most dominant relaxation process at radial frequency ω and temperature T . This analysis enables accurate determination of the fine structure of a distributed relaxation process.

The fine structure of the glass transition can also be analysed by this procedure. As was mentioned before, the relaxation time of the glass transition does not behave Arrhenius-like. An Arrhenius plot of the relaxation frequency versus the glass transition temperature yields a curved line. Therefore, it is impossible to assign a single (Arrhenius) activation energy to the glass transition. Instead, E_A gives a maximum in a plot of E_A versus T at constant ω . The location of this maximum corresponds with the glass transition temperature T_g . The value of $E_A(\text{max})$ is proportional to slope of the VFT curve in an Arrhenius plot. The slope of this line is expressed in the steepness index or the fragility parameter m , that can be determined from Eqn. 8.5 by taking the differential at $T=T_g$:

$$m = \frac{1}{T_g} \frac{d \ln(\tau)}{d(1/T)} = \frac{Ev}{k} \frac{T_g}{(T_g - Tv)^2} \quad (8.7)$$

The local activation energy $E_A(\omega, T)$ introduced by van Turnhout et al. [7] is also related to the amount of fractional free volume $f(\omega, T)$:

$$E_A(\omega, T) = kT^2 \frac{\alpha_f}{f(\omega, T)^2} \quad (8.8)$$

where α_f is the expansion coefficient of the material.

8.3 Experiments

8.3.1 Sample preparation

Experiments are performed on melt extruded PA6-nanocomposites containing between 0% and 20 wt% of organically modified clay. The melt extrusion of the nanocomposites is extensively described in Chapter 5 of this thesis. Prior to DRS measurements, the granules were compression moulded at 250 °C in plates of about 50 x 40 x 0.1 mm on a Fontijne laboratory press. Compression was performed in steps: 2 minutes at 0 kN and 250°C, 2 min at 10 kN and 250°C and 15 minutes at 180 kN while cooling down with an initial cooling rate of about 40°C/min. To assure good electrical contact the plates were coated with a Ø 35 mm layer of gold by using vapour deposition.

8.3.2 Dielectric measurements

Measurements of the dielectric constant ε' and the dielectric loss index ε'' are performed with a Novocontrol sample capacitor. For analysis of low frequency signals (0.1-1 kHz), a Schlumberger 1260 frequency response analyser (FRA) is used. The FRA applies an 1 V_{eff}

sinusoidal voltage to the upper plate of the sample capacitor. The response voltage of the lower plate is first amplified by a TNO build electrometer before it is analysed by the FRA. (TNO: Dutch Organisation for Applied Scientific Research). For analysis of high frequency signals (1 kHz-1 MHz) a Hewlett-Packard 4284A precision LCR-meter is used. This analyser applies a voltage of 1 V_{eff} to the upper plate of the sample cell and analyses the response voltage of the lower plate by an auto-balancing bridge method. The sample is heated with a flow of nitrogen gas, by a Novocontrol made cryostat.

Measurements are performed between -130 and 200 °C in steps of 5 °C. At every temperature, a frequency scan is performed at frequencies between 0.11 and 960000 Hz in steps of a factor 2 in frequency.

8.4 Results and discussion

Dielectric measurements of PA6 nanocomposites with 0, 5 and 20 wt% clay are plotted in Figs. 8.1 to 8.3. ϵ' is plotted on the left side (1a, 2a, 3a) and ϵ'' on the right side (1b, 2b, 3b).

To get an overall view of the effects of nanoclay on polymer mobility, the behaviour of ϵ' and ϵ'' is observed at low (0.11 Hz) and high frequencies (240 kHz). At 200 °C and 0.11 Hz, ϵ' is very high and is close to 10^4 . Here, the total polarisation of the samples is mainly caused by ionic polarisation. At 200 °C and 240 kHz, the dielectric constant is much lower and lies near 20. At low frequencies and high temperature, the ionic polarisation completely overshadows all other polarisation effects, while at high frequencies other polarisation mechanisms can still be distinguished.

8.4.1 Relaxation mechanisms

By going from high to low temperature, the first transition is found near 100°C at 0.11 Hz. The peak temperature of this transition strongly shifts to higher temperature as the frequency is increased, which is indicative of a low activation energy. At 240 kHz the peak lies well above 200 °C. The high strength of this transition and the fact that it is situated above the glass-transition indicate that this transition is due to electrode polarisation. This transition will be further referred to as the EP-transition. The position of this peak gives information about the mobility of ions in the polymer. This ionic mobility is related to the mobility of the polymer chains that surround the ions. Therefore, the EP-transition indirectly gives information on the mobility of the polymer chains.

In the neat polymer, the glass-transition is visible near 100 °C at 240 kHz. This transition will be referred to as the α_1 -transition. The glass transition shifts to lower temperatures as the frequency is decreased. The shift of the α_1 -transition is much smaller than the shift of the EP-peak. The α_1 -transition thus has a high activation energy. At 0.11 Hz it is very hard to distinguish the glass transition from the strong electrode polarisation.

In the nanocomposites with 5 and 20 wt% of clay (Figs. 8.2 and 8.3), the glass-transition is not as well defined as in the neat polymer. At 20 wt% and 240 kHz, no clear step is visible in ϵ' and no well-defined peak in ϵ'' . The glass-transition seems to be widened by the presence of nano-clay. Upon addition of clay, a new transition emerges near 10 °C. The temperature of this transition lies well below the glass transition temperature of the neat polymer. This peak will be referred to as the α_2 -transition. Below 0 °C, a secondary β -transition can be found that is too weak to be visible. It becomes very well visible though, by magnification of the graphs.

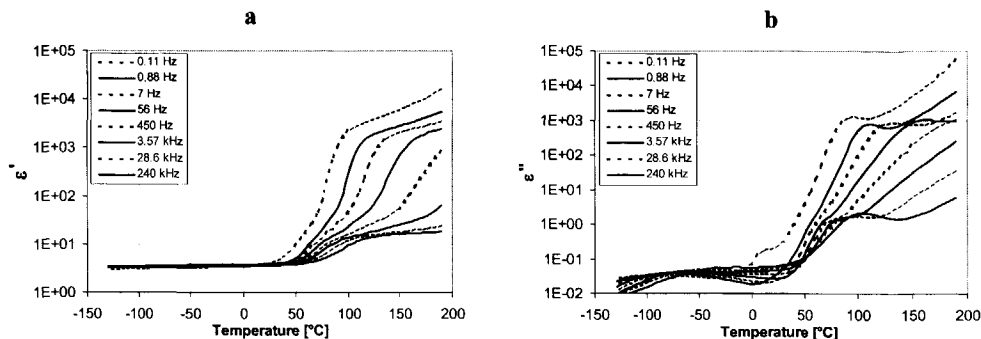


Figure 8.1 Dielectric constant ϵ' (1a) and loss index ϵ'' (1b) of PA6 with 0% clay

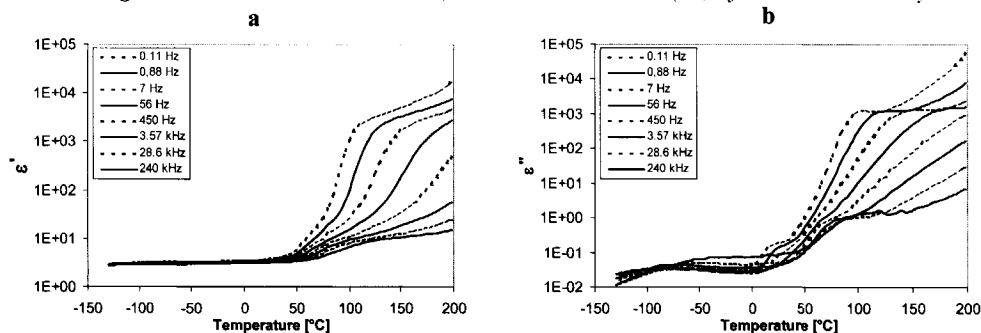


Figure 8.2 Dielectric constant ϵ' (2a) and loss index ϵ'' (2b) of PA6 with 5% clay

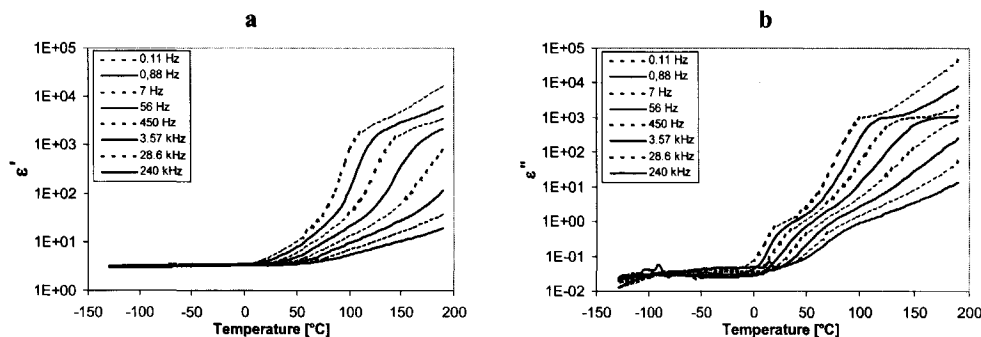


Figure 8.3 Dielectric constant ϵ' (3a) and loss index ϵ'' (3b) of PA6 with 20 % clay

An impression of the onset of the glass transition is obtained by observing at which temperature the dielectric constant is increased by 50% relative to the value at -130°C. The onset depends on frequency as can be seen in Figs. 8.1-8.3. At 0.88 Hz and 240 kHz, the onset of the glass transition of the unfilled sample is found at 50 °C and 75°C respectively. At 5 wt % the onset is found at 45°C and 75°C and at 20 wt% the onset lies at 30 °C and 85°C respectively. It can thus be concluded that, upon addition of clay, the onset shifts to lower temperatures at low frequency while it shifts to higher temperatures at high frequency. This is an indication for broadening of the glass transition. At 240 kHz, the dielectric loss index shows that the glass transition is much more pronounced in the unfilled sample than in the sample with 20 wt% of clay. At 20 wt% the glass transition is much more flattened. The loss

index also shows that at 5 and 20 wt% of clay a new transition emerges near 10 °C. It appears as if the glass transition is split in two separate transitions. To better distinguish the different relaxation mechanisms, $d\epsilon'/dT$ was calculated. $d\epsilon'/dT$ is closely related to ϵ'' [7]:

$$\frac{\partial \epsilon'(\omega, T)}{\partial T} \approx \frac{2E_A}{\pi k T^2} \epsilon''(\omega, T) \quad (8.9)$$

The virtue of $d\epsilon'/dT$ above ϵ'' is that the contributions of conductivity are not included in ϵ' . Peaks that are obscured by a strong conductivity are better visible this way. An other advantage of $d\epsilon'/dT$ is that it magnifies relaxations with a high activation energy, like the glass transition. In Fig. 8.4, $d\epsilon'/dT$ of all nanocomposites is plotted at 0.11 Hz and at 240 kHz. The α_1 and α_2 and EP peaks are clearly better separated than in the ϵ'' plot. The figure shows that the relaxation strength of the α_2 -transition systematically increases as the amount of clay is increased. At 0.11 Hz, the α_1 and α_2 relaxations can be distinguished separately, while at high frequencies only a single wide transition remains. The EP-transition is also well separated in Fig. 8.4.

The most striking effect in Fig. 8.4 is that a new α_2 -transition emerges near 10 °C when the concentration of clay is increased, while simultaneously the strength of the α_1 -transition decreases. As will be shown in Chapter 9 this low temperature glass transition is also found by dynamic mechanical analyses.

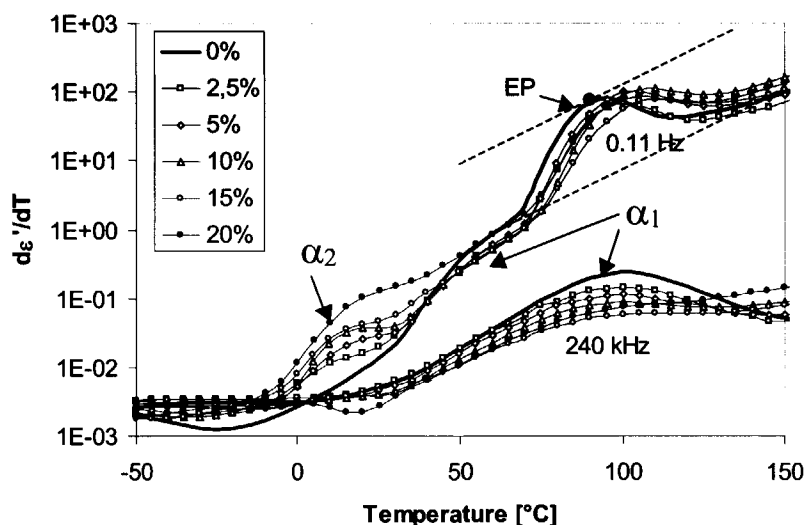


Figure 8.4 $d\epsilon'/dT$ of PA6 nanocomposites with 0-20 wt% of clay as a function of temperature. The glass-transition is better visible in $d\epsilon'/dT$ than in ϵ'' . The base line is drawn as a dotted line. The peak position is determined by the point of contact with the shifted base line, as is indicated in the graph. Note the emergence of a new α_2 glass transition near 10 °C.

It is attempted to determine the strengths and peak-temperatures of the α_1 and α_2 transitions by multiple regression of $\epsilon''(\omega, T)$. The frequency dependence was modelled by the Havriliak-Negami Eqn. 8.3) and the temperature dependence by the VFT-Eqn. 8.5).

Regrettably, the weak separation of the α_1 and α_2 peaks in an ε'' - T or ε'' - ω plot made an accurate determination of the position of the relaxation maxima impossible.

Therefore the position of the α_1 , α_2 and EP maxima are determined graphically from the plot of $d\varepsilon'/dT$ versus temperature. This was done by drawing a straight base line and subsequently shifting this baseline as indicated by the dotted lines in Fig. 8.4. The point of contact of the shifted baseline with the curve determines the position of the relaxation peak. The advantage of this procedure is that a peak position can be determined, even if the peak is only visible as a shoulder without a real maximum. A disadvantage of the procedure is that a systematic error is made this way and no information on the strength of the relaxation ($\Delta\varepsilon$) is obtained. The true maximum of the peak is a little higher than the maximum determined graphically.

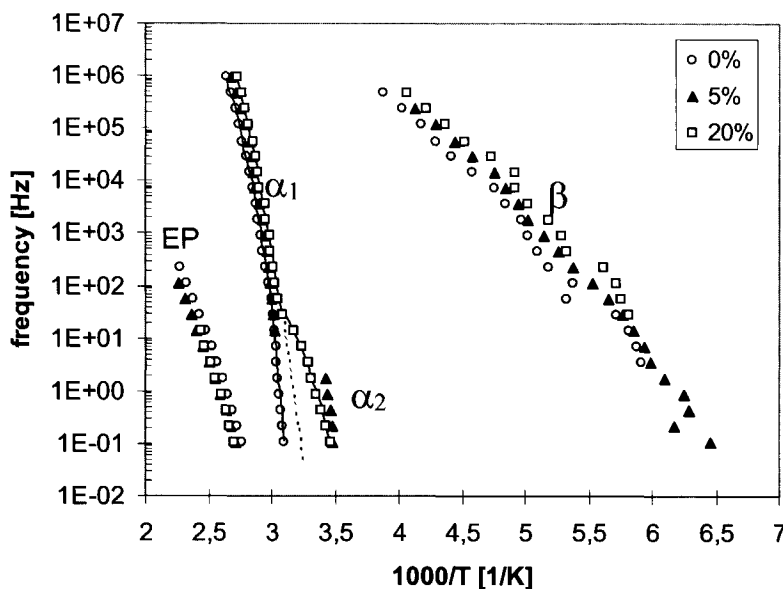


Figure 8.5 Arrhenius plot of the EP, α_1 , α_2 and β transitions in PA6 nanocomposites.

In Fig. 8.5 the β , α_1 , α_2 and EP transitions of the nanocomposites with 0, 5 and 20% of clay are plotted in an Arrhenius graph. From this graph, it can be seen that the effect of the clay on the position of the transition peaks is limited. It is remarkable that the EP-transition is not seriously shifted, because it was expected that the mobility of ions would be seriously hindered by the presence of the clay platelets.

Fig. 8.6 shows a magnification of the α_1 and α_2 transitions of a selected number of PA6-nanocomposites. The points represent the measured peak positions while the lines denote a VFT-fit through the measured points. The VFT parameters of the α_1 -transition that were determined by the fit are listed in Table 8.1.

Although the α_1 -curves in the Arrhenius plot, do not differ very much, the calculated VFT constants scatter much. No systematic change in the VFT-constants is noticed. Clearly, the error in the determination of the α_1 -peak positions is too large to obtain reliable VFT constants. The VFT-fits in Figs. 8.5 and 8.6 should therefore be considered as a guide to the eye.

% clay	0 (α_1)	2.5 (α_1)	5 (α_1)	10 (α_1)	15 (α_1)	20 (α_1)	20 (α_2)
$E_v/k, K$	1190	808	574	932	320	3573	756
$T_v, ^\circ C$	6.2	19.5	27	12.3	37	-49.9	-37.8
τ_v, sec	$1.2 \cdot 10^{-12}$	$1.1 \cdot 10^{-11}$	$7.2 \cdot 10^{-11}$	$2.4 \cdot 10^{-12}$	$9.8 \cdot 10^{-10}$	$2.6 \cdot 10^{-18}$	$9.2 \cdot 10^{-7}$
$T_g(d\epsilon'/dT \text{ 0.88Hz})$	45.5	48.5	49	44	-	33	7,5
$T_g(E_a-0.88Hz)$	44	45	45.5	46.5	51-59*	57.5	10

Table 8.1 Calculated VFT-constants of the glass transition of PA6-nanocomposites.

*Two maxima at 51 and 59 $^\circ C$.

Fig. 8.6 shows that the position of maximum $d\epsilon'/dT$ shifts to lower temperatures as the amount of clay is increased. The neat polymer only shows a single glass transition that is well described by a single set of VFT-constants. The nanocomposites all show a second glass transition that is separated from the 'normal' glass transition. At 20 wt% of clay it is impossible to separate the two transitions. By probing at a high frequency, the 'normal' α_1 -transition is found, at a temperature close to that of the neat polymer.

Probing at low frequencies does not give the normal α_1 -transition but instead gives a new α_2 -transition at a temperature far below the α_1 -transition. The presence of two separate glass-transitions indicates that the nanocomposites contain two separate polymer phases, one bulk polymer phase, and one confined polymer phase. In the nanocomposite with 20 wt % of clay the separation of these two phases is less obvious.

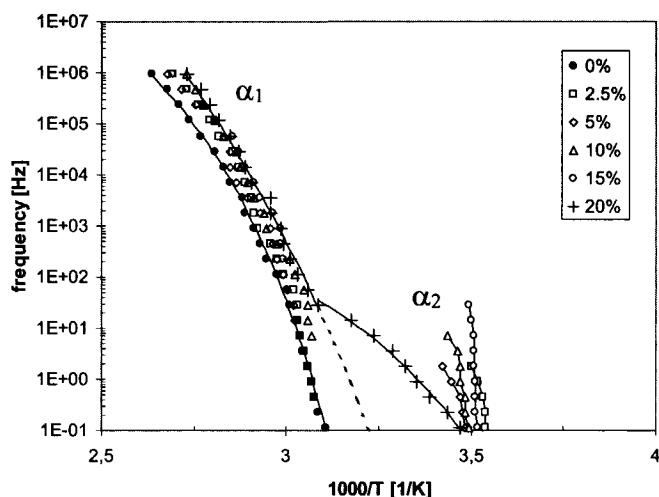


Figure 8.6 Arrhenius plot of the α_1 and α_2 transitions in PA6 nanocomposites.

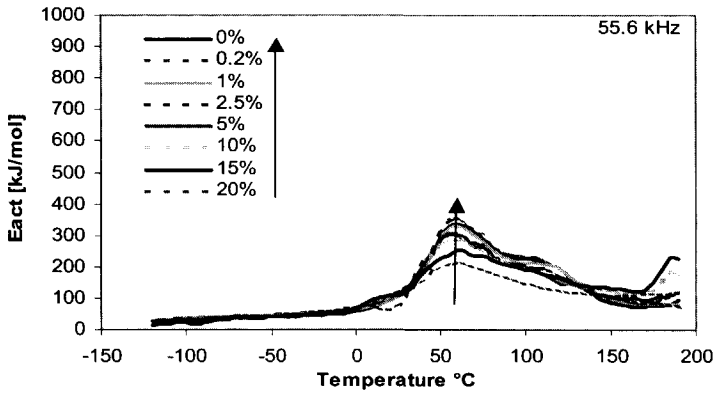


Figure 8.7 Activation energy fine-structure of PA6 nanocomposites as a function of temperature. Calculated at a frequency of 55.6 kHz.

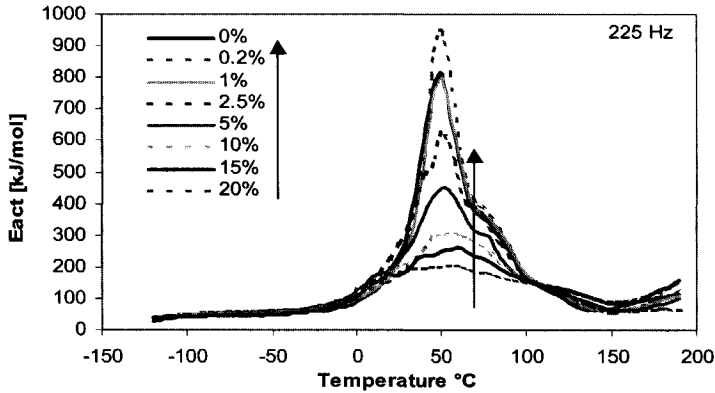


Figure 8.8 Activation energy fine-structure of PA6 nanocomposites as a function of temperature. Calculated at a frequency of 225 Hz.

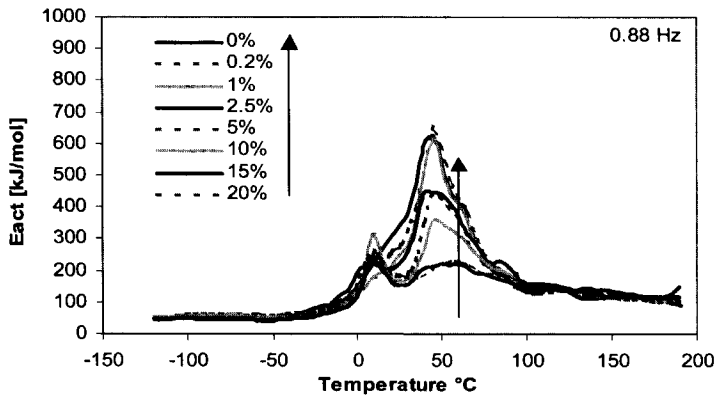


Figure 8.9 Activation energy fine-structure of PA6 nanocomposites as a function of temperature. Calculated at a frequency of 0.88 Hz.

8.4.2 Activation energy fine structure

Another way of studying relaxation mechanisms with dielectric spectroscopy is the activation energy fine structure analysis, based on differential sampling. From Eqn. 8.6 it is clear that this analysis relies on determination of $d\varepsilon'/dT$ and $d\varepsilon'/d\ln\omega$. This requires accurate determination of $\varepsilon'(\omega, T)$ at a low noise level. Figs. 8.7, 8.8 and 8.9 show the activation energy fine-structure of the PA6-nanocomposites at 55.6 kHz, 225 Hz and at 0.88 Hz. The local activation energy is calculated with Eqn. 8.6.

The curve maxima gradually decrease with increasing clay content. It is further evident that at low frequency the effect of clay on E_A is much more pronounced than at high frequency. By comparing the curves at 20 wt% of clay in the figures, it can be further concluded that at high clay content E_A is independent of frequency. Only at low frequencies, a second peak emerges near 10 °C. This peak is only found in samples with 2.5 wt% of clay or more. The temperature of maximum activation energy is indicative of the glass transition temperature and is listed in Table 8.1 (determined at 0.88 Hz). The fact that the this peak only occurs at low frequencies indicates that it concerns a slow process.

Let us first try to explain E_A at high frequencies. At high frequencies (Fig. 8.7) E_A is smaller than at low frequencies (Fig. 8.9), and the effect of clay on E_A is small. The cooperativity argument given by Anastasiadis [4] can explain these results. At high frequencies the characteristic length scale of cooperatively rearranging regions (ξ) is supposed to be smaller than at low frequencies. If the distance between the clay platelets (d) is larger than ξ , then the cooperative motion is relatively unhindered and the effect of clay is small. Furthermore, the activation energy of the cooperative motion is likely to be smaller for small groups of molecules than for large groups. This last argument explains why E_A is small at high frequencies.

The same arguments can be used to explain the results found at low frequencies. At low frequencies, E_A is strongly decreased by the addition of clay because the cooperative length in the nanocomposites is smaller than in the bulk polymer. To explain this, it is again supposed that the cooperative length of the bulk polymer (ξ_{bulk}) is smaller at high frequencies than at low frequencies. In a nanocomposite, the chains are confined and the cooperative length cannot exceed d : $\xi_{confined} \leq d$. If the frequency is sufficiently low, ξ_{bulk} becomes larger than $\xi_{confined}$. The smaller cooperative length in nanocomposites then lowers the activation energy.

At high clay contents the distance between the platelets is so small that $\xi_{confined} \leq \xi_{bulk}$ for all frequencies used. This would explain why, at 20 wt% E_A is insensitive to frequency.

By increasing the content of clay, a relaxation peak emerges near 10°C at low frequency (Fig. 8.9). At high frequencies (Fig. 8.7) or low amounts of clay, this peak is not present. The emergence of this peak corresponds with the low temperature α_2 -transition transition that was discussed before. Several explanations can be devised for the nature of this new transition. Possibly, a polymer phase is created near the surface of the clay that is confined in two dimensions. Only a limited number of polymer chains can be fitted in such a confined space. If the last polymer chain has entered the confined space, there might still be a lot of space left. This space is too small to allow another chain to enter the confined space, yet big enough to give the remaining chains a strongly increased free volume. This increased free volume would decrease the glass transition temperature.

Another explanation for the low-temperature relaxation peak is related to the plastication of the bulk polymer by the surfactant molecules on the surface of the clay. It is well known that mixing of polymers with low molecular molecules lowers the glass transition temperature T_g . The surfactant molecules are connected firmly to the clay surface and cannot

dissolve freely in the PA6 phase. Near the surface of the clay, an inter-phase will be formed with the ends of surfactant molecules being dissolved in PA6. This inter-phase will have a constant concentration of surfactant molecules that only depends on the surface density of surfactant molecules on the clay. It does not depend on the amount of organic modified clay added. The T_g of a mixture of a polymer and a surfactant can be estimated by the Fox equation:

$$\frac{1}{T_g} = \frac{w}{T_{g(\text{surfactant})}} + \frac{1-w}{T_{g(\text{polymer})}} \quad 8.10)$$

where w is the weight fraction of surfactant. The T_g of the surfactant molecules is about -60°C [8].

From Fig. 8.9 it follows that at 0.88Hz the T_g of the unfilled PA6 is about 44°C . By using the Fox equation it can be calculated that the concentration of surfactant molecules in this new inter-phase must be about 25 wt% to obtain a mixture T_g at 10°C . This is a reasonable concentration.

8.5 Conclusions

- It turns out that the glass transition is broadens by addition of clay.
- Arrhenius plots of the relaxation mechanisms of PA6-nanocomposites reveal that in PA6-nanocomposites a new glass transition is found well below the glass transition of neat PA6. The strength of this new transition increases as the amount of clay in the nanocomposite increases. The new transition is only found at low frequencies below 100 Hz indicating that it is a slow process. Evidence for this new transition was also found with dynamic mechanical measurements.
- It is suggested that at low contents of clay two separate phases are present in the nanocomposites, one bulk phase and one confined phase. The bulk phase behaves much like the neat polymer, while the confined phase causes the emergence of the second glass transition.
- Two mechanisms are suggested to explain the emergence of the low temperature glass transition:
 - Increase in free volume due to packing constraints in the confined space between clay layers.
 - Mixing between the surfactant molecules and the PA6 molecules near the clay surface.
- Confinement is a relative notion. At high frequencies near 100 kHz, the polymer does not experience any confinement because most motion occurs at a scale much smaller than the distance between the clay platelets. Confinement is only experienced at low frequencies if the characteristic length scale of cooperatively rearranging regions exceeds the distance between the platelets. At this point, the activation energy of the nanocomposite becomes lower than the activation energy of the bulk polymer.

8.6 References

- [1] S. H. Anastasiadis, K. Karatasos, G. Vlachos, E. Manias and E.P. Giannelis, *Confinement effects on the local motion in nanocomposites*, Mat. Res. Soc. Symp. Proc. **543**, 1999, p 125-130.
- [2] S. H. Anastasiadis, K. Karatasos, G. Vlachos, E. Manias, E.P. Giannelis, *Local dynamics under severe confinement in nanocomposites*, Pol. Mat. Sci. Eng. **82**, 2000, p 211-212.
- [3] E. Manias, D.B. Zax, S.H. Anastasiadis, *Polymer/silicate intercalated nanocomposites: confinement induced segmental dynamics in 2nm slits*, Pol. Mat. Sci. Eng. **82**, 2000, p 259-260.
- [4] S. H. Anastasiadis, K. Karatasos, G. Vlachos, E. Manias, E.P. Giannelis, *Nanosopic-confinement effects on local dynamics*, Phys. Rev. Let. **84(2)**, 2000, p 915-918.
- [5] P. A. M. Steeman, J. van Turnhout, *Fine structure in the parameters of dielectric and viscoelastic relaxations*, Macromolecules **27**, 1994, p 5421-5427.
- [6] M. Wübbenhorst, J. van Turnhout, *Analysis of dielectric spectra by means of differential sampling and three-dimensional modeling*, J. Non-Cryst. Sol., 2001, to be published.
- [7] J. van Turnhout, *Elektrische eigenschappen van kunststoffen*, in, *Kunststoffen 1986 Terugblik en Toekomst*, Ed. Brüggeman, Wijt, Rotterdam, the Netherlands, 1986, p 285-295.
- [8] D. Ellul, *Novel low temperature resistant thermoplastic elastomers for specialty applications*, Plast. Rubber Comp. Proc. Appl. **26(3)**, 1997, p 137.

Mechanical properties of nanocomposites

Abstract

This chapter discusses the stiffness and thermal expansion of PA6-clay and PE-clay nanocomposites. These properties are compared with the properties of polymer-mica micro composites and with the properties that are predicted by the composite models introduced in Chapter 3. The stiffness of both PA6-clay and PE-clay nanocomposites is measured by dynamic mechanical thermal analysis (DMA) and by tensile testing.

Both types of nanocomposites become more rigid by increasing the amount of clay or the aspect ratio of the clay. At low contents of clay (< 5 wt% silicate), the experimental stiffness of nanocomposites corresponds to the stiffness of polymer-mica micro-composites and to the stiffness predicted by composite models. The stiffness of nanocomposites with more than 10 weight percent of clay is lower than that of corresponding polymer-mica micro-composites. At these loadings, composite models overestimate the stiffness of polymer-clay nanocomposites.

The measurements and calculations show that the high stiffness of nano composites mainly originates from the high aspect ratio and not from the small size of the clay platelets.

At high loadings of clay, the polymer chains become severely confined between the clay layers. In contrast with general expectations, this confinement increases the mobility of the polymer chains. This increased mobility of the polymer chains is thought to be an important reason for the relatively low reinforcement at high clay loading. Low crystal perfection of the polymer matrix and imperfect exfoliation of clay platelets also contribute to the low stiffness at high clay loadings.

By inverse use of composite modelling the effective aspect ratio and the effective stiffness of the PA6-matrix inside a PA6-clay nanocomposite is calculated. It is shown that at high loadings the effective aspect ratio becomes decreases while simultaneously the glass transition of the PA6 matrix inside the PA6-clay nanocomposites broadens.

9.1 Viscoelastic properties of compression moulded PA6 nanocomposites

9.1.1 Preparation of samples and experimental technique

The preparation of melt extruded PA6-nanocomposites was discussed extensively in Chapter 5. Before DMA measurements the extruded nanocomposite pellets were compression moulded into sheets of about 50 x 40 x 0,1 mm at 250°C on a Fontijne laboratory press. Compression was performed in steps: 2 minutes at 0 kN and 250°C, 2 min at 10 kN and 250°C and 15 min at 180 kN while cooling down with an initial cooling rate of about 40°C/min. Prior to testing, strips of 50 x 2 x 0.1 mm were punched out of the compression moulded sheets. The thickness of the strips was measured with an accuracy of 1 µm using a Heidenhahn MT30B film thickness apparatus. The width of the film was determined with an accuracy of about 5 µm by using a Mitutoyo toolmakers microscope TM-101.

The clamped length of the sample was about 22 mm and was measured with an accuracy of about 0.5 mm by using a simple ruler. The storage modulus E' and the loss modulus E'' are determined in a temperature range between -120 °C and 250 °C using a Rheometrics Solid Analyser (RSA) at a frequency of 1 Hz, a static strain of 0.3% and a strain amplitude of 0.2%.

9.1.2 DMA results

Figs. 9.1 and 9.2 show DMA measurements on PA6-nanocomposites containing between 0 and 20 wt% silicate. Data at -100, 23 and 125°C are listed in Table 9.1 and plotted in Figs. 9.3 and 9.4. From Fig. 9.1 it can be seen that at 0.2 wt% of silicate the stiffness is clearly increased compared to the stiffness of the unfilled PA6. Above the glass transition the increased stiffness is more apparent than below. Between 0.2 and 10 wt% of clay the stiffness increases continuously. Above 10 wt% the increase becomes smaller than below 10 wt%.

wt %	vol %	Tg °C	-100°C			23°C			125 °C		
			E-exp	E-theory		E-exp	E-theory		E-exp	E-theory	
				unidir	random		unidir	random		unidir	random
			GPa	GPa	GPa	GPa	GPa	GPa	GPa	GPa	GPa
0	0	63	3.37	3.37	3.37	2.63	2.63	2.63	0.41	0.41	0.41
0.2	0.09	60	3.48	3.48	3.48	2.86	2.86	2.86	0.63	0.63	0.63
1.0	0.43	61	3.89	3.82	3.61	3.21	3.17	2.99	0.75	0.74	0.68
2.5	1.08	58	4.36	4.46	3.89	3.71	3.76	3.25	0.91	0.97	0.78
5	2.19	61	4.59	5.57	4.36	3.93	4.78	3.68	1.14	1.35	0.94
10	4.52	62	5.44	7.92	5.3	4.66	6.95	4.55	1.35	2.19	1.28
15	6.99	68	6.54	10.5	6.27	5.12	9.30	5.44	1.55	3.11	1.62
20	9.62	82	6.74	13.2	7.24	5.27	11.9	6.35	1.68	4.13	1.98

Table 9.1 Measured and theoretical stiffness of compression moulded PA6/clay nanocomposites as a function of clay content at -100°C, 23°C and 125°C.

Above 10 weight % of clay, the glass transition peak of the loss modulus E'' in Fig. 9.2 starts to shift to higher temperatures. Table 9.1 lists the position of the glass transition temperature T_g . At 20 wt% clay the glass transition temperature is shifted by about 20°C compared to the unfilled PA6.

Near 150 °C a relaxation mechanism is emerging at high clay content. This relaxation mechanism might be caused by hindered PA6-chains close to the clay platelets. Also near 10 °C, a new transition emerges. The position of this transition coincides with the α_2 -transition found with dielectric spectroscopy in Chapter 8. It is assigned to the highly mobile phase in the inter-galleries of clay at some distance from the clay's surface.

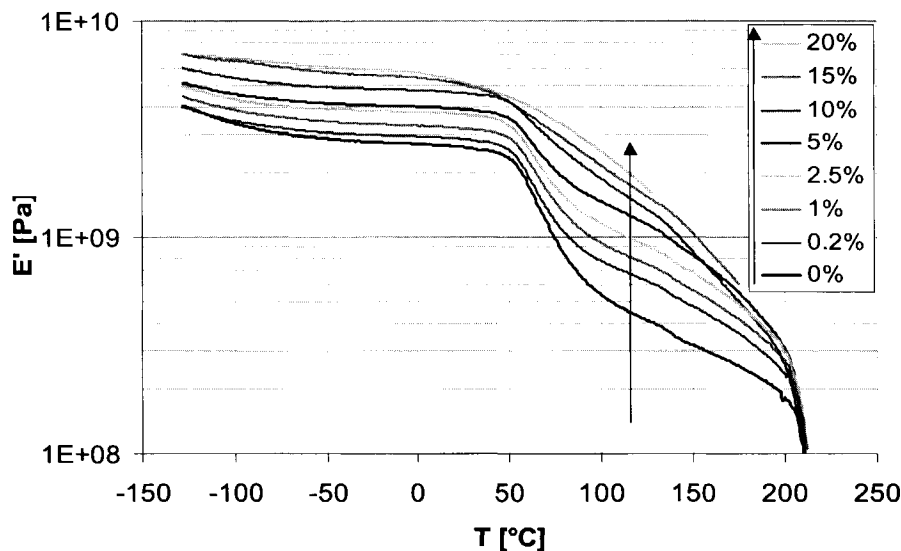


Figure 9.1 1 Hz storage Young's modulus of PA6-clay nanocomposites containing between 0 and 20 weight% of silicate.

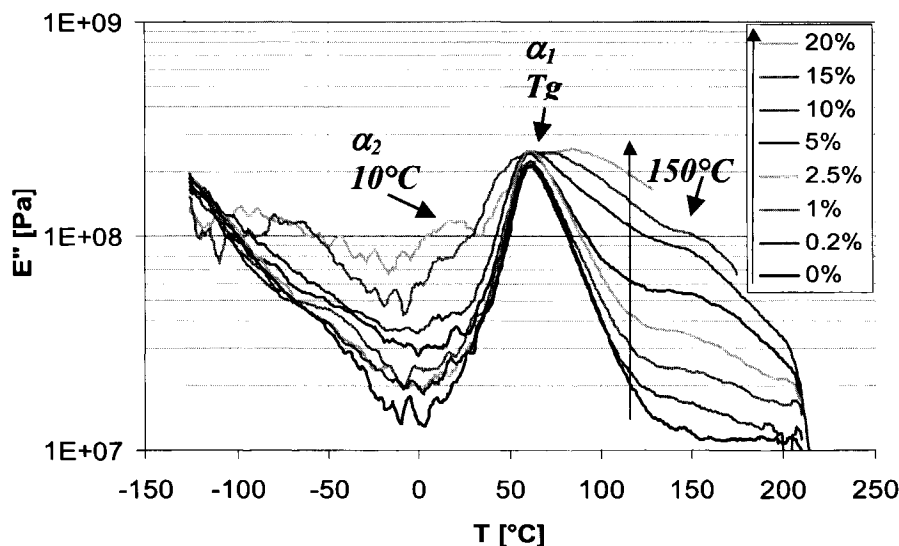


Figure 9.2 1 Hz loss Young's modulus of PA6-clay nanocomposites containing between 0 and 20-weight% of silicate. Note the emergence of two new transitions near 10 °C and 150 °C.

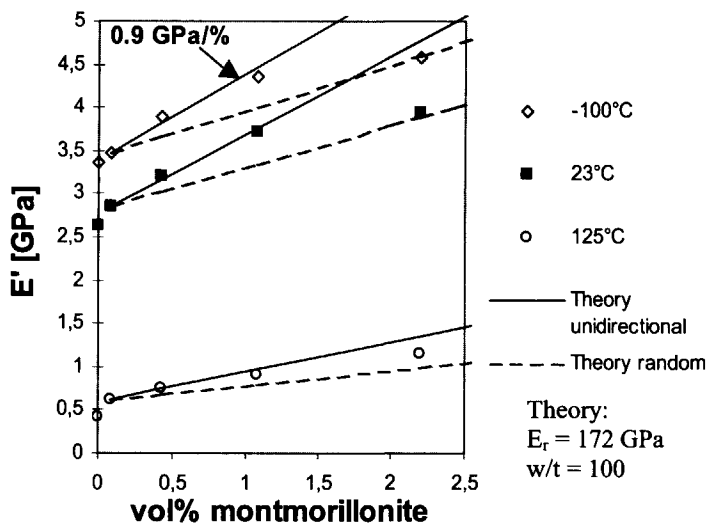


Figure 9.3 In plane stiffness of compression moulded PA6/clay nanocomposites as a function of clay content at -100°C , 23°C and 125°C . Symbols represent experimental values and lines represent composite calculations for unidirectional (—) and random (---) reinforced composites

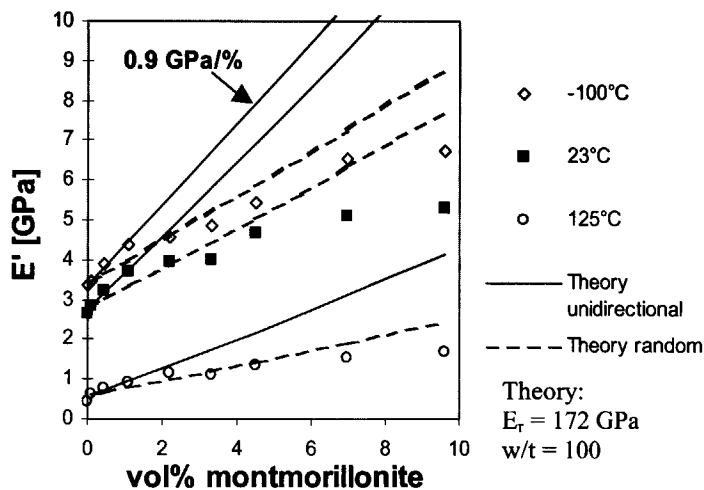


Figure 9.4 As figure 9.3 but plotted up to higher clay contents.

For a better comparison of results, the data on PA6-nanocomposites are re-plotted as E' versus clay content in Figs. 9.3 and 9.4. In both figures also the Halpin-Tsai predictions for platelet reinforcement ($\zeta = 2/3 w/t$) are plotted using a clay Young's modulus of 172 GPa and an aspect ratio of 100, as was estimated from TEM pictures in Figs. 6.1 and 6.2.

To account for the changes in matrix properties due to nucleation of the crystalline structure, calculations were performed using the stiffness of the nanocomposite with 0.2wt% clay as the stiffness of the matrix (E_m). Composite calculations for unidirectional orientation, accurately predict the experimental results at 1 and 2.5 wt% clay at all temperatures, as can be seen in Fig. 9.3. At these concentrations the efficiency of the clay to stiffen the PA6 is 0.9 GPa per volume percent of silicate added. This compares well with the 1.3 GPa/vol.% of polymer-mica micro-composites that were shown in Chapter 4, Fig. 4.1.

Above 2.5 wt% the unidirectional composite model predicts higher values than found experimentally, while the random composite model gives better predictions. At 15 and 20wt%, experimental values are even lower than predicted by the random composite model. Clearly the stiffness of the PA6 nanocomposites cannot be explained over the whole range of loadings tested, by assuming that the platelets are perfectly oriented and have an invariable Young's modulus and aspect ratio.

Several features might be responsible for the low effectiveness of nanoclay at high loadings. As can be concluded from TEM analysis in Figs. 6.1-6.7, the morphology at high loadings is different from the morphology at low loading. Clearly visible is the lower macroscopic orientation at high loading that will lead to lower stiffness as was discussed in Chapter 3.

Another morphological feature that might contribute to the lower stiffness is the grouping of platelets on a local microscopic scale as can be observed from TEM pictures. This grouping resembles the nematic ordering of polymer chains in a liquid crystalline polymer. On a local scale the platelets are highly ordered, but on a macroscopic scale the ordering is low or absent. It is difficult to transmit stresses from one localised group to another because the amount of overlapping platelets between localised groups is low. It is anticipated that the grouping of particles and the lack of overlap lead to a lower stiffness of the nanocomposite.

Further the high mobility of the confined polymer chains inside the clay galleries, as was found with NMR and DRS, will also decrease the stiffness of the PA6-clay nanocomposites.

9.1.2.1 Composite modelling of the DMA curve of PA6 nanocomposites

To find the reason for the low reinforcing effect of the clay at high loading, it is attempted to use composite modelling to fit the whole DMA curve. The model used is the Halpin-Tsai model modified for platelets ($\zeta=2/3 \text{ } \mu\text{t}$) as was introduced in Chapter 3. In order to calculate the loss modulus, the Halpin-Tsai equation was written as a complex equation by replacing every (real) modulus by its complex counterpart (E becomes $E'+iE''$). In doing so not only E' can be predicted but also E'' .

To account for the orientation of the platelets either perfect unidirectional or random orientation was assumed. To calculate the random stiffness, the simplified equation ($\langle E \rangle_{3D} = 0.49E_{//} + 0.51E_{\perp}$) for random orientation is used, as is explained in Chapter 3 of this thesis. This equation requires knowledge of the parallel ($E_{//}$) and perpendicular (E_{\perp}) moduli of the perfect oriented composite, which can be calculated with the modified Halpin-Tsai equations. TEM pictures in Figs. 6.1-6.7 show that at low clay loadings the compression moulded nanocomposites are mainly uniaxially oriented (1-5 wt% of clay). No preferred orientation is found at a clay loading of 10 wt% and above. For this reason the samples at 1 to 5 wt% of clay are fitted by assuming perfect uni-axial orientation, while samples with a clay loading of 10 wt% and above are fitted by assuming random orientation.

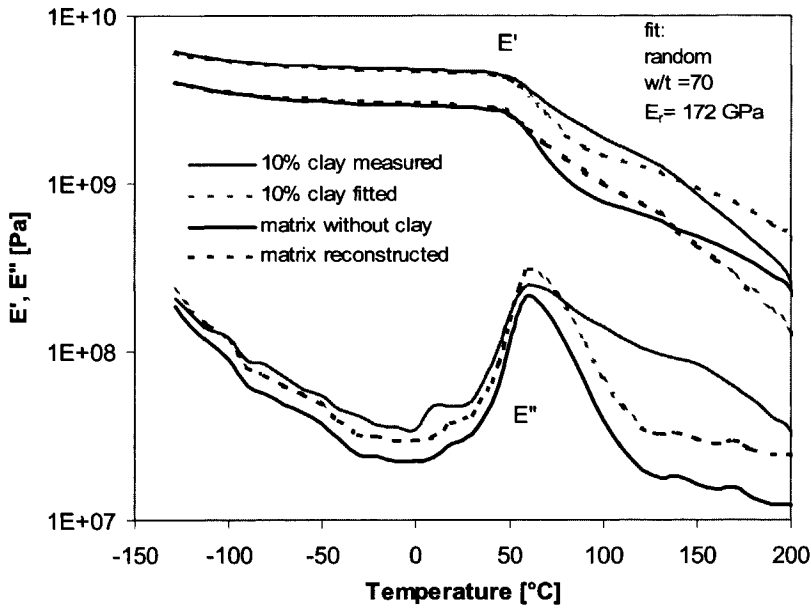


Figure 9.5 Example of a complex Halpin-Tsai fit to the DMA measurement of a PA6-nanocomposite with 10 wt% of clay. Modelling (dotted grey line) gives rather good predictions below the glass transition. Above the glass transition modelling only gives a crude estimate of E' , while the estimate for E'' is much too low. The reconstructed effective matrix storage and loss moduli inside the nanocomposite are given by a dotted black line.

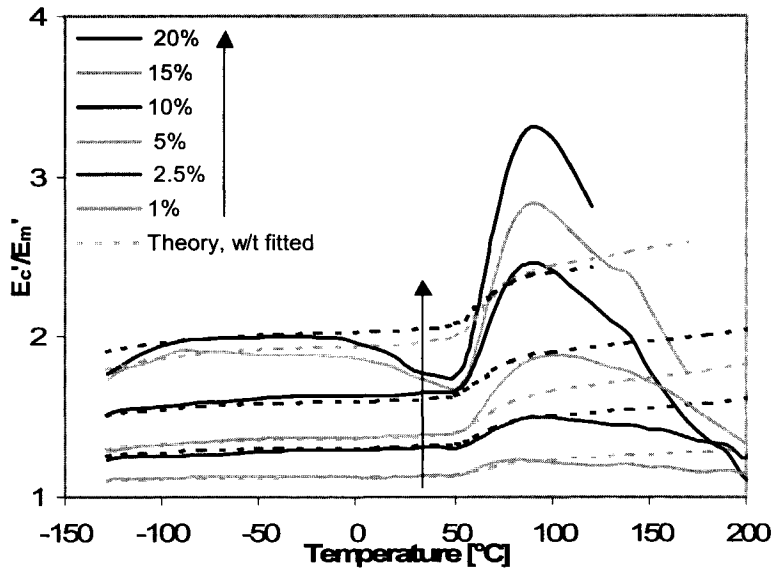


Figure 9.6 Relative Young's modulus E_c/E_m of PA6 nanocomposites as a function of temperature. The Halpin-Tsai equations are fitted to the measurements below the glass transition by adjusting the aspect ratio of the platelets. Modelling fails to predict the large jump near the glass transition.

Fig. 9.5 shows an example of such a fit of E' and E'' for a PA6 nanocomposite with 10 wt% of clay. Below the glass-transition temperature the storage modulus E' and the loss modulus E'' are fitted accurately. Above 50 °C the Halpin-Tsai model gives a crude estimate of the storage modulus, but fails to predict the loss modulus. The measurements show that the transition near 150 °C cannot be predicted. This transition is introduced in the polymer by the clay platelets.

In Fig. 9.6 the ratio of Young's moduli of the nano-composites and the polymer matrix E_c'/E_m' are plotted as a function of temperature. In this graph, the differences between the nanocomposites and the polymer matrix are magnified. It is attempted to fit the Halpin-Tsai equation to the measurements by adapting the aspect ratio of the clay platelets, while keeping the stiffness of the clay platelets constant at 172 GPa. The stiffness of the clay platelets is assumed to be the same as the stiffness of a pure mica crystal [1]. The aspect ratio is adapted such that the fit is perfect at low temperature. The parameters used to fit the measurements are given in Table 9.2.

It is remarkable that the apparent aspect ratio of the clay platelets decreases continuously as the amount of clay increases. A lower apparent aspect ratio does not necessarily mean that the platelets themselves have a lower aspect ratio. As two platelets form a tactoid, the aspect ratio of the tactoid is smaller than that of the individual the platelets. Mechanically, it is the aspect ratio of the tactoid that counts. *So poor exfoliation of platelets will result in a lower effective aspect ratio.* Apparently, tactoids with a few platelets are formed at high clay loading, which lowers the effective aspect ratio of the clay. This is qualitatively confirmed by TEM measurements in Chapter 6, which show tactoids of 2-3 platelets at high clay concentrations.

clay wt%	vol%	w/t fitted	orientation
1.0	0.428	150	unidirectional
2.5	1.08	100	unidirectional
5	2.19	40	unidirectional
10	4.52	70	Random
15	6.99	70	Random
20	9.62	43	Random

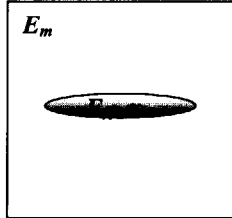
Table 9.2 Parameters used to fit the DMA curves of PA6-nanocomposites

As can be seen in Fig. 9.6 the fit is good up to 75 °C, at a clay loading of 1 wt% and 2.5 wt%. The jump in E_c'/E_m' at 50 °C is predicted correctly for these samples. At loadings above 2.5 wt % clay, the magnitude of the jump near 50 °C is not predicted correctly. Above 10 % of clay the fit is poor over the whole range of temperatures. At 15 wt% and 20 wt% the measurements show a minimum in the E_c'/E_m' curve just before the glass transition. This minimum is not predicted by the composite model. It is probably a consequence of the shift in the glass transition at high clay loading as was indicated in table 9.1.

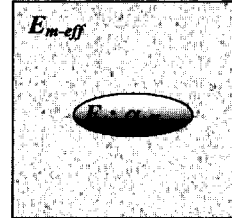
Apparently, some features in the DMA curve cannot be explained by the simple reinforcing effect of the clay platelets. For some reason, the stiffness of the polymer matrix is changed by the presence of the clay platelets. The largest changes in polymer properties are found at high loadings of clay.

Composite models make use of the properties of the unchanged phases to predict the properties of the ensemble. Therefore, the failure to predict the composite stiffness at high loading is due to a *change in the properties of the matrix polymer*. It is interesting to find out what effect the clay platelets have on the properties of the polymer matrix. It is possible to reconstruct these properties by using the measured stiffness of the nanocomposite. The properties of the polymer matrix inside the nanocomposite are reconstructed by following the

same fit procedure as described above. Additionally, the properties of the matrix are adjusted at every temperature, such that the fit is perfect over the whole temperature range. This procedure is elucidated in Fig. 9.7a. The so obtained matrix stiffness is a good estimate of the stiffness of the polymer matrix inside the nanocomposite. The reconstructed storage moduli and loss moduli of the PA6 matrix inside the PA6 nanocomposites are plotted in Fig. 9.7b.



Usual modelling:
 $E_c = f(c_r, \alpha, E_m, E_r)$



New approach:
 $E_c = f(c_r, \alpha_{eff}, E_{m-eff}, E_r)$

Figure 9.7a By using 'inverse' modelling it is possible to calculate the effective aspect ratio α_{eff} and the effective matrix modulus E_{m-eff} inside a (highly loaded) nanocomposite.

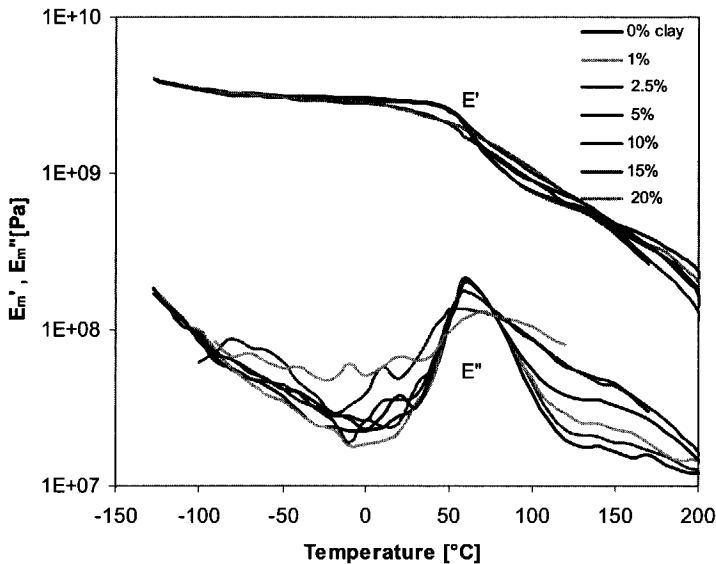


Figure 9.7b Reconstructed effective storage and loss moduli of the PA6 matrix polymer inside the PA6-nanocomposites

Fig. 9.7b shows that the glass transition of the polymer matrix broadens as the amount of clay increases. The broadening can be observed at the low temperature side as well as at the high temperature side of the glass transition. Broadening at the low temperature side implies that some polymer chains experience an increased mobility while at the high temperature side it implies that polymer chains experience a decreased mobility. These findings agree with the findings of solid state NMR in Chapter 6 and of dielectric spectroscopy in Chapter 8. As a result of this, the stiffness of the PA6 matrix in the nanocomposites is different from the stiffness of unfilled PA6. Below the glass transition, this

stiffness is decreased and above the glass transition, it is increased. At 20 wt% of clay, the loss modulus starts to deviate from the unfilled matrix already near -100°C . The increase in loss modulus is accompanied by a small decrease in storage modulus.

A possible explanation for the mechanical behaviour of the polymer matrix inside the nanocomposites can be found by considering the mechanisms that cause the glass transition. The glass transition is caused by large-scale cooperative motion of large parts of polymer chains as was concluded from dielectric spectroscopy in Chapter 8. The cooperative motion is activated by the presence of free volume between the polymer chains. The polymer chains will experience the glass transition if the amount of free volume is large enough to allow large scale cooperative motion.

In nanocomposites, polymer chains are confined on a molecular scale between hard clay platelets. This fixes the free volume of polymer chains between the platelets. Usually the free volume increases as the temperature increases. Due to the fixation of the free volume, such increase is no longer possible. The hypothesis is that below the glass transition the fixed free volume of the confined chains is higher than that of polymer chains in an unfilled polymer, while above the glass transition it is smaller. This leads to a decreased stiffness below the glass transition and an increased stiffness above the glass transition.

This hypothesis is in perfect agreement with the findings of Krishnamoorti et al. [2]. Using NMR and molecular dynamics, Krishnamoorti observed a slow and a fast mode in PEO-clay nanocomposites. The fast mode corresponds to polymer segments far away from the clay surface while the slow mode (whose slowing down depends on the strength of the surface interaction) corresponds to the polymer segments close to the clay surface. The hypothesis is also in good agreement with the solid state NMR results of Chapter 6 that proved the existence of a highly mobile phase in the nanocomposites below the glass transition temperature. Dielectric measurements in Chapter 8 confirm broadening of the glass transition and are also in agreement with the DMA data.

Due to the extra transition near 150°C the stiffness of the PA6 matrix in the nanocomposites drops below the stiffness of the unfilled PA6. It is thought that the transition at 150°C is a consequence of the imperfect crystalline structure of the nanocomposites. The imperfect crystalline structure of the PA6 in the nanocomposites was experimentally proven in Chapter 7 of this thesis, where this subject is studied in more detail.

9.2 Mechanical properties of injection moulded PA6-nanocomposites

PA6 nanocomposites with 0-7.5 wt% montmorillonite were injection moulded on a $\varnothing 30\text{mm}$ Engel 80A injection moulding machine at 100 rpm. The melt temperature was 283°C and the mould-temperature 85°C . The raw materials were dried overnight at 110°C in vacuum prior to injection moulding.

To test the flexural modulus, thermal expansion and mould shrinkage, plates of $80 \times 80 \times 3.2\text{ mm}$ were injection moulded. For the tensile test, dog bone shaped samples were injection moulded. The prismatic part of the tensile samples had dimensions: $60 \times 10 \times 4.2\text{ mm}$. In order to test for anisotropy, samples of $80 \times 10 \times 3.2\text{ mm}$ were cut out of the $80 \times 80 \times 3.2\text{ mm}$ plates, in directions parallel and perpendicular to the injection moulding direction. The samples are tested for thermal expansion and flexural modulus under dry and under water saturated conditions. To saturate the samples, they were stored at 70°C and 68% relative humidity for at least 1000 hours. More details on water absorption in the PA6-nanocomposites can be found in Chapter 10.

The expansion coefficient is determined between -30°C and $+30^{\circ}\text{C}$ according to ASTM D692 T2. The flexural modulus is determined at 23°C according to ISO 178 A. The

tensile modulus is determined between 0.05 and 0.25% strain according to DIN-53457 at 23 °C and 5 mm/min. Toughness was determined by IZOD tests at room temperature on injection moulded notched bars of 8 mm in width and 4 mm in thickness.

Table 9.3 shows the results of the measurements. The difference in parallel and perpendicular Young's modulus is small for all clay loadings tested. It can thus be concluded that the anisotropy of the injection-moulded plates is small. The anisotropy increases a little at increasing content of clay. Although the differences are small, the parallel stiffness is consistently higher than the perpendicular stiffness. Consequently in the parallel direction the expansion coefficient and the mould shrinkage are a little smaller than in the perpendicular direction. For modelling purposes the samples are considered to be isotropic in the plane of the plate. The fact that the properties are nearly isotropic in the plane of the plate does not mean that they are isotropic in 3 dimensions. It is likely that the platelets are oriented in the plane of the plate.

9.2.1 Flexural and tensile modulus of injection moulded PA6 nanocomposites.

Table 9.3 lists the tensile and flexural properties of dry and wet, injection moulded PA6 nanocomposites. As a comparison also the stiffnesses measured by DMA at 23 °C are listed.

Test	Norm	Units	weight% clay					
			0	0.2	1	2.5	5	7.5
Dry as moulded								
Tensile modulus (23°C)	ISO 527/1A	GPa	3.29	3.41	3.72	4.22	5.04	5.41
Yield Stress (23°C)	ISO 527/1A	GPa	80.2	81.4	86.4	88.6	-	-
Yield strain	ISO 527/1A	%	3.54	3.55	3.48	3.19	-	-
Flexural modulus // (23°C)	ISO 178 A	GPa	3.19	3.25	3.43	4.01	4.78	5.50
Flexural modulus ⊥ (23°C)	ISO 178 A	GPa	3.20	3.24	3.41	3.84	4.50	5.38
E' DMA		GPa	2.63	2.86	3.21	3.71	3.93	4.01
Thermal expansion // -30-+30°C	ASTM D696 T2	10 ⁻⁵ /K	7.01	6.9	6.55	6.11	5.95	5.45
Thermal expansion ⊥ -30-+30°C	ASTM D696 T2	10 ⁻⁵ /K	7.44	7.28	7.38	6.23	6.2	5.46
Mould shrinkage //	ISO 2577	%	1.60	1.50	1.37	1.28	1.12	1.06
Mould shrinkage ⊥	ISO 2577	%	1.88	1.85	1.83	1.71	1.48	1.35
Izod notched	ISO-180	kJ/m ²	3.23	3.33	3.52	3.52	4.05	4.08
Conditioned								
Tensile modulus (23°C)	ISO 527/1A	GPa	0.990	1.04	1.26	1.61	2.1	2.56
Flexural modulus // (23°C)	ISO 178 A	GPa	0.935	0.999	1.17	1.48	1.95	2.38
Flexural modulus ⊥ (23°C)	ISO 178 A	GPa	0.909	0.947	1.08	1.32	1.75	2.31
Thermal expansion // -30-+30°C	ASTM D696 T2	10 ⁻⁵ /K	9.31	9.6	8.58	7.8	7.12	6.03
Izod notched	ISO-180	kJ/m ²	2.50	3.51	2.99	1.89	1.62	1.63
H ₂ O saturation concentration		%	3.6	3.5	3.4	3.5	3.6	3.5

Table 9.3 Stiffness, thermal expansion coefficient and mould-shrinkage of injection moulded PA6 nanocomposites

Fig. 9.8 shows the Young's moduli as a function of clay loading. As expected, the dry samples are stiffer than the wet samples. In most cases the tensile modulus is a little higher than the flexural modulus. Probably the tensile samples are oriented more perfectly.

Surprisingly the Young's moduli of the injection-moulded samples do not level off above 5% loading as the DMA samples do. A possible explanation for this discrepancy might be found in the preparation of the samples. During compression moulding the DMA samples undergo a long melt step during which no mechanical mixing takes place. So, during compression moulding the clay might demix. In contrast, during injection moulding the samples stay in the melt phase for a much shorter time and are vigorously sheared. Therefore it is probable that during injection moulding the clay cannot demix, because the melt is sheared continuously and the time for demixing is short.

H. Fischer [3] showed that exfoliated clay can indeed demix and become intercalated again. X-ray analysis on exfoliated PE and IPP nanocomposites during melting showed the appearance of a d_{001} peak, which is typical for intercalated clay platelets. He argued that nanocomposites, that are exfoliated by melt extrusion, do not necessarily are in thermodynamic equilibrium. Mechanical shearing can be enough to separate the clay layers, even if this is not the thermodynamically favoured state. Given enough time the clay will demix if the melt is left without shear.

The quaternary ammonium salt used to modify the clay of the PA6 nanocomposites has paraffinic chains with low polarity. During the course of this research it was recognised that this kind of modified clay needs more shear to exfoliate in PA6 than clay that is modified with more polar groups. So it is very well possible that the clay used indeed tends to demix during compression moulding.

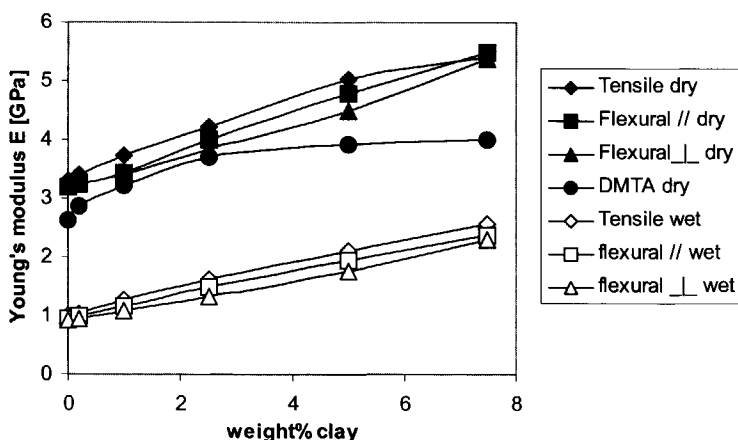


Figure 9.8 Young's modulus of dry and wet PA6 nanocomposites measured by different techniques and made by different preparation techniques.

9.2.2 Yield stress and toughness of PA6-nanocomposites

Although properties like yield stress and toughness do not fall within the scope of this thesis, their values are given in table 9.3. Figure 9.9 shows the stress strain tests on the dry and wet ($\approx 3.5\%$ water) PA6 nanocomposites. The figure clearly shows the low stiffness of conditioned PA6 samples. Considering the low stiffness of the conditioned samples their low strain at break of the conditioned samples is unexpected. Obviously no necking occurred in

these samples during the stress strain test. Their strain at break is so low that they do not yield in the stress strain test. This explains why no yield stresses are listed in table 9.1 for the conditioned samples.

The yield stress of the dry nanocomposites systematically increases upon addition of clay. Simultaneously the strain at yield decreases, as is indicated by the arrow. Up to 2.5% of clay the strain at break is relatively large ($\approx 30\%$) and is comparable to that of the unfilled PA6. At concentrations of 5% and 7.5% the samples do not show a yield-point and break below 3% strain.

All samples failed brittle in the IZOD test and consequently showed low impact energy. Adding more clay to the nanocomposites increased the impact energy of the dry samples somewhat, while it decreased that of the wet samples.

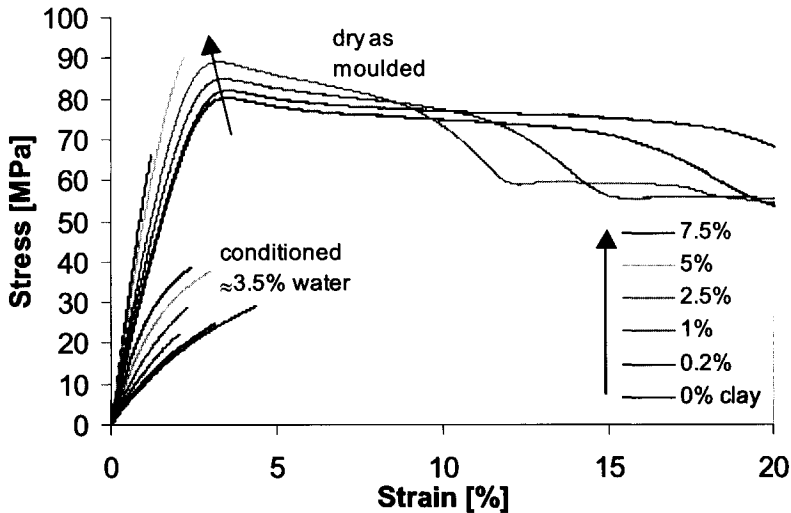


Figure 9.9 Stress strain tests of dry and wet PA6 nanocomposites at 23 °C

9.3 Thermal expansion of PA6-nanocomposites

9.3.1 Procedure to determine the thermal expansion coefficient

As explained in Chapter 3, the thermal expansion coefficient of a composite material is closely related to the 3-dimensional stiffness of the composite. Most often, only one or two elastic constants of the composite are known. This is not enough to calculate the thermal expansion coefficient because for that, the complete stiffness tensor of the composite must be known.

In order to construct the stiffness tensor, all independent elastic constants like the shear moduli, Poisson's ratios, bulk moduli etc. should be measured. This is a very tedious job as can be concluded from the work of Ward [4], who performed these types of measurements on oriented polyethylene. An easier way to construct the stiffness tensor is to use composite modelling and use the constructed stiffness tensor to calculate the thermal expansion coefficient.

To construct the stiffness tensor the orientation distribution of the filler must be known. Very often not enough information is available to construct the orientation distribution function. Therefore the weak point in the construction of the stiffness tensor is mainly the uncertainty of the orientation distribution function. It was attempted to measure the

orientation distribution of the clay platelets by FTIR dichroism. This attempt failed because the absorptency of clay in the infrared spectrum is too high, making it impossible to obtain accurate absorption peaks.

Since no information is available on the orientation distribution of the injection moulded specimens either perfect unidirectional or perfect random orientation is assumed for calculation of the expansion coefficient.

The Mori-Tanaka model that was introduced in Chapter 3, was used to determine the stiffness tensor of a unidirectional oriented composite. For calculation of the expansion coefficient it is not good enough to use the Halpin-Tsai approximation. Using Halpin-Tsai, the approximation of the out of plane Young's modulus is not accurate enough to predict the subtle relationship between stiffness and expansion coefficient. The effect of random orientation is accounted for by setting the Legendre coefficients $a_0 = 1$, $a_2 = 0$ and $a_4 = 0$ as was explained in Chapter 3. Of course any other orientation distribution function can be accounted for by using another set of Legendre coefficients. The use of Legendre polynomials to characterise the orientation function is described in Chapter 3. The calculated stiffness tensor is then used to calculate the tensor of the thermal expansion coefficient. By using this procedure, estimations can be obtained for the thermal expansion in all three orthogonal directions. In Appendix B a listing is given of a MATLAB computer program that calculates the stiffness tensor and the tensor of the expansion coefficient. The program requires knowledge of the Legendre coefficients to characterise the orientation distribution function. It also needs input of the stiffnesses and expansion coefficients of the phases.

9.3.2 Modelling the thermal expansion of PA6-nanocomposites.

Equation 3.73 predicts that the expansion coefficient is a function of the stiffness of the composite. The equation is valid for composites that obey continuum mechanical rules. The thermal expansion coefficient of the PA6 nanocomposites is studied in order to find out if, also in this respect, nanocomposites behave like conventional composites.

In Fig. 9.10 the in-plane thermal expansion coefficient $\alpha_{inplane}$ of the PA6 nanocomposites is plotted as a function of the in-plane Young's modulus $E_{inplane}$. The in-plane Young's modulus is calculated as: $E_{inplane} = (E_{flexural} + E_{Jflexural})/2$, and the in-plane thermal expansion coefficient as: $\alpha_{inplane} = (\alpha_{//} + \alpha_{\perp})/2$. The points in the graph denote the measurements while the lines denote theoretical predictions. The theoretical predictions are calculated using equation 3.73. Either perfect or random-3D orientation is assumed. The MATLAB computer program to calculate the theoretical curves is listed in Appendix B.

As predicted by equation 3.73 the in-plane thermal expansion coefficient decreases as the in-plane stiffness increases. The measurements lie between predictions of perfect orientation and random 3D orientation. It is concluded that equation 3.73 gives a good prediction of the thermal expansion coefficient of nanocomposites. This equation is based on continuum mechanics and does not require knowledge of the size of the filler particles. Beside properties of the two phases only the stiffness tensor of the composite needs to be known. As was shown in paragraph 3.2.1.2. and Appendix A, the stiffness tensor of the nanocomposite composite mainly depends on the aspect ratio of the platelets. Like in conventional composites the expansion coefficient of PA6-nanocomposites can be predicted by equation 3.73.

It is interesting to observe the theoretical estimates of the in plane and out of plane expansion coefficients. These are plotted as a function of the amount of silicate in Fig. 9.11. An aspect ratio of 100 is assumed and an isotropic filler stiffness of 172 GPa. The calculations show that in a unidirectional oriented composite the expansion in the out of plane direction α_{\perp} is higher than the expansion of the unfilled polymer while the expansion in the in

plane direction $\alpha_{//}$ is much smaller. This is a direct result of the high resistance of the polymer against change in volume (high bulk modulus). To keep the change in volume as small as possible, the out of plane direction must expand more strongly to compensate for the small in-plane expansion.

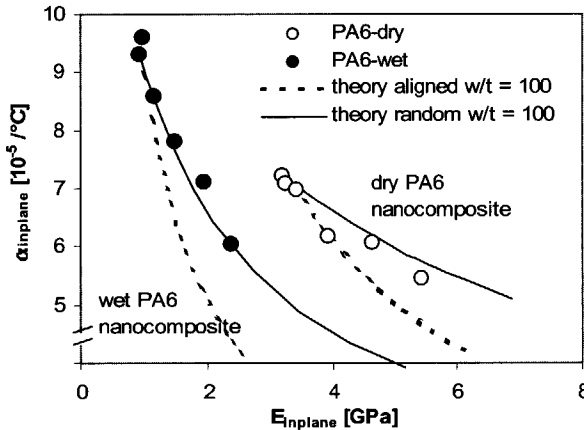


Figure 9.10 Thermal expansion coefficient of PA6 nanocomposite as a function of the parallel stiffness of the nanocomposite. Included are measured and theoretical data. Parameters used for composite modelling:

Dry nanocomposite: $\alpha_m = 7.23 \cdot 10^{-5} /^{\circ}\text{C}$; $E_m = 3.2 \text{ GPa}$
 $\alpha_r = 1.5 \cdot 10^{-5} /^{\circ}\text{C}$; $E_r = 172 \text{ GPa}$; $w/t = 100$
 Wet nanocomposite: $\alpha_m = 9.31 \cdot 10^{-5} /^{\circ}\text{C}$; $E_m = 0.94 \text{ GPa}$
 $\alpha_r = 1.5 \cdot 10^{-6} /^{\circ}\text{C}$; $E_r = 172 \text{ GPa}$; $w/t = 100$

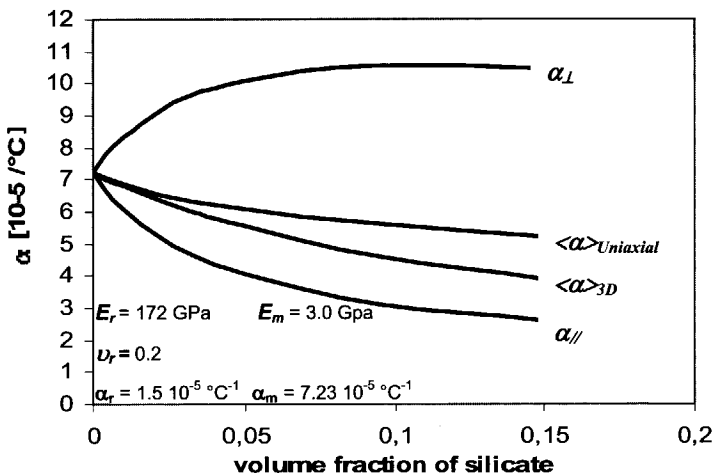


Figure 9.11 The theoretical expansion coefficient as a function of the silicate loading of composite filled with plates:

Out of plane expansion of an oriented composite(α_{\perp})

In plane expansion of an oriented composite($\alpha_{//}$)

Average(=volume) expansion of an oriented composite ($\langle\alpha\rangle_{\text{Uniaxial}}$)

Average (=volume) expansion of a 3D- randomly oriented composite ($\langle\alpha\rangle_{3D}$)

The volume expansion of the unidirectional composite $\langle \alpha \rangle_{\text{Uniaxial}}$ is slightly smaller than that of the unfilled polymer. This indicates that the total volume of the unidirectional composite expands almost as much as the unfilled polymer. The expansion of the randomly oriented composite $\langle \alpha \rangle_{3D}$ is smaller than the volume expansion of the unidirectional composite $\langle \alpha \rangle_{\text{Uniaxial}}$. So, to obtain a small in-plane expansion coefficient it is best to orient the platelets, while for a small volume expansion coefficient it is best to have random orientation.

9.4 Visco-elastic properties of compression moulded PE-clay nanocomposites

Composite models predict a strong effect of the aspect ratio of the clay particles on the stiffness of nanocomposites. In this section the effect of clay aspect ratio on the visco-elastic properties of PE-nanocomposites is studied. The objective is to understand how nanocomposites are reinforced and to show that clay with a low aspect ratio is less effective in reinforcing a polymer than clay with a high aspect ratio. To this end, composite modelling is used to quantify the effectiveness of the clay by calculating an effective aspect ratio.

9.4.1 Materials

Three types of clays are exfoliated in PE, a synthetic smectite with an estimated aspect ratio of about 20 (SAN from Unicoop), a montmorillonite with an aspect ratio of about 100 (Cloisite 20A from Southern Clay Products) and synthetic mica with an aspect ratio of about 200 (MAE from Unicoop). Preparation of PE-nanocomposites from these clays is described in Chapter 5. Exfoliation of the clays in PE is very good as can be concluded from the TEM pictures given in Chapter 6.

9.4.2 DMA measurements

The PE-nanocomposite pellets were compression moulded into sheets of about 80 mm x 50 mm x 0.5 mm at 250°C on a Fontijne laboratory press. Compression was performed in steps: 2 minutes at 0 kN and 200°C, 2 min at 10 kN and 200°C and 15 min at 180 kN while cooling down with an initial cooling rate of about 40°C/min. The samples for DMA testing were punched out of the compression-moulded sheets into samples of 50 x 2 x 0.5 mm.

DMA measurements were performed on a Perkin Elmer DMA 7E using compression moulded sheets. The apparatus used was operated at a frequency of 1 Hz and at a dynamic strain of 0.05%. To prevent buckling of the samples the static strain is automatically adjusted to 110% of the dynamic strain at each temperature. The temperature was varied between -150 °C and 115 °C, at a heating rate of 3 °C/min. The actual dimensions of the samples inside the DMA apparatus were about 14 x 2 x 0.5 mm.

9.4.3 DMA results

The DMA measurements on the PE nanocomposites are plotted in Figs. 9.12 a-c. The figures show both E' and E'' as a function of temperature.

In Fig. 9.12a, the storage moduli of PE-nanocomposites with synthetic smectite clay are much lower than that of the PE nanocomposites with montmorillonite in Fig. 9.12b or with synthetic mica in Fig. 9.12c.

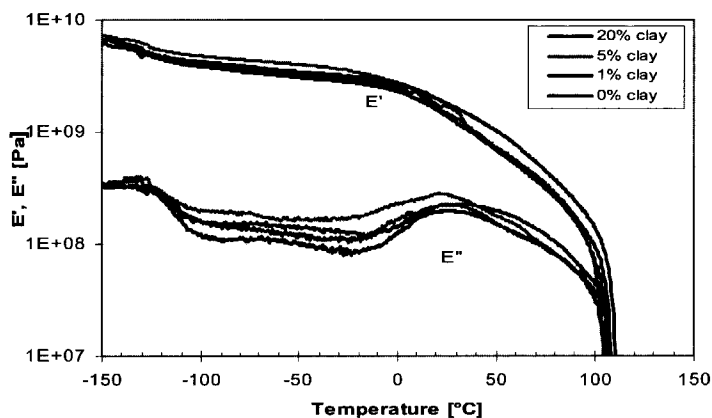


Figure 9.12a Storage and loss Young's modulus of PE-clay nanocomposites containing between 0 and 20 wt% 2M2HT treated synthetic smectite clay ($w/t \approx 10$).

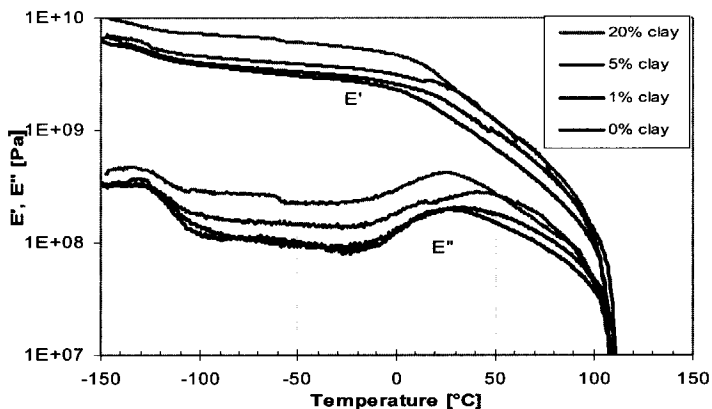


Figure 9.12b Storage and loss Young's modulus of PE-clay nanocomposites containing between 0 and 20 wt% 2M2HT treated montmorillonite clay ($w/t \approx 100$).

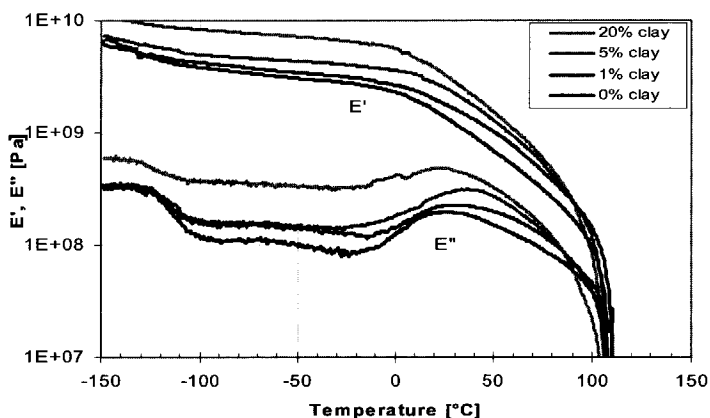


Figure 9.12c Storage Young's modulus of PE-clay nanocomposites containing between 0 and 20 weight% 2M2HT treated synthetic mica ($w/t \approx 200$).

Judging from these results the synthetic smectite has the lowest and the synthetic mica has the highest reinforcing effect while the effectiveness of the montmorillonite clay lies in between these two.

The effect of the type of clay on the Young's modulus is better illustrated in Figs. 9.13 a) and b) at 23 °C and -140 °C. Points denote measurements, while solid lines are drawn through the points to guide the eye. Both figures show that clay with large aspect ratio (synthetic mica) increases the stiffness much more than clay with low aspect ratio (synthetic smectite). At 23 °C the effect of clay on the relative modulus is larger than at -140 °C. This is a consequence of the lower matrix stiffness at 23 °C.

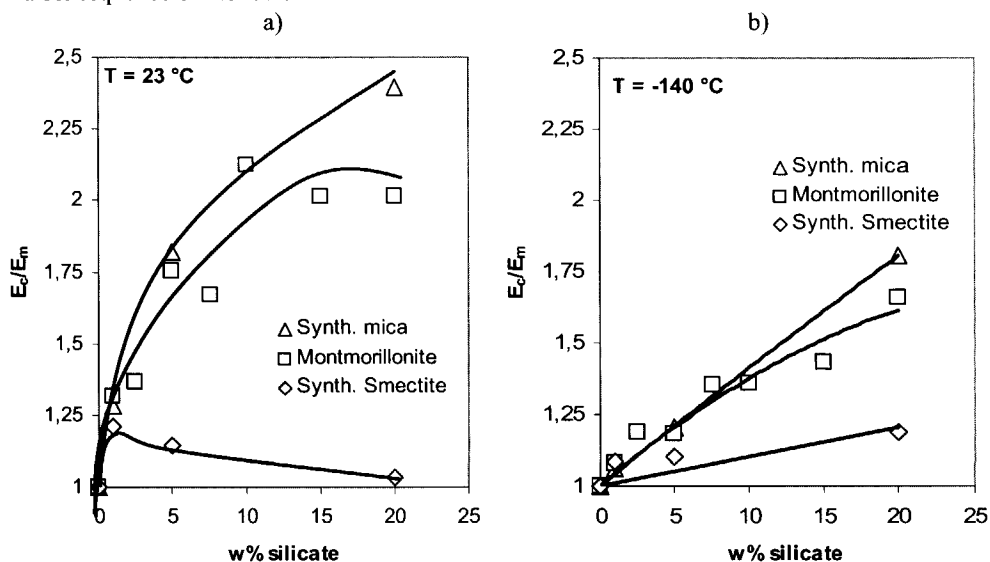


Figure 9.13 a-b Relative Young's modulus of PE-nanocomposites with 3 different types of clay versus wt% clay a) 23 °C and b) -140 °C.

To quantify the reinforcing effectiveness of the three types of clays, composite modelling is used. It is attempted to quantify the effectiveness of the clay by assigning an effective aspect ratio to it. The procedure used to fit the results is analogous to the one used for the PA-nanocomposites in the preceding section. The aspect ratio in the complex Halpin-Tsai equation is adjusted such that the fit is perfect at low temperature (-145 °C).

For the fit it is assumed that the samples are randomly oriented. This assumption is justified by observing the orientation in the TEM pictures in Figs. 6.8-6.10. An example of such a fit on the PE-nanocomposites filled with synthetic mica is given in Figs. 9.14a-9.14c. The stiffness of the unfilled PE (E_m' and E_m'') is used as the stiffness of the matrix. As before the stiffness of the nanoclay is assumed to be 172 GPa. This is the same stiffness as that of a perfect mica crystal.

Fig. 9.14a shows that, between -145 and 0 °C, the composite model gives a good prediction of the storage modulus E_c' of the nanocomposites. Table 9.4 lists the effective aspect ratio of the clay platelets in the PE nanocomposites. The effective aspect ratio of the clay decreases as the amount of clay increases. This is probably a consequence of incomplete exfoliation, local ordering and grouping of particles as was discussed earlier. This finding is in line with the findings for the PA6-nanocomposites of the preceding section. In Fig. 9.14c the differences between the filled and unfilled samples are enhanced by plotting the relative storage modulus E_c'/E_m' . The figure shows that above 0 °C the fit starts to deviate strongly

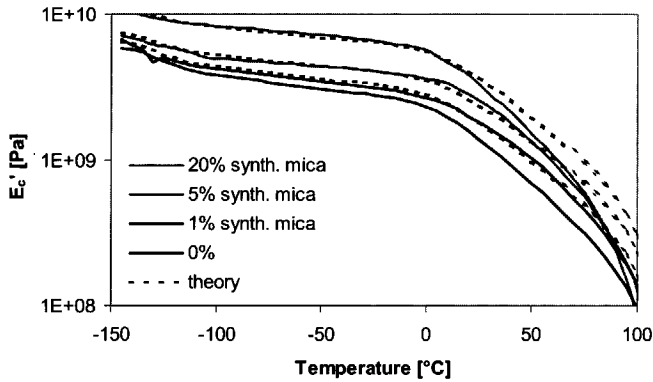


Figure 9.14a Storage modulus of PE-clay nanocomposites containing 2M2HT treated synthetic mica. Grey lines are measured values; dotted lines are fitted using the complex version of the Halpin-Tsai model.

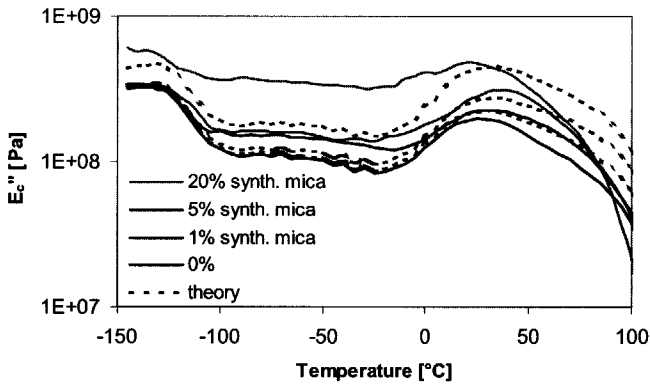


Figure 9.14b Loss modulus of PE-clay nanocomposites containing 2M2HT treated synthetic mica. Grey lines are measured values; dotted lines are fitted using the complex version of the Halpin-Tsai model.

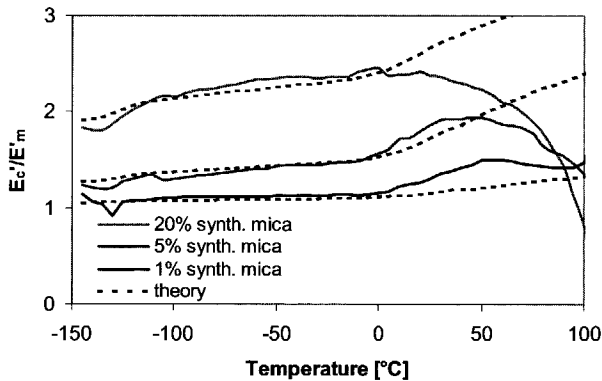


Figure 9.14c Relative storage modulus of PE-clay nanocomposites containing 2M2HT treated synthetic mica. Grey lines are measured values; dotted lines are fitted using the complex version of the Halpin-Tsai model.

from the measured results. This is similar to what was found for the PA6-nanocomposites in the preceding chapters.

DSC measurements on the PE-nanocomposites that are presented in Chapter 7 reveal that the heat of crystallisation of the PE phase in the nanocomposites decreases systematically as the amount of clay is increased. The low storage modulus above 0°C is therefore attributed to a low crystallinity and low crystal perfection of the PE phase in the nanocomposites.

Prediction of the loss modulus E_c'' in Fig. 9.13b is poor; the measured loss modulus is systematically higher than predicted by the composite model. Evidently, the nanoclay increases the visco-elastic energy loss.

Clay wt%	w/t fitted	Orientation
Synt. Smectite		
1.0	10	Random
5	10	Random
20	2	Random
Montmorillonite		
1.0	150	Random
5	70	Random
20	25	Random
Synthetic Mica		
1	250	Random
5	200	Random
20	60	Random

Table 9.4 Effective aspect ratio and orientation used to fit the DMA curves of PE-nanocomposites

9.5 Discussion

As was discussed in the introduction of this thesis several authors fail to recognise the importance of the aspect ratio for the stiffness of polymer-clay nanocomposites. As an example we will discuss recent work of Shelley [4] on the properties of nanocomposites. Her explanation given for the high stiffness of nanocomposites is exemplary for the explanations given by other authors like Giannelis [5] and Kojima [6]. Shelley explicitly rejected composite modelling because the composite model she used (from Hui et al. [7]) predicted too high values of the stiffness of polymer-clay nanocomposites. She recognised that this composite model is not accurate for platelet reinforcement. Instead of looking for an accurate model she assumed that the high stiffness of polymer-clay nanocomposites is caused by the high stiffness of the constrained polymer. She even assumed that the clay platelets themselves do not contribute to the stiffness of the polymer nanocomposite.

The results from this chapter prove the opposite. First of all the stiffness of polymer-clay nanocomposites is the result of the high stiffness and aspect ratio of the clay platelets.

Secondly, because of the emergence of a high mobile phase and because of hindrance of crystal growth, the clay platelets tend to reduce the stiffness of the polymer matrix instead of increasing it. Further it can be shown that the model suggested in this thesis can very well explain both Shelley's and Kojima's [4] experimental results.

The wrong conclusions drawn by the authors cited above illustrate the importance of using a correct composite model for polymer-clay nanocomposites. It also justifies the elaborate effort conducted in this thesis to find and validate such a model.

9.6 Conclusions

- At low clay loadings of clay, the Young's moduli of PA6 and PE nanocomposites are similar to that of conventional composites with high aspect ratio mica platelets. These Young's moduli can be predicted accurately by composite modelling.
- The theoretical relationship between thermal expansion and composite stiffness holds for nanocomposites. Once the stiffness of the nanocomposite is known, the thermal expansion can be calculated.
- The stiffness of nanocomposites increases as the aspect ratio of clay is increased. This is correctly predicted by composite modelling.
- By inverse composite modelling the effective aspect ratio and effective matrix Young's modulus inside a nanocomposite can be calculated.
- At loadings above 5-10 wt% of clay the true stiffness of PA6 and PE nanocomposites is smaller than that of comparable mica composites. This is assigned to a lower effective aspect ratio and lower effective matrix stiffness.
- At high loadings of clay, the platelets can only fit in the polymer matrix by aligning themselves along each other. The alignment leads to imperfect exfoliation of clay platelets and consequently to a lower effective aspect ratio and a lower stiffness.
- In contrast to statements in literature, at high loadings the clay platelets do not increase the stiffness of the polymer matrix but instead decrease it. The decreased stiffness of the polymer matrix is thought to be the result of the extremely small distance between clay platelets in nanocomposites, especially at high clay loadings.
- The small distance between clay platelets results in severe confinement of polymer chains, which, according to NMR results in Chapter 6 and DRS results in Chapter 8, results in the appearance of a high mobile phase in PA6-clay nanocomposites.
- As was shown by DSC in Chapter 7, the small distance between the platelets also hinders crystallisation and results in a decreased crystallinity and decreased crystal perfection. Both these effects lead to a relatively low stiffness.

9.7 References

- [1] H.R. Shell and K.H. Ivey, *Fluorine Micac*, Bulletin 647, Bureau of Mines, U.S. Department of the interior, 1969.
- [2] R. Krishnamoorti, R.A. Vaia, E.P. Giannelis, *Structure and dynamics of polymer-layered silicate nanocomposites*, Chem. Mater. **8**, 1996, p 1728-1734
- [3] H. Fischer, Presentation at the conference 'Nanocomposites 2000' 6-7 November 2000, Brussels.
- [4] J. Stebbins Shelley, *Mechanical Reinforcement and Environmental Effects on a Nylon6/Clay Nanocomposite*, PhD Thesis University of Utah, May 2000
- [5] E.P. Giannelis, *Polymer layered nanocomposites*, Adv. Mater. **8**, 1996 p 29-35
- [6] Y. Kojima et al, *Mechanical properties of nylon 6-clay hybrid*, J. Mat. Res. **8**(5), 1993, p 1185-1189.
- [7] C.Y. Hui and D. Shia, *Simple formula for the effective moduli of unidirectional aligned composites*, Pol. Eng. Sci. **38**(5), 1998, p774-782.

Permeability of nanocomposites

Abstract

Clay platelets in nanocomposites are known to retard the diffusion of gases or liquids. In order to find out what mechanisms are responsible for the retardation of diffusion, the water uptake of a series of PA6-clay nanocomposites has been monitored. Simple Fickian diffusion proved to give an accurate description of the water uptake in PA6-clay nanocomposites. The diffusion coefficient of water in the PA6-clay nanocomposites is determined by fitting the water uptake to Fickian diffusion models.

The permeability of polymer-clay nanocomposites is compared with the predictions of composite models. To this end several analytical models, found in the literature, are introduced that relate permeability to the morphology of multi-phase materials.

At small loadings, when the product of volume fraction and aspect ratio is smaller than unity ($c_r \alpha < 1$), Hatta's diffusion model [1], originally derived for thermal diffusion, is thought to be the best analytical model available to predict mass diffusion through platelet-reinforced composites. Of all models found in the literature, it relies on the smallest amount of simplifications and assumptions. Hatta's diffusion model is derived by using the equivalent inclusion method as was also used in Eshelby's mechanical model that was introduced in Chapter 3. Like Eshelby's model, Hatta's model uses spheroid shaped filler particles. Surprisingly the predictions of Hatta's model almost coincide with Nielsen's diffusion model [2], which has a much weaker theoretical basis. It is found that at low loadings of clay, Hatta's model accurately predicts diffusion of gases through PA6-clay nanocomposites. At higher loadings, if ($c_r \alpha > 1$), Hatta's model is no longer valid.

Brydges model is more appropriate then. The two-dimensional approach in deriving Brydges model makes the model suitable only for ribbons and not for platelets. By adjusting Brydges model such that it coincides with Hatta's model at low volume fractions, a new model is created that is thought to be suited for the diffusivity of platelet filled composites over the whole range of volume fractions.

By adjusting Nielsen's diffusion equation, a theory is derived to estimate the effect of misalignment of platelets on diffusivity. It is found that, compared to perfect alignment, random alignment of clay platelets can seriously increase diffusivity.

A good agreement between experiments and Hatta's model is found, which indicates that mainly the aspect ratio and the amount of clay platelets determine the diffusivity of nanocomposites. Changes in polymer properties, due to the high surface area of the clay platelets, do not significantly change the diffusivity of PA6-clay nanocomposites.

10.1 Introduction

Improved resistance of polymers against transport of gases or liquids is of importance for packaging purposes. To prevent spoiling of food for example, food packaging must have a large barrier resistance against oxygen and water. Beverage bottles must keep the carbon dioxide inside the bottle. For safety, environmental and economical reasons, fuel should not diffuse through the walls of fuel containers. Increased resistance against transport of oxygen also improves the oxidation stability of polymers.

In most applications the requirements on barrier resistance are met by selecting a polymer with high intrinsic barrier properties or by increasing the thickness of the polymer. Often this thickness is larger than strictly necessary for mechanical properties. This increases the amount of polymer needed for the application, and thus increases the costs of manufacturing and of transportation. So, for economical reasons it would be beneficial to increase the barrier resistance of polymers.

Diffusion of gases and liquids through polymers mainly occurs in the amorphous phase. In general the crystalline phase is supposed to be impenetrable. Diffusion through the amorphous phase consists of activated jumps, in the order of 5-10 Å, between pre-existing voids in the polymer matrix. By using this so called free-volume concept, the gas diffusion in low barrier amorphous polymers can be predicted accurately [3].

A semi-crystalline polymer contains both amorphous and crystalline phases. The presence of the crystalline phase makes the diffusion mechanism more complex than in pure amorphous polymers. The molecules that diffuse through the amorphous phase are now forced to travel around the impenetrable crystalline phase. This effectively increases the tortuous path length of the diffusing molecules. Lützow et al. [4] studied the diffusion of toluene and n-heptane in HDPE, LDPE and LLDPE. The high crystalline HDPE was found to have a much lower permeability than LDPE or LLDPE. This was not only attributed to a higher tortuosity but also to a decreased amount of free volume in the amorphous phase of HDPE. Hernandez et al. [5] studied the sorption and transport of water in PA6 films. The diffusivity of water in PA6 decreased strongly by lowering the temperature, while the solubility was almost not affected. Both Lützow and Hernandez use free-volume concepts to explain the observed sorption and transport phenomena.

Polymer composites filled with micrometer sized impenetrable ribbons [6-8] or platelets [8-10] are known to have an improved barrier resistance against the transport of liquids and gases. Since micrometer sized filler particles are relative large compared to molecular size, the matrix properties of these composites are not expected to change much by the presence of the fillers. In these kinds of composites all changes in barrier properties can therefore be attributed to the obstacle effect of the platelets.

Polymer-clay nanocomposites also show improved barrier resistance. The Toyota group has done a lot of work in this field. They reported improved barrier properties in rubber-clay [11], polyimide-clay [12,13] and PA6-clay [14] nanocomposites. They successfully used Nielsen's tortuosity model [2] to estimate the effect of aspect ratio and volume fraction on permeability. Improved barrier resistance was also found by Matayabas et al. [15] for polyester clay nanocomposites. Messersmith et al. [16] reported on the permeability of polycaprolactone-clay nanocomposites. In two data sheets [17,18] Unitika mentions that the rate of water uptake of PA6 is strongly reduced by addition of nano-dispersed clay.

As Kojima [19] showed the clay platelets in PA6-clay nanocomposites change the crystalline structure of PA6 from α to γ -crystalline and impose a preferred orientation to the crystals. It can thus be expected that this change in crystalline structure changes the diffusivity of water in a PA6 nanocomposite. So two mechanisms are active in PA6

nanocomposites that could change the permeability: the high aspect ratio of the clay platelets and the altered polymer crystallinity. As was discussed before with mechanical properties in Chapter 9, the question arises whether nanocomposites have improved barrier resistance only because of the high aspect ratio of the platelets, or also because the clay platelets significantly change the diffusivity of the polymer matrix. Again it is attempted to answer this question by comparing the results of diffusion measurements with the results of composite modelling. If composite modelling can quantitatively explain the experiments there is no reason to assume that the improved barrier-resistance of nanocomposites are caused by a change in matrix properties. On the other hand, if composite modelling cannot give a quantitative explanation, the unexplained part of the barrier resistance is most likely caused by a change in polymer properties.

In Section 10.2 a general introduction on diffusion theory is given. Here some basic equations are introduced that explain the effect of sample thickness and time on diffusion. Section 10.3 introduces some theories to estimate the barrier resistance of polymers filled with platelets. The effect of misalignment on diffusivity is estimated and discussed in Section 10.4. Section 10.5 compares the diffusivity of nanocomposites to the predictions of the theoretical models introduced earlier. All results are evaluated and conclusions are drawn in Section 10.6.

10.2 Elementary diffusion theory

Diffusion is a statistical process that occurs if particles start travelling through a phase as a result of their thermal motion. Suppose that a group of labelled particles is concentrated in a small volume of a substance. All particles are moving because of their thermal motion. By chance some labelled particles will move outside the small volume. This causes the group of particles to spread out. A net flux of labelled particles can thus be observed moving from a high to a low concentration.

10.2.1 Fick's first and second law of diffusion

A method to measure the transport of liquids or gases through a polymer is to make a film, apply a concentration difference over it, and measure the amount of liquid or gas that is transported through the film per unit of time. The rate of transport N (mol/s) through the film is proportional to the concentration difference ΔC (mol/m³) and to the surface area A (m²) of the film while it is inversely proportional to the thickness h (m):

$$\frac{N}{A} = -\frac{D}{h} \Delta C \quad 10.1)$$

where D (m²/s) is the proportionality constant known as the diffusivity or the diffusion coefficient. The minus sign indicates that the direction of mass flow is from regions of high concentration to regions of low concentration. In a differential form Eqn. 10.1) is written as Fick's first law:

$$J = -D \frac{dC}{dx} \quad 10.2)$$

where J is the flux density ($\text{mol/m}^2\text{s}$) of molecules diffusing across a unit area in unit time. Fick's first law can only be used for steady state situations where the flux does not vary with time.

The earliest methods to measure the permeability of water through a polymer film were performed by test dishes containing desiccants that were covered by the barrier film. The dish was placed in an environment with known relative humidity and the water permeability was determined by the increase in weight of the desiccant. In newer methods (Fig. 10.1), water is placed in a dish covered by the barrier film. The vapour transmission rate is determined by measurement of the relative humidity on the dry side, by a humidity sensor or by an infrared sensor.

Gas permeability is generally measured by exposing the high-pressure side of the film to gas by constant flushing. The transmission rate is then usually determined by one of the two following two methods. In one method a vacuum is applied on the low-pressure side of the film and the rate of increase in pressure is recorded by a pressure gauge.

More modern methods use gas-chromatography techniques to measure the increase in gas concentration on the low-pressure side (Fig. 10.2).

A drawback of all these methods and any other method that directly measures permeability through a thin film is their sensitivity to leakage. The amount of material transported through the film is extremely small. So any small pinhole or leak significantly contributes to the error in the measurement.

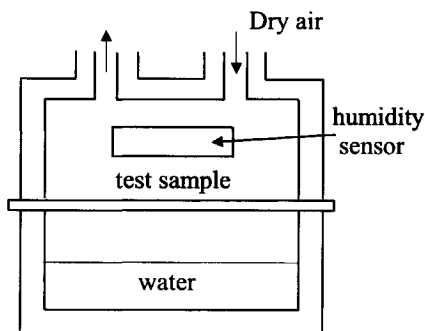


Figure 10.1 Apparatus for measurement of water transmission

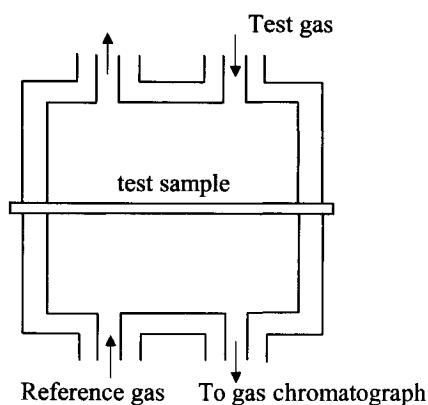


Figure 10.2 Apparatus for measurement of gas transmission

Another method to determine the transport kinetics of a gas or a liquid in a polymer is to measure the rate of sorption or desorption of the gas in a test sample. To use this method the solvability of the test gas in the sample must be high enough to be measured accurately. Water absorption in PA6 nanocomposites can be determined by measuring the weight increase of an originally dry sample in a controlled humid atmosphere. By measuring the increase in weight of the sample as a function of time, it is possible to determine the diffusivity as well as the solubility of water in the PA6 nanocomposites. Small holes have no influence on the outcome of this measurement.

Absorption is a non-equilibrium process. During absorption the diffusing phase accumulates in the polymer. Fick's first law does not account for accumulation since it can only be used for equilibrium transport of the diffusing phase. Fick's second law does account for accumulation (and depletion):

$$\frac{\partial C}{\partial t} = D \frac{\partial^2 C}{\partial x^2} \quad (10.3)$$

If a gas or liquid is absorbed in a homogeneous, infinitely long sheet, the sheet increases in mass (ΔM) as a function of time t until saturation is reached (ΔM_{\max}). Using Fick's second law, an expression can be derived for the time dependent absorption of a gas or liquid into a sheet [5]:

$$\frac{\Delta M}{\Delta M_{\max}} = 1 - \frac{8}{\pi^2} \sum_{n=0}^{\infty} \left(\frac{1}{(2n+1)^2} \exp\left(-\frac{Dt}{h^2} \pi^2 (2n+1)^2\right) \right) \quad (10.4)$$

where $\frac{\Delta M}{\Delta M_{\max}}$ is the relative change in mass, t is the time and h is the thickness of the sheet.

This series converges very rapidly, for $Dt/h^2 > 0.01$, 3 terms suffice.

At short times ($Dt/h^2 < 0.06$, or equivalently $\Delta M/\Delta M_{\max} < 0.55$) this expression can be approximated as a linear relationship between the relative mass gain and the square root of time:

$$\frac{\Delta M}{\Delta M_{\max}} \cong \frac{4}{\sqrt{\pi}} \sqrt{\frac{Dt}{h^2}} \quad (10.5)$$

By fitting experimental absorption data to Eqns. 10.4) or 10.5) the diffusivity D and the solubility $S = \Delta M_{\max}/M$ can be determined. Here M is the initial mass of the sheet.

If the sample is not a perfect sheet, but a thick plate, absorption not only occurs from the top and bottom of the plate but also from the sides. To account for absorption from the sides of the plate Eqn. 10.5) must be adapted:

$$\frac{\Delta M}{\Delta M_{\max}} \cong \frac{A_{\text{side}} + A_{\text{uplow}}}{A_{\text{uplow}}} \frac{4}{\sqrt{\pi}} \sqrt{\frac{Dt}{h^2}} \quad (10.6)$$

Here A_{side} is the area of the sides and A_{uplow} is the area of the upper and lower surfaces.

10.3 Modelling of diffusion in a material filled with impenetrable platelets

This subsection will start with some general relationships between transport properties of composites and their morphology. Then several models are introduced to calculate the transport properties of composites filled with platelets.

10.3.1 Relationship between permeability and diffusivity

Diffusivity (D) is a measure of the velocity at which molecules travel through a substance, while permeability (P) is a measure of the amount of molecules transported per unit of time. By definition the relationship between permeability and diffusivity is given by:

$$P \equiv SD \quad (10.7)$$

where S is the solvability of the molecules in the substance. The permeability of a composite material P_c can thus be written as:

$$P_c = S_c D_c \quad (10.8)$$

where S_c is the solvability and D_c the diffusivity of the molecules in the composite. The same relation ship holds for the permeability of the matrix P_m :

$$P_m = S_m D_m \quad (10.9)$$

where S_m is the solvability and D_m the diffusivity of the molecules in the matrix. In a composite filled with impenetrable particles the molecules can only dissolve in the matrix of the composite. The solvability of molecules in the whole composite is thus proportional to the volume fraction of matrix material $1-c_r$:

$$S_c = (1 - c_r) S_m \quad (10.10)$$

By combination of Eqns. 10.8), 10.9) and 10.10) the relative permeability of the composite P_c/P_m can be related to the relative diffusivity D_c/D_m :

$$\frac{P_c}{P_m} = (1 - c_r) \frac{D_c}{D_m} \quad (10.11)$$

Some measurements or analytical models give P_c/P_m while others give D_c/D_m . In these cases Eqn. 10.11) is useful to calculate the permeability of a composite if the diffusivity is known or vice versa.

10.3.2 Similarities between diffusion models for platelet filled composites

Before introducing models for the permeability of composites filled with platelets, let us first look at how the diffusion of a substance is influenced by the presence of an impenetrable plate with large aspect ratio. To this end, consider the plates in Fig. 10.3 that are subjected to a flow in vertical direction, as indicated by the arrow.

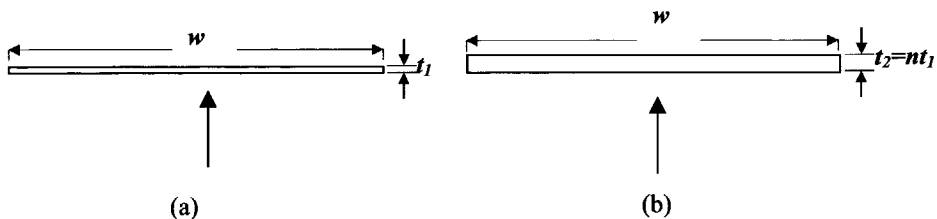


Figure 10.3 Resistance against flow of (a) a single plate with thickness t and of (b) a plate with thickness nt .

In Figs. 10.3a and 10.3b the thickness of the plate is much smaller than the width of the plate: $w/t \gg 1$. If the thickness of the plate in Fig. 10.3a is increased n times while its width

remains constant (Fig. 10.3b) it is intuitively clear that the resistance of the plate against the flow is hardly changed. Now the volume of the plate has increased n times, while its aspect ratio $\alpha = w/t$ is decreased n times. During this operation the product of aspect ratio and volume fraction: $c_r\alpha$, remains constant (c_r = volume fraction).

So as long as the volume fraction is low ($c_r \ll 1$) and the aspect ratio is large ($\alpha \gg 1$), any model for the diffusivity of a composite filled with impenetrable platelets will be a unique function of the parameter $c_r\alpha$. This relationship will prove to be a useful check for the validity of diffusion models.

10.3.3 Analytical models for transport properties of platelet filled composites

Several analytical models have been developed to calculate the diffusivity of heterogeneous materials. An early attempt was made by Barrer et al. [20] who modelled the diffusion through a composite filled with regularly spaced parallelepipeds. Since Barrer did not account for overlap of filler particles his theory is less useful for nanocomposites. Nielsen's model [2], which will be treated below, relates the permeability to the tortuosity of a composite filled with ribbons. Both Brydges [7] and Cussler [21] give theories for ribbon-reinforced composites. They derive their theories by calculation of the resistance against flow in the channels between platelets. Frederickson [22] used a multiple scattering formalism to derive equations for the transport properties in the dilute and semi dilute regime of composites filled with randomly placed oriented platelets.

The mathematical analogy between equations of elasticity and transport properties inspired Mehta et al. [6] to use Halpin-Tsai's equations to estimate the diffusivity of ribbon reinforced composites. By using a shape factor $\zeta = [c_r(w/t)^{1.38}]^I$, the Halpin-Tsai equations (see Chapter 3) could be accurately fitted to permeability data of oxygen and nitrogen through cellulose acetate films filled with glass ribbons.

Batchelor [23] gave a good overview on equations for transport properties of two-phase materials. His solution for the thermal diffusivity of a composite with a dilute concentration of non-interacting ellipsoids is directly applicable for diffusion of mass and will be discussed below. Hatta [1] extended Batchelor's result to composites with non-touching ellipsoids by using Eshelby's equivalent inclusion method.

The mathematical modelling of mass diffusion does not differ from the modelling of other transport properties like thermal conductivity, electrical conductivity, magnetic permeability or dielectric constants [24]. So expressions for mass diffusion can be obtained by using models that are derived for other transport properties.

10.3.3.1 Length of the tortuous path; Nielsen's model

For a material filled with impenetrable platelets, oriented perfectly perpendicular to the diffusion direction, Nielsen [2] derived a simple equation that relates the diffusivity of a composite (D_c) to the diffusivity of the matrix (D_m), the volume fraction c_r and the aspect ratio $\alpha = w/t$ of the platelets:

$$\frac{D_c}{D_m} = \frac{L_0}{L_c} = \frac{1}{1 + \frac{c_r\alpha}{2}} \quad 10.12)$$

In an unfilled material the shortest path length is L_0 while in a composite the shortest path length is L_c as is shown in Fig. 10.4. If a permeating molecule moves in vertical direction and hits a platelet, it is forced to travel along the platelet in horizontal direction until it reaches the end of the platelet. The assumption made by Nielsen is that on average a molecule travels half the length of the platelet along its surface before it can continue to the next platelet:

$$\frac{L_c}{L_0} = 1 + \frac{c_r \alpha}{2} \quad (10.13)$$

Nielsen's model fulfils the requirement in that it is a unique function of $c_r \alpha$ as is required by the reasoning in paragraph 10.3.2.

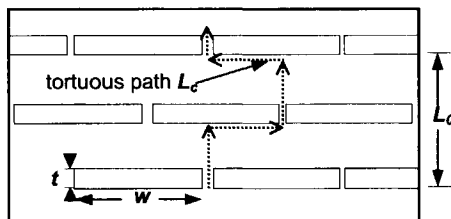


Figure 10.4 Tortuous path of a molecule diffusing through a material filled with ribbons.

In deriving Nielsen's equation several assumptions are made:

- The diffusivity of the matrix is not changed by the presence of the platelets.
- The platelets are perfectly oriented.
- All platelets have the same size.
- The platelets are supposed to overlap perfectly as in Fig. 10.4. Here the centres of each platelet are placed just above the gap between two platelets in adjacent rows.
- All platelets are separated; they do not touch each other.
- No preferred transport occurs along the interfaces of the platelets and the polymer matrix.

The simplicity of the model has the big advantage that it gives insight in the mechanisms that retard the transport of a substance in a composite filled with platelets. A disadvantage is that it neglects several features that occur in real composites:

- Essentially it is a two dimensional theory. This implies that the filler particles in Fig. 10.4 are thought to be infinitely long in the direction perpendicular to the drawing and therefore represent ribbons rather than platelets. This leads to a too low estimate of diffusivity.
- Misalignment of platelets can seriously decrease the length of the tortuous path. This is not accounted for in Nielsen's theory. By using randomising techniques the effect of misalignment can be estimated, as will be shown later.
- In real composites the size of platelets is not uniform but polydisperse. As can be estimated from Nielsen's model, long platelets have a much stronger effect on the length of the tortuous path than small platelets.
- The platelets are supposed to overlap perfectly as in Fig. 10.4. Random overlapping of platelets will give a lower length of the tortuous path and consequently a higher diffusivity.

- Transport of the diffusing substance at the interface can often not be neglected. This is especially true if the adhesion between matrix and polymer is low [9].
- At high loadings the effect of touching platelets cannot be neglected. If the sides of two platelets touch each other, the tortuous path is increased and the diffusivity is decreased. This is not accounted for in Nielsen's theory.
- The effective area that is available for transport decreases because of the thin channels between the platelets. This will decrease the diffusivity further than only tortuosity does.

In Nielsen's equations only the length of the tortuous path is taken into account. The same permeability would be obtained by using a plate that is a factor L_c/L_0 thicker than the original unfilled plate. So in fact Nielsen calculates the change in flow through a plate when the plate is increased in thickness by a factor L_c/L_0 without changing the area normal to the flow.

10.3.3.2 Resistance against transport by channels between platelets: Brydges' model

In reality flow is restricted to channels that are formed by the platelets, as is shown in Fig. 10.5. Not only the length of the tortuous path is increased, but simultaneously the surface area normal to the flow is decreased. Based on this concept Brydges et al. [7] developed a different and easy to understand model for diffusion in a ribbon-filled composite. Instead of calculating the length of the tortuous path they calculated the resistance against transport of the thin channels in a ribbon-filled composite as is shown in Fig. 10.5.

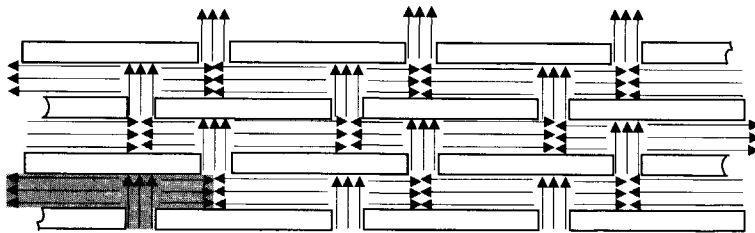


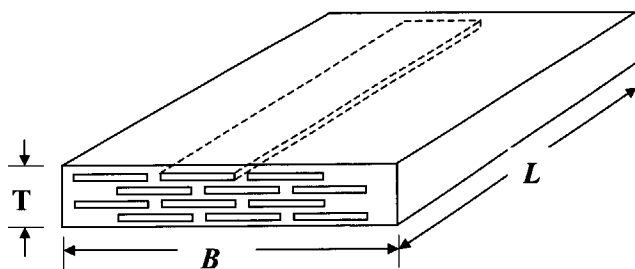
Figure 10.5 Diffusion through channels in a ribbon-filled composite

The geometrical parameters of the ribbon-filled composite are shown in Fig. 10.6. The plate in Fig. 10.6a contains n layers of ribbons, so that $T=n(d+t)$. Similarly the plate with B is considered as m multiples of the distance $(w+g)$, where w is the ribbon width and g the gap between the ribbons in each layer. Using the unit cell in Fig. 10.6b Brydges arrived at the following expression for the permeation coefficient for flow through a composite plate:

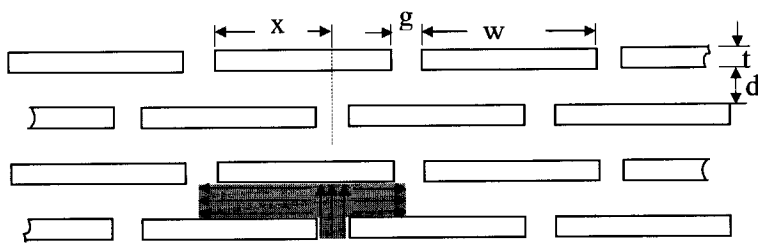
$$\frac{P_c}{P_m} = \frac{1}{\frac{w+g}{d+t} \left(\frac{t+d}{g} + \frac{w}{d} \gamma(1-\gamma) \right)} \quad 10.14)$$

where γ is the overlap factor, see Fig. 10.6. In a composite usually the width and thickness of the platelets are known. This leaves 3 unknown variables in Eqn. 10.14, d , g and γ . It is easy to show from Fig. 10.6b that the ribbon volume fraction c_r is given by:

$$c_r = \frac{1}{\left(1 + \frac{d}{t}\right)\left(1 + \frac{g}{w}\right)} \quad 10.15)$$



(a)



(b)

$$\gamma = \frac{x}{w}$$

Figure 10.6 (a) Ribbon-filled plate. (b) parameters describing the geometry.

By using Eqn. 10.15) d can be expressed as a function of c_r , t , g and w . By inserting this in 10.14), P_c/P_m can be expressed as a function of the volume fraction c_r , the plate width w , the plate thickness t , the gap g and the overlap factor γ . Compared to Nielsen's equation, two extra parameters must be known, the gap g and the overlap factor γ . These parameters hold information on the relative position of the platelets in the composite. Perfect overlap is achieved if $\gamma=0.5$, while $\gamma=0$ in the absence of overlap. Random overlap gives an average overlap factor of $\gamma = 0.25$. The factor $\gamma(1-\gamma)$ that accounts for the overlap in Eqn. 10.14) changes from 0.25 to 0.19 by changing γ from 0.5 to 0.25. So the result of the calculation is not sensitive for the precise value of γ . Therefore the only important unknown parameter in Eqn. 10.14) is the gap distance. Brydges assumed that $g \gg t$ and $\alpha \gg 1$. Under these conditions Eqn. 10.14 takes the form:

$$\frac{P_c}{P_m} \cong \frac{1 - c_r}{(c_r \alpha)^2 \gamma (1 - \gamma)}; \quad g \gg t \text{ and } \alpha \gg 1 \quad 10.16)$$

It must be reminded that Eqn. 10.14) holds for perfectly straight ribbons that are positioned in perfect layers as is shown in Fig. 10.6. Brydges used his model to calculate the permeability

of gas pipes that were made by winding glass ribbons around a tube. In these kinds of composites the configuration of ribbons is realistically represented by Fig. 10.6. Eqn. 10.16) should give a reasonable estimate of the permeability of such a composite. In composites filled with platelets the existence of a well-defined gap between platelets is questionable since in reality platelets are not aligned in layers. In contrast it can be expected that the centres of gravity of the platelets are randomly positioned as is depicted in Fig. 10.7. Definition of a gap distance g becomes difficult under these circumstances.

As can be seen in Fig. 10.7 only a few particles have edges that come close to the edges of other particles. Furthermore narrow gaps can only exist if the platelets have perfectly straight sides, while in reality the platelets will be irregularly shaped and certainly will not be perfectly straight. So for platelet-reinforced composites the gap will never be extremely small. The condition introduced by Brydges that $g=t$ is therefore much too strict for composites reinforced with platelets.

A more realistic assumption is that $g=d$ as was already assumed in the 3D-Takanayagi model introduced in Chapter 3. Figure 10.7 shows that this is a reasonable assumption. If additionally it is assumed that the platelets have a high aspect ratio ($w \gg t$) equation 10.14 can be written as:

$$\frac{P_c}{P_m} \approx \frac{1 - c_r}{(c_r \alpha + 1 - c_r)(c_r \alpha \gamma (1 - \gamma) + 1)} \quad (10.17)$$

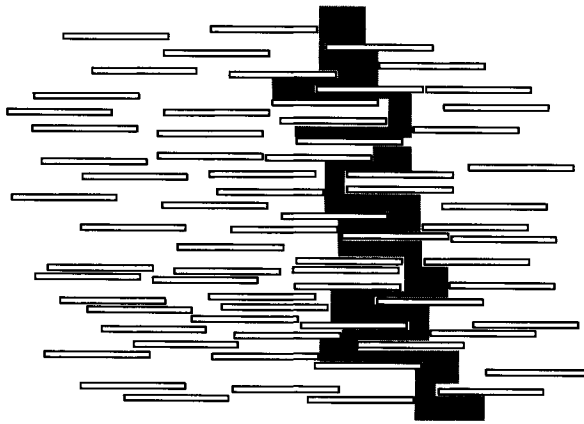


Figure 10.7 A possible diffusion path through a realistic configuration of platelets in a composite.

In the diluted region if $c_r \alpha \ll 1$ Eqn. 10.17) reduces to:

$$\frac{P_c}{P_m} \approx \frac{1 - c_r}{1 + c_r \alpha (1 + \gamma (1 - \gamma))} \quad (10.18)$$

which has much resemblance with Nielsen's model. At intermediate to large volume fractions as $c_r \alpha \gg 1$ Eqn. 10.17) reduces to equation 10.16). Equation 10.17) is therefore thought to have a wider range of applicability than equation 10.16). Especially in the diluted region if $c_r \alpha \ll 1$ equation 10.17) is better suited.

10.3.3.3 Resistance against transport by channels between platelets: Cussler's model

Cussler [21] derived expressions for the permeability of membranes filled with ribbons of variable width and variable gap distance as is shown in Fig. 10.8 :

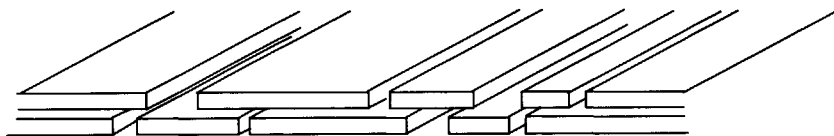


Figure 10.8 Membrane with randomly spaced slits.

By using a statistical approach he calculated the probability of a diffusing molecule to hit a ribbon. He assumes that once the molecule hits a ribbon, it travels a distance of μw along the ribbon before traveling to the next layer of ribbons, w being the width of the ribbon. By combining statistical calculations with calculations of the flow resistance in the channels and slits he arrived at the following expression for the diffusivity:

$$\frac{D_c}{D_m} = \frac{1}{1 + \mu \alpha^2 \frac{c_r^2}{1 - c_r}} \quad 10.19)$$

Cussler shows that μ is 0.25 if the platelets are regularly placed as shown in Fig. 10.5. As such, μ fulfils exactly the same role as the factor $\gamma(1-\gamma)$ in Brydges model which also is equal to 0.25 for the same configuration of platelets. The models of Brydges and Cussler coincide if $c_r \alpha \gg 1$.

10.3.3.4 Barrier properties of oriented disk composites, dilute and semi-dilute concentrations: Frederickson

Recently Frederickson and Bicerano [22] used a multiple scattering formalism to derive equations for the transport properties of composites filled with randomly placed oriented platelets in the dilute and semi dilute regime. They assumed that the aspect ratio of the disks is always much greater than unity: $\alpha \gg 1$. In the dilute regime it is assumed that $c_r \alpha \ll 1$, while in the semi-dilute regime $c_r \ll 1$ and $c_r \alpha \gg 1$. Frederickson concludes that in the dilute regime an adapted version of Nielsen's model should be used, while in the semi-dilute regime an adapted version of Cussler's model is more appropriate.

In the dilute regime:

$$\frac{D_c}{D_m} \cong \frac{1}{1 + \kappa c_r \alpha} \quad 10.20)$$

where for oriented disks:

$$\kappa = \frac{\pi}{2} \frac{1}{\ln(\frac{1}{2} \alpha)} \quad 10.21)$$

and for randomly oriented disks:

$$\kappa = \frac{\pi}{6} \frac{1}{\ln(\frac{1}{2} \alpha)} \quad 10.22)$$

In the semi-dilute regime:
$$\frac{D_c}{D_m} \cong \frac{1}{\mu(c, \alpha)^2} \quad 10.23)$$

where
$$\mu = \frac{\kappa^2}{16} \quad 10.24)$$

Frederickson also constructed an equation that reduces to Eqn. 10.20) if $\kappa c, \alpha < 3$ and to Eqn. 10.22) if $\kappa c, \alpha > 12$:

$$\frac{D_c}{D_m} = \frac{1}{4} \left(\frac{1}{1 + a_1 \kappa c, \alpha} + \frac{1}{1 + a_2 \kappa c, \alpha} \right)^2 \quad 10.25)$$

where $a_1 = (2 - \sqrt{2})/4 \approx 0.146447$ and $a_2 = (2 + \sqrt{2})/4 \approx 0.853553$.

10.3.3.5 Transport properties of a composite with a dilute suspension of non-interacting ellipsoids: Batchelor's model

Models for the transport properties of a composite filled with non-interacting unidirectionally oriented ellipsoids were given by Batchelor [23]. He used mean field theory to calculate the thermal conductivity of a composite. Since the mathematics of thermal diffusion and mass diffusion are exactly the same, his equation can also be used to calculate mass diffusion. If all ellipsoidal particles have semi-diameters a_1, a_2, a_3 and have the same orientation, the principal axes of the permeability tensor are parallel to the principal axes of the ellipsoids. The three principal diagonal elements are then found to be:

$$\frac{P_{c,i}}{P_m} = \left\{ 1 + \frac{(\beta - 1)c_r}{1 + S_i(\beta - 1)} \right\}, \quad i = 1, 2, 3 \quad 10.26)$$

where
$$S_i = \frac{a_1 a_2 a_3}{2} \int_0^\infty \frac{d\rho}{(a_i^2 + \rho) \{ (a_1^2 + \rho)(a_2^2 + \rho)(a_3^2 + \rho) \}^{1/2}} \quad 10.27)$$

β is the ratio between the permeability of the reinforcement and the matrix: $\beta = P_r/P_m$. For impenetrable platelets $\beta = \infty$. This expression is equivalent to an expression for the dielectric constant of composites, derived in 1937 by Sillars [25].

To find an expression for composites filled with impenetrable platelets Eqn. 10.27) is solved for oblate spheroids with $a_3 < a_1$ and $a_1 = a_2$:

$$S_1 = S_2 = \frac{\alpha^2}{2(\alpha^2 - 1)^{3/2}} \left(\cos^{-1}(1/\alpha) - \frac{\sqrt{\alpha^2 - 1}}{\alpha^2} \right); \quad S_3 = 1 - 2S_1 \quad 10.28)$$

where the aspect ratio $\alpha = a_1/a_3$. This shape factor S is also used in the description of dielectric and mechanical properties. In Appendix A the same shapefactor is used for the description of the Eshelby tensor. In Appendix E more attention is given to the resemblance

of models for barrier, dielectric and mechanical properties. By assuming that $\alpha \gg 1$ Eqn. 10.28) can be approximated as:

$$S_1 = S_2 \cong \frac{\pi/4}{\alpha}, \quad S_3 \cong 1 - \frac{\pi/2}{\alpha} \quad (10.29)$$

And Eqn. 10.26) then becomes:

$$\frac{P_{c,3}}{P_m} \cong 1 - \frac{c_r \alpha}{\pi/2} \quad (10.30)$$

So for large aspect ratios the permeability is a function of the product of aspect ratio and volume fraction. The requirement that the ellipsoids are non-interacting implies that $c_r \alpha \ll 1$. At dilute concentrations if $c_r \alpha \ll 1$ Nielsen's equation can be approximated as:

$$\frac{P_c}{P_m} \cong 1 - \frac{c_r \alpha}{2} \quad (10.31)$$

Eqn. 10.30) has much resemblance to Nielsen's equation. At dilute concentrations the only difference between both theories is a factor of $\pi/2 \cong 1.6$ instead of a factor 2.

10.3.3.6 Eshelby's equivalent inclusion method: Hatta's model

Hatta et al. [1] derived a theoretical model to calculate the thermal conductivity of an aligned platelet reinforced composite, by using Eshelby's equivalent inclusion model. Based on the mathematical analogy between thermal conductivity and mass transport this model can be used without adaptation for gas permeability. They arrived at the following equation:

$$\frac{P_{c,i}}{P_m} = \left\{ 1 + \frac{(\beta-1)c_r}{1 + S_i(1-c_r)(\beta-1)} \right\} \quad i=1,2,3 \quad (10.32)$$

where S_i is defined as in Eqn. 10.28. By using a mean field approach van Beek [26] found the same expression for the dielectric constant. If the platelets are impenetrable $P_r=0$ and by using Eqn. 10.29), Eqn. 10.32) can be simplified to:

$$\frac{P_c}{P_m} \cong \frac{1}{1 + \frac{2c_r \alpha}{\pi(1-c_r)}} \quad (10.33)$$

Except for the factor $1-c_r$ in the denominator Eqn. 10.32) is equal to Eqn. 10.26). Therefore the models of Hatta and Batchelor coincide at small volume fractions. Hatta's model has the advantage that it is valid up to larger volume fractions.

10.3.3.7 Assessment of diffusivity models

In Fig. 10.9 the relative diffusivity D_c/D_m at a volume fraction of 1 wt% is calculated with the models discussed above and plotted as a function of aspect ratio. The models of Batchelor and Cussler are not plotted because within their range of applicability they overlap with the models of Hatta and Brydges respectively. The models of Hatta and Nielsen give comparable results. The model proposed by Brydges clearly gives wrong results at low aspect ratios since this model is only applicable at high c, α .

The adjusted Brydges model performs much better at low aspect ratios and coincides with the original Brydges model at high aspect ratios as was indicated in subsection 10.3.3.2. The predictions of the adjusted Brydges model lie below Hatta and Nielsen's predictions, while the predictions of the model of Frederickson lie above. It is clear that the range of diffusivities predicted by the models is rather wide. At an aspect ratio of 100 and a volume fraction of 1% the adjusted model of Brydges predicts $D_c/D_m = 0.39$ while the model of Frederickson predicts $D_c/D_m = 0.71$.

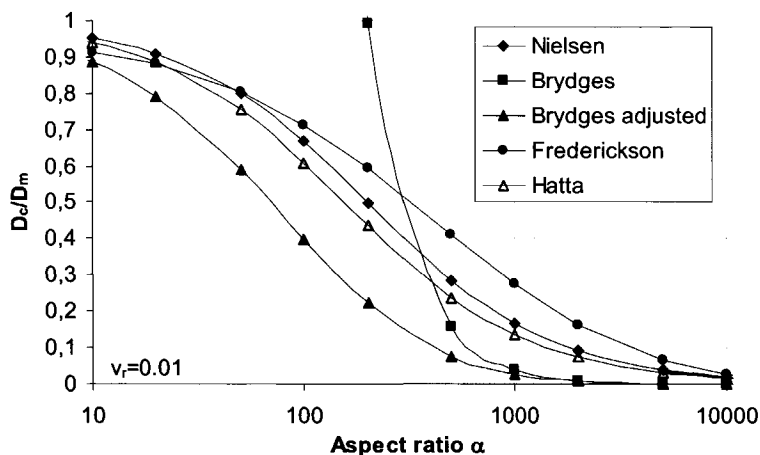


Figure 10.9 Relative diffusivity as a function of aspect ratio of several models introduced in this Chapter at 1 vol% of filler.

Nielsen: Eqn. 10.12); Brydges: Eqn. 10.16); Brydges adjusted : Eqn. 10.17)
Frederickson Eqn. 10.25); Hatta: Eqn. 10.32)

As was discussed, Nielsen's model gives a very simplified representation of the diffusion process in a ribbon-reinforced composite. Since it is a two-dimensional theory, it is valid for ribbons rather than for platelets. Further it only includes the tortuosity of the diffusing path and neglects the effect of reduced channel area. It is therefore expected that Nielsen's model only gives a qualitative prediction of the diffusivity of platelet filled composites.

Brydges and Cussler use flow resistance to calculate the diffusivity of a platelet filled composite. It is shown that their models are only meaningful to predict the diffusivity at intermediate to high volume fractions as $c, \alpha \gg 1$. At small volume fractions as $c, \alpha \ll 1$ a Nielsen's like model is more appropriate.

The adjusted Brydges model is more appropriate at low volume fractions than the original Brydges model. It is appropriate for ribbons and therefore underestimates the permeability of platelets reinforced composites.

The models of Batchelor and Hatta have a sound theoretical basis and are exactly valid within the boundary conditions given. Also they are valid for platelets instead of ribbons. Batchelor's model is only valid at very dilute concentrations if the flow around the particles is not disturbed by the presence of other particles. This is true only if $c_r\alpha \ll 1$. In nanocomposites this can only be achieved at very small volume fractions ($<0,1\%$). Hatta's model has a wider range of applicability. At small concentrations it reduces to Batchelor's model. The essential assumption in both models is that every particle experiences a flow field that is parallel to the flow field applied to the whole composite. Usually this flow field is directed perpendicularly to the plane of the platelets. In Hatta's model the interaction between particles is accounted for by changing the magnitude of the flow field. It is supposed that the direction of the flow field is not changed by the presence of other particles. Fig. 10.5 shows that at large volume fractions, as $c_r\alpha > 1$, the flow field that is experienced by the particles is no longer parallel but mainly perpendicular to the to the applied flow field (vertical flow lines instead of horizontal flow lines). So Hatta's equation is not valid if $c_r\alpha > 1$.

Based on plausible arguments it was concluded earlier that at large aspect ratios and small volume fractions, the permeability should be a unique function of $c_r\alpha$. The models of Nielsen, Batchelor, Hatta, Brydges, and Cussler indeed fulfil this requirement. Frederickson finds that the permeability is a unique function of $c_r\alpha/\ln(\alpha)$. The factor of $\ln(\alpha)$ does not vanish at high aspect ratio. Therefore it is thought that the model introduced by Frederickson cannot hold.

After examining all available models found in the literature, it is concluded that Hatta's model should give good predictions at small to intermediate volume fractions (if $c_r\alpha < 1$). At higher volume fractions, when the direction of the flow around the platelets is changed by the presence of the other platelets (if $c_r\alpha > 1$), Hatta's model is expected to predict too high values for the diffusivity of a composite. At these concentrations the adjusted model of Brydges, suited for ribbons, is thought to be more appropriate.

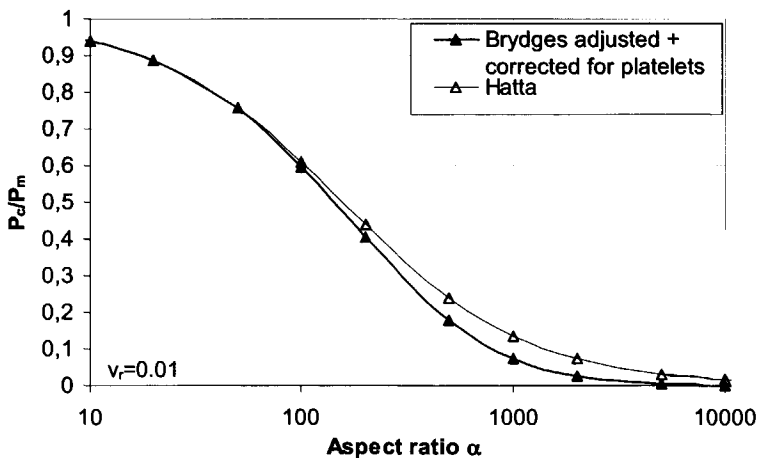


Figure 10.10 Suggested model for diffusivity through a composite filled with platelets. Hatta: Eqn. 10.32) suitable for low volumes fractions and New model based on Brydges approach Eqn. 10.33)

It can be shown that the adjusted model of Brydges in Eqn. 10.17) can be made to coincide with Hatta's model in Eqn. 10.32) at small volume fractions (if $c_r\alpha \ll 1$). Both models coincide at a low volume fraction and perfect overlap ($\gamma = 0.5$) by replacing α in

equation 10.17) by $\beta = \frac{8}{5\pi} \frac{w}{t} \approx \frac{1}{2} \frac{w}{t}$. This correction is necessary to account for platelets instead of ribbons. The final equation for diffusion through a composite filled with oriented impenetrable platelets now becomes:

$$\frac{P_c}{P_m} = \frac{1 - c_r}{(c_r \beta + 1 - c_r)(c_r \beta \gamma (1 - \gamma) + 1)} \quad 10.34$$

where $\beta = \frac{8}{5\pi} \frac{w}{t} \approx \frac{1}{2} \frac{w}{t}$. This model is suited for small volume fractions (if $c_r \alpha < 1$) as well as for intermediate and high volume fractions (if $c_r \alpha \gg 1$). As is shown in Fig. 10.10, it coincides with Hatta's model at low volume fractions.

In Fig 10.11 equation 10.34 is compared with finite element calculations, which were recently published by Gusev et al. [27]. The model uses complete 3 dimensional finite element modelling. In this respect these results are more reliable than earlier publications found on FE modelling of diffusion through composites like that of Matsuoka [28] who used 2 dimensional finite element modelling. Like stated before by using 2D modelling one implicitly assumes ribbons instead of platelets.

Fig 10.11 shows that the values calculated with equation 10.34) closely follow the finite element predictions given by Gusev. A perfect fit is found by using $\beta = 0.4 w/t$ instead of the theoretical value for β .

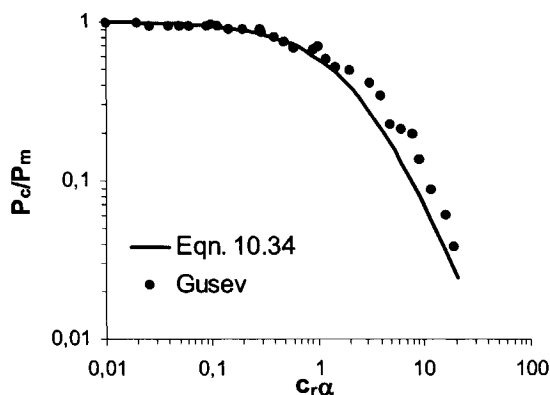


Figure 10.11. Comparison of the proposed equation for permeability of platelet filled composites 10.34) with results of finite element calculations [27].

10.3.4 Random walk simulation of transport through platelet filled composites

Eitzman et al. [29] modelled the diffusion through composites filled with ribbons, by simulating the molecular trajectories through this medium. Each molecule is supposed to move randomly with steps equal to the length of the mean free path λ . By calculating the average root mean square distance through the composite of many random walks, Eitzman calculated the effective diffusivity of a composite filled with impenetrable ribbons.

Eitzman studied the transport through composites at intermediate to high volume fractions, where the flow is mostly parallel to the plane of the platelets. In that case not only the length of the tortuous path is increased, but simultaneously the cross sectional area through which diffusion can occur is decreased. The combination of these two effects means that the alteration of the diffusion is proportional to the square of the volume fraction of the platelets. It was concluded that, Cussler's analytical model adequately describes the diffusion through such a composite.

Eitzman also conducted a thorough study to the diffusion of CO₂ through mica filled block copolymers of silicone and polycarbonate at concentrations between 5 and 17 vol% and at aspect ratios between 20 and 110. In general $3 < c_r \alpha < 10$, well outside the range where the

equation of Hatta is valid. She found a linear dependence between $\frac{D_m}{D_c} - 1$ and $\frac{c_r^2}{1 - c_r}$, and

between $\frac{D_m}{D_c} - 1$ and α^2 as is predicted by the model of Cussler. Although qualitatively the

agreement between model and experiments was excellent, the model systematically overestimated the effect of volume fraction and aspect ratio on diffusion. It is thought that this is mainly due to the fact that Eitzman uses a 2 dimensional model just like Cussler and Brydges. So essentially she modelled the diffusion through aligned ribbons instead of aligned platelets.

Eitzman showed that the calculation of the diffusivity becomes insensitive for the distance between the platelets (d) if the Knudsen number ($N_{Kn} = \bar{\lambda}/d$) is less than 0.1. The minimum distance between platelets for undisturbed diffusion through the matrix phase can now be estimated by assuming that λ is equal to the jump length of 5-10 Å found in polymers. The minimum distance then is 100 Å. For nanocomposites this is the case at volume fractions below 10 vol%.

10.3.5 Effect of polydispersity of platelet diameters

If Nielsen's model is used to predict the diffusivity of platelet filled composites, polydispersity of the aspect ratio be accounted for by averaging the patch lengths around particles with high and low aspect ratio's. According to Nielsen's assumption a particle with a width w_i increases the path length by $\frac{1}{2} w_i$. If a diffusing molecule has passed n layers of platelets, the total path length is equal to:

$$L_c = L_0 + \frac{1}{2} \sum_{i=1}^n w_i \quad (10.35)$$

which can be written as

$$\frac{D_0}{D_c} = \frac{L_c}{L_0} = 1 + \frac{1}{2} c_r \bar{\alpha} \quad \text{where} \quad \bar{\alpha} = \frac{1}{c_r} \sum c_i \alpha_i \quad (10.36)$$

where c_i is the volume fraction of platelets with aspect ratio α_i . $\bar{\alpha}$ could be called the 'mass average aspect ratio' analogous to the 'mass average molecular weight' in polymer chemistry.

10.4 Effect of misalignment of platelets on diffusivity

By using Nielsen's equation it is possible to estimate the effect of misalignment of the platelets on diffusivity. Consider the case in which all platelets are aligned under an angle θ with the plane of the film as shown in Fig. 10.12. If a molecule travels from point A to point B it will cover a distance equal to l_{AB} :

$$l_{AB} = x + \frac{1}{2}w \quad (10.37)$$

The vertical distance travelled is equal to:

$$l_{AB-y} = x + \frac{1}{2}w \sin \theta \quad (10.38)$$

To completely diffuse through the film the molecule must travel a total vertical distance L_0 . The amount of platelets encountered during this travel is equal to:

$$n = \frac{L_0}{l_{AB-y}} = \frac{L_0}{x + \frac{1}{2}w \sin \theta} \quad (10.39)$$

From geometrical considerations it can be seen in Fig. 10.12 that:

$$x = \frac{t/c_r}{\cos \theta} \quad (10.40)$$

The total distance travelled through the film now becomes:

$$L_c(\theta) = n l_{AB} = n(x + \frac{1}{2}l) = \frac{L_0}{x + \frac{1}{2}w \sin \theta} (x + \frac{1}{2}w) = L_0 \frac{(1 + A \cos \theta)}{(1 + A \cos \theta \sin \theta)} \quad (10.41)$$

where $A = \frac{1}{2} c_r \alpha$.

By using Eqn. 10.41, the diffusivity as a function of misalignment angle is calculated and plotted in Fig. 10.13. As expected the platelets with a large aspect ratio give a lower diffusivity than platelets with a smaller aspect ratio. At small misalignment the large aspect ratio platelets also show a steeper increase in diffusivity than the small aspect ratio platelets do. This indicates that at high aspect ratio the diffusivity is more sensitive for misalignment. The sensitivity for small misalignment can be estimated by calculating the relative change in path length due to small misalignment:

$$\lim_{\theta \rightarrow 0} \frac{\partial L_c / L_c}{\partial \theta} = \frac{1}{1 + A} \lim_{\theta \rightarrow 0} \frac{(1 + A \cos \theta \sin \theta)(A \sin \theta) + (1 + A \cos \theta)A(\cos^2 \theta - \sin^2 \theta)}{(1 + A \cos \theta \sin \theta)^2} = -A \quad (10.42)$$

Since $A = \frac{1}{2} c_r \alpha$, the sensitivity for misalignment increases when either the volume fraction or the aspect ratio increases. If the orientation of the platelets fluctuate within an angle $\pm \theta^\circ$ around the parallel direction, the effect on diffusivity can be estimated by calculating the average of $L_c(\theta)$ between $+\theta$ and $-\theta$. Since $L_c(\theta)$ is symmetric around $\theta=0$, it is sufficient to integrate between 0 and θ .

$$\overline{L_c(\theta)} = \frac{1}{\theta} \int_{\theta'=0}^{\theta} L_c(\theta') d\theta' \quad 10.43)$$

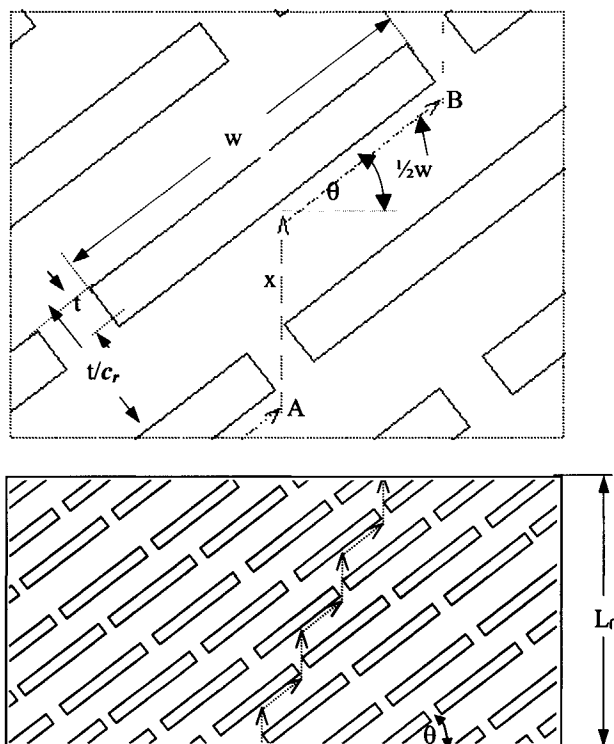


Figure 10.12 Tortuous path in a polymer film filled with platelets making an angle θ with the plane of the film.

In Fig. 10.13 this 'moving average' is plotted as a broken line. An estimate for the effect of random orientation can be obtained by calculating the average path length of platelets oriented between 0° and 90° . Fig. 10.13 shows that the barrier properties in nanocomposites with serious misalignment are expected to be much lower than in perfectly aligned nanocomposites. At random orientation (broken line at $\theta = 90^\circ$) the diffusivity of the nanocomposite with high aspect ratio platelets ($w/t = 500$) is almost 4 times higher than that for perfect orientation (broken line at $\theta = 0^\circ$). This illustrates the dramatic effect that misalignment can have on diffusivity. So in practise great care should be taken to get good orientation of the platelets.

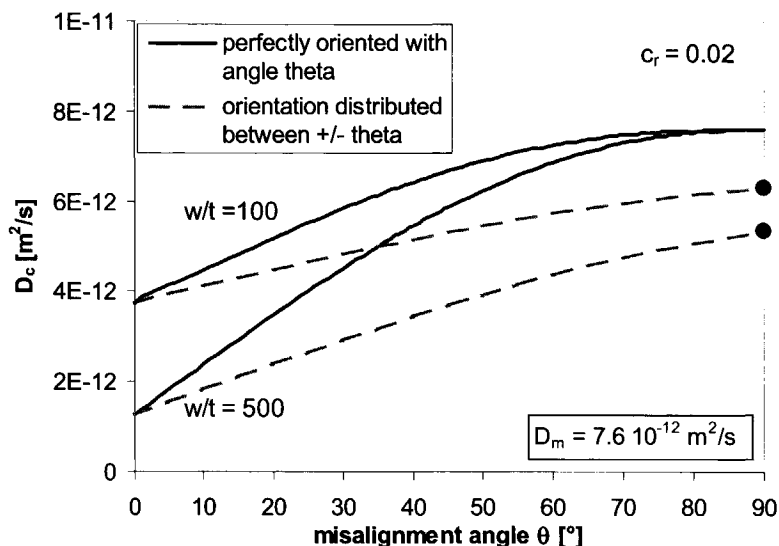


Figure 10.13 Effect of misalignment angle on the diffusivity of a material filled with impenetrable platelets. Solid line shows diffusivity if all platelets have the same misalignment angle, while the broken line shows the diffusivity if the orientation angle is randomly distributed between $\pm \theta$.

10.5 Diffusion of water in PA6 nanocomposites

In this section some experimental results are presented on the diffusion of water in PA6 nanocomposites. The experimental results are compared to theoretical predictions.

10.5.1 Absorption measurement and determination of diffusivity

To measure the effect of clay platelets on the rate of diffusion, dry injection moulded PA6 nanocomposite bars (4 x 10 x 75 mm), were stored at 70 °C and 68% relative humidity (%RH) for up to 1000 hours. The increase in weight was monitored until saturation was obtained. The nanocomposites contained between 0 and 7.5 weight % of silicate. The high storage temperature of 70 °C is chosen to accelerate the diffusion process. At room temperature diffusion of water in PA6 is very slow. It takes a few months or longer for a 4 mm sample to reach equilibrium. By increasing the temperature, the rate of water uptake can be accelerated substantially. The weight increase is monitored at selected time intervals and is listed in Table 1 ($\Delta M\%$). The samples used, do not have a sheet like shape as is assumed in Eqn. 10.4.

To calculate the diffusivity, Eqn. 10.6 was used to account for water absorption from the sides of the sample. The diffusivity was estimated by taking into account only the water uptake during the first 6 hours of absorption. Fig. 10.14 shows the weight increase of the PA6 nanocomposites as a function of time. Points denote measurements while lines are calculated by fitting Eqn. 10.4 through the experimental points. The lines are meant to guide the eye, not to calculate the diffusivity.

In order to get a good impression of what happens at short time, the data are plotted against \sqrt{t} in Fig. 10.15. As predicted by Eqn. 10.6 at short time the water uptake increases linearly with the square root of time.

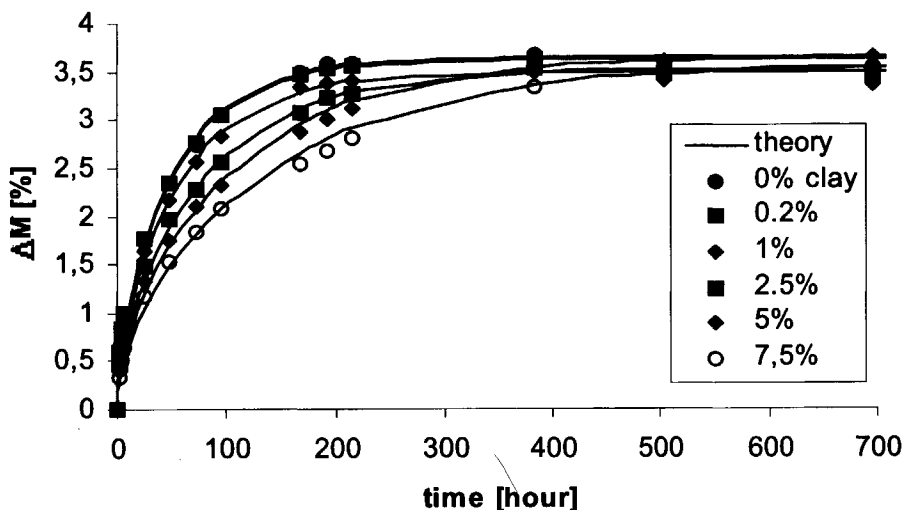


Figure 10.14 Absorption of water in PA6 nanocomposites at 70 °C and 62% relative humidity. Different symbols represent measurements on nanocomposites with different clay content. Lines to guide the eye are fitted to the experiments using Eqn. 10.4.

	Weight% silicate					
	0	0.2	1	2.5	5	7.5
Time [hr]	ΔM%	ΔM%	ΔM%	ΔM%	ΔM%	ΔM%
0	0	0	0	0	0	0
2	0,60	0,59	0,53	0,46	0,40	0,34
4	0,85	0,85	0,77	0,68	0,57	0,51
6	1,00	1,00	0,93	0,84	0,73	0,65
24	1,74	1,76	1,64	1,48	1,33	1,17
48	2,34	2,35	2,17	1,96	1,74	1,53
72	2,74	2,76	2,56	2,27	2,11	1,84
96	3,05	3,05	2,83	2,57	2,33	2,07
168	3,50	3,47	3,33	3,08	2,87	2,55
192	3,58	3,54	3,38	3,23	3,01	2,68
216	3,59	3,55	3,41	3,28	3,11	2,81
384	3,67	3,62	3,50	3,53	3,59	3,33
504	3,57	3,49	3,40	3,47	3,60	3,44
696	3,53	3,45	3,35	3,45	3,65	3,52
840	3,52	3,43	3,32	3,43	3,62	3,56
1008						3,54
D [m ² /s]	7.6 10 ⁻¹²	7.8 10 ⁻¹²	6.9 10 ⁻¹²	5.4 10 ⁻¹²	3.7 10 ⁻¹²	3.0 10 ⁻¹²

Table 10.1 Relative increase in weight of PA6 nanocomposites, during water uptake at 70°C and 68 % relative humidity. The diffusion coefficient is listed in the last row.

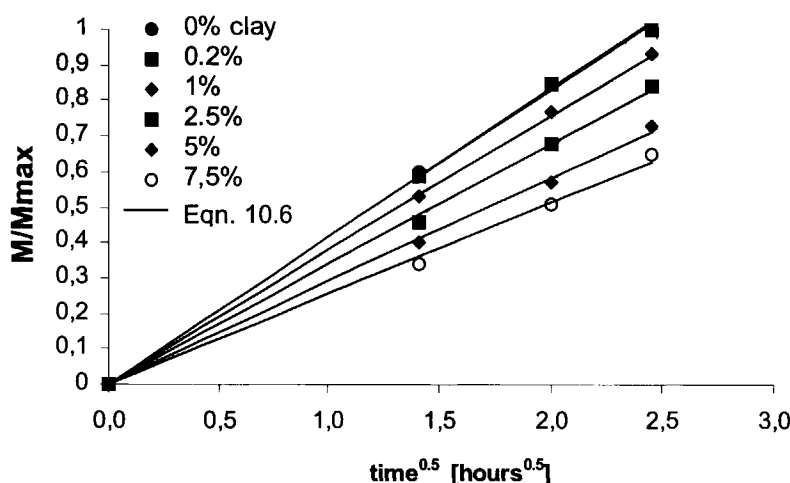


Figure 10.15 Absorption of water in PA6 nanocomposites during the first 6 hours at 70 °C and 62 % relative humidity, plotted versus the square root of time. Different symbols represent measurements on nanocomposites with different clay content. Lines are fitted to the experiment using Eqn. 10.6.

10.6 Evaluation and conclusions

10.6.1 Evaluation

The linear relationship at short times in Fig. 10.15 proves that the nanocomposites show simple Fickian diffusion of water. In Fig. 10.16 the experimental and theoretical diffusion coefficients of the injection moulded PA6 nanocomposites are plotted against the volume fraction of silicate. Theoretical results are calculated with Eqn. 10.12, using an aspect ratio $w/t=100$, as was found from TEM pictures.

Fig. 10.16 shows that Nielsen's model (solid line) predicts the experimental results very well. According to Eqn. 10.42 the diffusivity is very sensitive to misalignment of the platelets. The good fit with Nielsen's equation indicates that the orientation of the clay platelets in the injection-moulded plates is high.

Results of Katz et al. [8] confirm the high orientation of platelets in injection-moulded specimens. They showed that the orientation of mica platelets in an injection moulded polypropylene-mica composite is good, except for a thin region in the centre.

X-ray measurements of Kojima et al. [19] on 3mm thick injection moulded PA6-clay nanocomposites also give evidence for high orientation of clay platelets in an injection-moulded specimen. They found that in the skin (0-0.5 mm) the clay platelets are oriented perfectly parallel to the surface of the specimen. In the intermediate layers (0.5-1.2 mm) the clay platelets are mainly parallel to the specimen's surface with a fluctuation of $\pm 15^\circ$. In the centre of the sample (1.2-1.8 mm) the platelets are oriented perpendicular to the surface of the sample. Figure 10.17 shows the orientation of clay platelets in an injection moulded plate.

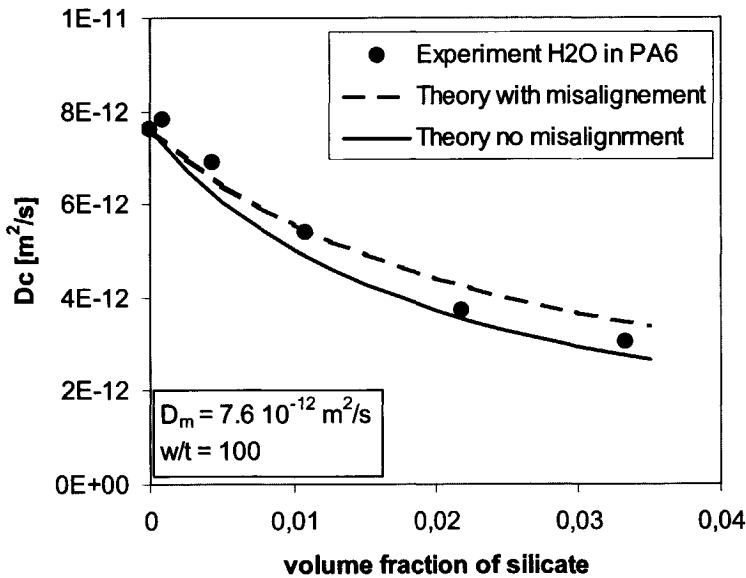


Figure 10.16 Comparison between experimental and theoretical diffusivity of injection moulded PA6 clay nanocomposites. Experimental results are shown as symbols while theoretical predictions are shown as lines. The theoretical diffusivity is calculated using an aspect ratio of $w/t = 100$ and a matrix diffusivity of $D_m = 7.6 \cdot 10^{-12} \text{ m}^2/\text{s}$. Solid lines were calculated assuming perfect alignment and broken lines by assuming the same misalignment as was found by Kojima [19] in an injection moulded bar.

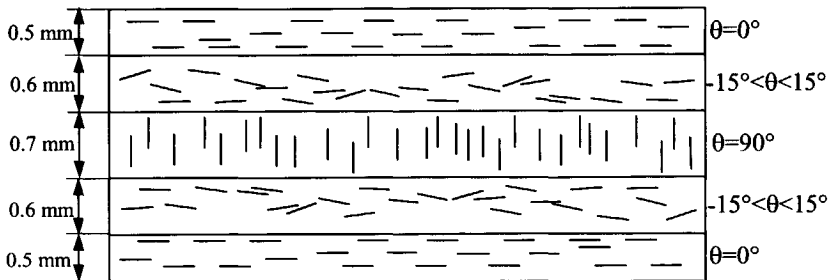


Figure 10.17 Orientation of clay platelets in 3 mm an injection moulded PA6-clay nanocomposite plate according to Kojima [19]

Although Kojima et al. find a relatively high orientation of the clay platelets, the orientation they find is not perfect throughout the specimen. It is therefore useful to calculate how serious diffusivity is influenced by the misalignment given by Kojima. If it is assumed that our samples have the same orientation distribution as the samples of Kojima, the effect of misalignment can be calculated. To calculate the effect of this 'laminated' misalignment, the tortuous path lengths of the skin, the intermediate layer and the middle layer are calculated

separately. Next these lengths are summed, to obtain the total tortuous path length of the 'laminated' nanocomposite:

$$D_c = D_m \frac{L_0}{L_{c_tot}} = D_m \frac{L_{0_tot}}{2L_{c_skin} + 2L_{c_intermediate} + L_{c_middle}} \quad (10.44)$$

where the tortuous path length of each layer can be calculated by using Eqn. 10.43). A numerical example is given below for a composite with 2 vol% of platelets having an aspect ratio $w/t = 100$ and a matrix diffusivity of $D_m = 7.6 \cdot 10^{-12} \text{ m}^2/\text{s}$:

$$D_c = 7.6 \times 10^{-12} \frac{3}{2 \times 0.5 \times 2 + 2 \times 0.7 \times 1.78 + 0.6} = 4.48 \times 10^{-12}$$

This correction for misalignment was calculated and plotted in Fig. 10.16. As can be seen in Fig. 10.16 the effect of the small misalignment on diffusivity is not large.

Yano et al. [12, 13] determined the permeability of polyimide nanocomposite films containing 2 wt% of clay. They used clays with different aspect ratios: hectorite ($w/t = 46$), saponite ($w/t = 165$), montmorillonite ($w/t = 218$) and synthetic mica ($w/t = 1230$). TEM pictures showed that the platelets were oriented parallel to the film surface. The montmorillonite and mica nanocomposites were well exfoliated while the hectorite and saponite nanocomposites contained aggregates of clay particles. Fig. 10.18 shows the effect of aspect ratio on the diffusivity of the polyimide nanocomposites. Symbols represent the measurements while the solid line represents Nielsen's equation (Eqn. 10.12). The diffusivity is strongly decreased by adding synthetic mica with a very large aspect ratio. This is also predicted by Nielsen's equation, which gives a reasonable fit with the experimental results. The poor fit at small aspect ratios (hectorite and saponite) was attributed to poor exfoliation of the nanocomposites.

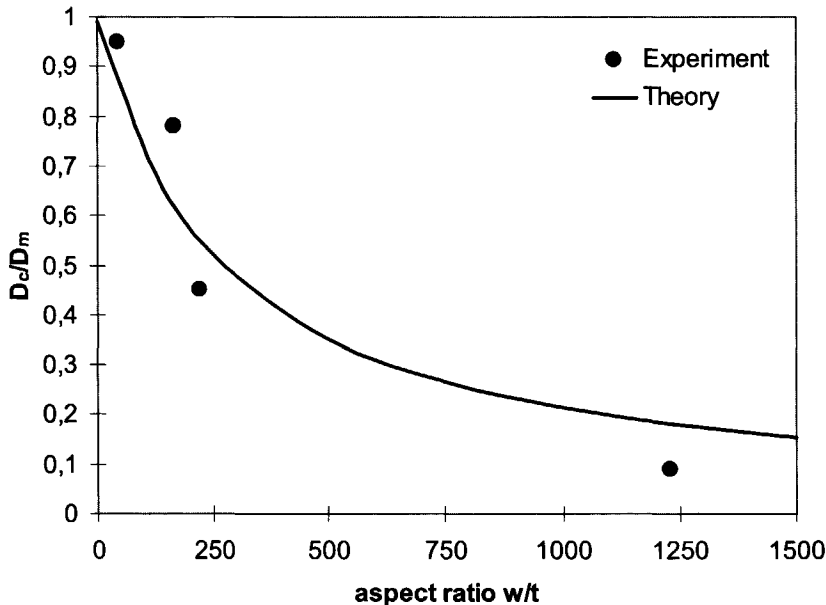


Figure 10.18 The effect of clay aspect ratio on the diffusivity of water in polyimide nanocomposites. From [12, 13].

10.7 Conclusions

- A new model for diffusion through platelet filled composites is introduced. Contrary to existing models it is suited for platelets instead of ribbons and allows calculation of diffusivity at low ($c, \alpha < 1$) and high volume fractions of clay ($c, \alpha > 1$). The model closely follows the predictions of finite element calculations.
- A numerical model was derived that shows that misalignment of platelets can strongly increase the diffusivity a composite filled with platelets.
- It is theoretically derived that the diffusivity of a platelet filled composite depends on the 'mass average' aspect ratio.
- The diffusion of water in injection moulded PA6-nanocomposites can be described very well by simple Fickian diffusion.
- The experimental diffusivity of water through PA6 and polyimide nanocomposites agrees well with the predictions of Nielsen's model.
- The good agreement between experiment and theory indicates that the aspect ratio of the clay platelets determine the permeability of nanocomposites. Changes in polymer properties, caused by the large surface area of the clay platelets, do not significantly change the diffusivity of PA6-clay or polyimide-clay-nanocomposites.

10.8 References

- [1] Hatta H., Taya M., Kulacki F.A., Harder J.F., *Thermal diffusion of composites with various types of filler*, J. Comp. Mat. **26**(5), 1992, p 612-625
- [2] L.E. Nielsen, *Models for the permeability of filled polymer systems*, J. Macromol. Sci. **A1**(5), 1967, p 929-942
- [3] N.F.A. van der Vegt, *Molecular dynamics simulations of sorption and diffusion in rubbery and glassy polymers*, PhD Thesis, University of Twente, The Netherlands, 1998
- [4] N. Lützow, A. Tihminlioglu, R.P. Danner, J.L. Duda, A. de Haan, G. Warnier, J. M. Zielinski, *Diffusion of toluene and n-heptane in polyethylenes of different crystallinity*, Polymer **40**, 1999, p 2797-2803
- [5] R.J. Hernandez and R. Gavara, *Sorption and transport of water in nylon-6 films*, J. Polym. Sci. B Pol. Phys. **32**(14), 1994, p 2367-2374
- [6] B.S. Mehta, A. T. Dibenedetto and J.L. Kardos, *Prediction of transport properties from equations of elasticity*, Pol. Eng. Sci. **18**(2), 1978, p 114-119.
- [7] W.T. Brydges, S.T. Gulati and G. Baum *Permeability of glass ribbon-reinforced composites*, J. Mat. Science **10**, 1975, p 2044-2049.
- [8] H.S. Katz and J.V. Milewski, *Handbook of Fillers and Reinforcements for Plastics*, van Nostrand Reinhold, New York, 1978, section VIII.
- [9] M. Fenton and G. Hawley, *Properties and economics of mica-reinforced plastics related to processing conditions*, Polym. Compos. **3**(4), 1982, p 218-229.
- [10] A. Södergård, K. Ekman, B. Stentlund and A. Lassas, *The influence of EB-crosslinking on barrier properties of HDPE-mica composites*, J. Appl. Pol. Sci. **59**, 1996, p 1709-1714.
- [11] Y. Kojima, K. Fukumori, A. Usuki and A. Okada and T. Kurauchi, *Gas permeability in rubber-clay hybrid*, J. Mat. Sci. Let. **12**, 1993, p 889-890.
- [12] K. Yano, A. Usuki and A. Okada, T. Kurauchi and O. Kamigaito, *Synthesis and properties of polyimide-clay hybrid*, J. Pol. Sci. A: Pol. Chem. **31**, 1993, p 2493-2498.
- [13] K. Yano, A. Usuki and A. Okada, *Synthesis and properties of polyimide-clay hybrid films*, J. Pol. Sci. A: Pol. Chem. **35**(11), 1997, p 2289-2294.

- [14] Y. Kojima et al, *Sorption of water in nylon-6-clay hybrid*, J. Appl. Pol. Sci. **49**, 1993, p 1259-1264.
- [15] J. C. Matayabas, S. R. Turner, B. J. Sublett, G. W. Conell, J.W. Gilmer and R.B. Barbee, *High I.V. polyester compositions containing platelet particles*, Patent WO 98/29499, 9 July 1998.
- [16] P.B. Messersmith and E. Giannelis, *Synthesis and barrier properties of poly (ϵ -caprolactone)-layered silicate nanocomposites*, J. Pol. Sci. A: Pol. Chem. **33**, 1995, p 1047-1057.
- [17] Datasheet, *Unitika polyamide 6-based nanocomposite (M1030D)*.
- [18] Datasheet, *Nylon6/clay composites*, Unitika, October 1993.
- [19] Y. Kojima, A. Usuki, M. Kawasumi, A. Okada, T. Kurauchi, O. Kamigaito, K. Taji, *Novel preferred orientation in injection-molded Nylon-6 clay hybrid*, J. Pol. Sci. B: Pol. Phys. **33**, 1995, p 1039-1045.
- [20] Barrer R.M. and J.H. Petropoulos, *Diffusion in heterogeneous media: Lattices of parallelepipeds and a continuous phase*, Brit. J. Appl. Phys. **12**, 1961, p 691-697.
- [21] E.L. Cussler, S.E. Hughes, W.J. Ward, R. Aris, *Barrier membranes*, J. Membrane Sci. **38**, 1988, p 161-174.
- [22] G. H. Frederickson and J. Bicerano, *Barrier properties of oriented disk composites*, J. Chem. Phys. **110(4)**, 1999, p 2181-2188.
- [23] Batchelor G.K., *Transport properties of two-phase materials with random structure*, Ann. Review of Fluid Mechanics **6**, 1974, p 227-255.
- [24] J. M. Whitney, R.L. McCullough, *Micromechanical Modeling*, Delaware Composite Design Encyclopedia-volume 2, Technomic Publishing Company, 1990.
- [25] Sillars R. W., *The properties of a dielectric containing semi-conducting particles of various shapes*, J. Inst. Electr. Eng. **80**, 1937, p 378-394.
- [26] van Beek L.K.H. , *Dielectric behaviour of heterogeneous systems*, Progress in Dielectrics, Ed. J.B. Birks, 1967, p 476-491.
- [27] A.A. Gusev and H.R. Lusti, *Rational design of nanocomposites for barrier applications*, Adv. Mat., 2001, to be published.
- [28] T. Matsuoka, *Numerical simulation of water diffusion through polymer filled with plate-like particles*, Toyota Chuo Kenyusho R&D Rebyu **29(1)**, 1994, p 49-57.
- [29] D.M. Eitzman, R.R. Melkote and E.L. Cussler, *Barrier membranes with tipped impermeable platelets*, AIChE Journal **42(1)**, 1996, p 2-9.

Rheology of nanocomposites

Abstract

Some remarkable features of the melt rheology of nanocomposites are highlighted by comparing the melt rheology of nanocomposites with that of microcomposites. The effect of particle size and aspect ratio were investigated by filling PE and PA6 with nanometer and micrometer sized particles of high and low aspect ratio. Shear rheology at small and large shear deformation was performed and melt strength and melt extensibility were determined.

The visco-elastic behaviour of polymer nanocomposites in the molten state proves to be very different from that in the solid state. In the molten state, the effect of particle size on visco-elasticity is huge, whereas the effect of clay aspect ratio is small. In contrast, the solid-state visco-elasticity is hardly affected by particle size while the aspect ratio has a strong influence. Unlike microcomposites, nanocomposites have a high melt strength and a high viscosity that does not collapse at large shear deformation.

Several mechanisms are considered to explain the strong visco-elastic response, the lasting viscosity at large shear deformation and the high melt-strength of nanocomposites. By a process of exclusion only two mechanisms remain that can qualitatively explain the observed results: tethering of polymer chains on the clay platelets and the existence of an electrical double layer on the clay platelets.

11.1 Introduction

In previous chapters, it was shown that the solid-state stiffness of nanocomposites is insensitive to the size of the clay platelets. Consequently, the visco-elastic behaviour of nanocomposites in the solid state is similar to that of conventional composites. Also the viscosity and elasticity of conventional filled molten polymers is insensitive to particle size, as long as the particles are relatively large ($>10\text{ }\mu\text{m}$) and particle-particle interactions can be neglected.

By contrast, the viscosity and elasticity of a molten polymer increases strongly by filling it with small nano-sized clay platelets or by sub-micron particles in general [1]. Several mechanisms are proposed in the literature to explain the dramatic increase in polymer viscosity and elasticity upon addition of small particles. The elasticity might be a consequence of the formation of a network of touching particles [2].

The surface energy of the interface between particle and polymer is also mentioned to contribute to viscosity and elasticity [3]. Formation of an electrical double layer can increase the interaction between particles and contribute to the elasticity [4]. Rotation of particles due to Brownian motion [5] or shear flow also increases viscosity and elasticity.

The objective of this chapter is to find out what mechanism is causing the elastic behaviour of nanocomposites, by comparing the rheology of nanocomposites with that of conventional composites.

Three different series of samples were made to investigate the effect of particle size and particle shape on rheology. In the first series the effect of particle size was studied by filling HDPE with inert BaSO_4 particles of low aspect ratio. In a second series the effect of particle shape was studied using HDPE-clay nanocomposites containing clays with different aspect ratio. Also a series of PA6-silicate microcomposites and nanocomposites were studied with sphere shaped (glass spheres and aerosils) and plate shaped fillers (mica, nanoclay).

11.1.1 Conventional particulate filled polymers

Malkin [1] gave a review of the effects that fillers can have on the rheology of polymers. According to Malkin, the most important rheological characteristic of filled polymers is the existence of a yield stress. Below the yield stress, the polymer will not flow. The yield stress is a consequence of a network that is formed by chains of filler particles. Quite surprisingly, the magnitude of the yield stress is independent of polymer viscosity. This is illustrated in an experiment on carbon black in poly(isobutylene). By increasing the temperature, the polymer viscosity decreased one hundred times, while the yield stress remained unchanged. So yield stress is determined by the strength of the network and not by the viscosity of the polymer.

Kamphuis et al. [2] proposed a mathematical model where the network is formed by chains of connecting particles. In this model, chains break because of thermal motion or external stresses. The equilibrium between breaking and formation of chains determines the stiffness of the network. Although this model closely approaches the true morphology of a dispersion of small particles, its practical use is limited because of the complexity of the model and the difficulty in determining parameters like chain stiffness, chain density and interaction forces. The model gives good insight though, in the parameters that determine the stiffness of a network of filler particles.

The probability of particles to connect and form chains depends on inter-particle distance. The smaller the distance is between two particles the higher the probability that the particles connect. The strength of the connection, and consequently the strength of the whole chain, is determined by the attractive forces between the particles. The stiffness and strength

of the network will thus increase by lowering the inter-particle distance or by increasing the attractive forces between particles.

The inter-particle distance can be lowered by increasing the concentration, by lowering the particle size or by increasing the aspect ratio of the filler particles. In practise, it is indeed found that these three parameters strongly increase the viscosity of a filled polymer.

The attractive forces between particles are sensitive to the properties of the filler particles and the properties of the polymer interface between the particles. Particles with a high polarity will have higher attractive forces than particles with a low polarity. If a polymer interface exists between particles, the properties of this interface will also strongly influence the magnitude of the attractive forces between the particles. By adding a binding agent that connects the particles to the polymer, a layer of absorbed polymer is formed on the surface of the particles. This increases the apparent volume of solid particles, but it inhibits direct contact between the filler surfaces. So interfacial treatment can increase or decrease the strength of the network, depending on the nature of the filler and the interface.

Also the surface energy of the interface between polymer and filler can contribute to the elastic behaviour of a compound. If the surface area between polymer and filler is increased, because of detachment or otherwise, the total surface energy of the compound is increased. This will lead to an elastic rheological response. Therefore, fillers with a large surface area will have a larger rheological response than fillers with a small surface area.

Rucker and Bike [3] investigated the effect of interfacial adhesion on the rheological behaviour of silica-filled polymers. Dynamic experiments showed that the resistance to flow of the filled polymers was inversely related to the work of adhesion between polymer and filler. Stronger adhesion thus resulted in lower viscosity. This trend was found to be true within the linear visco-elastic range for all filler volume fractions over all frequencies tested. Furthermore they found that the mechanisms of energy storage and dissipation only change slightly with filler volume fraction when there is strong adhesion between the two components.

This is not the case when there is poor adhesion. Large (3 orders of magnitude) changes in the dynamic moduli result from changes in the filler volume between 3 and 33%, indicating that the mechanism of energy storage changes, especially at low frequencies. From the findings of Rucker and Bike it can be concluded that without adhesion the polymer contains a lot of deformable surface area at the interface between polymer and filler. The energy needed to deform these surfaces strongly contributes to the viscosity and elasticity of filled polymers. The inverse relation between work of adhesion and resistance to flow also suggests that a high work of adhesion prevents the formation of a network of touching particles and thus lowers the elasticity and viscosity.

A network does not necessarily exist of particles that physically touch each other. The most important thing is that the particles feel each other's presence and are able to transfer stresses. Clay particles in suspension owe their stability to mutual repulsion when the electrical double layers on their surfaces interact on approach [4]. As was mentioned in Chapter 2, clay platelets are negatively charged. A layer of positively charged counter ions surrounds each platelet, forming an electrical double layer. If two clay particles approach, their positively charged outside layers will provide a repulsive force. Therefore, even if clay platelets do not touch each other, they are able to transfer stress. If two clay platelets approach at very close distance ($<10\text{\AA}$) the structure of the double layers can change. Instead of two separate layers of counter ions between approaching surfaces, one central layer might be formed and electrostatic attraction is created. In this case, particles tend to aggregate and form a network of touching particles. Polymer molecules and surfactants are able to stabilise a clay suspension and prevent aggregation to some extent. Luckham et al. [4] wrote a review article on this subject.

11.1.2 Nanocomposites

In a nanocomposite, the particles are very small, they have a large aspect ratio, a good interaction with the surrounding polymer and they have an electrical double layer. Thus in a nanocomposite all parameters are combined to create a strong network. Therefore, it can be expected that a molten nanocomposite will have a high elasticity, a high viscosity and a high yield stress.

B. Krishnamoorti et al. [6,7] investigated the rheology of poly(ϵ -caprolactone) (PCL), poly(dimethylsiloxane) (PDMS) and nylon-6 (PA6) nanocomposites. They found that by addition of only 5-wt% of layered silicate, the low frequency dynamic modulus of molten PCL and PA6 increases about two decades in a Dynamic Mechanical Spectrometry (DMS) measurement. At high frequencies ($\omega > 100$ radian/s) the dynamic modulus approaches the dynamic modulus of the unfilled polymer. At very low frequencies ($\omega < 1$ radian/s) the dynamic modulus of the PCL and PA6 nanocomposites shows a plateau, as evidence for elastic behaviour, while the PDMS nanocomposite shows Newtonian behaviour. It was suggested that the reason for elastic behaviour of the PCL and PA6 nanocomposites was tethering of polymer chains to the clay particles while the PDMS nanocomposites showed Newtonian behaviour because of the absence of tethered chains.

Lee et al. [8] found that the rheological behaviour of polymer/layered silicate nanocomposites not only strongly depends upon their microstructure but also upon their interfacial characteristics. A simple intercalated polymer (polystyrene), with a low interaction with the clay, only shows a small enhancement of viscosity at low frequency. A polymer with an intercalated structure but a strong interaction with the clay surface like (Polystyrene-co-maleic anhydride) shows distinct plateau behaviour at low frequencies. Polyethylene-g-maleic anhydride/clay nanocomposite, having both good exfoliation and strong interaction, exhibits plateau like behaviour at low frequency and enhanced dynamic modulus at high frequency. Lee also mentioned the formation of a percolating structure of clay particles as a possible reason for plateau like behaviour of nanocomposites.

Hoffmann et al. [9] studied the rheology of in situ polymerised PA12-clay nanocomposites. They studied the effect of temperature, polymer molar mass and tethering of polymer chains on the rheology of PA12-clay nanocomposites. Their research was strongly complicated because the molar mass of the tethered chains decreased at increasing clay concentration. It was concluded that the time-temperature superposition principle holds for PA-12 nanocomposites, enabling the creation of master curves. With tethered chains, the slopes of G' and G'' in the terminal region are considerably lower than for the neat polymer, indicating formation of a superstructure. If the polymer chains are not tethered, the slopes of G' and G'' are similar to that of the neat polymer. This indicates that by absence of tethering, the rheology of PA-12 nanocomposites is polymer dominated.

11.1.3 Scope

In the literature on nanocomposites [6-9] the plateau-like behaviour at low frequencies is attributed to strong interaction or tethering of polymer chains to the clay layers. In contrast, literature on filled polymers [3] indicates that the elasticity of a filled polymer decreases if the interfacial energy increases. Other publications [1,2] emphasises the role of network formation on elasticity.

It is very difficult to distinguish which mechanism is responsible for the elasticity of a filled polymer. Most often good interaction between polymer and filler is necessary to obtain

a good dispersion. Good dispersion in its turn promotes the formation of a network. So it is tempting to conclude that the good interaction between polymer and filler is causing the elastic behaviour, while in reality it might be the formation of a network that is causing it.

In the nanocomposites studied in the literature, this is just the case. All nanocomposites with a plateau like behaviour not only have good interaction with the clay, but also contain very small particles that make the formation of a network probable.

In Section 11.2, it is investigated if good interaction between polymer and filler is a prerequisite for plateau like behaviour. This is done by filling HDPE with inert particles with particle sizes ranging between 100 nm and 10 μm .

Section 11.3 discusses the effect of aspect ratio of nano-dispersed clay on rheology. To this end, a series of HDPE nanocomposites is made using clays with equal surface treatment but with different aspect ratios.

In Section 11.4, the effect of particle size and aspect ratio on the shear and extensional rheology of filled polymers is studied. This is done by filling PA6 with silicate particles of different sizes and aspect ratios. Both micrometer-sized silicates like glass-spheres and mica platelets and nanometer sized silicates like aerosils and nano-dispersed clay are used as model fillers for PA6.

11.2 HDPE with nano- and micrometer particles of low aspect ratio

In this section, the effect of particle size on rheological properties is discussed. To this end the rheology was measured of HDPE filled with inert cubical shaped BaSO_4 particles of varying size and level of dispersion.

11.2.1 Preparation

Untreated BaSO_4 was used as inert model filler for HDPE. Four types of BaSO_4 (K4, HN, HP and HU from Sachtleben) were added to HDPE (DSM Stamylan® 9089 F) at a concentration of 20 vol% (53.3 wt%). The BaSO_4 fillers differed in primary particle size as listed in Table 11.1.

Type	Average primary particle diameter [μm]	Average agglomerate diameter [μm]	A_{BET} Surface area [m^2/g]	$D_{\text{eq}} = 6/A_{\text{BET}}\rho$ Calculated from BET [μm]
K4	10*	10	0.4	11.6
HN	1*	1	2.7	0.52
HP	0.15*	10	9.1	0.15
HU	0.1*	10	12.2	0.11

*According to the producer (d50 from sedimentation measurements after 30 min ultrasonic vibration)

Table 11.1 Types of BaSO_4 used as inert filler in HDPE

SEM photographs of these fillers are shown in Figs. 11.1 to 11.3. The particles have an aspect ratio of about 1 and have cubical shape. The filler K4 (Fig. 11.1) contains no agglomerates and is easy to disperse. Type HN (Fig. 11.2) contains agglomerates of loosely connected particles. Type HU (Fig. 11.3) contains primary particles that are strongly connected into large agglomerates. The HP type BaSO_4 is not shown to limit the number of photographs. Like the HU type BaSO_4 , the HP-type consists of sphere shaped agglomerates of small primary particles.

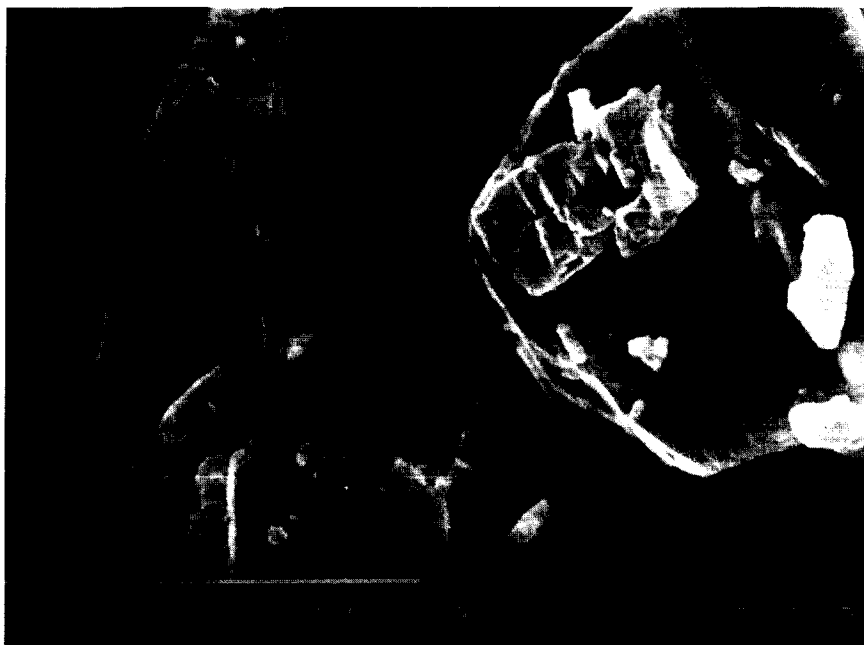


Figure 11.1 SEM photograph of BaSO₄ type K4. Primary particle size $\approx 10 \mu\text{m}$. No agglomerates.

The surface area of the particles is determined by the BET technique. This technique measures the amount of gas (nitrogen) needed to form a monolayer of gas molecules on the filler's surface. The BET surfaces are determined after vacuum pumping of the powders at 300 °C. The equivalent particle diameter (D_{eq}) is determined from the BET-surface area using the equation: $D_{eq} = 6 / A_{BET} \rho$, where A_{BET} is the surface area and ρ is the density of the particles. D_{eq} is the diameter of an equivalent spherical particle with the same density and surface/weight ratio as the particles tested.

Table 1 shows BET surface area and the equivalent diameters of the samples. As can be seen the diameters calculated from BET measurements correspond rather well with the diameters determined from sedimentation measurements.

Due to the strong attraction between filler particles, the HU and HP-fillers could not be dispersed at 170°C on a two-roll mill. After 1 hour of milling, the viscosity of these compounds still increased, indicating ongoing dispersion. Therefore, an ultrasound dispersion technique was used, to completely disperse the primary particles.

Before dispersing the BaSO₄ in HDPE, the agglomerates were broken by ultrasonic vibration. To prevent BaSO₄ particles from re-agglomeration, they were coated with a thin layer of HDPE immediately after ultrasonic treatment. Decaline was used as dispersing medium because this is a good solvent for HDPE. 64 grams of BaSO₄ was ultrasonically dispersed in 600 ml of decaline by means of an ultrasonic vibrator operating at a frequency of 25 kHz and a capacity of 1000 Watt. To obtain samples with different degrees of dispersion the BaSO₄ was vibrated for 0, 8, 16, 32 and 64 minutes respectively.

The dispersed BaSO₄ was coated with HDPE by adding it to a solution of 7 gram HDPE in 700 ml of decaline at 135 °C. After cooling to below 30°C, and crystallisation of the HDPE on the BaSO₄ surface, the decaline was largely removed by filtration.

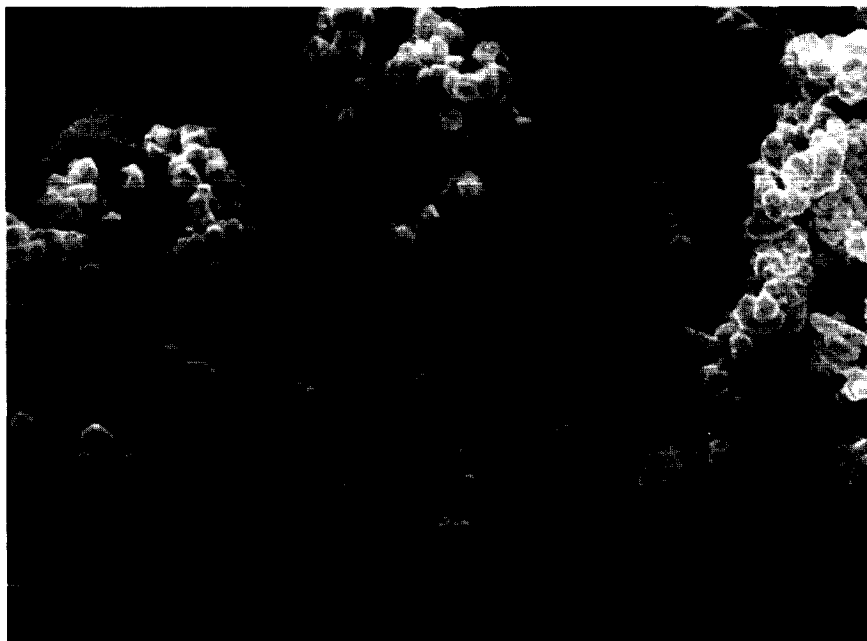


Figure 11.2 SEM photograph of BaSO_4 type HN. Primary particle size $\approx 1 \mu\text{m}$. Agglomerates have a loose structure

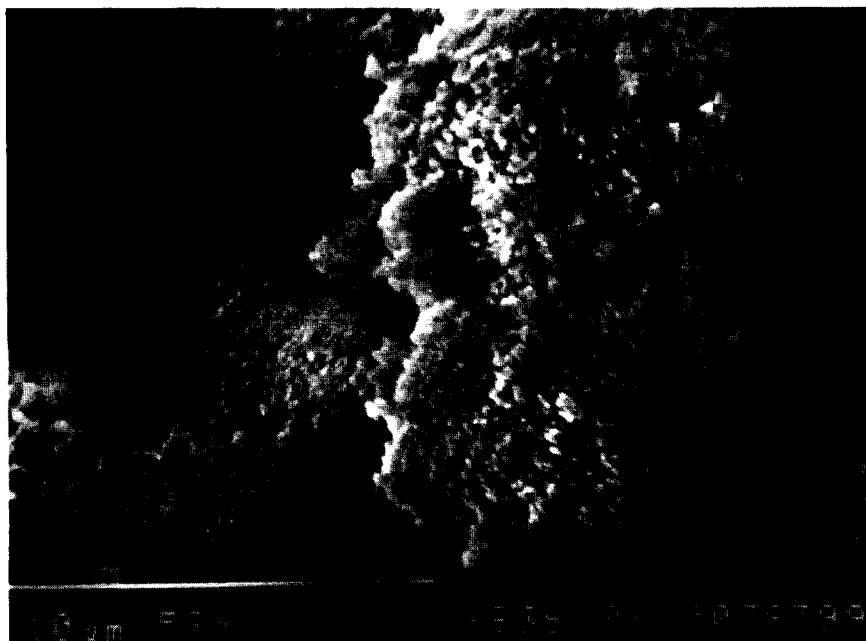


Figure 11.3 SEM photograph of BaSO_4 type HU. Primary particle size $\approx 0.1 \mu\text{m}$. Agglomerate size $\approx 10 \mu\text{m}$.

The decaline in the filtrate was further removed by rinsing with 1000 ml of acetone and drying in vacuum at 120 °C during 3 days. The rinsing and drying was performed twice.

From TGA measurements it was concluded that about 10 wt% of the coated powders existed of HDPE. The amount of HDPE to add to the BaSO₄, to obtain 20 vol% of BaSO₄, was calculated by using a density of 4400 kg/m³ for BaSO₄ and 963 kg/m³ for HDPE. HDPE and the BaSO₄ are mixed on a Schwabenthan two-roll mill at 170 °C during 15 minutes and pressed into plates of 150x150x2 mm at 190 °C.

11.2.2 Morphology

In order to obtain a quantitative measure of morphology, SEM images were made of the BaSO₄ composites. To this end, the samples were cut by a microtome in liquid nitrogen and the surface left after cutting was analysed. Due to the large difference between the size of the HU and HP-agglomerates (10 µm) and the primary particles (0.1-0.15µm) it was impossible to see both the small primary particles and the large agglomerates in one picture.

It was also found that the surface of the samples was smeared because of the large difference in deformability of the BaSO₄ particles and the HDPE matrix. Due to smearing, particles smaller than 1 µm could not be detected. Therefore, only particles larger than 1 µm are counted to determine the number and size of the particles.

Sample (Ø prim)	Dispers Time	<i>c</i>	<i>m_{prim}</i>	<i>A_{contact}</i>	<i>G_e/G_m</i> (1 rad/s)
	[min]	[-]	[-]	[m ² /cm ³]	[-]
K4 (10 µm)	0	0.222	0.53	0.16	1.91
K4	8	0.236	0.53	0.16	1.91
K4	16	0.192	0.53	0.16	1.91
K4	32	0.194	0.53	0.16	1.91
K4	64	0.186	0.53	0.16	1.91
HN(1 µm)	0	0.166	0.53	1.44	136
HN	8	0.135	0.53	1.44	91
HN	16	0.168	0.53	1.44	127
HN	32	0.194	0.53	1.44	136
HN	64	0.187	0.53	1.44	159
HP(0.15 µm)	0	0.203	0.29	2.60	150
HP	8	0.194	0.30	2.75	264
HP	16	0.191	0.31	2.80	364
HP	32	0.134	0.39	3.59	555
HP	64	0.049	0.49	4.46	655
HU(0.1 µm)	0	0.292	0.07	0.85	64
HU	8	0.205	0.28	3.44	218
HU	16	0.202	0.29	3.51	527
HU	32	0.109	0.43	5.2	636
HU	64	0.076	0.46	5.66	655

Table 2 Morphological data and relative dynamic modulus of HDPE filled with 20 vol% BaSO₄ particles varying in size and dispersion

The volume fraction of particles larger than 1 μm was calculated from the area fraction A_i of BaSO_4 in a SEM image: $c = \sum A_i / A$, where A is the total surface of the SEM image. The primary particles of types K4 (10 μm) and HN (1 μm) are not agglomerated and are therefore assumed to be fully dispersed. The fact that c in Table 2 is close to 0.2 confirms this assumption.

Close inspection of the SEM images revealed that the HU and HP types BaSO_4 were present either in large agglomerates or as fully dispersed primary particles. Therefore the amount of fully dispersed BaSO_4 in these types was determined by counting the amount of particles larger than 1 μm . All particles smaller than 1 μm were assumed to be fully dispersed. Agglomerates in BaSO_4 types HN and HP have a limited packing density and therefore have a lower density than well-dispersed particles.

Assuming a random closed packing density of 0.64, the true volume fraction of BaSO_4 present in agglomerates is equal to $0.64c$. The volume fraction of well dispersed primary particles then becomes: $c_{\text{prim}} = 0.2 - 0.64c$. From which the mass fraction of primary particles m_{prim} can be calculated using a density of 4400 kg/m^3 for BaSO_4 and 963 kg/m^3 for HDPE. As a measure of morphology, the surface of the filler that is in contact with the HDPE (A_{contact}) is estimated: $A_{\text{contact}} = A_{\text{BET}} m_{\text{prim}}$. Here, the small contribution of large agglomerates to the total contact area is neglected. The morphological parameters of all samples are listed in Table 11.2.

11.2.3 Rheology

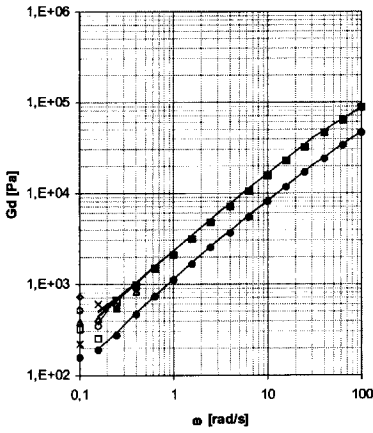
Dynamic mechanical spectroscopy (DMS) was performed on a RMS 605 Rheometrics Mechanical Spectrometer at a temperature of 170°C . The test frequency was varied between 0.1 and 100 rad/s in steps of 0.2 decades. Flat plates were used with a diameter of 50 mm and a distance of 2 mm. The rheology was sensitive to strain. Therefore, the strain amplitude was limited to 6%.

Fig. 11.4a shows that the rheological properties do not change much upon adding 20 vol% of large (K4, 10 μm) BaSO_4 particles. The dynamic shear modulus G_d is increased by a factor 1.91, which is a little more than the factor 1.64 predicted by the earlier introduced Mori-Tanaka model [10] or the factor 1.74 predicted by the van der Poel model [11].

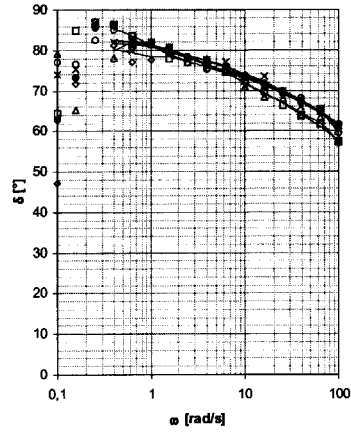
Fig. 11.4b shows that the phase angle is not changed by addition of the large K4 particles. This indicates that the rheology is only determined by the properties of the polymer and no network has been formed.

Fig. 11.4c shows that G_d strongly increases upon addition of 20 vol% 1 μm sized particles (HN). Ultrasonic treatment only slightly increases G_d . This indicates that the HN particles are relatively easy to disperse. The strong decrease of the phase angle in Fig. 11.4d is evidence for a strong elastic contribution to the rheological response. It indicates that the rheology of these compounds is dominated by particle-particle interactions.

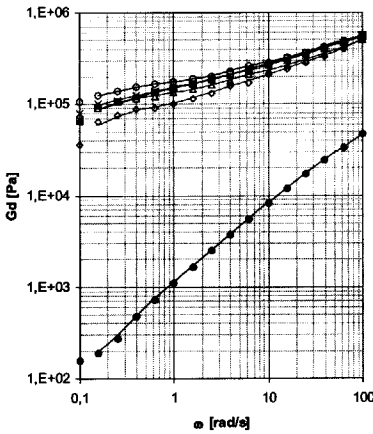
By adding BaSO_4 with 0.1 μm sized primary particles (HU) G_d is even further enhanced as can be seen in Fig. 11.4e. G_d is strongly increased by ultrasonic treatment. Without ultrasonic treatment (HU/0) the dynamic modulus is lower than the dynamic modulus of the well-dispersed 1 μm sized particles in Fig. 11.4c. 15 minutes roll-milling without ultrasonic treatment clearly is not enough to fully disperse the HU type filler into its primary particles. After 16 minutes of ultrasonic treatment, the primary particles are fully dispersed and G_d reaches a plateau value that is not further increased by longer ultrasonic treatment. At full dispersion, the shear modulus becomes almost independent of frequency and the phase angle in Fig. 4f reaches a very low value between 20° and 7° . These are both proofs for a nearly perfect elastic response and strong particle-particle interaction.



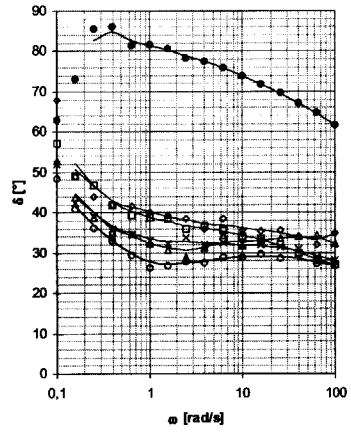
11.4a



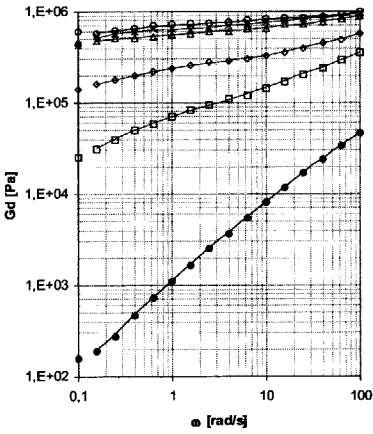
11.4b



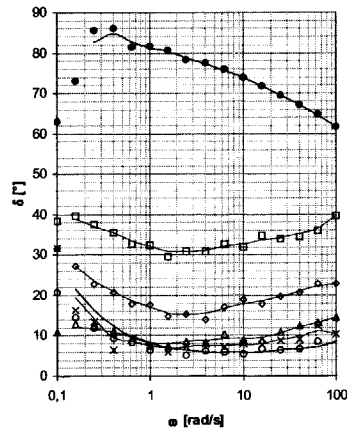
11.4c



11.4d



11.4e



11.4f

Figure 11.4 Rheological properties of HDPE filled with 20 vol% BaSO₄ particles that were ultrasonically vibrated for 0, 8, 16, 32 and 64 minutes. Graphs on the left show the dynamic modulus G_d and graphs on the right show the phase angle. The primary particle size is 10 μm (K4), 1 μm (HN), and 0.1 μm (HU).

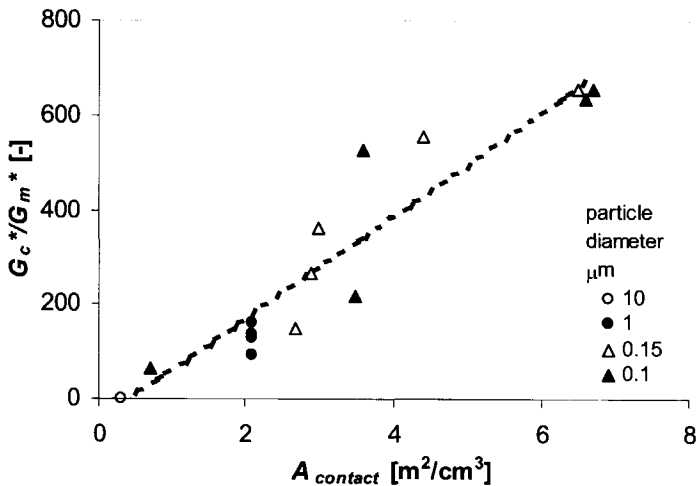


figure 11.5 Relative dynamic shear modulus versus the contact area between BaSO_4 and HDPE.

If the dynamic moduli in Figs. 11.4a, 11.4c and 11.4e are plotted in a single graph, the lines do overlap each other. This is a strong indication that a single mechanism is responsible for the increase of the dynamic modulus. This mechanism might be the formation of a network of touching particles. An attempt is made to relate the rheology of the sample to their morphology. To this end the dynamic shear modulus G_d at low frequency ($\omega = 1$ rad/s) is plotted against the contact area A_{contact} in Fig. 11.5. This graph shows that the dynamic shear modulus of the samples increases continuously as the contact area increases. This indicates that the rheological response is directly related to the state of dispersion of the BaSO_4 .

11.2.4 Conclusions on HDPE with low aspect ratio particles

The elasticity and viscosity of molten HDPE filled with inert BaSO_4 particles are strongly increased by improving the dispersion of the filler. SEM pictures give a good impression of the state of dispersion of the filler in the polymer. The state of dispersion could be quantified from the SEM pictures by image analysis. The contact area between filler and polymer is used as a measure of the state of dispersion. The dynamic shear modulus of molten HDPE filled with inert BaSO_4 particles increases continuously as the contact area between the filler and the polymer matrix increases.

This is attributed to the formation of a network of touching particles. The high sensitivity to shear supports this idea, since a network of touching particles breaks under large shear. At low frequencies the dynamic shear modulus reaches a plateau value and becomes frequency independent. The existence of a plateau is also reported for nanocomposites [6-8]. In nanocomposites the plateau is attributed to tethering of polymer chains to the surface of the clay particles. The rheological experiments on HDPE filled with inert BaSO_4 particles prove that a plateau can also develop in the absence of tethered chains.

11.3 HDPE-nanocomposites with clay platelets of high and low aspect ratio

11.3.1 Materials

HDPE-clay nanocomposites were made with three types of clays with different aspect ratio. The HDPE contained 2 wt% of grafted maleic anhydride for good dispersion of the clay. All samples contained 10 wt% of clay (≈ 3 vol%). All the clays contained the same alkyl ammonium modification (2-methyl 2-hydrogenated tallow ammonium, 2M2HT). The amount of alkyl ammonium was determined by incineration and was about 40 wt% in all cases. In Chapter 5, a detailed description of the preparation of these nanocomposites is given. TEM photographs in Figs. 6.8-6.11 show that all the nanocomposites are very well exfoliated. Only single clay layers and a few tactoids of 2-3 clay layers are visible in the nanocomposites.

11.3.2 The effect of clay aspect ratio on the rheology of HDPE nanocomposites

Small strain dynamic mechanical measurements are performed on a Rheometrics ARES LS dynamic mechanical spectrometer, at 230 °C, using a parallel plate system with a diameter of 25 mm. The distance between the plates was 1.8 mm. The dynamic melt viscosity, the dynamic shear modulus and the phase angle of the HDPE nanocomposites are plotted against angular frequency in Figs. 11.6a, 11.6b and 11.6c.

The rheological behaviour of the different nanoclays resembles that of HDPE filled with small BaSO₄ particles. As was found for the BaSO₄ particles, the phase angle becomes much smaller by the addition of the clays. This is indicative for strong elastic behaviour. At small frequencies, the dynamic shear modulus tends to become constant and shows a plateau like behaviour. The rheological effect is smaller as was found for the smallest 100 nm BaSO₄ particles. This is not surprising since the amount of clay used is much smaller (3 vol% versus 20 vol%).

The reinforcing effect of the three types of clay is also estimated by the Mori-Tanaka composite model that was discussed in Chapter 3. For simplicity, this model is approached by the Halpin-Tsai model by using the appropriate shape factor. In Chapter 3 it is shown that the Halpin-Tsai approach coincides with the more rigorous Mori-Tanaka approach within 5%, as long as $w/t > 5$ and $E_r/E_m > 10$. These conditions are certainly satisfied for the systems under study, since the smallest aspect ratio $w/t = 10$ and the modulus ratio $G_r/G_m > 1000$. Instead of a shape factor of $\zeta = 2/3 w/t$, a shape factor of $\zeta = 3/4 w/t$ is used as is required for calculation of the shear modulus. This is explained in Chapter 3.

In order to calculate the dynamic shear modulus G_d , not only G' but also G'' is calculated. To do this, the composite model is written in a complex manner by using the correspondence principle as is explained in Chapter 3. A shear modulus of 72 GPa is used for the clay platelets. This is calculated by assuming a Young's modulus of 172 GPa and a Poisson's ratio of 0.2 for the clay. The calculations are not sensitive to the actual value of the shear modulus of the clay. The reason for this is the extremely large difference in stiffness between the clay and the polymer melt. One might as well use an infinite shear modulus for the clay and obtain the same results.

In Fig. 11.6c the measured and the calculated dynamic shear modulus G_d of the molten nanocomposites is plotted versus angular frequency. It is remarkable that the aspect ratio of the clay has no significant effect on the rheological response of the PE-nanocomposites. At low frequencies the measured shear modulus is much larger than predicted by the composite model. The reason for this is that a network causes the high viscosity. This mechanism of reinforcement is not incorporated in the composite model. Judging from the dynamic shear

modulus, the stiffness of the network is in the order of about 10^5 to 10^7 Pa. Although this is much stiffer than the melt, it is still much softer than a solid polymer that has a shear modulus of typically 10^9 Pa. So the network does stiffen a molten polymer but it does not significantly stiffen a solid polymer

The shear modulus of a rubber with a low crosslink density is in the order of 10^4 to 10^6 Pa, which is comparable to the shear modulus of a typical polymer melt. Therefore a network of small particles should stiffen a rubber just like it stiffens a polymer melt. It is indeed well known that small particles like carbon black and fumed silica can strongly reinforce rubbers. This phenomenon is extensively used in the rubber industry.

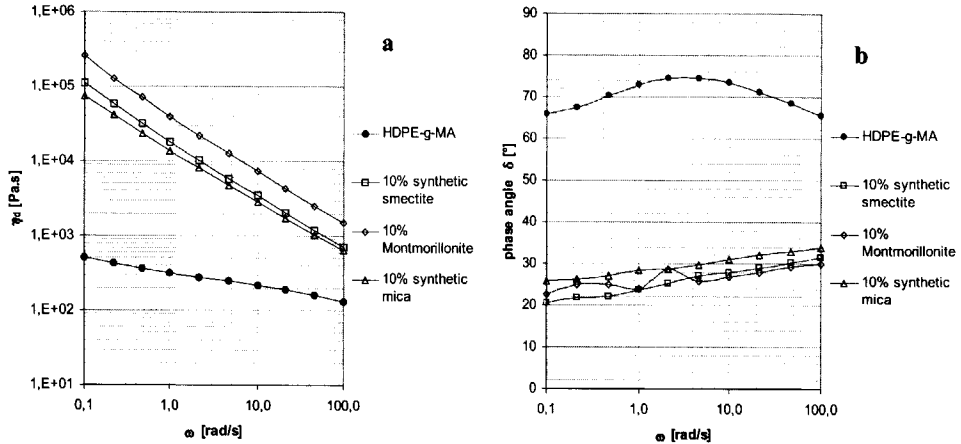


Figure 11.6a-b Rheological properties of HDPE-clay nanocomposites containing 10 wt% of clay.

a) Dynamic viscosity

Synthetic smectite: w/t \approx 20

b) Phase angle

Montmorillonite w/t \approx 100

Synthetic mica w/t \approx 200

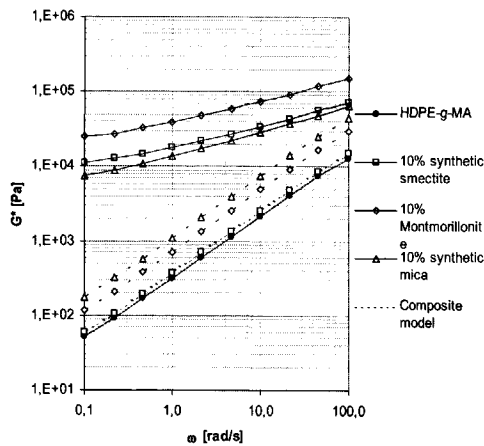


Figure 11.6c Dynamic shear modulus of HDPE-clay nanocomposites containing 10 wt% of clay.

Solid lines : measurement;

Dotted line: theory calculated with the complex version of Halpin-Tsai's model

11.3.3 Conclusions on HDPE nanocomposites

HDPE-clay nanocomposites show the same high elasticity, high viscosity and plateau like behaviour as HDPE BaSO₄ compounds do. Surprisingly the shear modulus of molten HDPE nanocomposites is not improved by increasing the aspect ratio of the clay. This is different from the solid state shear modulus of HDPE nanocomposites, which is strongly increased by increasing the aspect ratio.

11.4 PA6 with nano- and micrometer particles of high and low aspect ratio

PA6 is filled with micron- and nanometer-sized spherical and platelet shaped silicate particles. Two types of spherical fillers are used, micron-sized glass spheres and nanometer-sized aerosil. The micron-sized platelets were made of mica and the nanometer sized platelets of montmorillonite clay. PA6 (DSM Akulon K123) was selected as a matrix material. The PA6/clay nanocomposites were prepared as described in Chapter 4.

Material	1	2	3	4	5	6	7	8	9	10	11	12	13	14
	%	%	%	%	%	%	%	%	%	%	%	%	%	
PA6 Akulon K123	100	95	80	95	80	95	80	50	98.3	95.8	91.7	87.5	83.3	95
Glass spheres Ø 25 µm		5	20											
Aerosil TT600 Ø 40 nm				5	20									
Mica platelets Ø 350 µm w/t = 50						5	20	50						
Montmorillonite clay SCPX 1313 (%silicate) Ø 100 nm w/t = 100									1.7 (1)	4.2 (2.5)	8.3 (5)	12.5 (7.5)	16.7 (10)	
Montmorillonite clay SCPX 1447 (%silicate) Ø 100 nm w/t = 100														5 (5)

Table 11.3 Composition in weight%, of PA6 filled with spherical and platelet shaped particles of micro and nanometer size.

Beside a series of nanocomposites with nano clay that was treated with 40% alkyl-ammonium (Cloisite 20A;: 95 meq + 2-methyl 2-hydrogenated Tallow, 2M2HT) also a single nanocomposite with 5wt% of untreated clay (SCPX 1447, from Southern Clay Products) was tested. TEM photographs in Figs. 6.1-6.3 revealed that the untreated clay was very well exfoliated and dispersed in the PA6 matrix. The untreated clay SCPX 1447 comes from the same source as the clay used to make SCPX 1313. The other samples with spherical and micrometer sized particles were prepared on a 60 cc Haake kneader at 240 °C and 80 rpm during 10 min. The composition of the samples is listed in Table 11.3.

Both small strain and large strain shear rheology of the samples is determined. Extensional rheology was also performed, by measuring melt-strength and melt-extensibility during spinning.

11.4.1 Small strain shear rheology

Small strain rheological experiments were performed on a RMS 800 mechanical spectrometer, equipped with a 25 mm diameter parallel plate system. Dynamic mechanical measurements were performed as a function of frequency under nitrogen atmosphere at 230 °C. To determine the visco-elastic range, strain sweeps were performed on all samples. The reference material and the samples with a low content of filler show no effect of strain amplitude up to 100%. The strain amplitude of the highly filled samples had to be limited to 0.1-1% in order to stay within the linear visco-elastic range. The thermal stability of the samples was checked by performing frequency scans after 5, 10 and 15 minutes. It was found that the viscosity of most samples was increased by about 20% after 15 minutes. Therefore, only experiments after 5 minutes are used in this work.

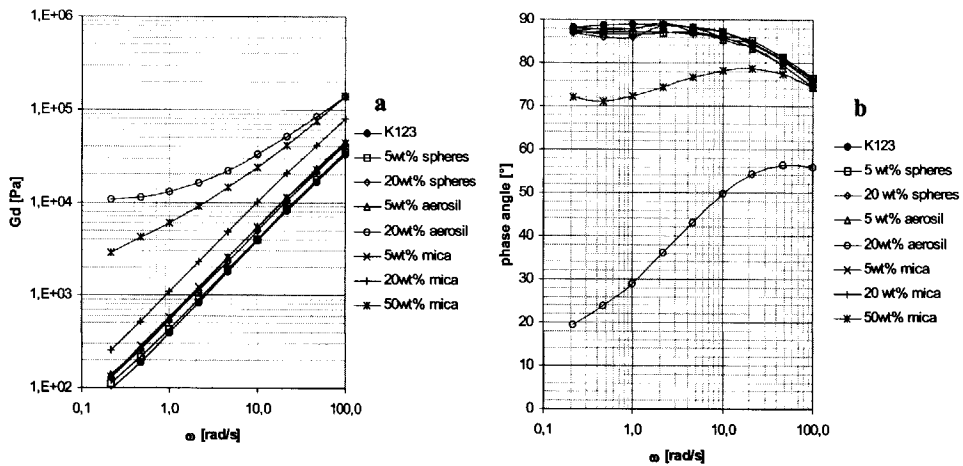


Figure 11.7 Small strain shear rheology of PA6 K123 with glass spheres, aerosil and mica

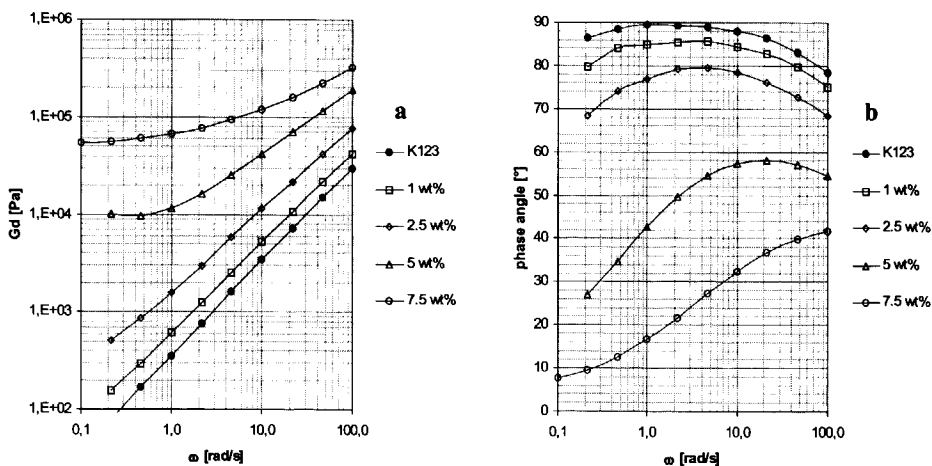


Figure 11.8 Small strain shear rheology of PA6 with nano-clay

Small strain shear experiments are shown in Figs. 11.7 and 11.8. Both the dynamic modulus G_d and the phase angle δ are plotted as a function of angular frequency. All samples have a higher dynamic shear modulus than the unfilled reference. At low frequency the sample with 20 wt% aerosil shows plateau like behaviour. In Figs. 11.7a and 11.7b all curves are identical in shape, except for the curves of the samples with 50 wt% mica and 20 wt% aerosil.

This indicates that only the samples 50 wt% mica or with 20 wt% aerosil have a visco-elastic behaviour that is significantly different from that of the reference. It is thought that the rheology of these samples is dominated by particle-particle interactions. The phase angle of the other samples is not different from that of the unfilled polymer. This indicates that their rheological behaviour is dominated by the polymer matrix.

Fig. 11.8 shows the dynamic mechanical behaviour of the PA6 nanocomposites. In contrast with the former experiments, the phase angle is already reduced at 1 wt% of clay, which indicates elastic behaviour. Increasing the clay content further increases the amount of elasticity. At 5 and 7.5 wt% the rheological behaviour is mainly elastic and G_d shows a plateau at low frequencies.

11.4.2 Large strain shear rheology

Rheological shear behaviour at large strains and high shear rates was performed at 230°C on a Göttfert Rheograph 2002 equipped with a 30/1 mm/mm round die. The measured volume flow versus pressure curves were converted to wall shear stress using the Rabinowitch method. Flow curves of reference sample K123 and of samples with spherical fillers are plotted in Fig. 11.9b. The viscosity is only slightly increased by addition of the spherical particles. The curves in Fig. 11.9b have the same shape as the reference curve, indicating that the large strain rheological behaviour is polymer dominated.

As a comparison, the dynamic viscosity measured at small strains is plotted in Fig. 11.9a. In contrast to the small strain results, the large strain viscosity in Fig. 11.9a of the sample with 20 wt% aerosil is strongly decreased. This indicates that during small strain measurements the network formed by the sub-micron aerosil particles stays intact, while the network is broken up during large strain measurements.

During the capillary measurements on the samples with mica, large pressure fluctuations were observed, making it impossible to perform reliable measurements. These fluctuations are probably caused by the relatively large size of the mica particles compared to the diameter of the die. The measurement indicated a large increase in viscosity but is left out because of inaccuracy.

In Fig. 11.10b, the flow curves of the nanocomposites are shown. A comparison can be made with the small strain dynamic viscosity in Fig. 11.10a. The flow curves of the nanocomposites in Fig. 11.10b show a strong increase in large strain viscosity, especially at small shear rates. At high shear rates the flow curves converge indicating shear(rate) thinning behaviour of PA6 nanocomposites.

11.4.3 Comparing small strain and large strain shear viscosities

Table 11.4 shows the small strain and large strain shear viscosity of the samples. Data are given at low and at high frequency and at low and high shear rate. Theoretical calculations are given too, using the Mori-Tanaka theory that was explained in Chapter 3 of this thesis. Both small strain and large strain viscosities can be compared by using the Cox-Merz rule.

According to the Cox-Merz relationship $\eta(\omega) = \eta(\dot{\gamma})$ if $\omega = \dot{\gamma}$. Of course, this relationship only holds if the material is not changed by the measurement. If a network of particles breaks due to large strain, the Cox-Merz rule evidently cannot hold. Therefore, breakdown of a network can be monitored by comparing the small strain viscosity at say $\omega = 100$ rad/s with the large strain viscosity at $\dot{\gamma} = 100$ s⁻¹. The Cox-Merz rule holds for the samples with glass beads and with 5 wt% of aerosil. The increase in relative viscosity of these samples is small and is mainly attributed to hydrodynamic effects (excluded volume). Apparently, no network has been formed in these samples.

The small strain viscosity at $\omega = 100$ rad/s of the sample with 20 wt% aerosil is much higher than the large strain viscosity at $\dot{\gamma} = 100$ s⁻¹. This indicates that a network of particles is broken due to the large strains in the capillary experiment.

The Mori-Tanaka theory was used for parallel and random orientation of particles by using G^* as measured by DMS as the stiffness of the matrix and assuming a matrix Poisson's ratio of 0.49. In the calculations the filler particles were assumed to be much stiffer than the polymer matrix. If the filler particles have the shape of a sphere, the reinforcement is independent of orientation and the viscosities at parallel and random orientation of particles are equal. This is the case for the samples filled with glass beads or aerosils.

In case of parallel orientation of platelets, two different shear viscosities can be distinguished, the out of plane shear modulus $\eta_{c(13)}$ and the in plane shear viscosity $\eta_{c(12)}$. As becomes clear from Fig. 3.18, the in plane shear viscosity is much larger than the out of plane shear viscosity. $\eta_{c(13)}$ is probed if the platelets lie parallel to the plates of the Rheometrics or parallel to the walls of the Rheograph. The shear viscosity at random orientation always lies between $\eta_{c(13)}$ and $\eta_{c(12)}$.

Filler	Content Weight%	Small strain		Large strain		Mori-Tanaka theory		
		η_c/η_m $\omega =$ 1 rad/s	η_c/η_m $\omega =$ 100 rad/s	η_c/η_m $\dot{\gamma} =$ 100 s ⁻¹	η_c/η_m $\dot{\gamma} =$ 8.10 ³ s ⁻¹	$\eta_{c(13)}/\eta_m$ theory parallel	$\eta_{c(12)}/\eta_m$ theory parallel	η_c/η_m theory random
glass sphere	5	1.1	1.1	1.2	1.2	1.05	1.05	1.05
glass sphere	20	1.4	1.3	1.4	1.4	1.25	1.25	1.25
Aerosil	5	1.4	1.3	1.3	1.2	1.05	1.05	1.05
Aerosil	20	33	4.2	1.6	1.4	1.25	1.25	1.25
Mica	5	1.5	1.3	-	-	1.02	1.85	1.44
Mica	20	2.8	2.4	-	-	1.10	5.06	3.08
Mica	50	15	4.2	-	-	1.39	17.2	9.31
nano-clay	1	1.7	1.4	1.9	1.2	1.00	1.32	1.16
nano-clay	2.5	4.4	2.5	2.9	1.3	1.01	1.82	1.415
nano-clay	5	32	6.4	5.1	2.2	1.02	2.68	1.85
nano-clay	7.5	187	10.7	7.1	2.6	1.03	3.59	2.31
nano-clay pure	5	64	6.4	-	-	1.02	2.68	1.85

Table 11.4 Small strain and large strain relative viscosities of PA6 nanocomposites and micro-composites. The columns with headings 'small strain' and 'large strain' show experiments, the last 3 columns show theoretical calculations using the Mori-Tanaka theory.

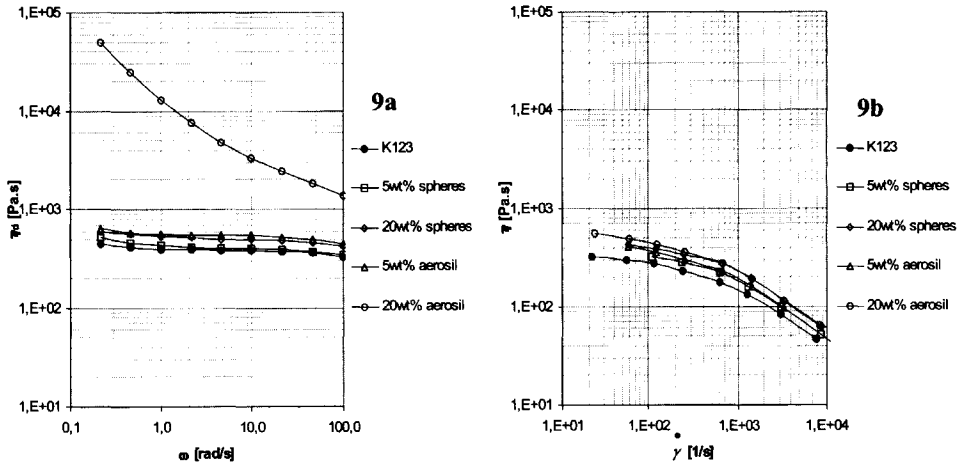


Figure 11.9 Small strain shear viscosity versus frequency and large strain shear viscosity versus shear rate of PA6 K123 with spherical fillers

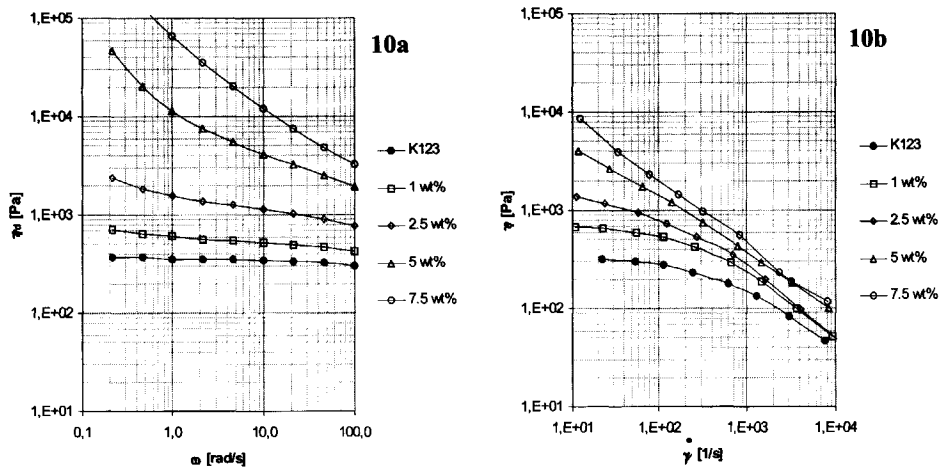


Figure 11.10 Small strain shear viscosity versus frequency and large strain shear viscosity versus shear rate of PA6 nanocomposites

With nanosized fillers like aerosils or nanoclay the Mori-Tanaka theory underestimates the viscosity of the filled HDPE. The difference between theory and measurement becomes larger as the particles become smaller and the amount of particles increases. The reason for this is that the Mori-Tanaka theory does not account for particle-particle interactions. At large volume fractions and small particle sizes, as particle-particle interactions become more important the difference between experiment and the Mori-Tanaka theory becomes very large.

This indicates that the viscosity of these samples is mainly caused by interactions between the particles and not by the viscosity of the polymer. All the nanocomposites show an increased viscosity. Surprisingly the Cox-Merz rule holds reasonably for the nanocomposites in spite of the strong elastic behaviour in the small strain experiments. It can thus be concluded that the mechanism that is responsible for the high elasticity and viscosity of nanocomposites is insensitive to large strain deformation.

The small strain rheological behaviour of the nanocomposite with 5 wt% pure clay is very similar to that of the nanocomposite with 5 wt% (silicate content) modified clay. Only at low frequencies, the pure clay is a little more effective in increasing the viscosity.

11.4.4 Extensional rheology

To investigate the effect of extensional strain, the melt-strength and the melt-extensibility of the samples are tested. Experiments are performed on a Göttfert Rheotens melt-spin instrument fitted to a Rheograph 2000 capillary rheometer. The spin force was measured as a function of melt extension. Melt-extension was determined as the ratio of the filament speed at the winding spool over the filament speed at the die exit. The maximum spin force (MSF) and maximum melt-extensibility (MME) are used to characterise the extensional rheology of the samples.

The reference polyamide has a very low melt-strength since its MSF was too low to be detected (<0.2 cN). The samples with glass spheres and with aerosols also had a MSF below the detection limit. The melt-strength of the samples with mica also were very low since they broke under their own weight.

Even the sample with 20% aerosils, that showed strong elastic response at small strain experiments, had a very low melt-strength. Only the nanocomposites had measurable melt-strengths that are listed in Table 11.5. The melt-strength is clearly increased by increasing the silicate content. The increase in melt strength is accompanied by a simultaneous decrease in melt extensibility.

Silicate content	MSF	MME
[wt%]	cN	[-]
0	<0.2	-
2.5	0.2 ± 0.1	20 ± 10
5	1.8 ± 0.1	15 ± 10
7.5	4.8 ± 0.1	5 ± 1
10	7.7 ± 0.1	2.5 ± 10

Table 11.5 Maximum spin-force (MSF) and maximum melt extensibility (MME) of PA6 nanocomposites

11.4.5 Discussion

To explain the remarkable rheological behaviour of nanocomposites, let us look at some mechanisms that cannot explain the observed results. Clearly, the high elasticity of the nanocomposites is not a consequence of a network of touching particles. Such a network would certainly break down, or at least lose much of its strength, if it is deformed up to large shear.

An example of such a shear sensitive network is the PA6 sample filled with 20 weight% aerosil. Apparently, the high viscosity of the nanocomposites is formed by a

mechanism that does not rely on direct contact between clay platelets. The mechanism that is looked for must thus prevent the formation of a network of touching particles, since such a network would increase the small strain viscosity and would break down under large shear strain.

Suppose that polymer chains, which are tethered to more than one clay platelet, interconnect the clay particles chemically. In that case nanocomposites would have a perfect elastic behaviour, much like a rubber and could not withstand steady state shear deformation as in the capillary experiments. So chemical connection of clay plates by tethered polymer chains can not explain the observed results.

The most obvious candidate is tethering of single end groups to the clay platelets. As Krishnamoorti [6] suggested, brush-like molecules would be formed in that case. This mechanism would explain at least some features that are found in the rheology of PA6 nanocomposites.

First of all, tethering increases the viscosity of the polymer since the molar mass of a brush-like molecule is much larger than that of a single molecule. Secondly, the many tethered chains prevent formation of a network because they form a shield that prevents the clay platelets from approaching each other. Thirdly, tethered chains would behave much like a branched polymer or star-shaped molecules, which are known to show shear-thinning and extensional hardening.

Three physical mechanisms were mentioned in the introduction that also might be good candidates, the double layer around the clay platelets, Brownian motion and spinning of the platelets in a polymer flow. These mechanisms all increase viscosity without relying on a direct connection between particles. The double layer mechanism relies on electrostatic repulsion, Brownian motion is a thermodynamical concept while particle spinning is caused by flow of the polymer. The double layer mechanism has the appealing feature that it prevents particles from actually touching each other.

But also Brownian motion of small clay layers might be so fast and exert so much mechanical force that any connection between particles is instantaneously broken, making it impossible to form a network of touching particles. If Brownian motion were the mechanism that is looked for, it would be very hard to orient platelets in a polymer flow, since Brownian spinning would swiftly erase any orientation. Since it is known that clay platelets in PA6-nanocomposites are strongly oriented by polymer flow [12], Brownian motion is an unlikely candidate. A method to estimate the effect of Brownian motion on viscosity is given by Brenner [5].

In a polymer flow, the hydrodynamic forces tend to orient the major axis of a platelet with the flow, while Brownian motion tends to randomise the orientation. The relative importance of these mechanisms is expressed in the rotary Peclet number. The Peclet number is the ratio of the time scale for Brownian rotation ($1/D_r$) to that of convective motion $1/\dot{\gamma}$:

$$Pe = \frac{\dot{\gamma}}{D_r} \quad (11.2)$$

For circular disks the rotary Brownian diffusion coefficient is:

$$D_r = \frac{kT}{8\pi\eta w^3} \quad (11.3)$$

Brenner showed that for a dilute suspension of oblate spheroids, the viscosity is dominated by Brownian motion if $Pe < 10$. The polymer matrix in the PA6 nanocomposites has a viscosity η of about 300 Pa.s. The diameter w of the platelets is about 100 nm and the temperature T is close to 500 K. The rotary diffusion coefficient then becomes $D_r \approx 0.001 \text{ s}^{-1}$. So according to

this calculation the Brownian motion would dominate if $\dot{\gamma} < 0.01$. This indicates that at the large shear rates in the capillary experiment ($\dot{\gamma} > 10$), orientation due to shear dominates over rotation due to Brownian motion. This is true for dilute concentrations where particle-particle interactions can be neglected. In the nanocomposites under study the concentrations cannot be considered to be dilute as will be discussed below.

As the concentration increases, particles start to enter the neighbourhood of surrounding particles. This disturbs the flow around the particles and consequently increases viscosity. At low concentrations, bi-particle interactions are most probable, while at high concentration more than two particles can interact simultaneously. If particle-particle interactions occur, the viscosity can increase dramatically. The concentration at which strong viscosity effects become noticeable depends on the morphology of the dispersed phase and on the different kinds of forces that are active between particles. The aspect ratio is an important morphological parameter. Particles with high aspect ratios will feel each other's presence at much lower concentrations than spheres.

Mewis and Macosko [13] discussed the most important inter-particle forces like van der Waals forces, electrostatic forces and polymeric (steric) forces. Long ranging forces like electrostatic forces will increase viscosity at a much lower concentration than short ranging forces like van der Waals forces. Two neighbouring particles can experience a repulsive force if polymer layers, which are attached to the surface of the particles, overlap.

Clay particles in nanocomposites have an electrostatic double layer, they have a high aspect ratio and they have polymer chains that are attached to their surface. So all conditions are fulfilled for strong inter-particle interactions.

The double layer mechanism is mentioned in the literature as an important mechanism in stabilising clay-suspensions in water [5]. Unlike the PA6-nanocomposites, these suspensions are known to collapse under shear deformation. By connecting polymer molecules to the clay surface, the suspension is stabilised largely. Luckham et al. [5] speculate that this is caused by stabilisation of the diffuse double layer around the clay platelets. The stabilisation of the double layer by absorbed or tethered polymer molecules might be the reason for the stability of PA6-nanocomposite under high shear deformation.

With the knowledge up to date, the double layer mechanism can not be ruled out as a possible candidate. Calculation suggests that Brownian spinning is not important for the shear rates considered. It is likely that the viscosity of polymer-clay nanocomposites is a combined result of the double layer mechanism, the tethered polymer molecules and the high aspect ratio of the clay platelets. Systematic research of the effect of these parameters on the viscosity of nanocomposites could reveal the relative importance of these parameters. It might also result in tools to tailor the rheology of nanocomposites.

11.5 Conclusions

- The viscosity and elasticity of polymer-clay nanocomposites are strongly increased with respect to the unfilled polymer. The nanoclay increases the viscosity more effectively than other submicron fillers do. The increase is much stronger than estimated by continuum mechanical models.
- Even at large strains, nanocomposites retain their high melt viscosity and high melt strength. This is in contrast with the behaviour of polymers containing common sub micron particles, which lose their high viscosity at large shear strain.
- In polymers with common sub-micron particles it is thought that a network of directly connected particles is formed. At high shear the connections are broken and the viscosity drops strongly.

- Since in nanocomposites the viscosity does not drop at high shear, it is concluded that the network is not broken. Therefore, the clay platelets experience each other's presence by another mechanism than direct connectivity.
- After considering several possibilities, two mechanisms remain that can explain the high shear stiffness of nanocomposites. In one mechanism that was already suggested in literature, the viscosity is increased by polymer chains that are tethered to the clay.
- The other mechanism relies on the repulsive forces that clay particles experience because of the charged double layer on the surface of the clay.
- Although theoretical considerations predict differently, experiments show that the rheology is not significantly affected by the aspect ratio of the clay platelets. This remarkable result is not yet understood and is an interesting subject for further study.

11.6 References

- [1] A.Y. Malkin, *Rheology of filled polymers*, Adv. Polym. Sci., 1990, 69-96.
- [2] Kamphuis, *A transient network model describing the rheological behaviour of concentrated dispersions*, Rheol. Acta **23**, 1984, 329-344.
- [3] D. P. Rucker and S. G. Bike, *Rheological behavior of silica-filled polymers: effect of interfacial adhesion*, AIChE's 1997 Annual Meeting Nov. 16-21, paper 110b
- [4] P.F. Luckham and S. Rossi, *The colloidal and rheological properties of bentonite suspensions*, Adv. Colloid Interface Sci. **82**, 1999, 43-92.
- [5] H. Brenner, *Rheology of a dilute suspension of axisymmetric Brownian particles*, Int. J. Multiphase Flow **1**, 1974, 195-341.
- [6] R. Krishnamoorti and E.P. Giannelis, *Rheology of end-tethered polymer layered silicate nanocomposites*, Macromolecules **30**, 1997, 4097-4102.
- [7] R. Krishnamoorti, R.A. Vaia and E. P. Giannelis, *Structure and dynamics of polymer-layered silicate nanocomposites*, Chem. Mater. **8**, 1996, 1728-1734.
- [8] Y. T. Lee and O.O. Park, *Phase morphology and rheological behaviors of polymer / layered silicate nanocomposites*, Rheologica Acta, 2001, to be published.
- [9] B. Hoffmann, J. Kressler, G. Stöppelmann, Chr. Friedrich and G. M. Kim, *Rheology of nanocomposites based on layered silicates and polyamide-12*, Colloid Polym. Sci. **278**, 2000, 629-636.
- [10] Chapter 3 of this thesis.
- [11] F.H.J. Maurer, *Zur Beschreibung des Elastischen und Viscoelastischen Verhaltens Teilchengefüllter Verbundwerkstoffe mit einer Zwischenschicht*, PhD Thesis, University of Duisburg, 1983.
- [12] Y. Kojima, A. Usuki, M. Kawasumi, A. Okada, T. Karauchi, O. Kamigaito, K. Taji, *Novel preferred orientation in injection-molded Nylon-6 clay hybrid*, J. Pol. Sci. B: Pol. Phys. **33**, 1995, 1039-1045.
- [13] J. Mewis and C.W. Macosko, Chapter 10: *Suspension Rheology*, in: C.W. Macosko, *Rheology Principles, Measurements, and Applications*, VCH, N.Y., 1994

Appendix A

Eshelby's equivalent inclusion method

A.1 The elastic field in an inclusion with an eigenstrain

To simulate the stress field caused by the presence of an inhomogeneity, consider a matrix \mathbf{D} containing a domain Ω as depicted in Fig. A.1. Following Mura [1], it is referred to Ω as an inhomogeneity if the elastic properties of the material in Ω differ from those of the matrix. If the elastic properties of the material in Ω are equal to those of the matrix Ω is called an inclusion.

First suppose that Ω contains an inclusion with the same stiffness \mathbf{C}_m as the matrix. Then take the inclusion out of the matrix and give it an eigenstrain $\boldsymbol{\varepsilon}^*$ (i.e. a thermal strain by heating it). This eigenstrain causes no stress and is therefore also named stress-free strain. Now force the inclusion back into the cavity and weld the surface of the cavity to the surface of the inclusion.

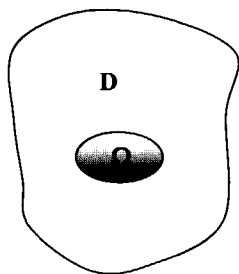


Figure A.1 Ellipsoidal inclusion in a matrix

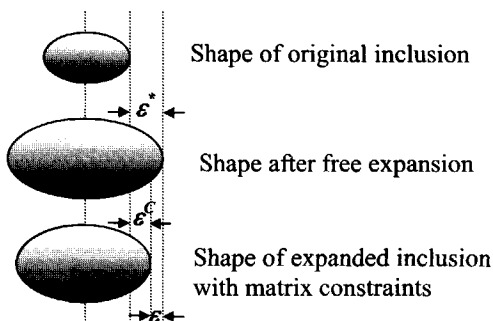


Figure A.2 Constrained strain $\boldsymbol{\varepsilon}^c$ of an ellipsoid with eigenstrain $\boldsymbol{\varepsilon}^*$.

If the inclusion would be completely free to expand it would be without stress and attain a strain equal to the eigenstrain $\boldsymbol{\varepsilon}^*$. As a result of the constraints of the matrix the natural expansion of the ellipsoid is hindered. The actual strain $\boldsymbol{\varepsilon}^c$ will therefore be different from the eigenstrain $\boldsymbol{\varepsilon}^*$. Eshelby [2] has shown that the actual strain in the inclusion is related to the eigenstrain of the inclusion as:

$$\boldsymbol{\varepsilon}^c = \mathbf{P}\boldsymbol{\varepsilon}^* \quad \text{A.1)}$$

where \mathbf{P} is known as Eshelby's tensor. In general the Eshelby tensor is a function of the shape of the inclusion and of the stiffness tensor \mathbf{C}_m of the matrix. The Eshelby tensor expresses the confinement that the matrix imposes on an inclusion with an eigenstrain that has the same elastic properties as the matrix.

The difference between the actual strain $\boldsymbol{\varepsilon}^c$ and the eigenstrain $\boldsymbol{\varepsilon}^*$ causes an elastic stress in the inclusion (Fig. 2). The resulting elastic stress in the inclusion is related to the actual strain and the eigenstrain by Hooke's law:

$$\boldsymbol{\sigma}_{incl} = \mathbf{C}_m (\boldsymbol{\varepsilon}^c - \boldsymbol{\varepsilon}^*) \quad \text{A.2)}$$

Now apply a surface traction on the boundary of D to give a uniform matrix stress $\boldsymbol{\sigma}_m$ and matrix strain $\boldsymbol{\varepsilon}_m$. Since matrix and inclusion are made of the same material, the stress inside the inclusion now becomes:

$$\boldsymbol{\sigma}_{incl} = \mathbf{C}_m (\boldsymbol{\varepsilon}_m + \boldsymbol{\varepsilon}^c - \boldsymbol{\varepsilon}^*) \quad \text{A.3)}$$

A.2 The elastic field in an inhomogeneity

Remove the inclusion and fill the domain Ω with a inhomogeneity, without an eigenstrain and with stiffness \mathbf{C}_r . The stiffness of this hypothetical material is chosen such that the stresses and strains in this new situation are equivalent with those of the previous one. To do this, the new material must have the same actual strain ($\boldsymbol{\varepsilon}_r = \boldsymbol{\varepsilon}_m + \boldsymbol{\varepsilon}^c$) and the same stress as the removed inclusion:

$$\mathbf{C}_r (\boldsymbol{\varepsilon}_m + \boldsymbol{\varepsilon}^c) = \mathbf{C}_m (\boldsymbol{\varepsilon}_m + \boldsymbol{\varepsilon}^c - \boldsymbol{\varepsilon}^*) \quad \text{A.4)}$$

Now an expression is derived for the *strain concentration tensor* \mathbf{A} that is defined by:

$$\boldsymbol{\varepsilon}_r = \mathbf{A} \boldsymbol{\varepsilon}_m \quad \text{A.5)}$$

The strain in the inclusion is given by

$$\boldsymbol{\varepsilon}_r = \boldsymbol{\varepsilon}_m + \boldsymbol{\varepsilon}^c = \boldsymbol{\varepsilon}_m + \mathbf{P} \boldsymbol{\varepsilon}^* \quad \text{A.6)}$$

From A.3) and A.5) it follows that:

$$\mathbf{C}_r (\boldsymbol{\varepsilon}_r) = \mathbf{C}_m (\boldsymbol{\varepsilon}_r - \boldsymbol{\varepsilon}^*) \quad \text{A.7)}$$

or by writing $\boldsymbol{\varepsilon}^* = \mathbf{P}^{-1} (\boldsymbol{\varepsilon}_r - \boldsymbol{\varepsilon}_m)$ by using A.6):

$$(\mathbf{C}_r - \mathbf{C}_m) (\boldsymbol{\varepsilon}_r) = -\mathbf{C}_m \boldsymbol{\varepsilon}^* = -\mathbf{C}_m \mathbf{P}^{-1} (\boldsymbol{\varepsilon}_r - \boldsymbol{\varepsilon}_m) \quad \text{A.8)}$$

I.e.:

$$(\mathbf{C}_r - \mathbf{C}_m + \mathbf{C}_m \mathbf{P}^{-1}) (\boldsymbol{\varepsilon}_r) = \mathbf{C}_m \mathbf{P}^{-1} (\boldsymbol{\varepsilon}_m) \quad \text{A.9)}$$

By multiplication with $\mathbf{P} \mathbf{C}_m^{-1}$ and rearrangement one gets:

$$\varepsilon_r = (PC_m^{-1}(C_r - C_m) + I)^{-1} \varepsilon_m \equiv A\varepsilon_m \quad A.10)$$

in which A is the strain concentration tensor. Eqn. A.10) shows that the strain concentration tensor is a function of Eshelby's tensor P . In case of spheroidal inclusions it is possible to obtain an analytical expression for P . In the following two sections, expressions for P are given in case the matrix has isotropic or transverse symmetry.

A.3 Eshelby's Tensor

A.3.1 Spheroid with axes a_1, a_2, a_3 ; $a_1=a_2$, $\alpha=a_3/a_1$ in an isotropic matrix

If the ellipsoid is an isotropic or anisotropic spheroid in an isotropic matrix, the components of Eshelby's tensor P_{ijkl} only depend on the aspect ratio α of the spheroid and on the Poisson's ratio ν_m of the isotropic matrix. If the principle axis of the spheroid is parallel to the 3-axis the tensor components P_{ijkl} of Eshelby's tensor are [1-3]:

$$P_{1111} = P_{2222} = \frac{3}{8(1-\nu_m)} \frac{\alpha^2}{\alpha^2 - 1} + \frac{1}{4(1-\nu_m)} \left[1 - 2\nu_m - \frac{9}{4(\alpha^2 - 1)} \right] g$$

$$P_{3333} = \frac{1}{2(1-\nu_m)} \left\{ 1 - 2\nu_m + \frac{3\alpha^2 - 1}{\alpha^2 - 1} - \left[1 - 2\nu_m + \frac{3\alpha^2}{\alpha^2 - 1} \right] g \right\}$$

$$P_{1122} = P_{2211} = \frac{1}{4(1-\nu_m)} \left\{ \frac{\alpha^2}{2(\alpha^2 - 1)} - \left[1 - 2\nu_m + \frac{3}{4(\alpha^2 - 1)} \right] g \right\}$$

$$P_{1133} = P_{2233} = \frac{1}{2(1-\nu_m)} \frac{\alpha^2}{\alpha^2 - 1} - \frac{1}{4(1-\nu_m)} \left[1 - 2\nu_m - \frac{3\alpha^2}{\alpha^2 - 1} \right] g$$

$$P_{3311} = P_{3322} = -\frac{1}{2(1-\nu_m)} \left[1 - 2\nu_m + \frac{1}{\alpha^2 - 1} \right] + \frac{1}{2(1-\nu_m)} \left[1 - 2\nu_m + \frac{3}{2(\alpha^2 - 1)} \right] g$$

$$P_{1313} = P_{2323} = \frac{1}{4(1-\nu_m)} \left\{ 1 - 2\nu_m - \frac{\alpha^2 + 1}{\alpha^2 - 1} - \frac{1}{2} \left[1 - 2\nu_m - \frac{3(\alpha^2 + 1)}{\alpha^2 - 1} \right] g \right\}$$

$$P_{1212} = \frac{1}{4(1-\nu_m)} \left\{ \frac{\alpha^2}{2(\alpha^2 - 1)} + \left[1 - 2\nu_m - \frac{3}{4(\alpha^2 - 1)} \right] g \right\}$$

For a fibre-like (prolate) spheroidal inclusion g is given by:

$$g = \frac{\alpha}{(\alpha^2 - 1)^{3/2}} \{ \alpha(\alpha^2 - 1)^{1/2} - \cosh^{-1} \alpha \} \quad \text{if } (\alpha > 1)$$

and for a platelet-like (oblate) spheroidal inclusion by:

$$g = \frac{\alpha}{(1-\alpha^2)^{3/2}} \left\{ \cos^{-1} \alpha - \alpha(1-\alpha^2)^{1/2} \right\} \quad \text{if } (\alpha < 1)$$

For a fibre-like inclusion the aspect ratio α is given as l/d where l is the length of fibre and d the diameter. For a disk-shaped inclusion α is defined as t/w , where t is the length of the minor and w the length of the major axis.

A.3.2 Spheroid with axes a_1, a_2, a_3 ; $a_1=a_2, \rho=a_1/a_3$ in an anisotropic matrix

For the more general case of anisotropic spheroids in an anisotropic matrix, Mura [1] gave expressions in case the matrix has a stiffness tensor with hexagonal or transverse isotropic symmetry. In a transverse isotropic matrix with the 3-axis as the axis of symmetry, 5 independent stiffnesses can be distinguished:

$$C_{11}^m = d$$

$$(C_{11}^m - C_{12}^m)/2 = e$$

$$C_{44}^m = f$$

$$C_{13}^m - C_{44}^m = g$$

$$C_{33}^m = h$$

In a general anisotropic matrix the Eshelby tensor P_{ijkl} becomes [3 p117]:

$$P_{ijkl} = (1/8\pi) C_{pqkl}^m (\bar{G}_{ipjq} + \bar{G}_{jpiq})$$

In the case of a hexagonal matrix the nonzero components of \bar{G}_{ijkl} are given below:

$$\Delta^{-1} = [e(1-x^2) + f\rho^2 x^2] \{ [d(1-x^2) + f\rho^2 x^2] [f(1-x^2) + h\rho^2 x^2] - g^2 \rho^2 x^2 (1-x^2) \}$$

$$\bar{G}_{1111} = \bar{G}_{2222} = \frac{\pi}{2} \int_0^1 \Delta(1-x^2) \{ [f(1-x^2) + h\rho^2 x^2] [(3e+d)(1-x^2) + 4f\rho^2 x^2] - g^2 \rho^2 x^2 (1-x^2) \} dx$$

$$\bar{G}_{3333} = 4\pi \int_0^1 \Delta \rho^2 x^2 [d(1-x^2) + f\rho^2 x^2] [e(1-x^2) + f\rho^2 x^2] dx$$

$$\bar{G}_{1122} = \bar{G}_{2211} = \frac{\pi}{2} \int_0^1 \Delta(1-x^2) \{ [f(1-x^2) + h\rho^2 x^2] [(e+3d)(1-x^2) + 4f\rho^2 x^2] - 3g^2 \rho^2 x^2 (1-x^2) \} dx$$

$$\bar{G}_{1133} = \bar{G}_{2233} = 2\pi \int_0^1 \Delta \rho^2 x^2 \{ [f(1-x^2) + h\rho^2 x^2] [(e+d)(1-x^2) + 2f\rho^2 x^2] - g^2 \rho^2 x^2 (1-x^2) \} dx$$

$$\bar{G}_{3311} = \bar{G}_{3322} = 2\pi \int_0^1 \Delta(1-x^2) [d(1-x^2) + f\rho^2 x^2] [e(1-x^2) + f\rho^2 x^2] dx$$

$$\bar{G}_{1212} = \frac{\pi}{2} \int_0^1 \Delta(1-x^2)^2 \{ g^2 \rho^2 x^2 - (d-e) [f(1-x^2) + h\rho^2 x^2] \} dx$$

$$\bar{G}_{1313} = \bar{G}_{2323} = -2\pi \int_0^1 \Delta g \rho^2 x^2 (1-x^2) [e(1-x^2) + f\rho^2 x^2] dx$$

A3.3 Expressing the Eshelby tensor as a 6x6 matrix

If stresses and strains are expressed as 6x6 engineering matrices instead of 3x3x3 tensors, one must account for the factor 2 difference in the definition of tensor and engineering shear strain. The non-zero components in engineering matrix notation are:

$$\begin{array}{llll} P_{11} = P_{1111} & P_{12} = P_{1122} & P_{13} = P_{1133} & P_{44} = 2 P_{2323} \\ P_{21} = P_{2211} & P_{22} = P_{2222} & P_{23} = P_{2233} & P_{55} = 2 P_{1313} \\ P_{31} = P_{3311} & P_{32} = P_{3322} & P_{33} = P_{3333} & P_{66} = 2 P_{1212} \end{array}$$

Note that Eshelby's tensor, or matrix generally is not symmetric i.e. $P_{13} \neq P_{31}$ and $P_{12} \neq P_{21}$.

A.4 Matlab subroutines to calculate Eshelby's tensor

A.4.1 Isotropic matrix

```
function S = Eshtensor(alf,nu0);
%Calculation of the components Eshelby's tensor in case of an isotropic matrix.
%
%Input:      alf      (0<alf<=inf),the aspect ratio of the spheroid shaped filler
%
%              if alf < 1 then spheroid is platelet like
%              if alf < 1 then spheroid is fibre like
%              nu0      The Poisson's ratio of the matrix polymer:
%
%Output:      S        The 4th ordered Eshelby's tensor represented as a 6X6
%                      matrix
%The 3-axis is supposed to be the rotation axis of the spheroid

if alf > 1
    g = alf/(alf^2-1)^1.5*(alf*(alf^2-1)^0.5-acosh(alf));
else
    g = alf/((1-alf^2)^1.5*(acos(alf)-alf*(1-alf^2)^0.5));
end

% Calculate the elements of Eshelby's tensor
S3333= 1/(2*(1-nu0))*(1-2*nu0+(3*alf^2-1)/(alf^2-1)-g*(1-2*nu0+3*alf^2/(alf^2-1)));
S1111=3/(8*(1-nu0))*alf^2/(alf^2-1)+g/(4*(1-nu0))*(1-2*nu0-9/(4*(alf^2-1)));
S1122= 1/(4*(1-nu0))*(alf^2/(2*(alf^2-1))-g*(1-2*nu0+3/(4*(alf^2-1))));
S1133= -1/(2*(1-nu0))*alf^2/(alf^2-1)+g/(4*(1-nu0))*(3*alf^2/(alf^2-1)-(1-2*nu0));
S3311= -1/(2*(1-nu0))*(1-2*nu0+1/(alf^2-1))+g/(2*(1-nu0))*(1-2*nu0+3/(2*(alf^2-1)));
S1212= 1/(4*(1-nu0))*(alf^2/(2*(alf^2-1))+g*(1-2*nu0-3/(4*(alf^2-1))));
S1313= 1/(4*(1-nu0))*(1-2*nu0-(alf^2+1)/(alf^2-1)-g/2*(1-2*nu0-3*(alf^2+1)/(alf^2-1)));

S2222=S1111;
S2211=S1122;
S2233=S1133;
```

```
S3322=S3311;
S2323=S1313;
```

```
% Transform the tensor components in matrix components
```

```
S = zeros(6,6);
S(1,1:3)=[S1111 S1122 S1133];
S(2,1:3)=[S2211 S2222 S2233];
S(3,1:3)=[S3311 S3322 S3333];
S(4,4)=2*S2323; % factor of two!
S(5,5)=2*S1313;
S(6,6)=2*S1212;
```

A.4.2 Anisotropic matrix

```
% Program to calculate the Eshelby tensor of a transvers isotropic spheroid
```

```
% According to: Toshio Mura, 'Mechanics of elastic and inelastic solids 3',
```

```
% Martinus Nijhoff Publishers, The Hague, ISBN 247 2560 7, 1982 Mura p 119
```

```
function M = Muratens(alf,C);
```

```
%
```

```
%Input:   alf (0<alf<=inf), the aspect ratio of the spheroid shaped filler.
```

```
%         if alf < 1 then spheroid is a platelet.
```

```
%         if alf < 1 then spheroid is a fibre.
```

```
%         C   The 6X6 stiffness matrix of the transvers symmetric filler.
```

```
%Output:  M   The Eshelby's Tensor according to Mura represented as a6X6 matrix.
```

```
%The 3 direction is supposed to be the symmetry axis of the spheroid
```

```
d=C(1,1);
```

```
e=(C(1,1)-C(1,2))/2;
```

```
f=C(4,4);
```

```
g=C(1,3)+C(4,4);
```

```
h=C(3,3);
```

```
ro=1/alf;
```

```
S=zeros(3,3,3,3);
```

```
G=zeros(3,3,3,3);
```

```
% Integrate between 0 and 1 to obtain the G values
```

```
G(1,1,1,1)= (quad('G1111int',0,1,[],[],ro,d,e,f,g,h));
```

```
G(2,2,2,2)= G(1,1,1,1);
```

```
G(3,3,3,3)= (quad('G3333int',0,1,[],[],ro,d,e,f,g,h));
```

```
G(1,1,2,2)= (quad('G1122int',0,1,[],[],ro,d,e,f,g,h));
```

```
G(2,2,1,1)= G(1,1,2,2);
```

```
G(1,1,3,3)= (quad('G1133int',0,1,[],[],ro,d,e,f,g,h));
```

```
G(2,2,3,3)= G(1,1,3,3);
```

```
G(3,3,1,1)= (quad('G3311int',0,1,[],[],ro,d,e,f,g,h));
```

```
G(3,3,2,2)= G(3,3,1,1);
```

```
G(1,2,1,2)= (quad('G1212int',0,1,[],[],ro,d,e,f,g,h));
```

```
G(1,2,2,1)=G(1,2,1,2);
```

```
G(2,1,1,2)=G(1,2,1,2);
```

```
G(2,1,2,1)=G(1,2,1,2);
```

```
G(1,3,1,3)= (quad('G1212int',0,1,[],[],ro,d,e,f,g,h));
```

```
G(1,3,3,1)= G(1,3,1,3);
```

```
G(3,1,1,3)= G(1,3,1,3);
```

```
G(3,1,3,1)= G(1,3,1,3);
```

```
G(2,3,2,3)= G(1,3,1,3);
```

```
G(2,3,3,2)= G(1,3,1,3);
```

```
G(3,2,2,3)= G(1,3,1,3);
```

```
G(3,2,3,2)= G(1,3,1,3);
```

% Calculate the elements of Eshelby's tensor

```
S(1,1,1,1)=C(1,1,1,1)*G(1,1,1,1)+C(2,2,1,1)*G(1,2,1,2)+C(3,3,1,1)*G(1,3,1,3);
S(1,1,2,2)=C(1,1,2,2)*G(1,1,1,1)+C(2,2,2,2)*G(1,2,1,2)+C(3,3,2,2)*G(1,3,1,3);
S(1,1,3,3)=C(1,1,3,3)*G(1,1,1,1)+C(2,2,3,3)*G(1,2,1,2)+C(3,3,3,3)*G(1,3,1,3);
S(2,2,1,1)=C(1,1,1,1)*G(2,1,2,1)+C(2,2,1,1)*G(2,2,2,2)+C(3,3,1,1)*G(2,3,2,3);
S(2,2,2,2)=C(1,1,2,2)*G(2,1,2,1)+C(2,2,2,2)*G(2,2,2,2)+C(3,3,2,2)*G(2,3,2,3);
S(2,2,3,3)=C(1,1,3,3)*G(2,1,2,1)+C(2,2,3,3)*G(2,2,2,2)+C(3,3,3,3)*G(2,3,2,3);
S(3,3,1,1)=C(1,1,1,1)*G(3,1,3,1)+C(2,2,1,1)*G(3,2,3,2)+C(3,3,1,1)*G(3,3,3,3);
S(3,3,2,2)=C(1,1,2,2)*G(3,1,3,1)+C(2,2,2,2)*G(3,2,3,2)+C(3,3,2,2)*G(3,3,3,3);
S(3,3,3,3)=C(1,1,3,3)*G(3,1,3,1)+C(2,2,3,3)*G(3,2,3,2)+C(3,3,3,3)*G(3,3,3,3);
S(1,2,1,2)=C(1,2,1,2)*G(1,1,2,2);
S(1,3,1,3)=C(1,3,1,3)*G(1,1,3,3);
S(2,3,2,3)=C(2,3,2,3)*G(2,2,3,3);
```

% Transform Eshelby's tensor components into matrix components

```
M=tensmat(S);
```

```
function Y = G1111int(X,ro,d,e,f,g,h)
```

```
dimension = size(X);
```

```
length_X = dimension(2);
```

```
Y=X;
```

```
Y(1:length_X)=0;
```

```
for a = 1:length_X;
```

```
    x=X(a);
```

```
    delta=1/((e*(1-x^2)+f*ro^2*x^2)*((d*(1-x^2)+f*ro^2*x^2)*(f*(1-x^2)+h*ro^2*x^2)-g^2*ro^2*x^2*(1-x^2)));
```

```
    Y(a)=0.5*pi*delta*(1-x^2)*((f*(1-x^2)+h*ro^2*x^2)*((3*e+d)*(1-x^2)+4*f*ro^2*x^2)-g^2*ro^2*x^2*(1-x^2));
```

```
end
```

```
function Y = G1122int(X,ro,d,e,f,g,h)
```

```
dimension = size(X);
```

```
length_X= dimension(2);
```

```
y(1:length_X)=0;
```

```
for a = 1:length_X;
```

```
    x=X(a);
```

```
    delta=1/((e*(1-x^2)+f*ro^2*x^2)*((d*(1-x^2)+f*ro^2*x^2)*(f*(1-x^2)+h*ro^2*x^2)-g^2*ro^2*x^2*(1-x^2)));
```

```
    y=0.5*pi*delta*(1-x^2)*((f*(1-x^2)+h*ro^2*x^2)*((e+3*d)*(1-x^2)+4*f*ro^2*x^2)-3*g^2*ro^2*x^2*(1-x^2));
```

```
    Y(a)=y;
```

```
end
```

```
function Y = G1133int(X,ro,d,e,f,g,h)
```

```
dimension = size(X);
```

```
length_X= dimension(2);
```

```
y(1:length_X)=0;
```

```
for a = 1:length_X;
```

```
    x=X(a);
```

```
    delta=1/((e*(1-x^2)+f*ro^2*x^2)*((d*(1-x^2)+f*ro^2*x^2)*(f*(1-x^2)+h*ro^2*x^2)-g^2*ro^2*x^2*(1-x^2)));
```

```
    y=2*pi*delta*ro^2*x^2*(((d+e)*(1-x^2)+2*f*ro^2*x^2)*(f*(1-x^2)+h*ro^2*x^2)-g^2*ro^2*x^2*(1-x^2));
```

```
    Y(a)=y;
```

```
end
```

```
function Y=G1212int(X,ro,d,e,f,g,h)
```

```
dimension = size(X);
```

```
length_X= dimension(2);
```

```

y(1:length_X)=0;
for a = 1:length_X;
    x=X(a);
    delta=1/((e*(1-x^2)+f*ro^2*x^2)*((d*(1-x^2)+f*ro^2*x^2)*(f*(1-x^2)+h*ro^2*x^2)-
    g^2*ro^2*x^2*(1-x^2)));
    y=0.5*pi*delta*(1-x^2)^2*(g^2*ro^2*x^2-(d-e)*(f*(1-x^2)+h*ro^2*x^2));
    Y(a)=y;
end

function Y=G1313int(X,ro,d,e,f,g,h)
dimension = size(X);
length_X= dimension(2);
y(1:length_X)=0;
for a = 1:length_X;
    x=X(a);
    delta=1/((e*(1-x^2)+f*ro^2*x^2)*((d*(1-x^2)+f*ro^2*x^2)*(f*(1-x^2)+h*ro^2*x^2)-
    g^2*ro^2*x^2*(1-x^2)));
    y=-2*pi*delta*g*ro^2*x^2*(1-x^2)*(e*(1-x^2)+f*ro^2*x^2);
    Y(a)=y;
end

function Y=G3311int(X,ro,d,e,f,g,h)
dimension = size(X);
length_X= dimension(2);
y(1:length_X)=0;
for a = 1:length_X;
    x=X(a);
    delta=1/((e*(1-x^2)+f*ro^2*x^2)*((d*(1-x^2)+f*ro^2*x^2)*(f*(1-x^2)+h*ro^2*x^2)-
    g^2*ro^2*x^2*(1-x^2)));
    y=2*pi*delta*(1-x^2)*(d*(1-x^2)+f*ro^2*x^2)*(e*(1-x^2)+f*ro^2*x^2);
    Y(a)=y;
end

function Y = G3333int(X,ro,d,e,f,g,h)
dimension = size(X);
length_X= dimension(2);
y(1:length_X)=0;
for a = 1:length_X;
    x=X(a);
    delta=1/((e*(1-x^2)+f*ro^2*x^2)*((d*(1-x^2)+f*ro^2*x^2)*(f*(1-x^2)+h*ro^2*x^2)-
    g^2*ro^2*x^2*(1-x^2)));
    y=4*pi*delta*ro^2*x^2*(d*(1-x^2)+f*ro^2*x^2)*(e*(1-x^2)+f*ro^2*x^2);
    Y(a)=y;
end

```

A.5 References

- [1] T. Mura, *Micromechanics of Defects in Solids*, Nijhoff, The Hague, 1982
- [2] J.D. Eshelby, *The determination of the elastic field of an ellipsoidal inclusion and related problems*, Proc. R. Soc. **A241**, 1957, p 376-396
- [3] T.S. Chow, *Elastic moduli of filled polymers: The effect of particle shape*, J. Appl. Phys. **48(10)**, 1977, p 4072-4075.

Appendix B

Numerical calculation of composite stiffness

In this appendix, it will be explained how to perform actual calculation of the tensor equations of Chapter 3. To perform numerical calculations it is very convenient to use the condensed notation. First of all, this reduces the amount of components from 81 in a 4-ordered tensor, to 36 in an equivalent 6x6 matrix. Even more important is the presence of matrix algebra in most scientific computer languages. This greatly simplifies programming and considerably increases calculation speed. The use of matrices has its drawbacks. A lot of confusion might occur by transforming tensor quantities into matrices. In matrix-notation, stress and strain each have 6 components, while in tensor notation they have 9. This reduction of the amount of components must be accounted for. The second possible source of confusion is the difference of a factor two, between engineering shear strain and tensor shear strain.

In the first section of this appendix it will be explained how to transform tensor elements into matrix elements. The second section shows how to rotate a 6x6 matrix. At the end of this chapter some MATLAB computer programs are listed that are used to calculate the stiffness of a material filled with spheroids.

B.1 Transforming tensors into matrices

One must be very careful in translating tensors into engineering matrices and vice versa. This translation is prone to errors because one has to account for the change of 9 stress elements to 6 and for the factor of two difference between engineering shear strain and tensor shear strain.

To illustrate this we try first to transform the compliance tensor S_{ijkl} to a compliance matrix $[S]$. In tensor notation it is written:

$$\varepsilon_{ij} = S_{ijkl} \sigma_{kl} \quad \text{B.1)}$$

By using $\varepsilon_{ij} = \varepsilon_{ji}$ and $\sigma_{ij} = \sigma_{ji}$ Eqn. B.1 may also be written as a matrix equation:

$$\underline{\epsilon} = [\tilde{S}] \underline{\sigma} = \begin{bmatrix} \epsilon_{11} \\ \epsilon_{22} \\ \epsilon_{33} \\ \epsilon_{23} \\ \epsilon_{13} \\ \epsilon_{12} \end{bmatrix} = \begin{bmatrix} S_{1111} & S_{1122} & S_{1133} & 2S_{1123} & 2S_{1113} & 2S_{1112} \\ S_{2211} & S_{2222} & S_{2233} & 2S_{2223} & 2S_{2213} & 2S_{2212} \\ S_{3311} & S_{3322} & S_{3333} & 2S_{3323} & 2S_{3313} & 2S_{3312} \\ S_{2311} & S_{2322} & S_{2333} & 2S_{2323} & 2S_{2313} & 2S_{2312} \\ S_{1311} & S_{1322} & S_{1333} & 2S_{1323} & 2S_{1313} & 2S_{1312} \\ S_{1211} & S_{1222} & S_{1233} & 2S_{1223} & 2S_{1213} & 2S_{1212} \end{bmatrix} \begin{bmatrix} \sigma_{11} \\ \sigma_{22} \\ \sigma_{33} \\ \sigma_{23} \\ \sigma_{13} \\ \sigma_{12} \end{bmatrix} \quad \text{B.2)}$$

In engineering matrix notation this has the form:

$$\underline{e} = [S] \underline{\sigma} \quad \text{B.3)}$$

Here \underline{e} is the engineering strain. If engineering strain is used, one must account for the factor two difference between engineering strain and tensor strain. This can elegantly be done by introduction of a new matrix $[W]$:

$$\underline{e} = [W] \underline{\epsilon} \quad \text{B.4)}$$

$$\text{with } [W] = \begin{bmatrix} 1 & 0 & 0 & 0 & 0 & 0 \\ 0 & 1 & 0 & 0 & 0 & 0 \\ 0 & 0 & 1 & 0 & 0 & 0 \\ 0 & 0 & 0 & 2 & 0 & 0 \\ 0 & 0 & 0 & 0 & 2 & 0 \\ 0 & 0 & 0 & 0 & 0 & 2 \end{bmatrix} \quad \text{and} \quad [W]^{-1} = \begin{bmatrix} 1 & 0 & 0 & 0 & 0 & 0 \\ 0 & 1 & 0 & 0 & 0 & 0 \\ 0 & 0 & 1 & 0 & 0 & 0 \\ 0 & 0 & 0 & 1/2 & 0 & 0 \\ 0 & 0 & 0 & 0 & 1/2 & 0 \\ 0 & 0 & 0 & 0 & 0 & 1/2 \end{bmatrix} \quad \text{B.5)}$$

By using Eqn. B.4) and combining Eqns. B.2) and B.3) one gets:

$$[S] = [W] [\tilde{S}] = \begin{bmatrix} S_{1111} & S_{1122} & S_{1133} & 2S_{1123} & 2S_{1113} & 2S_{1112} \\ S_{2211} & S_{2222} & S_{2233} & 2S_{2223} & 2S_{2213} & 2S_{2212} \\ S_{3311} & S_{3322} & S_{3333} & 2S_{3323} & 2S_{3313} & 2S_{3312} \\ 2S_{2311} & 2S_{2322} & 2S_{2333} & 4S_{2323} & 4S_{2313} & 4S_{2312} \\ 2S_{1311} & 2S_{1322} & 2S_{1333} & 4S_{1323} & 4S_{1313} & 4S_{1312} \\ 2S_{1211} & 2S_{1222} & 2S_{1233} & 4S_{1223} & 4S_{1213} & 4S_{1212} \end{bmatrix} \quad \text{B.6)}$$

Following the same procedure one can show that all elements of the stiffness matrix are equal to the elements of the stiffness tensor:

$$[C] = [\tilde{C}] [W]^{-1} = \begin{bmatrix} C_{1111} & C_{1122} & C_{1133} & C_{1123} & C_{1113} & C_{1112} \\ C_{2211} & C_{2222} & C_{2233} & C_{2223} & C_{2213} & C_{2212} \\ C_{3311} & C_{3322} & C_{3333} & C_{3323} & C_{3313} & C_{3312} \\ C_{2311} & C_{2322} & C_{2333} & C_{2323} & C_{2313} & C_{2312} \\ C_{1311} & C_{1322} & C_{1333} & C_{1323} & C_{1313} & C_{1312} \\ C_{1211} & C_{1222} & C_{1233} & C_{1223} & C_{1213} & C_{1212} \end{bmatrix} \quad \text{B.7)}$$

For the strain concentration tensor we can write:

$$\varepsilon_{ij}^r = A_{ijkl} \varepsilon_{kl}^m \quad \text{B.8)}$$

Eqn. B.8) can also be written as a matrix:

$$\underline{\varepsilon}^r = [\tilde{A}] \underline{\varepsilon}^m = \begin{bmatrix} \varepsilon_{11}^r \\ \varepsilon_{22}^r \\ \varepsilon_{33}^r \\ \varepsilon_{23}^r \\ \varepsilon_{13}^r \\ \varepsilon_{12}^r \end{bmatrix} = \begin{bmatrix} A_{1111} & A_{1122} & A_{1133} & 2A_{1123} & 2A_{1113} & 2A_{1112} \\ A_{2211} & A_{2222} & A_{2233} & 2A_{2223} & 2A_{2213} & 2A_{2212} \\ A_{3311} & A_{3322} & A_{3333} & 2A_{3323} & 2A_{3313} & 2A_{3312} \\ A_{2311} & A_{2322} & A_{2333} & 2A_{2323} & 2A_{2313} & 2A_{2312} \\ A_{1311} & A_{1322} & A_{1333} & 2A_{1323} & 2A_{1313} & 2A_{1312} \\ A_{1211} & A_{1222} & A_{1233} & 2A_{1223} & 2A_{1213} & 2A_{1212} \end{bmatrix} \begin{bmatrix} \varepsilon_{11}^m \\ \varepsilon_{22}^m \\ \varepsilon_{33}^m \\ \varepsilon_{23}^m \\ \varepsilon_{13}^m \\ \varepsilon_{12}^m \end{bmatrix} \quad \text{B.9)}$$

In engineering matrix notation it has the form:

$$\underline{e}^r = [A] \underline{e}^m \quad \text{B.10)}$$

By using the $\underline{e} = [W] \underline{\varepsilon}$ and combining Eqns. B.09) and B.10) one gets:

$$[A] = [W] [\tilde{A}] [W]^{-1} = \begin{bmatrix} A_{1111} & A_{1122} & A_{1133} & A_{1123} & A_{1113} & A_{1112} \\ A_{2211} & A_{2222} & A_{2233} & A_{2223} & A_{2213} & A_{2212} \\ A_{3311} & A_{3322} & A_{3333} & A_{3323} & A_{3313} & A_{3312} \\ 2A_{2311} & 2A_{2322} & 2A_{2333} & 2A_{2323} & 2A_{2313} & 2A_{2312} \\ 2A_{1311} & 2A_{1322} & 2A_{1333} & 2A_{1323} & 2A_{1313} & 2A_{1312} \\ 2A_{1211} & 2A_{1222} & 2A_{1233} & 2A_{1223} & 2A_{1213} & 2A_{1212} \end{bmatrix} \quad \text{B.11)}$$

The stress concentration tensor is defined as:

$$\sigma_{ij}^r = B_{ijkl} \sigma_{kl}^m \quad \text{B.12)}$$

which can also be written as a matrix equation:

$$\underline{\sigma}' = [\tilde{B}] \underline{\sigma}'' = \begin{bmatrix} \sigma_{11}'' \\ \sigma_{22}'' \\ \sigma_{33}'' \\ \sigma_{23}'' \\ \sigma_{13}'' \\ \sigma_{12}'' \end{bmatrix} = \begin{bmatrix} B_{1111} & B_{1122} & B_{1133} & 2B_{1123} & 2B_{1113} & 2B_{1112} \\ B_{2211} & B_{2222} & B_{2233} & 2B_{2223} & 2B_{2213} & 2B_{2212} \\ B_{3311} & B_{3322} & B_{3333} & 2B_{3323} & 2B_{3313} & 2B_{3312} \\ B_{2311} & B_{2322} & B_{2333} & 2B_{2323} & 2B_{2313} & 2B_{2312} \\ B_{1311} & B_{1322} & B_{1333} & 2B_{1323} & 2B_{1313} & 2B_{1312} \\ B_{1211} & B_{1222} & B_{1233} & 2B_{1223} & 2B_{1213} & 2B_{1212} \end{bmatrix} \begin{bmatrix} \sigma_{11}'' \\ \sigma_{22}'' \\ \sigma_{33}'' \\ \sigma_{23}'' \\ \sigma_{13}'' \\ \sigma_{12}'' \end{bmatrix} \quad \text{B.13)}$$

Since tensor stress equals engineering stress, it follows that $[B] = [\tilde{B}]$.

B.2 Rotating a matrix

In general, the components of a fourth ordered tensor could be rotated by Eqn. 3.41). Therefore, every fourth ordered tensor is rotation transformed the same way. In condensed matrix notation, each type of matrix has its own specific method of transformation. The type of transformation depends on the type of the matrix. The stiffness matrix $[C]$ changes stresses into strains, while the compliance matrix $[S]$ changes strains into stresses. Therefore, the transformation of $[C]$ differs from the transformation of $[S]$. Likewise, the transformation of the strain concentration matrix $[A]$, which changes strains into strains, differs from the stress concentration matrix $[B]$, which changes stresses into stresses.

To find the correct transformation rules for each type of matrix, we will first look at the transformation of stresses and strains in tensor and in engineering matrix notation. From Eqn. 3.40) it follows:

$$\epsilon_{i'j'} = \omega_{i'i} \omega_{j'j} \epsilon_{ij} = \sum_{i=1}^3 \sum_{j=1}^3 \omega_{i'i} \omega_{j'j} \epsilon_{ij} \quad \text{and} \quad \sigma_{i'j'} = \omega_{i'i} \omega_{j'j} \sigma_{ij} = \sum_{i=1}^3 \sum_{j=1}^3 \omega_{i'i} \omega_{j'j} \sigma_{ij}$$

In matrix notation, stresses and strains are written as '1x6 vectors'. Eqn. 3.40) then gets the form:

$$\underline{\epsilon}' = [T] \underline{\epsilon} \quad \text{and} \quad \underline{\sigma}' = [T] \underline{\sigma} \quad \text{B.14)}$$

where $\underline{\epsilon}'$ and $\underline{\epsilon}$ are the strain 'vectors' in global and local coordinates respectively, while $\underline{\sigma}'$ and $\underline{\sigma}$ are the corresponding stresses. Note that here $\underline{\epsilon}$ only contains elements of tensor strain, the factor of two between tensor shear strain and engineering shear strain is not incorporated yet. $[T]$ is a 6x6 orientation transformation matrix. The elements of $[T]$ can be found by carefully comparing all tensor elements of Eqn. 3.64) with the corresponding matrix elements of Eqn. 3.65). $[T]$ is given by Whitney and McCullough [1]:

$$\begin{aligned}
 & \text{Rotation transformation Matrix} \\
 [T] = & \begin{bmatrix}
 \omega_{11}^2 & \omega_{12}^2 & \omega_{13}^2 & 2\omega_{12}\omega_{13} & 2\omega_{11}\omega_{13} & 2\omega_{11}\omega_{12} \\
 \omega_{21}^2 & \omega_{22}^2 & \omega_{23}^2 & 2\omega_{22}\omega_{23} & 2\omega_{21}\omega_{23} & 2\omega_{21}\omega_{22} \\
 \omega_{31}^2 & \omega_{32}^2 & \omega_{33}^2 & 2\omega_{32}\omega_{33} & 2\omega_{31}\omega_{33} & 2\omega_{31}\omega_{32} \\
 \omega_{21}\omega_{31} & \omega_{22}\omega_{32} & \omega_{23}\omega_{33} & \omega_{22}\omega_{33} + \omega_{23}\omega_{32} & \omega_{21}\omega_{33} + \omega_{23}\omega_{31} & \omega_{21}\omega_{32} + \omega_{22}\omega_{31} \\
 \omega_{11}\omega_{31} & \omega_{12}\omega_{32} & \omega_{13}\omega_{33} & \omega_{12}\omega_{33} + \omega_{13}\omega_{32} & \omega_{11}\omega_{33} + \omega_{13}\omega_{31} & \omega_{11}\omega_{32} + \omega_{12}\omega_{31} \\
 \omega_{11}\omega_{21} & \omega_{12}\omega_{22} & \omega_{13}\omega_{23} & \omega_{12}\omega_{23} + \omega_{13}\omega_{22} & \omega_{11}\omega_{23} + \omega_{13}\omega_{21} & \omega_{11}\omega_{22} + \omega_{12}\omega_{21}
 \end{bmatrix} \quad \text{B.15}
 \end{aligned}$$

Now suppose that a matrix $[T^*]$ exists to rotate the components of engineering strain:

$$\underline{e}' = [T^*] \underline{e} \quad \text{B.16}$$

Then, by using $\underline{e} = [W] \underline{\epsilon}$ and combining Eqns. B.14) and B.16) it is easy to show that:

$$[T^*] = [W] [T] [W]^T \text{ and } [T] = [W]^T [T^*] [W] \quad \text{B.17}$$

It can also be shown that:

$$[T]^T = [T^*] \quad \text{B.18}$$

and similarly:

$$[T^*]^T = [T] \quad \text{B.19}$$

With the transformation matrices $[T^*]$ and $[T]$ it is also possible to perform a coordinate transformation of a 6x6 matrix in contracted engineering notation. The type of transformation depends on the type of matrix. First the transformation of the stiffness matrix $[C]$ and the compliance matrix $[S]$ will be observed. In local coordinates, Hooke's law has the form $\underline{\sigma} = [C] \underline{e}$ while in global coordinates it has the form $\underline{\sigma}' = [C'] \underline{e}'$. Using Eqns. B.14) and B.16) it follows that:

$$\underline{\sigma}' = [C'] \underline{e}' = [T] \underline{\sigma} = [T] [C] \underline{e} = [T] [C] [T^*]^{-T} \underline{e}' \Rightarrow$$

$$\text{or:} \quad [C'] = [T] [C] [T^*]^{-T} = [T] [C] [T]^T \quad \text{B.20}$$

$$\text{Similarly:} \quad [S'] = [T^*] [S] [T]^{-T} = [T^*] [S] [T]^T \quad \text{B.21}$$

$[C]$ and $[S]$ change stresses into strains and vice versa, while the strain concentration matrix $[A]$ changes strains into strains and the stress concentration matrix $[B]$ changes stresses into stresses. Therefore, $[A]$ and $[B]$ each require a different type of coordinate transformation. The transformation rules for the strain concentration matrix $[A]$ are derived first:

$$\underline{e}' = [A'] \underline{e}^m = [T^*] \underline{e}' = [T^*] [A] \underline{e}^m = [T^*] [A] [T^*]^{-T} \underline{e}' \Rightarrow$$

$$[A'] = [T^*] [A] [T^*]^{-T} = [T^*] [A] [T]^T \quad \text{B.22)}$$

Similarly, transformation of the stress concentration matrix becomes:

$$[B'] = [T] [B] [T]^T = [T] [B] [T^*]^T \quad \text{B.23)}$$

B.3 MATLAB computer programs

With the Matlab programs below the stiffness matrix and the thermal expansion of a composite are calculated. The program needs input of the elastic properties of the phases like the Young's modulus, the Poisson's ratio and the coefficient of linear thermal expansion (CLTE). Additionally it requires information on the morphology of the composite like the aspect ratio and the orientation distribution of the inclusions. It is assumed that the inclusions are spheroid-like shaped and are oriented transversely symmetric around the 3-axis of the composite. The program has a convenient user interface, which is too long to be listed in this thesis. In Fig. B.1 an impression is given of the input window.

On the right, the input window allows input of elastic properties of the matrix and of the filler. An index *m*, indicates the matrix and index 1 indicates the filler. *E* denotes the Young's modulus, *Nu* the Poisson's ratio and *Alfa* the thermal expansion coefficient. The fields **Massfraction_1_min** and **Massfraction_1_max** allow input of the minimum and maximum amount of filler. The fields **Aspect_1_min** and **Aspect_1_max** expect input of the minimum and maximum aspect ratio. After calculation, a pop-up menu appears that allows free choice of elastic or morphological variables, to plot along x-axis or y-axis. In the upper left of the input window, the type of composite model can be chosen to perform the calculations. In the lower right, the type of orientation can be specified. As it is now, the input window program is suited for a single isotropic filler in an isotropic matrix. The calculation routines are more versatile. In principle they allow multiple fillers, with orthorhombic symmetry.

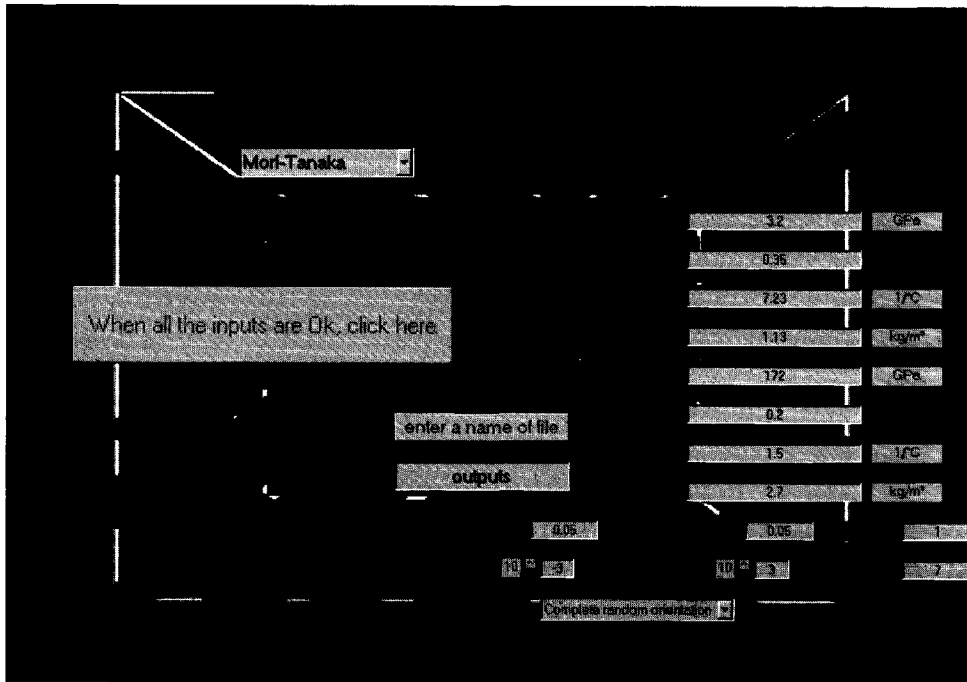


Figure B.1 Input window for analytical composite modelling

B.3.1 The Mori-Tanaka function

The Mori-Tanaka function calculates the stiffness of a composite filled with transversely isotropic oriented ellipsoids. It requires input of the elastic properties and of morphological parameters. It uses the Mori-Tanaka equations in Chapter 3 to calculate the stiffness and expansion coefficient of the composite. The averaging techniques from Chapter 3 are used to account for the orientation distribution and calculate the averaged stiffness matrix and the averaged thermal expansion.

```
function [E11_av,E33_av,Nu31_av,G12_av,G13_av,alfa_av11,alfa_av33] = Mori_Tanaka(E0,...
    nu0,ro0,alfa0,E1,nu1,ro1,alfa1,m1,Aspect1,a0,a2,a4);
```

```
% Function to calculate the stiffness of a transversely isotropic oriented composite
```

```
% Polymer&Filler properties
```

```
% Input    E0, E1      Young's modulus of matrix and filler
%          nu0, nu1    Poisson's ratio
%          alfa0, alfa1 Thermal expansion coefficient
%          ro0, ro1    Density
%          m1         Mass fraction of filler. This is a vector!
%          Aspect1    Aspect ratio of filler. This is a vector!
%          a0, a2, a4  Moments of the Legendre orientation distribution function
```

```
% Output    E11_av, E33_av, Nu31_av, G12_av, G13_av Elastic constants of composite
%          alfa_av11_alfa_av33                      Thermal expansion of composite
```

```
C0= material(E0,nu0);% Fill 6X6 matrix with polymer properties
S0=inv(C0);
```

```

C1=material(E1,nu1);% Fill 6X6 matrix with filler properties
S1=inv(C1);

vol1= (m1/ro1)./(m1/ro1+(1-m1)/ro0);% volume fraction of filler

m=0;
for c1=vol1; %volume fraction filler
    m=m+1;
    c0 = 1-c1;% volume fraction polymer
    n=0; %counter for aspect_ratio
    for aspect_ratio=Aspect1;
        n=n+1;
        %Prevent aspect_ratio=1
        if aspect_ratio== 1 ;
            aspect_ratio=1.001;
        end

        %Initialisation of tensors and matrices

        A_av=zeros(6,6);
        B_av=zeros(6,6);
        Cc_av=zeros(6,6);

        P= Eshensor(aspect_ratio,nu0); % Calculate Eshelby's Tensor assuming filler is isotropic ellipsoid
        A = inv(eye(6)+P*S0*(C1-C0)); % A = Average strain concentration tensor
        B = C1*A*S0; % B = Average stress concentration tensor

        % Stiffness matrix of unidirectional ellipsoid filled polymer
        Cc = (c0*C0+c1*B*C0)*inv(c0*eye(6)+c1*A);
        Sc=inv(Cc);
        alfa=alfa0+(alfa1-alfa0)*inv(S1-S0)*(Sc-S0);
        alfa11(m,n)=alfa(1);
        alfa33(m,n)=alfa(3);
        E11(m,n)=1/Sc(1,1);
        E33(m,n)=1/Sc(3,3);

        % Randomisation
        number_phi = 16; % Number of phi angles to perform Simpson's integration
        number_theta = 20; % Number of theta angles to perform Simpson's integration

        % Calculate the average A_matrix and B_matrix using the orientation parameters
        [A_av,B_av]=rand2ang(A,B,a0,a2,a4,number_phi,number_theta);

        % Calculate the average composite stiffness matrix Cc_av and compliance matrix Sc_av.
        Cc_av = (c0*C0+c1*B_av*C0)*inv(c0*eye(6)+c1*A_av);
        Sc_av=inv(Cc_av);
        % Calculate the average thermal expansion matrix alfa_av.
        alfa_av=alfa0+(alfa1-alfa0)*inv(S1-S0)*(Sc_av-S0);

        E33_av(m,n)=1/Sc_av(3,3);
        E11_av(m,n)=1/Sc_av(1,1);
        Nu31_av(m,n)=-Sc_av(3,1)*E33_av(m,n);
        G12_av(m,n)=1/Sc_av(6,6);
        G13_av(m,n)=1/Sc_av(4,4);
        alfa_av11(m,n)=alfa_av(1);
        alfa_av33(m,n)=alfa_av(3);
    end
end

```

B.3.2 The functions 'material' and 'orthomat'

The function 'material' creates a 6x6 stiffness matrix of an isotropic material with Young's modulus E and Poisson's ratio. The function 'orthomat' creates the stiffness matrix of a material with orthorhombic symmetry and requires an input of nine elastic constants.

```
function [C]=material(E,nu);
% Input      E      Young's Modulus in GPa
%           nu      Poisson's ratio
% Output     C0      Stiffness matrix

G = E/(2*(1+nu)); % Shear modulus matrix

% Compliance matrix of polymer
S = zeros(6,6);
S(1:3,1:3)=-nu/E;
S(1,1) = 1/E;
S(2,2) = 1/E;
S(3,3) = 1/E;
S(4,4) = 1/G;
S(5,5) = 1/G;
S(6,6) = 1/G;
%stiffness matrix of polymer
C = inv(S);

function C = Orthomat(E11,E22,E33,G23,G13,G12,n12,n13,n23)
% Input 9 elastic constants E11,E22,E33 Young's Moduli in GPa
%           G23,G13,G12 Shear moduli
%           n12,n13,n23 Poisson's ratios
% Output      C      Stiffness matrix of material with orthorhombic symmetry

S=zeros(6,6);

S(1,1) = 1/E11;
S(1,2) = -n12/E11;
S(1,3) = -n13/E11;
S(2,1) = S(1,2);
S(2,2) = 1/E22;
S(2,3) = -n23/E22;
S(3,1) = S(1,3);
S(3,2) = S(2,3);
S(3,3) = 1/E33;
S(4,4) = 1/G23;
S(5,5) = 1/G13;
S(6,6) = 1/G12;

C=inv(S);
```

B.3.3 Functions to calculate the Eshelby tensor

The function 'Eshtensor' is used to calculate the components of the Eshelby tensor, which is discussed in Chapter 3 and in Appendix A. The function translates the Eshelby tensor to an equivalent 6x6 matrix. It assumes that the matrix has isotropic properties. It requires the aspect-ratio of the filler and the Poisson's ratio of the matrix as input values. If the matrix is anisotropic then the function 'Muratens' should be used instead. This function is not listed.

```

function P = Eshtensor(aspect,nu0);
%Input:   aspect  aspect ratio of the spherodic shaped filler: aspect  (0<aspect<=inf)
%         if aspect < 1 then spheroid is flake like.
%         if aspect > 1 then spheroid is fibre like.
%         nu0     Poisson's ratio of the matrix polymer:
%Output:  P       Eshelby's Tensor represented as a 6X6 engineering matrix.
%
%The 3-axis is supposed to be the main symmetry axis of the spheroid

if aspect > 1
    g = aspect/(aspect^2-1)^1.5*(aspect*(aspect^2-1)^0.5-acosh(aspect));
else
    g = aspect/(1-aspect^2)^1.5*(acos(aspect)-aspect*(1-aspect^2)^0.5);
end

P3333= 1/(2*(1-nu0))*(1-2*nu0+(3*aspect^2-1)/(aspect^2-1)-g*(1-2*nu0+3*aspect^2/(aspect^2-1)));
P1111= 3/(8*(1-nu0))*aspect^2/(aspect^2-1)+g/(4*(1-nu0))*(1-2*nu0-9/(4*(aspect^2-1)));
P1122= 1/(4*(1-nu0))*(aspect^2/(2*(aspect^2-1))-g*(1-2*nu0+3/(4*(aspect^2-1))));
P1133= -1/(2*(1-nu0))*aspect^2/(aspect^2-1)+g/(4*(1-nu0))*(3*aspect^2/(aspect^2-1)-(1-2*nu0));
P3311= -1/(2*(1-nu0))*(1-2*nu0+1/(aspect^2-1))+g/(2*(1-nu0))*(1-2*nu0+3/(2*(aspect^2-1)));
P1212= 1/(4*(1-nu0))*(aspect^2/(2*(aspect^2-1))+g*(1-2*nu0-3/(4*(aspect^2-1))));
P1313= 1/(4*(1-nu0))*(1-2*nu0-(aspect^2+1)/(aspect^2-1)-g/2*(1-2*nu0-3*(aspect^2+1)/(aspect^2-1)));

P2222=P1111;
P2211=P1122;
P2233=P1133;
P3322=P3311;
P2323=P1313;

P = zeros(6,6);
P(1,1:3)=[P1111 P1122 P1133];
P(2,1:3)=[P2211 P2222 P2233];
P(3,1:3)=[P3311 P3322 P3333];
P(4,4)=2*P2323; %P(4,4);P(5,5) and P(6,6) are multiplied by two because of transformation rules.
P(5,5)=2*P1313;
P(6,6)=2*P1212;

```

B.3.4 Function to average a matrix

The function 'rand2ang' is the heart of the program and is used to average the A and B matrices according to an orientation distribution function as is explained in Chapter 3. It needs two matrices, the moments of the distribution function and two numbers for the integration steps as input values and gives the averaged matrices as output. As was indicated in Chapter 3 using Mori-Tanaka theory to calculate average properties can lead to non physical behaviour.

```
function [A_av,B_av]=rand2ang(A,B,a0,a2,a4,number_phi,number_theta);
```

```

% Use this function to transversely isotropic randomise two 6*6 matrices.
% It is assumed that the matrix is transversely isotropic around the 3' axis. Rotation around the 3' axis
% doesn't change the orientation. Therefore randomisation is only
% performed around two axes.
% Input   A,B:   Two matrices to randomise. It is assumed that the matrix has 12 elements.
%         A=strain concentration matrix
%         B=stress concentration matrix

```

```

%      a0,a2,a4   The orientation function, as terms of Legendre polynomials
%                  a0=1; a2=5*<P2> ; a4=9*<P4>
%                  P2=1.5*cos(theta))^2-.5;
%                  P4=(35*cos(theta(t))^4-30*cos(theta(t))^2+3)/8;
%      number     The number of summation steps in each integration loop; must be even!
%                  Simpson's rule is used.
% Output  A_av, B_av The transversely isotropic (around the global 3-axis) randomised A and B
%                  matrices.
%
% (R.C.G. Arridge, 'An introduction to polymer mechanics', 1985, Taylor&Francis, London, p147)
% Complete random orientation a0=1 a2=0 a4=0.
% Full alignment             a0=1 a2=5 a4=9
% Equatorial sheet (i.e. SMC) a0=1 a2=-5/2 a4=27/8
% Maximum at theta = 30°     a0=1 a2=25/8 a4=27/128

% Initialize integration borders & steps
theta_max=pi/2; %Integrate between 0<=theta<=pi/2
d_theta=theta_max/number_theta;
theta= [0:d_theta:theta_max];
phi_max=2*pi; %Integrate between 0<=phi<2pi
d_phi=phi_max/number_phi;
phi= [0:d_phi:phi_max];
%-----
% Calculate P2 and P4
dim_theta = size(theta);
length_theta= dim_theta(2);
dim_phi = size(phi);
length_phi= dim_phi(2);

P2(1:length_theta)=0; % Initialize P2 and P4
P4=P2;
sinus=P2; % Initialize 'sinus' for later use in integration loop

P2=1.5*(cos(theta)).^2-.5;
P4=(35*(cos(theta)).^4-30*(cos(theta)).^2+3*ones(1,length_theta))/8;
sinus=sin(theta);

A_phi_theta=zeros(6,6,length_phi,length_theta); % big matrix with all rotated A_matrices
B_phi_theta=zeros(6,6,length_phi,length_theta); % big matrix with all rotated B_matrices

% W = matrix to facilitate transformation between matrix and tensor notation
W=zeros(6,6);
W(1,1)=1;
W(2,2)=1;
W(3,3)=1;
W(4,4)=2;
W(5,5)=2;
W(6,6)=2;
invW=zeros(6,6);
invW(1,1)=1;
invW(2,2)=1;
invW(3,3)=1;
invW(4,4)=.5;
invW(5,5)=.5;
invW(6,6)=.5;

A_to_int=zeros(6,6,length_phi,length_theta);
B_to_int=zeros(6,6,length_phi,length_theta);

for t=1:length_theta;

```

```

theta_loop=theta(t);

for s=1:length_phi;
    phi_loop= phi(s);
    T = rotmatrix(phi_loop,theta_loop);
    A_phi_theta(:,s,t)=(W*T*invW)*A*(transpose(T)); % Rotate A_matrix
    B_phi_theta(:,s,t)=T*B*(transpose(W*T*invW)); % Rotate B_matrix
    %A_to_int(:,s,t)=A_phi_theta(:,s,t)*(a0+a2*P2(t)+a4*P4(t))*sinus(t);
    %B_to_int(:,s,t)=B_phi_theta(:,s,t)*(a0+a2*P2(t)+a4*P4(t))*sinus(t);
end

%faster way to multiply by the distribution function(depending only on theta) and by sinus(theta)
%for a fixed theta, every element of the sub-matrix is multiplied by the same number.
A_to_int(:,t)=(reshape(A_phi_theta(:,t),6,6,length_phi)).*((a0+a2*P2(t)+a4*P4(t))*sinus(t));
B_to_int(:,t)=(reshape(B_phi_theta(:,t),6,6,length_phi)).*((a0+a2*P2(t)+a4*P4(t))*sinus(t));
end

% Perform double integration using function int_mat
A_av=int_mat(A_to_int,phi,theta)/(2*pi);
B_av=int_mat(B_to_int,phi,theta)/(2*pi); %

```

B.3.5 Rotation of the matrices

The function 'rotmatrix' calculate for every theta and phi the matrix T necessary to rotate the A and B matrices over these phi and theta, according to the theory developed above. As input it needs two angles, thet and phi over which the elements are be rotated.

```

function T = rotmatrix(phi,theta);

% Input    phi, theta    The angles over which to rotate
% Output   T             Matrix to rotate a stress vector, this is an engineering version of a second
%                               order rotation tensor

```

```

w=zeros(3,3); % w is a rotation matrix to rotate a 1st order vector

```

```

w(1,1)= cos(theta)*cos(phi);
w(1,2)= -sin(phi);
w(1,3)= sin(theta)*cos(phi);
w(2,1)= cos(theta)*sin(phi);
w(2,2)= cos(phi);
w(2,3)= sin(theta)*sin(phi);
w(3,1)= -sin(theta);
w(3,2)= 0;
w(3,3)= cos(theta);

```

```

T=zeros(6,6);

```

```

T(1:3,1:3)=w.*w;
T(1:3,4)=2*w(1:3,2).*w(1:3,3);
T(1:3,5)=2*w(1:3,1).*w(1:3,3);
T(1:3,6)=2*w(1:3,1).*w(1:3,2);
T(4,1:3)=w(2,1:3).*w(3,1:3);
T(5,1:3)=w(1,1:3).*w(3,1:3);
T(6,1:3)=w(1,1:3).*w(2,1:3);
T(4,4)=w(2,2)*w(3,3)+w(2,3)*w(3,2);
T(4,5)=w(2,1)*w(3,3)+w(2,3)*w(3,1);
T(4,6)=w(2,1)*w(3,2)+w(2,2)*w(3,1);
T(5,4)=w(1,2)*w(3,3)+w(1,3)*w(3,2);

```

```

T(5,5)=w(1,1)*w(3,3)+w(1,3)*w(3,1);
T(5,6)=w(1,1)*w(3,2)+w(1,2)*w(3,1);
T(6,4)=w(1,2)*w(2,3)+w(1,3)*w(2,2);
T(6,5)=w(1,1)*w(2,3)+w(1,3)*w(2,1);
T(6,6)=w(1,1)*w(2,2)+w(1,2)*w(2,1);

```

B.3.6 Integration of the matrices

The functions 'int_mat' and 'doubleintegral' calculate only the independent terms (reduced because of symmetry) of the matrix, and fill-in the rest of the matrix. As input it needs the big matrix (the 6x6 matrix at every theta and phi) and the two angles over which to integrate.

```
function Mav=int_mat(M_to_int,phi,theta);
```

```

dim_theta = size(theta);
length_theta= dim_theta(2);
dim_phi = size(phi);
length_phi= dim_phi(2);

```

```

Mav=zeros(6,6);
Mav(1,1)=doubleintegral((reshape(M_to_int(1,1,:),length_phi,length_theta)),phi,theta);
Mav(2,2)=Mav(1,1);
Mav(3,3)=doubleintegral((reshape(M_to_int(3,3,:),length_phi,length_theta)),phi,theta);
Mav(1,2)=doubleintegral((reshape(M_to_int(1,2,:),length_phi,length_theta)),phi,theta);
Mav(2,1)=Mav(1,2);
Mav(3,1)=doubleintegral((reshape(M_to_int(3,1,:),length_phi,length_theta)),phi,theta);
Mav(3,2)=Mav(3,1);
Mav(1,3)=doubleintegral((reshape(M_to_int(1,3,:),length_phi,length_theta)),phi,theta);
Mav(2,3)=Mav(1,3);
Mav(4,4)=doubleintegral((reshape(M_to_int(4,4,:),length_phi,length_theta)),phi,theta);
Mav(5,5)=Mav(4,4);
Mav(6,6)=doubleintegral((reshape(M_to_int(6,6,:),length_phi,length_theta)),phi,theta);

```

```

function phi_theta_int_int = doubleintegral(function_phi_theta,phi,theta)
%Double integration of function(phi,theta) by Simpson's rule
% Input      function_phi_theta : A matrix representing a function of phi and theta
%           phi,theta,          : Vectors containing the variables over which the integration is to
%                               be performed. The elements in these vectors are equidistantly
%                               spaced. Odd number of elements is required
% Output     Double integral of function_phi_theta over phi and theta

```

```

% Determine the amount of elements in 'phi'
dimension_phi = size(phi);
number_phi= dimension_phi(2); % number of variables in the vector phi
%Determine the low and high limits of integration over phi
lowlimit_phi =phi(1);
highlimit_phi=phi(number_phi);
%integration step size
d_phi=(highlimit_phi-lowlimit_phi)/(number_phi-1);

```

```

%Determine the amount of elements in 'theta'
dimension_theta = size(theta);
number_theta= dimension_theta(2);% number of variables in the vector theta
%Determine the low and high limits of integration over theta
lowlimit_theta =theta(1);
highlimit_theta=theta(number_theta);
%integration step size

```

```
d_theta=(highlimit_theta-lowlimit_theta)/(number_theta-1);
```

```
theta_int=zeros(1,number_phi);
```

```
%Use Simpson's rule to calculate integral of integrand over theta
```

```
a=function_phi_theta*Simpsonmatrix(number_theta);
```

```
theta_int =(d_theta/3)*sum(transpose(a)); % sum is summing the elements in each column
```

```
%(So we have to transpose to sum on theta), and gives a row vector
```

```
% Use Simpson's rule to calculate integral of integrand over phi
```

```
b=theta_int*Simpsonmatrix(number_phi);
```

```
phi_theta_int_int =(d_phi/3)*sum(b);
```

B.4 References

[1] J.M. Whitney and R.L. McCullough, *Micromechanical Materials Modeling*, Technomic, Lancaster, USA, 1990.

Appendix C

Universal use of composite models

Different theories for mechanical, dielectrical and transport properties of composites have a common theoretical origin since they all are based on the Laplace equation. Since they have the same theoretical background they can be unified to one common expression. In doing so the Halpin-Tsai equations are proven to be theoretically correct. The factor $\zeta=3/4$ w/t introduced in Chapter 3 to calculate the in-plane shear modulus of composites with aligned platelets will be derived theoretically.

C.1 Models for mechanical, dielectrical and transport properties

The Halpin-Tsai equations of Eqns 3.13 and 3.14 can also be written as:

$$\frac{M}{M_m} = 1 + \frac{c}{\frac{M_r - M_m}{M_r - M_m} + \left(\frac{1}{1 + \zeta} \right) (1 - c)} \quad \text{C.1)}$$

where M is the composite modulus, c is the concentration of filler and ζ is the shape factor. Indices m and r denote matrix and reinforcing phase respectively. Provided $A_k = 1/(1 + \zeta)$, this equation is analogous to the Maxwell-Garnett equation [1-3] derived for the dielectric constant of a two-phase composite filled with oriented spheroids:

$$\frac{\epsilon}{\epsilon_m} = 1 + \frac{c}{\frac{\epsilon_r - \epsilon_m}{\epsilon_r - \epsilon_m} + A_k (1 - c)} \quad \text{C.2)}$$

here ϵ is the dielectric constant and A_k is a shape factor.

Using Eshelby and Mori-Tanaka theories, Tandon and Weng [4] derived an analytical expression for the shear modulus of a composite filled with aligned isotropic spheroids. If the axis of symmetry of the spheroids is parallel to the 3-axis of the composite, the shear modulus in the plane perpendicular to the 3-axis is given by:

$$\frac{G_{12}}{G_m} = 1 + \frac{c}{\frac{G_r - G_m}{G_r - G_m} + 2P_{1212} (1 - c)} \quad \text{C.3)}$$

P_{1212} is an element of the Eshelby tensor given in Appendix A. Equation C3) is equivalent to the Halpin-Tsai equation if $2P_{1212} = 1/(1+\zeta)$. For platelets with $t/w \ll 1$, $2P_{1212}$ reduces to:

$$2P_{1212} \approx \pi t/w \left(\frac{1}{2} - \frac{1}{16(1-\nu_m)} \right) \quad \text{C.4)}$$

Halpin-Tsai and Tandon and Weng's equations for platelets coincide if $\zeta = \frac{w}{t} \frac{16}{\pi} \frac{1-\nu_m}{7-8\nu_m}$.

Using the fact that $0 < \nu_m < 0.5$ it can easily be shown that: $0.73 \frac{w}{t} < \zeta < 0.85 \frac{w}{t}$. This is close to $\zeta = \frac{3}{4} \frac{w}{t}$ which was found by fitting in Chapter 3.

Hatta's equation for thermal conductivity [5] is also equivalent to the Halpin-Tsai equation, providing $S_i = 1/(1+\zeta)$:

$$\frac{K_i}{K_m} = \left\{ 1 + \frac{c}{\frac{K_r}{(K_r - K_m)} + S_i(1-c)} \right\} \quad i=1,2,3 \quad \text{C.5)}$$

As was shown in Chapter 10 Hatta's equation can also be used for mass transport by replacing the thermal conductivity K by the mass permeability P .

C.2 Conclusions

Provided the correct shape factor is taken, Halpin-Tsai's model is found to be equivalent to Maxwell Garnett's model for the dielectric constant, to Mori-Tanaka's model for the shear modulus and to Hatta's model for the thermal conductivity and mass permeability.

By exploring this similarity, the shape factor $\zeta = 0.75$ found by fitting in Chapter 3 for the in-plane shear modulus of aligned platelet reinforced composites, could be derived theoretically.

C.3 References

- [1] C.J.F. Böttcher and P. Bordewijk, *Theory of Electric Polarization*, vol. 2, Elsevier, Amsterdam, 1978, p 476-491
- [2] P.A.M. Steeman, *Interfacial Phenomena in polymer systems, A dielectric approach*, PhD Thesis, Technical University of Delft, 1992
- [3] A. Boersma, *A Dielectric Study on the Microstructure in Polymers and Blends; Orientation, Crystallization and Interfacial Phenomena in a Liquid Crystalline Polymer and its Blends*, PhD Thesis, Technical University of Delft, 1998
- [4] G.P. Tandon and G.J. Weng, *The Effect of Aspect Ratio of Inclusions on the Elastic Properties of Unidirectionally Aligned Composites*, *Pol. Composites* **5**(4), 1984, p 327-333
- [5] Hatta H., Taya M., Kulacki F.A., Harder J.F., *Thermal diffusion of composites with various types of filler*, *J. Comp. Mat.* **26**(5), 1992, p 612-625

Appendix D

Errors in data analysis of nanocomposite TEM images

D.1 Determining the volume fraction from TEM images

According to the theorems of Delesse (1847), Rosiwall (1898) and Glagoleff (1933) [1] the volume fraction (φ_V) of a component can be calculated from the corresponding area fraction (φ_A) of this component in a plane that intersects the whole material. The area fraction, for its turn, can be determined from the corresponding fractional length (φ_L) of a line drawn in the plane. That is:

$$\varphi_V = \varphi_A = \varphi_L \quad \text{D.1)}$$

Since the thickness of a ultramicrotomed section (about 70 nm) has the same order of magnitude as the size of a clay platelet (1-500 nm) a TEM image will always contain more platelets than actually intersect the upper plane of the section. As can be concluded from figure D.1, the amount of platelets in a TEM section is increased if the thickness of the section increases.

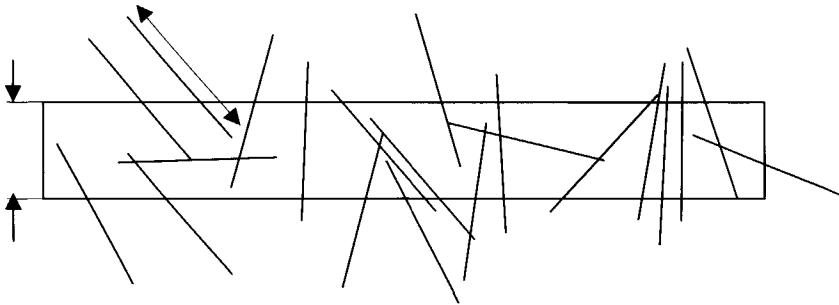


Figure D.1 The amount of clay particles in a TEM coupe is larger than the amount of particles that intersect the upper plane.

The apparent volume fraction of platelets in the TEM images of the PA6 nanocomposites is estimated using the fractional length method described above. A line was drawn perpendicular to the orientation direction of the section. The fractional length is determined by counting the amount of intersects of a line drawn on the TEM image. The fractional length of all the intersecting platelets is equal to:

$$\varphi_L = \sum_i^n \frac{L_n}{L \sin \theta_n} \quad \text{D.2)}$$

where n is the number of intersecting platelets, L_n is the thickness of the n -th intersecting platelet, L is the total length of the line drawn on the TEM image and θ_n is the angle between the n -th intersecting platelet and the line drawn on the TEM image. If the section is perfectly oriented and $\theta_n = 90^\circ$, Eqn. D.2) reduces to,

$$\varphi_L = \frac{nd}{L} \quad \text{D.3)}$$

where d is the thickness of a single clay platelet, which is 1nm for clay. In a not perfectly oriented nanocomposite Eqn. D.3) underestimates the true fractional length. By drawing a line perpendicular to the orientation direction of the platelets, Eqn. D.3) was used to calculate the volume fraction of clay platelets in the PA6 nanocomposites. The apparent distance between platelets was estimated by:

$$\bar{D} = (L - nd) / n = \frac{d}{\varphi_L} - d \quad \text{D.4)}$$

The calculated volume fractions φ_L and the average apparent distance between platelets \bar{D} of the PA6-nanocomposites are listed in table D.1

Weight fraction of silicate	True volume fraction of silicate	Calculated particle distance \bar{D}_{calc} nm	Estimated volume fraction of silicate from TEM	Measured particle distance \bar{D}_{TEM} nm
0.002	0.0008	1250	-	1350
0.01	0.004	250	0.004	256
0.025	0.01	100	0.01	71
0.05	0.02	50	0.04	25
0.075	0.03	33	0.07	13
0.10	0.05	20	0.06	15
0.15	0.07	14	0.13	7
0.20	0.10	10	0.19	4

Table D.1 Estimated volume fraction and interparticle distance obtained by the 'fractional length' method

It can be concluded from Table D.1. that the volume fraction of platelets, calculated by the 'fractional length' method, is equal or larger than the true volume fraction. This illustrates the earlier statement that the amount of platelets seen on a TEM image is larger than the amount of platelets intersecting the upper plane. Of course this is due to the finite thickness of the section.

D.2 Why are clay platelets depicted as single lines in a TEM image?

The contrast in TEM images is usually formed by the absorption of scattered electrons in the object and in the objective lens aperture. This contrast is known as amplitude contrast because it decreases the amplitude of the transmitted wave. Amplitude contrast of thick amorphous objects such as microtomed sections is determined by the projected electrostatic potential (electrons and nuclei). For specimen without too much hydrogen this is proportional to the mass thickness (=density \times thickness of the object). Since a clay platelet has a thickness of only 1 nanometer, the local mass thickness of a TEM section with a thickness of about 70 nanometers, is only marginally increased if the clay platelet lies perpendicular to the electron beam.

According to mass thickness, a clay platelet would only be represented as a single sharp line, if it were perfectly flat and parallel to the electron beam. In not perfectly oriented samples, one would expect that only a very small portion of the platelets line up perfectly with the electron beam. So according to this reasoning only a low portion of the platelets would be visible as sharp lines and most platelets would appear as vague light grey areas. In the previous section only sharp lines were counted to determine the amount of platelets in a coupe. Judging from Table D.1 the volume fraction of platelets that appear as sharp lines is rather high. Since the samples are compression moulded, the clay platelets are not perfectly oriented and they are not perfectly flat. Therefore one would expect a much lower amount of sharp lines as are actually observed. So, in nanocomposites, another mechanism than amplitude contrast must be responsible for the imaging of the platelets.

A possible mechanism is diffraction of electrons by the crystalline clay platelets in well-defined directions (given by the angle, θ). According to Bragg's law this angle depends on the electron wavelength and the crystal lattice spacing:

$$2d \sin \theta = m\lambda \quad \text{D.4)}$$

where m = an integer, λ = the electron wavelength, d = the crystal lattice spacing between atomic planes and θ = the angle of incidence (angle with the plane, not with the normal)

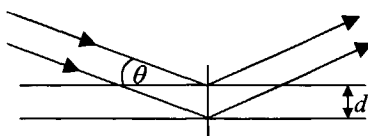


Figure D.2 Bragg's law

This relation gives the conditions for constructive interference of the scattered electron waves. For example, with 120 kV electrons, ($\lambda = 0.0033$ nm) and a d -spacing for a clay platelet of 1 nm, $\sin \theta = 0.00165$ and the Bragg's angle $\theta = 0.095^\circ$.

So only those parts of a clay platelet that are nearly parallel ($\theta = 0.095^\circ$) to the incident beam will diffract the electron beam and show up dark in a TEM image. The reflected beam makes an angle 2θ ($\approx 0.2^\circ$) with the incident beam and it is filtered from the image by a properly chosen objective aperture. The Bragg's condition is somewhat relaxed by the shape transform (spikes) of the platelets, so that it may readily be assumed that for generally curved specimen there will always be at least one line of unit cells in the proper Bragg orientation.

On the surface of a wavy clay crystal more than one line of unit cells can exist, in the proper Bragg orientation. This leads to multiple parallel lines on a TEM image that originate from a single clay particle, as is shown in Fig. D.3.

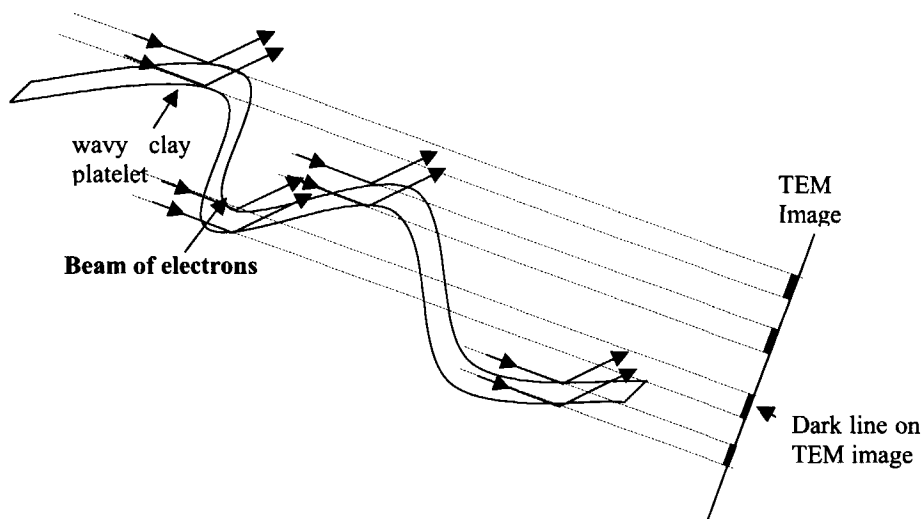


Figure D.3 A wavy clay particle with 4 places that are in the Bragg orientation gives 4 parallel dark lines on a TEM image.

D.3 Conclusions

All complications mentioned above, makes it difficult to perform a quantitative analysis on TEM images of nanocomposites. Therefore TEM images are not suited to quantify the volume fraction or the distance between clay platelets. However, TEM is a valuable tool to determine the length of the clay platelets and to qualitatively check the extent of exfoliation and orientation of clay platelets in a nanocomposite.

[1] G. Kämpf, *Characterization of Plastics by Physical Methods; Experimental Techniques and Practical Application*, Hanser, Munich, 1986

Appendix E

Time and frequency response of composites

Composite mixture formulae are often derived to solve the static response of composites. The question now arises how to calculate the viscoelastic response of composites. The answer to this problem can be found in a combination of Laplace and Fourier analysis and in the elastic-viscoelastic correspondence principle [1] as will be explained below.

E.1. Linear systems and Fourier or Laplace transformation

A linear viscoelastic material is a linear system. A fundamental property of a linear system is that sine waves and, exponential growing or decaying signals do not change their waveform when they pass through the system. They merely change their amplitude and phase. The relationship between complex exponential and sinusoidal signals is expressed by Euler's identity:

$$e^{j\omega t} = \cos \omega t + j \sin \omega t \quad \text{E.1)}$$

which for complex $s=r+j\omega$ is written as:

$$e^{st} = e^{r+j\omega t} = e^{rt} (\cos \omega t + j \sin \omega t) \quad \text{E.2)}$$

If a linear system with a transfer function $H(s)$ receives an input signal $a \cdot e^{st}$ it will produce an output signal $H(s) \cdot a \cdot e^{st}$. More generally any input signal that is a linear combination of complex exponentials $f(t) = \sum_{i=1}^n a_i e^{s_i t}$ will produce an output $r(t) = \sum_{i=1}^n b_i a_i e^{s_i t}$ which is also a linear combination of the same complex exponentials. This property of linear systems is the basis of the Laplace transformation:

$$f(t) = \frac{1}{2\pi j} \int_{r-j\infty}^{r+j\infty} F(s) e^{st} ds, \quad F(s) = \int_{-\infty}^{\infty} f(t) e^{-st} dt \quad \text{E.3)}$$

where $F(s)$ is the Laplace transform of the input signal $f(t)$. A convenient way to use Laplace transformation is to characterise the system under study by its response $h(t)$ to a Dirac pulse δ . It can be shown that if we transform the signals $f(t)$, $h(t)$ and $r(t)$ into their Laplace transforms $F(s)$, $H(s)$ and $R(s)$, then

$$R(s) = H(s)F(s) \quad \text{E.4)}$$

From which the time response $r(t)$ can be calculated by inverse Laplace transformation of $R(s)$. Alternatively the response to a unit step $C(t)$ can also be used to characterise the system:

$$H(s) = sC(s) \quad \text{E.5)}$$

A special case of Laplace transformation, also known as Fourier transformation, can be used if the input signal is periodic. In that case s can be written as $s = j\omega$ giving:

$$f(t) = \frac{1}{2\pi} \int_{-\infty}^{\infty} F(\omega) e^{j\omega t} d\omega, \quad a(\omega) = \int_{-\infty}^{\infty} f(t) e^{-j\omega t} dt \quad \text{E.6)}$$

where $F(\omega)$ is the Fourier transform of the input signal $f(t)$. To use Fourier transformation the input signal must in principle be periodical. The applicability of Fourier transformation is broader though than purely periodical signals, since any non-periodic function of finite duration can be represented by a periodic function.

So the response to an arbitrary input signal can be calculated either by Laplace transformation or by Fourier transformation. To use Laplace transformation the response of the system $h(t)$ to a Dirac pulse or to a unit step $C(t)$ should be known, while for Fourier transformation knowledge of the complex frequency response $R(\omega)$ is required. Either $h(t)$, $C(t)$ or $R(\omega)$ completely characterise the viscoelastic response of a material.

E.2. The correspondence principle

Given the solution for the static problem, it proves to be remarkably simple to calculate the viscoelastic response of a composite. Christensen [1] showed that the transfer function $H(s)$ of the composite can be calculated by replacing all elastic moduli C_i in the mixture formulae by $sC_i(s)$. The time response can then be calculated by taking the inverse Laplace transform of equation E.4. If the input signal is a periodic function the solution is even simpler. Static elastic solutions can be converted to viscoelastic solutions by simply replacing the static moduli C in the mixture formulae by their complex counterpart $C^* = C' + iC''$ (E becomes $E' + iE''$, α becomes $\alpha' + i\alpha''$, ε becomes $\varepsilon' - i\varepsilon''$ etc).

E.3. Practical calculation of the time response of composites

The correspondence principle gives a direct solution to determine the frequency response of a composite. This solution works in practice and does not need further explanation. Determination of the time response of a composite proves to be not so simple in practice. For example let us try to find the stress-response of a composite after a step in deformation (stress-relaxation experiment). We are thus looking for the stress relaxation function $C_c(t)$ of the composite. Let us suppose that either the frequency response $C_i(\omega)$ or the stress relaxation functions $C_i(t)$ of the phases are determined by measurement.

In the route to find $C_c(t)$ two cases should be distinguished, the case that the analytical expression for the mixture formula is simple and the case that no analytical expression is known or too complicated.

For simplicity let us use the mixture formula for a parallel connection of two phases:

$$C_c = c_r C_r + c_m C_m$$

Suppose we know the stress relaxation moduli of the phases $C_r(t)$ and $C_m(t)$ and want to calculate the stress relaxation modulus of the composite $C_c(t)$. To perform Laplace transformation we first fit the stress relaxation moduli $C_i(t)$ by a polynomial function:

$$C_i(t) = a_{i0} + a_{i1}t + a_{i2}t^2 + a_{i3}t^3 + a_{i4}t^4 + \dots$$

Since in most cases $C_i(t)$ is a smooth slowly changing function, the polynomial fit can be made rather accurately without using an excessive number of coefficients. Laplace transformation of $C_i(t)$ gives:

$$C_i(s) = \frac{a_{i0}}{s} + \frac{a_{i1}}{s^2} + 2! \frac{a_{i2}}{s^3} + 3! \frac{a_{i3}}{s^4} + 4! \frac{a_{i4}}{s^5} + \dots$$

Replacing every C_i in the mixture formula by $sC(s)$ gives:

$$C_c(s) = c_r C_r(s) + c_m C_m(s) =$$

$$\frac{c_r a_{r0} + c_m a_{m0}}{s} + \frac{c_r a_{r1} + c_m a_{m1}}{s^2} + 2! \frac{c_r a_{r2} + c_m a_{m2}}{s^3} + 3! \frac{c_r a_{r3} + c_m a_{m3}}{s^4} + \dots$$

after inverse Laplace transformation this gives

$$C_c(t) = (c_r a_{r0} + c_m a_{m0}) + (c_r a_{r1} + c_m a_{m1})t + (c_r a_{r2} + c_m a_{m2})t^2 + (c_r a_{r3} + c_m a_{m3})t^3 + \dots =$$

$$c_r C_r(t) + c_m C_m(t)$$

This example of an extremely simple composite illustrates the complications involved in Laplace and inverse Laplace transformation of mixture formulae. It proves to be relatively easy to obtain an expression in s for the Laplace transform of the composite. Finding the time response by inverse Laplace transformation is more difficult. If the mixture formulae are not too complicated, computer programs that perform symbolic algebra should be able to give an analytical expression for $C_c(t)$ expressed as a polynomial in t .

By fitting $C_i(t)$ by a sum of exponentials the inverse Laplace transformation will probably be easier to perform than with a polynomial fit.

If no analytical expression of the composite mixture formula is known or if the analytical expression is too complicated the above mentioned route can not be used. In that case it is better to switch to Fourier transformation.

E.4 References

- [1] R.M. Christensen, *Mechanics of composite materials*, Wiley, New York 1979, p 17 and p 288.

List of abbreviations

2D	Two Dimensional.
2M2HT	di-Methyl-di-Halogenated-Tallow Ammonium.
3D	Three Dimensional.
6T6I	6-Terephthalic/6-Isophthalic acid.
CLTE	Coefficient of Linear Thermal Expansion.
DMA	Dynamic Mechanical Analysis.
DMS	Dynamic Mechanical Spectroscopy.
DRS	Dielectric Relaxation Spectroscopy.
DSC	Differential Scanning Calorimetry.
EP	Electrode Polarisation.
FE	Finite Element.
FTIR	Fourier Transform Infrared.
HDPE	High Density Polyethylene.
IPP	Isotactic Polypropylene.
LDPE	Low Density Polyethylene.
LLDPE	Linear Low Density Polyethylene.
MEE	Maximum Melt Extensibility.
MSF	Maximum Spin Force (=melt strength).
NMR	Nuclear Magnetic Resonance.
PA	Polyamide.
PE	Polyethylene.
PE-g-MA	Polyethylene grafted with Maleic Anhydride.
PVC	Poly (Vinyl Chloride).
RVE	Representative Volume Element.
TEM	Transmission Electron Microscopy.
VFT	Vogel-Fulcher-Tammann.
vol%	Volume percent.
wt%	Weight percent.

List of symbols

Symbol	Description	SI-Unit
A	Strain concentration tensor.	[-]
$a_0 \ a_2 \ a_4$	0 th , 2 nd , and 4 th coefficients of the Legendre polynomial.	[-]
A_{BET}	BET-Surface area.	[m ² /g]
$A_{contact}$	Surface area of filler in contact with the polymer.	[m ² /g]
B	Stress concentration tensor.	[-]
c_m	Volume fraction of polymer.	[-]
c_r	Volume fraction of filler.	[-]
C_{ijkl}	Component of stiffness tensor.	[N/m ²]
$C_c \ C_m \ C_r$	Stiffness tensor of composite (c), polymer (m) or filler. (r).	[N/m ²]
C_{ij}	Component of stiffness matrix.	[N/m ²]
d	Diameter of fibre.	[m]
D	Diffusivity.	[m ² /s]
$D_c \ D_m \ D_r$	Diffusivity of polymer (m) or filler (r).	[m ² /s]
E_{\perp}	Perpendicular or lowest Young's modulus.	[N/m ²]
$E_{//}$	Parallel or highest Young's modulus.	[N/m ²]
E'	Storage Young's modulus.	[N/m ²]
E''	Loss Young's modulus.	[N/m ²]
E_A	Dielectric activation energy.	[J]
E_{xx}	Young's modulus in x direction.	[N/m ²]
$E_m \ E_r$	Young's modulus of polymer (m) or filler (r).	[N/m ²]
$E_{random \ 2D}$	Young's modulus after randomisation in two directions.	[N/m ²]
$E_{random \ 3D}$	Young's modulus after randomisation in three directions.	[N/m ²]
g	Distance between the ends of inclusions.	[m]
$G^* \ G_d$	Dynamic shear modulus = $(G' + G'')^{0.5}$.	[N/m ²]
G'	Storage shear modulus.	[N/m ²]
G''	Loss shear modulus.	[N/m ²]
G_{xy}	Shear modulus in xy-plane.	[N/m ²]
$G_c \ G_m \ G_r$	Shear modulus of composite (c), polymer (m) or filler (r).	[N/m ²]
ΔH	Change in Enthalpy.	[J/g]
I	Identity tensor.	[-]
k	Boltzmann's constant.	[J/K]
$K_m \ K_r$	Bulk modulus of polymer (m) or filler (r).	[N/m ²]
l	Length of fibre.	[m]
$l_{//}$	Long length of inclusion.	[m]
$L_{//}$	Long length of unit cell.	[m]
L_0	Length of diffusion path in absence of platelets.	[m]
L_c	Length of diffusion path.	[m]
ΔM	Mass increase.	[kg]
ΔM_{max}	Maximum mass increase.	[kg]
$P_c \ P_m \ P_r$	Permeability of composite (c), polymer (m) or filler (r).	[kg/ms]
$P_2 \ P_4$	2 nd and 4 th terms of Legendre polynomial.	[-]
$P_m \ P$	Eshelby's tensor.	[-]
$R_n(\phi)$	Rotation matrix.	[-]
S_{abcd}	Component of compliance tensor.	[m ² /N]
$S_c \ S_m \ S_r$	Compliance tensor of composite (c), polymer (m) or filler (r).	[m ² /N]
S_{mn}	Component of compliance matrix.	[m ² /N]

T	Temperature.	[K]
$[T]$	Rotation transformation matrix.	[-]
t	Thickness of platelet, time.	[m], [s]
T_1	NMR relaxation times of spin-lattice relaxations.	[s]
T_2	NMR relaxation times of spin-spin relaxations.	[s]
T_g	Glass transition temperature.	[K]
T_m	Melting temperature.	[K]
T_v	Vogel-Fulcher-Tammann temperature.	[K]
w	Width of platelet.	[m]
$[W]$	Matrix to transform tensor strain in engineering strain.	[-]
$\Phi(\theta, \phi, \psi)$	Orientation function.	[-]
α	Aspect ratio of inclusion (l/d for fibres ; w/t or t/w for platelets).	[-]
α_{\perp}	Thermal expansion coefficient in perpendicular direction.	[1/K]
$\alpha_{//}$	Thermal expansion coefficient in parallel direction.	[1/K]
α_{ij}	Thermal expansion coefficient in ij -direction.	[1/K]
β	Permeability ratio, shape factor.	[-], [-]
ε'	Real part of complex dielectric constant.	[-]
ε''	Imaginary part of complex dielectric constant.	[-]
ε_{∞}	High frequency dielectric constant.	[-]
ε^*	Complex dielectric constant.	[-]
ε_{ab}	Component of tensor strain.	[-]
ε_n	Component of engineering strain.	[-]
$\varepsilon_c, \varepsilon_m, \varepsilon_r$	Strain of composite (c), polymer (m) or filler (r).	[-]
γ	Shear deformation.	[-]
$\dot{\gamma}$	Shear rate.	[1/s]
η_d	Dynamic shear viscosity.	[Ns/m ²]
ν_{ij}	Poisson's ratio.	[-]
ν_c, ν_m, ν_r	Poisson's ratio of composite (c), polymer (m) or filler (r).	[-]
ρ	Density.	[kg/m ³]
σ	Normal stress or shear stress.	[N/m ²]
σ_{ab}	Component of tensor stress.	[N/m ²]
σ_n	Component of engineering stress.	[N/m ²]
τ	Dielectric relaxation time.	[s]
τ_{∞}	Shortest possible dielectric relaxation time.	[s]
ω	Radial frequency.	[1/s]
ω_{ij}	Component of rotation matrix.	[-]
ζ	Shape factor in Halpin-Tsai equation.	[-]
Ω	Rotation matrix.	[-]

Wat is een polymeer-klei nanocomposiet?

Door een polymeer te vullen met klei kan een materiaal ontstaan met een hoge stijfheid en een lage doorlaatbaarheid voor vloeistoffen en gassen. De beste eigenschappen ontstaan als de klei volledig geexfolieerd is. In dat geval is de klei zodanig goed opgebroken dat er nog slechts losse primaire kleiplaatjes aanwezig zijn van 1 nanometer dik en ongeveer 100 nanometer lang. In dat geval wordt er gesproken van polymeer-klei nanocomposieten. Tijdens het verdelen van de klei in het polymeer worden de kleideeltjes niet alleen veel kleiner, maar verandert ook hun vorm van kubische blokjes naar slanke plaatjes. De kleiplaatjes hebben door hun kleine afmetingen een groot specifiek oppervlak van ongeveer $700 \text{ m}^2/\text{gram}$. Als gevolg van de extreem kleine afmetingen van de kleiplaatjes zijn ook de afstanden tussen de plaatjes in een nanocomposiet zeer klein. Deze afstanden bedragen ongeveer 250 nanometer bij een vulling van 1 gewichtsprocent en slechts 10 nanometer bij een vulling van 20 gewichtsprocent.

Waarom hebben nanocomposieten goede eigenschappen?

In de wetenschappelijke literatuur worden de goede eigenschappen van polymeer-klei nanocomposieten vaak toegeschreven aan de extreem kleine afmetingen van de kleiplaatjes. De redenering is dat in een nanocomposiet een groot deel van de polymeermoleculen in direct contact staat met de kleiplaatjes. Dit verandert het gedrag van de polymeer moleculen zodanig dat het nanocomposiet de eerder vernoemde eigenschappen krijgt. Volgens deze redenering is de slankheid van de kleiplaatjes van ondergeschikt belang.

Twijfel aan deze redenering vormde de aanzet tot het hier beschreven onderzoek. De twijfel was ingegeven door de wetenschap dat de eigenschappen van gewone (micro)composieten met vezels of plaatjes van enkele micrometers of groter, vooral een gevolg zijn van de slanke vorm en niet van de absolute grootte van de vezels of plaatjes. Verder was het bekend dat de geadsorbeerde polymere fase aan het oppervlak van een vulstof gewoonlijk een dikte heeft van 1 tot 5 nanometer. In conventionele nanocomposieten met afstanden tussen de kleiplaatjes van ongeveer 100 nanometer, zou men dus mogen verwachten dat deze geadsorbeerde fase maar een bescheiden rol speelt.

In dit proefschrift wordt besproken welke eigenschappen van polymeer-klei nanocomposieten het gevolg zijn van de kleine afmetingen (hoog specifiek oppervlak) en welke van de slanke vorm van de kleiplaatjes.

De invloed van deeltjesvorm en deeltjesgrootte op de eigenschappen van nanocomposieten kan onderscheiden worden door de eigenschappen van nanocomposieten te vergelijken met die van microcomposieten of met de uitkomsten van micromechanische composiet berekeningen.

Micaplaitjes lijken qua vorm en kristalstructuur zeer veel op primaire klei-plaitjes. Alleen hun absolute afmetingen zijn ongeveer een factor 1000 groter. Vandaar dat de microcomposieten die als referentie gebruikt worden in dit proefschrift meestal micaplaitjes bevatten. Aangezien de slankheid van de micaplaitjes altijd wel iets verschilt van die van de kleiplaitjes, is een directe vergelijking van eigenschappen moeilijk.

Voor een wetenschappelijk juiste vergelijking van de eigenschappen van nanocomposieten met die van microcomposieten worden daarom mathematische composietmodellen gebruikt. Met composietmodellen kunnen de eigenschappen van een composiet berekend worden.

Doelstellingen van dit proefschrift

- Uitzoeken welke eigenschappen van polymeer-klei nanocomposieten het gevolg zijn van de kleine afmetingen en welke van de slankheid van de klei-plaatjes.
- Ontwikkelen en toetsen van composietmodellen voor de berekening van de elastische en barrière eigenschappen van met plaatjes gevulde composieten.
- In kaart brengen hoe kleiplaatjes de eigenschappen van polymeer-klei nanocomposieten beïnvloeden, zoals stijfheid, thermische uitzetting, kristallisatie, gasdiffusie, reologie en diëlektrische relaxatie.
- Inzicht krijgen in de verschillen tussen nanocomposieten en microcomposieten, door directe vergelijking van hun eigenschappen en door toepassen van composietmodellen.

Ontwikkeling en toetsing van een mechanisch composietmodel voor plaatjes versterking

Voor berekening van de stijfheid en thermische uitzetting van met plaatjes versterkte polymeren is gekozen voor het Mori-Tanaka model. In principe is dit analytische micromechanische model alleen geschikt voor composieten met perfect georiënteerde plaatjes. Met behulp van een oriëntatie-distributiefunctie kan ook rekening gehouden worden met willekeurig georiënteerde plaatjes.

Omdat het praktische gebruik van het Mori-Tanaka model en van de oriëntatie-distributie functie nogal omslachtig is, worden er ook enkele vereenvoudigde theorieën geïntroduceerd. Hiermee is het mogelijk om snel en relatief nauwkeurig composietberekeningen te doen.

Om de deugdelijkheid van het Mori-Tanaka model te toetsen zijn de uitkomsten van dit model vergeleken met experimentele gegevens van microcomposieten. Ook zijn de uitkomsten vergeleken met berekeningen van een op eindige elementen gebaseerd model. Het blijkt uit beide gevallen dat met het Mori-Tanaka model goede voorspellingen gedaan kunnen worden van de stijfheid en de thermische uitzetting van met plaatjes gevulde composieten.

Morfologie van nanocomposieten en mobiliteit van de polymere fase

Er zijn twee series nanocomposieten gemaakt door polyamide-6 of polyetheen samen met klei te extruderen. De klei was van tevoren zodanig behandeld dat deze goed in de polymeren zou verdelen. In de serie met polyamide-6 is de hoeveelheid klei gevarieerd en in de serie met polyetheen de slankheid van de kleiplaatjes.

De vorm en verdeling van kleiplaatjes in de polymeren is zichtbaar gemaakt met transmissie elektronen microscopie (TEM). Uit een kritische analyse blijkt dat de zwarte streepjes in TEM foto's van polymeer-klei nanocomposieten geen directe afbeelding van de kleiplaatjes betreft, maar een elektronen diffractiepatroon. Voorzichtigheid is daarom geboden bij de interpretatie van TEM foto's van polymeer-klei nanocomposieten.

De mobiliteit van de polymere fase in nanocomposieten werd onderzocht met proton vaste stof nucleaire magnetische resonantie (NMR). *Het blijkt dat een deel van de polymere fase in polyamide-6-klei nanocomposieten net zo beweeglijk is als een laagmoleculaire vloeistof.* De hoeveelheid polymeer met hoge beweeglijkheid stijgt naarmate de hoeveelheid klei toeneemt. Bij 20% klei is ongeveer 10% van de polyamide-6 in het nanocomposiet zo beweeglijk als een vloeistof.

Thermisch gedrag van nanocomposieten

Het kristallisatie- en het smeltgedrag van PA6 en PE-nanocomposieten is onderzocht met differentiële scanning calorimetrie (DSC) en met infrarood spectroscopie. Met DSC is gemeten bij welke temperatuur de nanocomposieten smelten en met infrarood spectroscopie werd de kristalvorm bepaald.

De onderzochte polyamide-6 nanocomposieten blijken drie verschillende smeltpunten te vertonen. Normaal gesproken bevat polyamide-6 uitsluitend α -kristallijn materiaal dat smelt rond 225°C. *Door toevoegen van klei ontstaan er twee nieuwe kristallijne fasen met smeltpunten beneden en boven die van de α -kristallijne fase.* Het smeltpunt van de laagsmeltende fase ligt bij 212°C en dat van de hoog smeltende fase bij 240 °C. De laagsmeltende fase is al vermeld in de wetenschappelijke literatuur en wordt toegekend aan γ -kristallijn materiaal.

De hoog smeltende fase was nog niet eerder beschreven. Uit infrarood spectroscopie blijkt dat deze fase ook bestaat uit γ -kristallijn materiaal. Het hoge smeltpunt ontstaat waarschijnlijk doordat een deel van de γ -kristallijne fase opgesloten zit tussen de kleiplaatjes en daardoor een beperkte bewegingsvrijheid ervaart. Hierdoor is er een hogere temperatuur nodig om dit deel van de γ -kristallijne fase te laten smelten. ($T_m = \Delta H / \Delta S$, ΔS daalt dus T_m stijgt).

Diëlektrisch gedrag van nanocomposieten

De mobiliteit en de relaxatiemechanismen van de polymere fase in polyamide-6 nanocomposieten is bepaald met diëlektrische relaxatie spectroscopie (DRS). Hiertoe zijn metingen gedaan met frequenties tussen 0,11 en 960 kHz. en temperaturen tussen -130 en 200°C.

Het belangrijkste verschil met ongevuld polyamide-6 is dat de nanocomposieten een tweede glasovergang vertonen welke ongeveer 40°C beneden de normale glasovergang ligt. De sterkte van deze overgang neemt toe naarmate de hoeveelheid klei toeneemt. Deze overgang wordt ook waargenomen met dynamisch mechanische analyse (DMA).

Uit bestudering van de activeringsenergie kan worden geconcludeerd dat opsluiting van polymeermoleculen een relatief begrip is en bepaald wordt door de frequentie en de temperatuur van de meting. Bij hoge frequenties of lage temperaturen voelt het polymeer zich niet opgesloten omdat de meeste beweging dan plaatsvindt over een lengte die kleiner is dan de afstand tussen de kleiplaatjes. Opsluiting wordt pas waargenomen bij lage frequenties en hoge temperaturen als de beweging plaatsvindt over een lengte die groter is dan de afstand tussen de kleiplaatjes.

Stijfheid en thermische uitzetting van nanocomposieten

De stijfheid van polyamide-6-klei en polyetheen-klei nanocomposieten werd bepaald met dynamisch mechanische thermische analyse (DMA) en door trekproeven. Beide types nanocomposieten worden stijver door toevoeging van klei.

Bij lage hoeveelheden klei (<5 gewichtsprocent) komt de stijfheid overeen met die van mica microcomposieten en met de eigenschappen die voorspeld worden door composietmodellen. *Uit de metingen en de composietberekeningen blijkt dat de hoge stijfheid van nanocomposieten een gevolg is van de hoge slankheid en niet van de kleine afmetingen van de kleiplaatjes.*

De stijfheid van nanocomposieten met meer dan 10 gewichts procent (wt%) klei is lager dan die van vergelijkbare mica-composieten en ook lager dan voorspeld wordt door composietmodellen. Deze lage effectiviteit van de kleiplaatjes bij hoge vulfracties wordt toegeschreven aan de kleinere afstand tussen kleiplaatjes zoals ook met transmissie electronen microscopie wordt waargenomen. Bijvoorbeeld, boven 10 wt% klei is de afstand tussen de kleiplaatjes kleiner dan 20 nanometer. Hierdoor neemt de effectieve slankheid van de kleiplaatjes af, terwijl gelijktijd een hoog mobiele fase verschijnt in de beperkte ruimte tussen de kleiplaatjes. Opsluiting van het polymeer tussen de kleiplaatjes leidt ook tot een lagere kristalliniteit en een lagere kristalperfectie. Al deze effecten kunnen alleen maar resulteren in een lagere stijfheid van het nanocomposiet tot gevolg hebben. *In tegenstelling tot*

beweringen in de wetenschappelijke literatuur laten de metingen zien dat de stijfheid van het nanocomposiet daalt door opsluiting van het polymeer tussen de kleiplaatjes.

Uit theoretische beschouwingen blijkt dat de thermische uitzettingscoëfficiënt van een composiet direct gerelateerd is aan de stijfheid van het composiet. Hoe stijver het composiet is hoe minder het zal uitzetten, terwijl het composiet het meeste zal uitzetten in de richting met de laagste stijfheid. Het blijkt dat de theorie een nauwkeurige voorspelling geeft van de relatie tussen de stijfheid en de thermische uitzetting van polyamide-6-klei nanocomposieten.

Barrière eigenschappen van nanocomposieten

Het is bekend dat kleiplaatjes de doorlaatbaarheid van gassen en vloeistoffen door nanocomposieten verlagen. Om uit te zoeken welke mechanismen hiervoor verantwoordelijk zijn werd de wateropname van een serie polyamide-6-klei nanocomposieten gemeten. De diffusiecoëfficiënt is bepaald aan de hand van eenvoudige Fickse diffusie.

De doorlaatbaarheid van polymeer-klei nanocomposieten is vergeleken met voorspellingen van composietmodellen. Verschillende modellen zijn hiertoe beschouwd welke de doorlaatbaarheid relateren aan de morfologie van meerfasige materialen. Omdat geen enkel model in staat is om de doorlaatbaarheid van plaatjes gevulde composieten bij hoge volume fracties te voorspellen werd er een nieuw model geïntroduceerd. Dit model is een combinatie van het model van Brydges, dat geschikt is voor composieten met linten, en het model van Hatta, dat geschikt is voor plaatjes bij lage volume fracties. De resultaten van dit nieuwe model komen overeen met de resultaten van eindige elementen berekeningen.

Door aanpassing van Nielsens transportmodel wordt een theorie afgeleid om het effect van niet perfecte oriëntatie van kleiplaatjes te verdisconteren. Het blijkt dat de doorlaatbaarheid van polyamide-6-klei nanocomposieten goed overeenkomt met de voorspellingen van de modellen van Nielsen en Hatta. *De goede overeenkomst tussen model en experiment geeft aan dat de doorlaatbaarheid voornamelijk bepaald wordt door de slankheid van de kleiplaatjes, de deeltjesgrootte van de kleiplaatjes is van ondergeschikt belang.*

Reologie van nanocomposieten

Het effect van afmeting en slankheid van deeltjes op het reologische gedrag van nanocomposieten en microcomposieten werd onderzocht. Hiertoe zijn polyamide-6 en polyetheen gevuld met bolletjes en plaatjes met afmetingen tussen 10^{-9} en 10^{-4} m. De reologie van deze materialen werd bepaald onder afschuif en rek-deformatie. Het visco-elastische gedrag van polymeer nanocomposieten in de gesmolten fase blijkt zeer sterk te verschillen van dat in de vaste fase. *Zo blijkt, in tegenstelling tot vaste nanocomposieten, dat de visco-elasticiteit van gesmolten nanocomposieten sterk afhankelijk is van de deeltjesgrootte, terwijl de slankheid van de kleiplaatjes geen invloed heeft.*

In tegenstelling tot microcomposieten blijken polymeer-klei nanocomposieten een hoge smeltsterkte te hebben en een hoge viscositeit die niet verdwijnt onder grote afschuifdeformatie. Twee mechanismen worden voorgesteld die deze effecten kwalitatief kunnen verklaren: hechting van polymeerketens aan de kleiplaatjes en de vorming van een elektrische dubbellaag op de kleiplaatjes.

Curriculum Vitae

Martin van Es werd geboren op 1 juni 1960 te Amsterdam en heeft zijn jeugd doorgebracht in Heerlen. Nadat hij in 1977 het HAVO diploma behaalde op het Rombouts College in Brunssum ging hij Fysische Techniek studeren aan de HTS in Heerlen. In 1981 studeerde hij af binnen de sectie Regeltechniek.

Wegens krapte op de arbeidsmarkt heeft hij vervolgens 2 jaar gewerkt als bouwvakker en als fabrieksmedewerker. In zijn vrije tijd werkte hij als lid van de vereniging 'Duurzame Energie Limburg'.

In 1983 hervatte hij de studie en begon aan de opleiding Technische Natuurkunde van de Technische Universiteit van Eindhoven waar hij de propedeuse en het tweede studiejaar grotendeels voltooide.

In 1984 begon hij als laboratoriummedewerker op de afdeling Humane biologie van de Universiteit van Maastricht, waar hij werkte met vacuümsystemen en massaspectrometers ter ondersteuning van een onderzoek naar de energiehuishouding van het menselijk lichaam.

In 1986 werd een baan aanvaard bij DSM-Research op het gebied van de mechanische eigenschappen van kunststoffen. Er werd voornamelijk gewerkt aan het combineren van mechanische testen met andere meetmethodes om zodoende meer te weten te komen over de relatie tussen de morfologie en de eigenschappen van kunststoffen. Zo werd er een methode ontwikkeld en geautomatiseerd om met IR-spectroscopie de kristalliniteit en oriëntatie van polymeermoleculen te bepalen tijdens een trekproef.

Vanaf 1994 tot heden vervulde hij bij DSM-Research de functie van productontwikkelaar van nieuwe materialen. Tot 1997 werd onder andere gewerkt aan het bestralen van kunststoffen, aan het radicalair enten van monomeren op polymeren in de vaste fase en aan de nucleatie van de kristalgroei in kunststoffen.

Vanaf 1997 is voornamelijk gewerkt aan het verbeteren van de eigenschappen van kunststoffen door het maken van polymeer-nanocomposieten. Gelijktijdig met het werk aan nanocomposieten op DSM-Research werd het hier beschreven promotiewerk uitgevoerd onder begeleiding van Professor J. van Turnhout van de faculteit Technische Natuurwetenschappen, afdeling Technische Materiaalwetenschappen, sectie Polymer Materials & Engineering.

Dankwoord

Promoveren binnen een bedrijf als DSM is onmogelijk zonder hulp van je collega's. Meer nog dan binnen een universiteit ben je dan afhankelijk van de steun van anderen bij het maken en testen van materialen. Ik wil met name Jos Put en Jef Vincent van de directie van DSM-Research bedanken voor de mogelijkheid die mij geboden is om dit promotieonderzoek binnen DSM-Research te voltooien.

Mijn dank gaat vooral uit naar een aantal mensen die op bijzondere wijze aan de totstandkoming van dit proefschrift hebben meegewerkt.

Allereerst gaat mijn dank uit naar mijn promotor Prof. van Turnhout voor zijn steun en voor de vele zaterdagen die hij heeft opgeofferd om mijn werk kritisch te analyseren.

Verder wil ik hier Prof. Marissen bedanken voor zijn niet nalatende aandacht, voor de vele discussies die wij voerden en voor het proeflezen van dit proefschrift.

Men name wil ik ook Patrick Voets bedanken voor zijn hulp bij het maken en testen van de nanocomposieten en voor zijn opbeurende woorden als het even tegenzat.

Prof. Maurer ben ik bijzonder erkentelijk voor zijn leerzame en stimulerende invloed. Zonder hem had ik niet de moed gehad om aan dit proefschrift te beginnen.

Feng Xiqiao en Prof. van der Giessen hebben een belangrijke bijdrage geleverd aan het theoretische gedeelte van dit proefschrift, hiervoor mijn dank.

Ik ben ook afgestudeerder Francois Simon zeer erkentelijk voor zijn hulp bij het schrijven van het computerprogramma ter berekening van de eigenschappen van composieten.

Andrei Gusev wil ik bedanken voor zijn eindige elementen berekeningen met het Palmyra computer programma.

Ik wil Monique Walet en Renate Tandler bedanken voor het maken van de TEM foto's, immers zonder TEM-foto's kun je geen nanocomposietonderzoek doen.

Ik ben Victor Litvinov zeer erkentelijk voor zijn waardevolle bepaling van de hoog mobiele fase in PA6 nanocomposieten met vaste stof NMR.

Lut Dirks wil ik bedanken voor haar DSC metingen aan PA-6 nanocomposieten.

Ben Noorder en afgestudeerder Vincent van de Heuvel ben ik dank verschuldigd voor de DSC en DMA metingen aan PE-nanocomposieten.

Ook wil ik Piet Droppert hartelijk bedanken voor het doen van de DRS-metingen en voor de vele mailtjes met opmerkingen van Professor Turnhout.

Jos Linsen en Herman Roolant hebben heel wat DMA metingen gedaan aan PA-6 nanocomposieten. Hun inzet en de hoge kwaliteit van hun werk heb ik steeds op prijs gesteld.

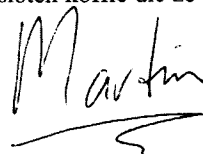
Met name Andre Brands heeft een grote bijdrage geleverd aan de metingen van de uitzettingscoëfficiënt, de wateropname, de trek-rek krommen en de slagvastheid van de PA-6 nanocomposieten, hiervoor mijn dank.

Voor de reologiemetingen wil ik Jo Palmen, Ton Sleijpen en Wilbert Janssen bedanken. Hun werk is van wereldklasse.

Ik ben ook Peer Froehling dankbaar voor de beeldverwerking en deeltjesgrootte analyse van de HDPE-BaSO₄ compounds.

Verder wil ik Paul Steeman, Hartmut Fischer, Rudy Deblieck, Vincent Mathot en Aylvin Dias, bijzonder bedanken voor het nakijken van verschillende hoofdstukken van dit proefschrift.

Last but not least wil ik Lucy bedanken. Zonder haar liefde en de sloten koffie die ze voor mij gezet heeft had ik dit proefschrift niet kunnen schrijven.



A

Amorphous phase, 78, 136
Anisotropic material, 13, 15
Average Stress Theory, 19, 22, 46

B

Barrier Resistance, 2-6, 136-137, 146, 154, 160-161

C

Clay, 9-11
 Cations, 7, 10, 11
 Crystalline Structure, 9-10
 Exfoliation, 9-11, 56-59, 60-61, 72-73, 81-82, 121, 125, 129, 134, 174, 176, 212
 Inter-layer, 11, 73
Compliance, 14, 16, 22, 27, 28, 30, 33, 40-41, 193, 196-197, 200-201
Compliance tensor, 22, 27-28, 30, 33, 40, 193
Composite modelling, 5, 6, 17, 19, 39, 45-46, 53, 115, 119, 121, 126, 129, 131, 133-137, 174, 198-199, 207
 Validation, 45-46, 50
Confinement, 6, 59, 73, 81-82, 93-96, 99-102, 113, 115, 134, 186
Continuum Mechanics, 13, 127
 Abbreviated Nomenclature, 14
 Coordinate Transformation, 28-30, 197
 Correspondence Principle, 39, 174, 213-214
Crystal growth, 133
Crystal perfection, 115, 133, 134
Crystalline structure, 5-6, 9-10, 73, 84-85, 93, 119, 123, 136
Crystallisation, 2, 5-6, 8, 83-87, 94-96, 133-134

D

Differential scanning calorimetry, 57-58, 79, 83-87, 92-98, 133-134, 217
Diffusion, 5-6, 17, 73, 135-161, 182
Diffusivity, 50, 73, 135-160, 182
Dilute systems, 20
Dimension stability, 3

E

Einstein summation convention, 30
Engineering stiffness or strain, 15-16, 33, 189, 193-197
Equivalent inclusion, 19, 46, 135, 141, 148, 185
Eshelby, 19, 21-22, 43, 46, 135, 141, 147, 148, 185-192, 200-202, 207-208, 219

F

Fibres, 1, 3, 4, 17, 19, 23, 26-27, 33-37, 39, 41
Fillers, 2, 164-168, 176-180, 183
Finite element modelling, 6, 45-46, 50-53, 151, 160
Flame retardancy, 2
Fractional length method, 60, 209
Free volume, 73, 104-105, 112-113, 123, 136
FTIR measurements, 85, 98

G

Global Coordinate System, 28

H

Halpin-Tsai, 17-18, 36-39, 45-49, 118-121, 131, 141, 174, 207-208
High temperature melting process, 83, 86, 93, 99

I

Immobilised polymer, 73
Interface, 4, 17, 73, 143, 164-165, 184, 198
Inter-particle distance, 60, 164-165
Interphase, 4, 73

L

Lamellar thickening, 84
Lamellar thickness, 93-96
Layered silicates, 2, 5, 7, 9, 10, 184

M

Making nanocomposites, 5
Master batch, 55-57
Mechanical Properties, 1, 5, 8, 17, 31, 43-44, 54, 84, 99, 115, 123, 136-137, 147
Melt enthalpy, 95, 96
Melting, 73, 83-86, 91-99, 125

Mica, 2-4, 8-11, 22, 36-37, 41, 44-50, 53, 115, 119, 134, 152, 157, 167, 176-181
Mobile phase, 75-82, 117, 123, 133-134
Montmorillonite, 7, 9, 11, 22, 55-70, 72, 75, 82-83, 85, 96, 123, 129, 131, 133, 159, 176
Mori-Tanaka, 17-22, 26-28, 32-33, 36-37, 41-46, 50-53, 127, 171, 174, 178-180, 199, 202, 207-208

N

Nucleation, 119

O

Organically treated clay, 56
Orientation average, 27, 30, 31, 32, 33
Orientation function, 5, 13, 30-32, 46, 126-127, 199-203
Orientation, 27-36, 119-121, 153-161

P

Packing constraints, 73, 113
Palmyra model, 46, 50-53
Particle-particle interactions, 19, 164, 171, 178, 180, 183
Permeability, 17, 50, 135-150, 159-160, 208
Polymer mobility, 59, 73, 106
Processing, 1, 2, 55-58

R

Random orientation, 6, 30-34, 49, 53, 119, 127, 129, 154, 179, 203
Randomisation, 13, 34-35, 200-202
Rigid phase, 78-82
Rule of mixtures, 23, 37, 39, 47

S

Self-diffusion coefficient, 73

Shape factor, 18, 36-39, 47-48, 141, 147, 174, 207, 208
Smectic clay, 2, 10
Solid-state NMR, 73
Spin-lattice relaxations, 73, 75
Spin-spin relaxations, 75
Stiffness tensor, 20, 22, 27-28, 30, 46, 126-127, 186, 188, 194
Strain concentration tensor, 21, 33, 186-187, 195, 200
Stress concentration tensor, 21-22, 33, 195, 200
Suppression of melting temperature, 83
Surface area, 73, 135, 137, 143, 160, 165, 168
Symmetry, 15-20, 30-31, 37, 40, 187-188, 190, 198, 201, 202, 205, 207
Synthetic mica, 57-58, 71-72, 82, 96, 129, 131, 159
Synthetic smectite, 57-58, 69, 72, 82, 96, 129, 131

T

T1-relaxation, 75
T2-relaxation, 74, 75
Tactoids, 59, 61, 72, 81, 121, 174
Takanayagi model, 17-18, 23-27, 145
Talc, 1-2, 10, 11, 51
Tensor notation, 14-15, 30, 193, 203
Tensor strain, 15, 194, 196
Thermal expansion 5, 13, 17, 39-41, 45, 50, 53, 82, 115, 123-127, 134, 198-200
Transmission electron microscopy 6, 57-72, 81-82, 118-121, 129, 131, 157, 159, 174, 176, 209-212

Z

Zeeman splitting, 74

Polymer-clay nanocomposites belong to a relatively new class of materials with a favourable combination of properties. They consist of polymers filled with clay platelets. These clay-platelets are extremely small. Their diameter is about 100 nanometers while their thickness is close to 1 nanometer, hence the name nanocomposites. Polymer-clay nanocomposites combine high stiffness and high barrier resistance with a smooth surface and good processability.

In this thesis various properties of nanocomposites are discussed. The author reacts against statements in the scientific literature, that attribute the properties of polymer nanocomposites to the high surface area and small size of the clay platelets. By comparing polymer-clay nanocomposites with microcomposites it is shown however, that the shape of the clay particles is much more important than their size in determining the high stiffness and high barrier resistance of polymer-clay nanocomposites.

Throughout this thesis, composite modelling is used as a tool to calculate the properties of polymer-clay nanocomposites. It allows a sound scientific comparison of properties of nanocomposites with those of microcomposites. Considerable effort has been put into the development of a reliable composite model for platelet reinforcement.

Only at high loadings, above 10 weight percent of clay and well outside the range of normal processable polymers, the size of the clay platelets becomes important. At such loadings polymer-clay nanocomposites show remarkable properties.